UNIVERSITY OF WUPPERTAL

School of Electrical, Information and Media Engineering

BERGISCHE UNIVERSITÄT WUPPERTAL

PhD Thesis

Charge Extraction and Recombination Layers for Organic and Hybrid Multi-Junction Solar Cells

Tim Becker

INSTITUTE OF ELECTRONIC DEVICES

First Examiner: Prof. Dr. Thomas Riedl
Second Examiner: Prof. Dr. Daniel Neumaier

Submission date: September 15, 2023

Contents

1 Introduction

A growing world population, higher standards of living in development countries and a more and more digitalized society lead to an ever increasing world energy demand. In addition to this, climate change as a result of carbon heavy energy production based on fossil fuels already causes increasing issues for millions of people around the planet and will continue to claim severe casualties if there is no change to global energy production and management. To reach the goal of a global average temperature increase of 1.5 °C (above pre-industrial levels) by 2050 a rapid and profound transformation of our energy system is required. This became increasingly visible in recent years, as the global demand for energy surged by 5.4 % in 2021 due to the global economic rebound following the COVID-pandemic and was partially met by new investments into fossil fuel infrastructure.[1] In addition to this, Russia's invasion of Ukraine and the following disputes in energy politics further manifested the need for a diversification of the energy portfolio to achieve stability and independence in this sector.

On this account, future generations depend on the extension of sustainable energy harvesting based on renewable sources. In addition to prominent examples of wind turbines and hydroelectric power plants, one of the most promising candidates to lastingly reduce carbon emissions and provide clean energy is solar power, especially photovoltaics. With the sun providing orders of magnitude more energy per year than the worlds demand, an area as small as 0.3 % of the planets land mass covered by photovoltaics could be sufficient to theoretically cover its electricity consumption.[2,3]

Within this field, organic photovoltaics (OPV) have emerged as a groundbreaking technology with the potential to revolutionize the

landscape of solar energy conversion. Unlike traditional silicon-based solar cells, OPV employs organic materials to convert sunlight into electricity, offering several advantages such as flexibility, lightweight, and ease of manufacturing on diverse substrates. Over the past few decades, extensive research efforts have been directed towards enhancing the efficiency, stability, and cost-effectiveness of organic photovoltaic devices, paving the way for their integration into various applications ranging from portable electronics to building-integrated solar panels.

The foundation of organic photovoltaics lies in the innovative utilization of organic semiconductors, which exhibit unique optoelectronic properties that can be tailored through molecular engineering. This affords researchers the ability to design materials with specific absorption characteristics and compatibility with low-cost deposition processes such as solution-based potentially roll-to-roll compatible fabrication techniques. As a result, the field of organic photovoltaics has witnessed a rapid evolution in material design, leading to the development of high-performance organic semiconductors and novel donor-acceptor systems that facilitate efficient charge separation and transport.

Apart from materials innovation, the optimization of device architecture plays a crucial role in achieving high power conversion efficiencies (PCE). Interfaces between different organic layers, electrodes, and interfacial layers all influence the overall device performance. Additionally, the delicate balance between exciton dissociation and recombination processes presents a significant challenge that demands meticulous engineering to maximize energy conversion efficiency. Moreover, device architecture has a crucial influence on device stability, tackling questions regarding the stringent lifetime requirements to be met for real-world applications.

In the field of organic photovoltaics (OPVs), multi-junction solar cells present a paradigm shift from single-junction devices by enabling the utilization of a broader portion of the solar spectrum. These types of devices consist of multiple sub-cells with varying energy gaps, each designed to capture photons from different parts of the solar spectrum. This design facilitates a drastic increase in device efficiency, but bares new challenges with regards to device architecture. The efficient extraction of photo-generated charges from multiple sub-cells is contingent on the establishment of balanced charge carrier generation, transport, and recombination. This is where recombination or interconnection layers (ICLs) play a pivotal role.

Strategically positioned between adjacent sub-cells, recombination layers are not only demanding concerning their optical characteristics. Furthermore, they regulate the flow of electrons and holes to ensure that recombination events occur predominantly at desired interfaces. Therefore, the optimization of recombination layers involves careful engineering of the interfacial energetics and charge mobility to mitigate unwanted charge accumulation and subsequent losses due to parasitic recombination. Moreover, they have to provide chemical resilience and protection of the underlying sub-cells against solvents used in subsequent fabrication steps. Taking into account the abovementioned criteria, recombination layers are probably one of if not even the single most demanding part of multi-junction photovoltaic architectures. Within this thesis, multiple approaches for efficient and widely applicable recombination layers will be presented. Utilizing combinations of robust deposition methods, novel approaches of ICLs combining only metal oxides will be demonstrated to facilitate multi-junction device architectures comprising either two organic sub-cells or

even a highly efficient combination of organic and halide perovskite sub-cells.

Further chapters will elaborate on specific advantages that come with the novel all-oxide approach and present different routes to even fabricate fully solution processed ICLs for efficient organic multi-junctions. The presented work will demonstrate crucial progress for both sub-cell species, perovskite and organic, in addition to a loss-free recombination layer building upon the preceding all-oxide concept, converging in a device achieving a new efficiency world record for perovskite-organic tandem solar cells of 24 %. Furthermore, a realistic prospect for solar cells of this kind to reach efficiencies of > 30 % will be illustrated by a dedicated semi-empirical electro-optical simulation. Following this, surprising findings on device stability of highly efficient organic photovoltaic materials will be presented and pathways to elucidate the degradation mechanisms will be discussed and strategies to their mitigation will be demonstrated.

2 Physical Fundamentals

In the following the fundamental groundwork for this thesis will be presented. Basic working principles and components of (organic) solar cells as well as their characterization, their elementary fundamental limits and challenges will be discussed. The approach of tandem or multi-junction solar cells will be introduced and it will be displayed how these architectures enable to overcome the aforementioned limits. Their working principles will be described and manufacturing as well as characterization challenges will be addressed. Moreover, this chapter will expand on the specifics of charge extraction and interconnection architectures and how they contribute to basic aspects like efficiency and stability in single- and multi-junction organic solar cells. Further, metal-halide perovskites will be introduced as a possible material class for hybrid multi-junction devices in combination with an organic sub-cell and the advantages and challenges of this species of devices will be depicted.

2.1 Organic Solar Cells

In organic photovoltaics (OPV), organic semiconductors are used as light absorbing photoactive materials. After the electrical conductivity of doped polyacetylene had been discovered in the end of the 1970s [4,5], demonstrating a polymer with metallic electronic properties for the first time, which led to the Nobel Prize for Shirakawa, MacDiarmid and Heeger in 2000, organic semiconductors have been subject of a wide range of investigations. Since then, many organic semiconductor materials have

been developed, leading to several applications inter alia in the field of optoelectronics.

The electronic properties of organic semiconductors are based on an alternating series of covalent single (σ-bonds) and double bonds (π-bonds) within the molecules and polymers, forming a conjugated π-electron system. This results in a delocalization of the molecule's electrons and gives rise to a band-like orbital structure with clearly defined energy gaps, which imparts the semiconducting features to the molecules (details in **Paragraph 2.1.1**). The different possibilities in molecule design allow for a tunability of the electronic levels of organic semiconductors, which made them interesting candidates for a large number of devices. Besides OPV there have been other applications like organic field-effect transistors (OFET) or organic light-emitting diodes (OLED).

In addition to their tunable optoelectronic characteristics, these materials provide other advantages compared to inorganic semiconductors like silicon (Si). Their solubility in organic solvents enables new roll-to-roll compatible methods for thin film deposition like slot-die coating or inkjet printing, which facilitates easier and potentially low-cost, large-area fabrication of organic thin film devices.

These advantages in possible adjusting of properties and solution based processing also rank among the decisive properties of organo-metal halide perovskite thin film electronics (see **Paragraph 2.2.4**). This opens the pathway for combining organic and perovskite thin films as "partners" in hybrid multi-junction photovoltaic devices (also see **Chapter 4**).

2.1.1 Charge Generation and Transport

In organic semiconductors, as they are used in OPV devices, the absorption of a photon with an energy E_{photon} that exceeds the energy gap E_g leads to the generation of a strongly bound pair of an electron and a defect-electron (or hole). Such electron-hole pairs with high binding energy are also called "Frenkel"-excitons. The energy gap of an organic semiconductor is defined as the energetic difference between the highest occupied molecular orbital (HOMO) and the lowest unoccupied molecular orbital (LUMO), which are a result of the delocalized π-electron system of these organic semiconducting molecules. The fact that the two carriers forming the exciton (the electron inside the LUMO and the hole inside the HOMO) are bound by a strong Coulomb interaction leads to a high exciton binding energy $E_{b,exciton}$ of up to 1 eV (electron volt)[6–8] and stands in stark contrast to inorganic crystalline semiconductors like e.g. Si, where the absorption of photons with suitable energy generally creates free charge carriers (electrons and holes), which can be easily separated.

To separate the Frenkel exciton into an electron and a hole it is necessary to overcome its binding energy, which can be achieved by introducing a second material in the active layer. If the LUMO level of the second material lies energetically below the LUMO of the first, it provides a preferable state for the electron. The material with the higher lying LUMO level can then be signified as the donor (D) and the one with the lower lying LUMO as the acceptor (A). In the case that the energetic difference between the two LUMO levels exceeds the binding energy of the exciton ($\Delta E_{LUMO} > E_{b,exciton}$), the separation of the charge carriers at the D/A-interface is enabled, whereupon the hole is still located in the HOMO of the donor whereas the electron has been transferred into the LUMO of the acceptor. This process (shown in **Figure 2.1**) describes the case of an exciton that has been

generated inside of the donor, which is typically the case for OPV applications, where fullerenes are the dominant acceptor species and polymers are used as donors and provide the most part of the absorption of the active layer.
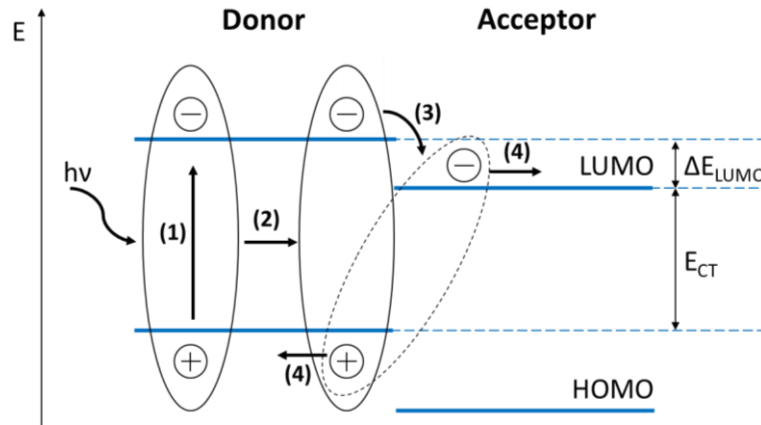
Figure 2.1: Energetic scheme of a Donor/Acceptor interface: Exciton generation (1), diffusion (2) and dissociation (3) followed by charge separation (4) are illustrated. The solid and dashed ellipses symbolize the bound exciton state and dissociated charge transfer state (with energy E_{CT}) of the electron hole pair, respectively.

More recently other acceptor molecules with higher absorption coefficients than fullerenes have been developed,[9–16] so that the absorption of the active layer does not exclusively rely on the donor polymer. This leads to more generated excitons inside the acceptor molecules and therefore more often a dissociation of the exciton due to the transfer of holes from the energetically lower lying HOMO of the acceptor into the energetically higher lying donor HOMO. The requirement of the energetic difference between both HOMO levels ($\Delta E_{HOMO} > E_{b,exciton}$) stays the same as for the LUMO levels in the case for donor-based absorption and in both cases the transfer happens on the order of ~ 50 femtoseconds and is therefore efficient compared to the competing exciton decay mechanisms on the timescale of nano- or even microseconds.[17,18] After dissociation, electron and hole are no longer bound within an exciton but reside in a so called charge transfer (CT) state. The CT state is an intermediate state between exciton and fully

separated charges, representing a remaining chance for intermolecular recombination.[19] From here, the completely separated holes propagate via the donor HOMO towards the anode and the electrons via the acceptor LUMO towards the cathode, respectively (**Figure 2.1**).[20–22] Different loss mechanisms are responsible for the fact, that the energy of the CT state (E_{CT}) is substantially higher than the actual highest energy harvested per photon. In a solar cell, this maximum energy is represented by its voltage equivalent the open circuit voltage (V_{OC}, **Figure 2.2**).
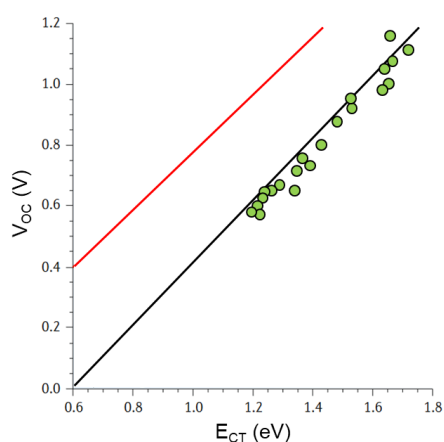
Figure 2.2: Reported charge transfer (CT) state energy (E_{CT}) and open circuit voltage (V_{OC}, see **Paragraph 2.1.2**) of organic solar cells comprising different polymer/fullerene bulk hetero junction (BHJ, see main text) active layers. The red line depicts the theoretical limit for V_{OC} according to the Shockley-Queisser Theory.[23] The black line is added as an eye guide. Modified from Ref.[24].

According to the Shockley-Queisser-Theory, the natural limit for V_{OC} is given by the material specific energetic difference between the two quasi-Fermi levels for electrons and holes. These split from the intrinsic Fermi level of a semiconductor through the generation of charges under illumination (quasi-Fermi-level splitting, QFLS).[25] The QFLS is material specific and therefore the highest achievable V_{OC} is given by the utilized donor/acceptor combination (see red line in **Figure 2.2**).

To grant an ideal absorption of the incoming light with suitable photon energy, active layers in a thickness range of ~ 100 nm are usually employed

in OPV devices. Although organic semiconductors - as they are used in photovoltaic applications - can provide relatively high absorption coefficients (up to 10^5 cm^{-1})[26], their charge carrier mobility is limited (10^{-6} – 10^{-3} cm^2/Vs).[27–29] This is due to the mostly amorphous nature of the layers and the transport mechanism ("hopping transport"), which also differs from crystalline semiconductors, where the band structure enables a much higher carrier mobility.[30] In a planar arrangement of donor and acceptor layers, this would firstly entail transport losses for the dissociated carriers on their respective ways to the electrodes. Secondly and more severely it would result in an inefficient dissociation of excitons in the first place because of the following reason. Due to its electrical neutrality, a Frenkel exciton does not move within electrical fields, resulting in its only movement inside a material being due to Brownian diffusion. Following this, taking into account the typical exciton diffusion length before recombination of around 10-100 nm, it becomes obvious, that a planar sequence of donor and acceptor will not allow for efficient exciton dissociation because not all generated excitons can reach the donor/acceptor interface. This problem has been solved by the introduction of the bulk heterojunction (BHJ) concept in which donor and acceptor are intermixed inside of one resulting active layer[31]. An optimal BHJ provides a proper separation of both donor and acceptor phases, which makes a D/A-interface accessible within the exciton diffusion length and simultaneously forms continuous percolation pathways towards the respective electrodes within each phase to allow for efficient propagation of dissociated charges.

2.1.2 Basic Electrical Characteristics

The basic characterization of an organic solar cell is associated with a plot of current density J versus applied voltage V and the extraction of the essential parameters thereof. This J/V characteristics can be approximated by the Shockley-equation known for ideal inorganic p-n-diodes (**Equation (*2.1*)**).[32]

$$J = \frac{1}{1 + \frac{R_s}{R_{sh}}} \cdot \left[J_s \cdot \left(e^{q \cdot \frac{V - J \cdot A \cdot R_s}{n \cdot k_B \cdot T}} - 1 \right) - \left(J_{ph} - \frac{V}{R_{sh} \cdot A} \right) \right] \tag{2.1}$$

Here J describes the current density through the diode, R_s is the series device resistance, R_{sh} the shunt resistance of the device, J_s is the dark saturation current density, q the elementary charge, V the applied voltage, A the device area, n the ideality factor, k_B the Boltzmann constant, T the device operation temperature, and J_{ph} the photo-generated current density.

Equation *(2.1)* is based on an equivalent circuit as shown in **Figure 2.3a**. The photo-generated current density J_{ph} is represented by a current source, which leads to a negative offset in case of illumination and is only determined by photon-to-charge conversion. In the description of a realistic device, the series resistance (R_s) and shunt resistance (R_{sh}) represent different parasitic effects. The macroscopic effect of of leakage currents and parasitic recombination is reflected by R_{sh}, while R_s illustrates losses due to energetic barriers at interfaces (more on this in **Paragraph 2.1.3**) and limitations in lateral electrode-conductivity and carrier mobility inside the BHJ (see **Paragraph 2.1.1**). It is to be noted, that the only carrier mobility impacting the device functionality is the effective value for the respective incorporated donor/acceptor-system with its specific process dependent BHJ morphology.
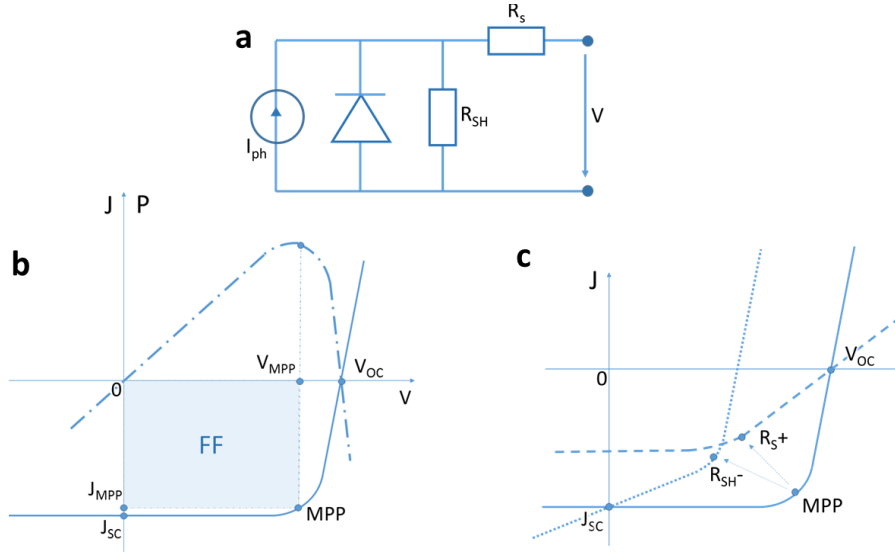
Figure 2.3: a) Equivalent circuit of a solar cell in the fourth quadrant of the J/V curve, b) schematic J/V (continuous) and P/V (dashed) curves of an illuminated solar cell including characteristic parameters, c) schematic depiction of the impact of increased series resistance (dashed curve marked with R_S^+) and a decreased shunt resistance (dotted curve marked with R_{sh}^-) on the FF of a J/V curve.

From **Equation (***2.1***)** one can derive characteristic parameters like the open circuit voltage V_{OC} and the short circuit current density J_{SC} of the device by assuming $J(V_{OC}) = 0$ and $V(J_{SC}) = 0$. [32]

$$V_{oc} = n \, \frac{k_B \, T}{q} \cdot \ln\left[1 + \frac{J_{ph}}{J_s} \cdot \left(1 - \frac{V_{oc}}{J_{ph} \cdot A \cdot R_{sh}}\right)\right] \tag{2.2}$$

$$J_{sc} = -\frac{1}{1 + \dfrac{R_s}{R_{sh}}} \cdot \left[J_{ph} - J_s \left(e^{q \cdot \frac{|J_{sc}| \cdot A \cdot R_s}{n \cdot k_B \cdot T}} - 1\right)\right] \tag{2.3}$$

In an idealistic consideration of the device, R_{sh} can be assumed to be infinite, while R_S is infinitesimal resulting in the V_{OC} only being dependent on the current of photo-generated charges. In this case J_{SC} is approximately equal to the photo-current J_{ph}. Generally, the V_{OC} of an organic solar cell increases logarithmically with incident light intensity and saturates at the maximum possible quasi Fermi-level splitting of the photoactive D/A-combination.[7]

Recombination losses at interfaces (due to poor selectivity, see **Paragraph 2.1.3**) and within the photoactive layer (due to suboptimal nanomorphology) lead to a lowering of R_{sh} and to a notable reduction in V_{OC} (**Figure 2.3c**).[8,33]

The J_{SC} is determined by the efficiency of a variety of processes in the device, including light absorption, exciton dissociation, charge carrier transport inside the active layer and charge carrier extraction at the electrodes. For devices with an optimized morphology of the active layer and negligible losses due to parasitic bi-molecular recombination, the J_{SC} depends linearly on the intensity of the incident light. J_{SC} increases until the number of photo generated charges surpasses the number of extracted charges and becomes limited by the space-charge of the photoactive organic.[34] Thermally improved hopping transport mobility can enable a further increase of the J_{SC} at elevated operation temperatures of the device, which is in contrast to many inorganic solar cells.[34]

The fourth quadrant of the J/V diagram represents the power generating regime of the device, where the maximum possible generated power for a certain illumination intensity can be derived from the maximum of the power vs. voltage plot (P/V curve, **Figure 2.3b**), i.e., the maximum power point (MPP). With the voltage and current density values at the MPP being V_{mpp} and J_{mpp} respectively, the fill factor FF of the device is defined:

$$FF = \frac{J_{MPP} \cdot V_{MPP}}{J_{sc} \cdot V_{oc}} \tag{2.4}$$

This characteristic parameter can be understood as a combinatory value outlining the quality of the device. In general it depicts the complex interaction of the effects introduced with R_S and R_{sh} and the underlying

physical phenomena.[35–37] Thus the quality of the device and with this its FF is reduced, when the MPP moves closer to the coordinate origin of the J/V diagram, due to either an increased series resistance (R_s+) or a decreased shunt resistance ($R_{sh}-$), as is qualitatively demonstrated in **Figure 2.3c**.[38] Finally the power conversion efficiency (PCE) of the device can be calculated using the characteristic parameters introduced above.

$$PCE \ = \ \frac{P_{out}}{P_{in}} = \frac{J_{MPP} \cdot V_{MPP}}{P_{in}} = \frac{J_{sc} \cdot V_{oc} \cdot FF}{P_{in}} \tag{2.5}$$

In this Pout describes the maximum output power density generated by the device and Pin is the illumination power density of the incident light, which is 100 mW/cm² in the case of the standardized AM1.5G (air-mass global) solar spectrum.

2.1.3 Charge Extraction and Device Architecture

To better understand the J/V characteristic of organic solar cells, one can utilize the metal-insulator-metal (MIM) model due to the usually intrinsic nature of organic semiconductors (**Figure 2.4**). After the dissociation of the photo-generated exciton, the separated charges have to drift through the material of the BHJ due to the electric field induced by the difference in surface potential (or work function WF) of both electrodes (built-in potential).[39] Resulting is a linear progression of the electrostatic potential inside the organic material, which can be influenced by applying different voltages to the device (**Figure 2.4**).
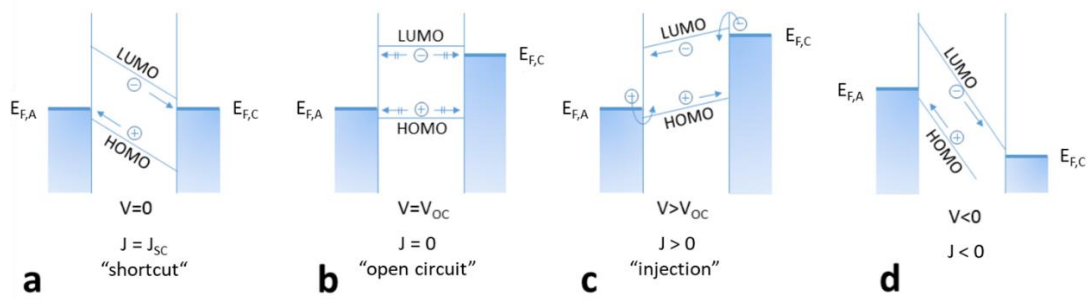
Figure 2.4: Schematic energy diagram of the MIM model for an organic layer in between two electrodes with different WF (anode with Fermi level $E_{F,A}$ and cathode with Fermi level $E_{F,C}$) at different applied voltages along the J/V curve.

For negative bias voltage V<0 (**Figure 2.4d**) the external field leads to an increase of the built-in difference by an absolute value of the applied voltage V, which improves hole transport to the anode and electron transport to the cathode. Thus the photo-generated current J_{ph} (or the number of exciton-generating photons) limits the current, independent of the reverse bias voltage (third quadrant of the J/V diagram). In the case of V=0 (**Figure 2.4a**) the current is only driven by the field supplied by the built-in potential, in an ideal case providing J(V=0) = J_{SC} = J_{ph}(V<0). Under positive bias voltage approaching the V_{OC} (fourth quadrant), the built-in potential is more and more overcompensated by the external field, limiting J_{ph} until it is finally cancelled under open circuit conditions (V = V_{OC}, **Figure 2.4b**). For higher bias voltage V > V_{OC} (first quadrant), injection of holes via the anode and electrons via the cathode becomes predominant and results in a positive diode injection current. According to this, the maximum V_{OC} of the solar cell is limited by the difference in electrode WFs. With the highest possible V_{OC} of an organic D/A-system being determined by the corresponding quasi Fermi level splitting (see **Paragraph 2.1.1**), a clear requirement for the device architecture can be identified. The electrode WFs should energetically align with the respective energy levels of the organic to accomplish the full potential of the photo active organic layer.
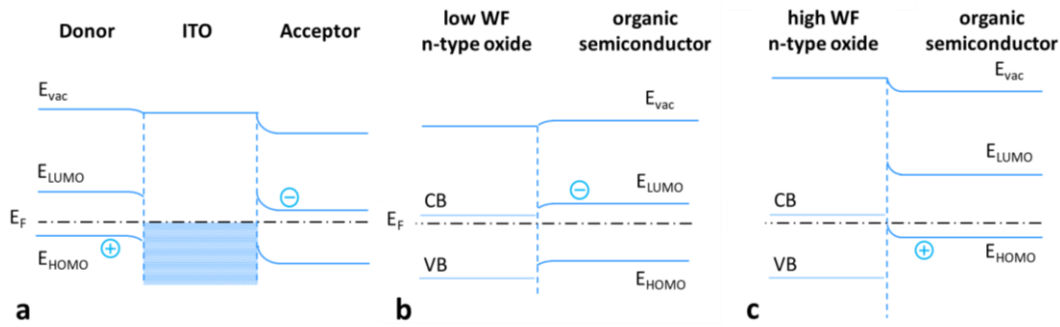
Figure 2.5: Simplified depiction of band bending at three types of organic/inorganic interfaces: donor and acceptor with ITO (a) and organic semiconductors with low WF n-type (b) and high WF n-type (c) oxides.

A typical OPV device contains a layer of highly-doped metal oxide like indium-doped tin oxide (ITO) or aluminum-doped zinc oxide (AZO) coated on top of a glass or foil substrate as the transparent bottom electrode and metals like Aluminum (Al), Silver (Ag) or Gold (Au) as reflective top electrode. While the energetic levels of organic semiconductors are variable due to the dependence on the molecular structure, the choice of different WFs of electrode materials is limited. In most cases this leads to an inevitable energetic misalignment at the electrode/organic interfaces. In the exemplary case of ITO, which develops metal like behavior due to its high doping level, this can result in the formation of Schottky-type contacts to both donor and acceptor creating extraction barriers for holes and electrons respectively.[40,41] The typical WF of ITO in the range of 4.7 - 4.9 eV thereby lies between typical values for $HOMO_D$ (5.2 - 5.5 eV) and $LUMO_A$ (3.7 - 4.2 eV) and thus does not allow for efficient extraction of none of both carrier species (displayed schematically in **Figure 2.5a**).[42] To achieve an alignment of the electrode WFs to the energetic levels of the active layer, additional interlayers (charge extraction layers) can be inserted between the electrode and active layer.[43] For hole extraction at the anode side of the

device a high WF is needed to energetically align with the typically deep lying $HOMO_D$ of the donor, while electron extraction at the cathode side is benefited by a low WF aligning with the higher lying $LUMO_A$ of the acceptor. A material class with widespread application in the modification of the energetic line-up at the ITO/organic and metal/organic interfaces are metal oxides. Besides their typically high optical transparency, there are suitable candidates with high and low WF available. For example, p-type oxides like nickel oxide (NiO_x) or copper oxide (CuO_x) are used as anode interlayers because of their high WF and additional electron blocking quality.[44,45] This results in a high selectivity for holes, which provides efficient hole extraction and reduces parasitic recombination with electrons. In analogy to this, low WF n-type metal oxides like zinc oxide (ZnO), titanium oxide (TiO_x) or tin oxide (SnO_x) qualify for good cathode interlayers. The favorable energetic alignment to the $LUMO_A$ allows for enhanced electron extraction with simultaneous blocking of holes from $HOMO_D$ (schematic shown in **Figure 2.5b**). In case of ZnO and TiO_x, proper alignment is only achieved under illumination conditions, that provide a certain amount of light in the ultra-violet (UV) part ($\lambda < 435$ nm) of the solar spectrum. This effect is known as "UV light-soaking" and can be mitigated by doping[46] or plasmonic sensitization of the oxide with incorporated metal nanoparticles[47] and was found to be essentially absent for SnO_x-based EELs.[48]

In contrast to the abovementioned low WF oxides, n-type transition metal oxides with high WF like molybdenum oxide (MoO_x), vanadium oxide (VO_x) and tungsten oxide (WO_x) can also be used at the anode side of the device.[49–51] Due to their alignment to the $HOMO_D$ and effective interfacial p-doping of donor and acceptor they create good hole extraction conditions while simultaneously repelling electrons from the LUMO levels of both

donor and acceptor (see **Figure 2.5c**). Due to their functionality in charge extraction, anode interlayers are also described as hole extraction layers (HEL) and - in analogy - cathode interlayers are called electron extraction layers (EEL).

The possibility of modifying the ITO or metal electrode WFs alike enables a wide choice of device architectures. If the transparent bottom electrode is chosen as the anode and the reflective metal top electrode thus forms the cathode, the architecture is termed "regular" (or "p-i-n" in analogy to classical semiconductor PV). Opposed to this is the so called "inverted" ("n-i-p") architecture with the cathode at the bottom and the anode at the top side of the device. Due to the discussed BHJ concept for the active layer, the donor and acceptor phase are intermixed and therefore both architectures are in general suitable approaches. However, depending on the specific active material system and the applied process parameters, vertical concentration gradients driven by thermo-dynamic effects can occur inside the BHJ.[52,53] So in the case of an accumulation of acceptor molecules at the bottom of the BHJ, a larger interface for electron extraction would be given at the bottom side and with this the choice of the "n-i-p" architecture (bottom cathode) should be favored and vice versa.[54,55]

2.1.4 External Quantum Efficiency

In many cases the standardized solar spectrum (AM1.5G) cannot be reproduced exactly by the light source used to illuminate the device during the measurement of the J/V curve. This results in a challenging determination of the PCE and the other characteristic parameters of the device. Considering the relation of the number of photo-generated charges to the absorption spectrum of the photoactive organic and the illumination

spectrum, it becomes clear, that especially the J_{sc} can be severely affected by even small deviations from the AM1.5G spectrum. In this regard the spectrum of the external quantum efficiency provides an avenue for the determination of Jsc under "true" AM1.5 illumination conditions. Such a spectrum can be generated by comparing the number of incident photons $N_{Ph}(\lambda)$ (calculated from the power spectrum $P(\lambda)$ of the used tunable light source) to the number of extracted charges $N_C(\lambda)$ (calculated from the spectral response current $I(\lambda)$ of the device measured under short circuit conditions) at different wavelengths λ. Thus the EQE of a device at a certain wavelength λ is defined as follows:

$$EQE\,(\lambda) = \frac{N_C(\lambda)}{N_{Ph}(\lambda)} \tag{2.6}$$

Forming the convolution integral over the wavelength of the EQE spectrum and the standardized AM1.5G power density spectrum $\Phi(\lambda)$ returns the J_{sc} generated by the corresponding device in the wavelength region $\lambda_1 < \lambda < \lambda_2$.

$$J_{sc} = \int_{\lambda_1}^{\lambda_2} EQE(\lambda) \cdot \Phi(\lambda)\, d\lambda \tag{2.7}$$

In addition to facilitating a correct determination of the J_{sc}, this method provides spectrally resolved information over the efficiency of photon harvesting within the device. This can help to identify wavelength regions suffering from parasitic absorption or to optimize the device architecture by examining possible optical interference phenomena.

2.2 Multi-Junction Solar Cells

Multi-junction solar cells use more than one active layer (junction) to increase the efficiency of the final device by reducing the impact of one or multiple loss mechanisms of single-junction devices. The tandem cells can basically be divided into two different types, connecting the sub-cells either in series or in parallel. Following Kirchhoff's law this either leads to an addition of the sub-cells' V_{OC} or J_{SC} when incorporated into the multi-junction device, respectively.

This work will focus on monolithic tandem devices (with two junctions), in which the two sub-cells are connected in series. In monolithic multi-junction devices, the individual sub-cells are processed on top of each other to create one final device stack. On the one hand, this creates additional challenges in device processing, especially when utilizing solution-processes like in the case of organic (and organo-metal halide perovskite) semiconductors (see **Paragraph 2.2.2**). On the other hand, the monolithic approach reduces the number of necessary electrodes and facilitates strategies to further increase device efficiency. One of the main contributing factors in limiting the efficiency of single-junction devices is the fact, that all excess energy ($\Delta E = E_{ph} - E_g$) of photons with higher energy than the energygap of the respective absorber layer is not converted to electrical but mostly thermal energy. By choosing active materials with complementary spectral absorption characteristics it is possible to minimize the number of non-converted photons and reduce the abovementioned thermalization losses.

Thus, organic semiconductors (and the abovementioned organo-metal halide perovskite) are very interesting candidates for the photo-active materials, due to their customizable optoelectronic properties. Moreover, optimizations of individual layer thicknesses can cause beneficial optical

interference phenomena within the device stack and therefore further improve light conversion and the overall efficiency of the device (details can be found in **Paragraph 2.2.1**).

2.2.1 Operation, Modeling, and Optimization

For an optimized tandem device the two sub-cells need intricate electrical and optical coordination to work in concert with each other. The generation of a stable photocurrent in the tandem device requires absorption of light in both sub-cells, where the front sub-cell (being the first to absorb incident photons) functions as a low-pass absorption filter for the back sub-cell. In addition to a general decrease in light intensity this also modifies the spectrum by absorbing only photons with sufficient energy above its bandgap $E_{g,front}$ ($E_{ph} > E_{g,front}$), transmitting low energetic photons to the back sub-cell. Photons that pass both sub-cells can then also be (partially) reflected by the (typically metallic) back electrode, providing another opportunity for the photons with $E_{ph} > E_{g,back}$ to be absorbed traversing the device in the other direction. Thus the absorption characteristic of the back sub-cell can also affect the performance of the front sub-cell. The fact that tandem architectures comprise several interlayers for charge extraction, transport and recombination further increases the complexity of the device. All layers of the device have different wavelength dependent refractive indices $n(\lambda)$ and extinction coefficients $k(\lambda)$ and exhibit layer thicknesses on the scale of the incident photon wavelengths creating a complex optical cavity within the device stack. As a result, a precise determination of the quantity of absorbed photons in every layer requires detailed optical modeling as first demonstrated by Dennler et al. in 2007.[56] This will be discussed further below.

Besides all optical effects, there are also electrical effects between both sub-cells that occur due to their connection in series. Dictated by Kirchhoff's laws the photocurrent through the device equals the lower of both sub-cell currents while the resulting bias voltage of the tandem device equals the addition of the individual sub-cell biases. This results in two basic equations (**Eq. (**2.8**)** & **Eq. (**2.9**)**) for current density and voltage, that are (ideally) satisfied at all time during steady state operation conditions.

$$J_{tandem} = J_{front\ sub-cell} = J_{back\ sub-cell} \tag{2.8}$$

$$V_{tandem} = V_{front\ sub-cell} + V_{back\ sub-cell} \tag{2.9}$$

The implications of these two equations are worth further outlining despite their apparent simplicity. If the tandem cell is put into short circuit condition (V_{tandem} = 0), it does not dictate both sub-cells to also be at short circuit, because it is only given that their respective bias voltages have to be equal opposites (see. **Eq. (**2.9**)**). In a more realistic case one can assume that the charge generation in both sub-cells is not always equal and sub-cell A is generating more charges then the other sub-cell B, even though the tandem is in short circuit condition. The excessive charges of A inducing an additional electric field over the less generating (current-limiting) sub-cell B result in reverse bias conditions over sub-cell B, which can entail an increase in photocurrent (in case of a finite $R_{sh,B}$). Therefore it is implied, that in practice the J_{SC} of a tandem device can in theory exceed the J_{SC} of the current-limiting sub-cell. Even though this scenario leads to an increase in J_{SC}, it has to be noted, that most of the excessively generated charges of sub-cell A will be lost due to parasitic recombination, diminishing the FF and with this the overall PCE of the device.

The open circuit condition (J = 0) presents a more simple situation, where both sub-cells operate under open circuit and the tandem V_{OC} is the addition

of both sub-cell V_{OC}s. Notably, the V_{OC} of each sub-cell is not necessarily identical to the V_{OC} of the respective single-junction device under AM1.5G illumination. The reduced light intensity and modified spectrum within the tandem stack can result in slightly lowered V_{OC} values for the sub-cells. Assuming that the J/V characteristics of both sub-cells under tandem illumination conditions are known, the J/V curve of the tandem device can then be constructed applying equations (2.6) and (2.7), adding the sub-cell voltages at constant current density. For further insight, a more detailed exercise concerning tandem device operation has been published by Hadipour et al. in 2008.[57]
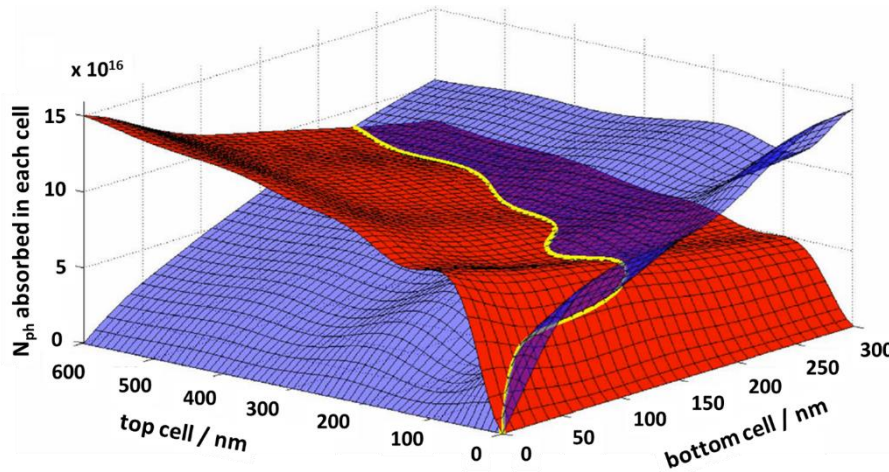
Figure 2.6: Optical modeling of a tandem solar cell: Number of photons absorbed in the bottom active layer (blue surface) and in the top active layer (red surface) vs. the thickness of the bottom and the top active layers. The yellow line depicts all thickness combinations providing "current matching conditions". Reproduced from Ref. [56].

As discussed above, a highly efficient tandem device necessitates the matching of the respective photocurrents produced in both sub-cells ("current matching" conditions, see **Figure 2.6**). If the choice of active materials has already been made, the easiest approach is a systematic variation of both active layer thicknesses in combination with optical modeling to identify the thickness combinations in which the same amount

of photons is absorbed in each sub-cell. In most cases a transfer matrix algorithm is used. It enables an accurate estimation of partial reflectance and transmittance at every interface as well as the share of photons absorbed in every layer, using spectrally resolved optical constants $n(\lambda)$ and $k(\lambda)$ of all implemented materials, which are experimentally accessible via methods like e.g. ellipsometry or optical absorption measurements.[56] This method however only takes optical absorption of the materials into account neglecting all electrical properties of the stack. For a more refined approach, thickness dependent parameters like the FF and the integrated internal quantum efficiency (IQE) of both sub-cells can be included. Those have first to be determined experimentally by the preparation and characterization of single-junction equivalents of each sub-cell with several active layer thicknesses. While the FF for each thickness can simply be derived from the respective device's J/V curve, the integrated IQE is defined as the ratio between the experimentally measured J_{SC} of the device and the theoretically possible J_{SC} given by the simulated photon flux absorbed inside the active layer. Gilot et al. presented a detailed method to incrementally optimize tandem devices using this combination of FF, IQE, and optical modeling.[58] A more complex modeling approach, which has been first published by Moet et al., utilizes drift-diffusion calculations to include electrical properties of the active layers in addition to the aforementioned optical simulations.[59] Within these approaches the optimization of the tandem device is achieved by varying the thicknesses of both active layers. Another possibility to adjust the sub-cells is via a thickness variation of the charge transport and extraction layers, which behave as optical spacers.[60–65] With this the spatial distribution of the electro-optical field inside the device stack can be modified and the amount of photons absorbed by the photoactive layers can be optimized. All of these optimization methods will only predict

the optimal efficiency for a given combination of photoactive materials (and their specific respective bandgaps), because the choice of active materials is not part of the electro-optical optimization process.

Due to the fact that the energy gap of conjugated polymers, as they are used in BHJs in organic solar cells, can be modified by customizing their molecular structure, the choice of optimal energy gaps is another possible optimization parameter. The emergence of organo-metal halide perovskites opened up even more pathways for device optimization, e.g. energy gap tunability of absorber layers, in solar cells (more on this in **Paragraph 2.2.4**). To implement different bandgaps into the optimization process of tandem devices, Chen et al. developed and utilized a simplified semi-empirical device model for hybrid tandem devices with one perovskite and one organic absorber layer.[66] In this approach the electrical characteristics were not implemented by a drift-diffusion model and no transfer matrix algorithm was used to calculate the absorption (and with this the J_{SC}) of the sub-cells resulting from the optical properties of the layers and light propagation within the device stack. Instead the respective sub-cell J_{SC}s were calculated using artificial EQE spectra (see **Paragraph 2.1.4**), which were assumed to be constant values in the relevant wavelength regions. To account for electrical transport losses, additional terms for radiative and non-radiative recombination of charges were applied according to literature.[67] Voltage losses have only been included for the organic absorber (further discussed in **Chapter 4**). The variations of layer thicknesses did not play the prominent role as in the methods described above. The only thickness variation was performed for the wide bandgap perovskite absorber layer and affected only the EQE values in the wide bandgap wavelength region. The goal of this approach was to find the best combination of bandgaps and to discuss the potential of such hybrid

devices. As elaborated, all of the abovementioned approaches omit or simplify different aspects of the device. Within this work, a different semi-empirical approach for an electro-optical simulation will be presented, which combines different aspects of the above mentioned methods, to provide a more accurate and adaptable assessment of the potential of hybrid multi-junction devices.

2.2.2 Interconnection Layers (ICLs)

Aside from the choice of the photo-active layers for the respective sub-cells with low voltage loss and complementary absorption spectra, a sophisticated design of the device stack is needed to achieve a matching of the respective photo currents and to avoid electrical transport losses. One essential (and arguably the most challenging) component of the stack design for multi-junction solar cells is the interconnection layer (short: interconnect or ICL). An ICL must facilitate recombination of both charge carrier species from the respective sub-cells without additional loss of open circuit voltage or fill factor. Exemplarily, in an inverted tandem device, electrons extracted from the upper sub-cell must ideally recombine with holes extracted from the bottom sub-cell. As a result, ICLs are multi-layer architectures comprised of an electron extraction layer (EEL) and a hole extraction layer (HEL), including the critical EEL/HEL-interface.

As introduced in **Paragraph 2.1.3**, materials used as EEL and HEL are often either p- or n-doped semiconductors, which results in three conceptually different types of interconnects. The schematic band diagrams and working principles of the two types relevant in this work, are depicted in **Figure 2.7**.
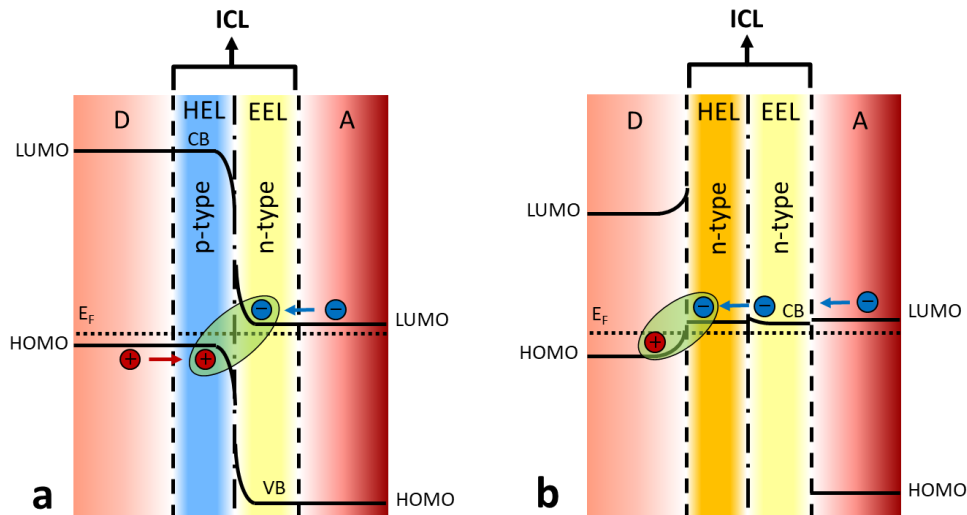
Figure 2.7: Schematic band diagrams and working principle of different types of interconnects: a) In the p/n-type ICL electrons from acceptor of sub-cell A (A_A) are extracted by the n-type EEL and holes from the donor of sub-cell B (D_B) are extracted by the p-type HEL and recombine at the HEL/EEL-interface. b) In the n/n-type ICL electrons from A_A are extracted by the n-type EEL, transferred into the n-type HEL and recombines with the hole from D_B at the D_B/HEL-interface.

In the case of a p/n-interconnect one can assume that the p-type layer forms the HEL of one sub-cell while the EEL of the other cell is represented by the n-type counterpart. This type of ICL forms a band structure which is similar to that of a p/n-tunnel-diode. In this case, both extracted charge carrier species - electrons via the EEL conduction band (CB) and holes via the HEL valence band (VB), respectively - are transported towards the EEL/HEL-interface inside the respective extraction layer. To facilitate an ideal recombination of charges both extraction layers are typically highly doped. This reduces the Debye length in the respective layer leading to stronger band bending and therefore decreasing the spacial distance (in x-direction) between both carrier species at the interface. This also (and maybe more importantly) brings the Fermi level (E_F) in both layers closer to the band edges where carrier transport is happening (EEL CB and HEL VB). This leads to a decrease of the energetic difference between those bands and therefore reduces the energy lost in the recombination process. Ideally the

layers are doped to degenerate levels inducing an Esaki-diode like behavior of the interconnect, where this recombination loss is minimized. This type of interconnect is the typical case for inorganic multi-junction photovoltaic devices[68], where all different semiconductor layers of the tandem are vacuum processed which allows for a high level of control over doping levels for different parts of the device. In this case the interconnect typically consists of the same materials as the two active layers, which each feature highly increased (degenerate) doping levels to achieve the effect of an Esaki-type tunnel recombination contact.

In contrast to this, the working principle of n/n-type (and p/p-type) interconnects is not based on carrier recombination at the interface of both extraction layers. Here, the exemplary case of an n/n-type interconnect will be discussed, because of its more prominent utilization in recent literature (mainly caused by availability of suitable materials) and the elevated relevance for the work presented in this thesis. Due to the fact that in this case both extraction layers are n-type semiconductors, their transport properties usually benefit only electrons and therefore don't allow for an efficient transport of holes towards the interface. Instead, an electron is extracted from the acceptor of sub-cell A (A_A) by the n-type EEL, transported to the EEL/HEL interface within its CB and is then transferred into the CB of the n-type HEL of sub-cell B. After that the recombination of electron and hole takes place at the interface between the HEL und the donor of sub-cell B (D_B). As described in **Paragraph 2.1.3**, n-type semiconductors can be utilized as HEL, because electrons from their deep lying CB recombine with holes from the active layer's HOMO level or VB in case of inorganic active layers. The high difference in WF between the EEL and HEL in this case typically leads to a strong band bending at the HEL/EEL-interface. This results in the formation of a counter diode, that

hinders the efficient transfer of electrons from the EEL CB to the HEL CB and therefore impairs the electronic functionality of this kind of architecture as interconnect. Examples for multi-junction devices based on this type of ICL can be found in literature; all of them demonstrating results of the mentioned counter diode effect. Early approaches used the insertion of thermally evaporated ultra-thin metal layers in-between HEL and EEL.[69–74] They proposed, that the addition of the metal mitigates the formation of the detrimental counter diode, as it helps to form an ohmic contact[69], and increases the carrier density at the interface thus the number of "recombination centers" in the recombination contact.[74,75] In any case, the metal layer critically affects the optical properties of the interconnect and severely compromises its transmittance (an example of this effect can also be seen in **Chapter 4.3**). Moreover, it is challenging to deposit thin metal films with sub-nm control and large-area homogeneity. Shim et al. reported a metal-free oxide-based ICL incorporating a highly-doped layer of transparent metal oxide (in this case AZO) processed by atomic layer deposition (ALD).[76] The resulting multi-junction solar cells however did not significantly exceed the efficiency of the according single-junction devices.

The issue of electrical functionality of n-n-type interconnecting architectures will be addressed in detail within **Chapter 3** and **Chapter 4** of this thesis, demonstrating two different and highly efficient methods to solve this problem for all-oxide ICLs.

As described above, aside from its electronic functionality, the recombination architecture of a monolithic tandem device has to be optically transparent. This is necessary to ensure that photons not absorbed by the front sub-cell are entering the second sub-cell and with this minimize the amount of non-converted photons within the whole device. As can be

seen by the examples in the last paragraph and elaborated above (**Paragraph 2.1.3**), the material class of metal oxides generally fulfills this set of requirements, leading to several examples of ICLs based on transition metal oxides like MoO_x and VO_x as HEL[69–74,76] and TiO_x[71,77] or ZnO[69,70,76] as EEL. In the case of solution-processed photo-active materials (see above), the interconnect must concomitantly provide chemical protection (resilience) for the bottom sub-cell against dissolution due to the solvents involved in the deposition of the upper sub-cell. There are a plethora of publications presenting solution-processed organic tandem devices, all addressing this issue to some extent. The presented approaches to circumvent this intrinsic problem comprise applying sophisticated material sequences and orthogonal solvents or applying one or more layers by vacuum deposition methods (e.g. magnetron sputtering[78] or ALD[76]). Despite the obvious relevance of this aspect of an ICL and the large number of mentions in literature, the exact physical or chemical origin of existent (or nonexistent) protection properties of individual layers is not discussed in detail. In case of the aforementioned vacuum-processes, compared to those deposited from solution, the increased resilience could be attributed to a higher resulting layer density or a negligible solubility in typically used solvents. Nevertheless, this is not the case for every vacuum process, as will be discussed in more detail within this work (see **Chapter 3.2**). The lack of design rules dedicated to resilience (especially for solution-processed layers) suggests, that this requirement of an ICL is commonly approached by empirical methods. The most prominent example of a solution-processed layer, which combines suitable charge extraction and resilience characteristics, is the poly(3,4-ethylenedioxythiophene) polystyrene (PEDOT:PSS). Due to its combination of a simple deposition process from an aqueous dispersion and attractive electric characteristics, the p-type

conductive polymer is a well-researched and widely applied material in organic optoelectronics (in OPV it is mainly used as HEL). However, PEDOT:PSS was proven to be the origin of reliability issues in organic electronic devices [50,79,80], and it suffers from a limited transmittance, which also becomes a significant issue, especially if more than one interconnect is required (e.g. in triple- or quadruple-junction cells).[81,82] Thus, substantial work has been devoted to replacing PEDOT:PSS within the ICL, especially by high WF metal oxides, resulting in n/n-type interconnects. Nonetheless, all of these architectures were lacking in either electrical or optical functionality and/or missing the feature of being completely solution-processed. As a result, most organic multi-junction devices still rely on the use of some form of PEDOT:PSS as HEL in the ICLs.[81,83–86] Within this work, an oxide-based approach to an efficient and resilient ICL without the necessity of additional metal interlayers or the incorporation of PEDOT:PSS will be presented. Additionally, elaborate resilience testing of a plethora architectures will lead to a route to a completely solution-processed all-oxide ICL (see **Chapter 3.2**).

2.2.3 Specific Characterization Challenges

(for Monolithic Two-Terminal Multi-Junction Devices)

As has been demonstrated before, utilizing tandem architectures presents a valuable pathway to increase the efficiency of organic solar cells (and solar cells in general). However, the complexity of the device, with two electrically (and optically) connected sub-cells, represents a challenge concerning the correct characterization, especially the measurement of the short circuit current density J_{SC}. In **Paragraph 2.1.4** the measurement of J/V characteristics under illumination in combination with a determination of

the J$_{SC}$ via EQE spectrum is presented, to account for possible optical mismatches in the illumination spectrum (compared to AM1.5G), as a possible pathway to characterize (organic) solar cells. While this method is a relatively facile option for organic single-junction devices it is not simply applicable for cells with tandem (or in general multi-junction) architectures. Measuring the EQE of a tandem device is fundamentally impeded by the fact that the two sub-cells are electrically connected in series and therefore have to be excited simultaneously for the device to produce any photocurrent. If both sub-cells are not balanced (producing different amounts of photocurrent), the current of the tandem device is limited by the sub-cell that generates the lower photocurrent. For a well-designed multi-junction device, the overlap of the sub-cells' absorption spectra is often minimized to achieve more efficient light harvesting of the solar spectrum, resulting in one of the sub-cells being current-limiting for nearly every wavelength in case of monochromatic illumination. Thus, by measuring the spectral response with a variable monochromatic probe light, as for single-junction devices, the overall measured spectral response I(λ) for each wavelength will always be limited by the sub-cell absorbing less of the provided light. This results in an EQE spectrum of the tandem device following the lower envelope of the EQE of the individual sub-cells (see **Figure 2.8a**).
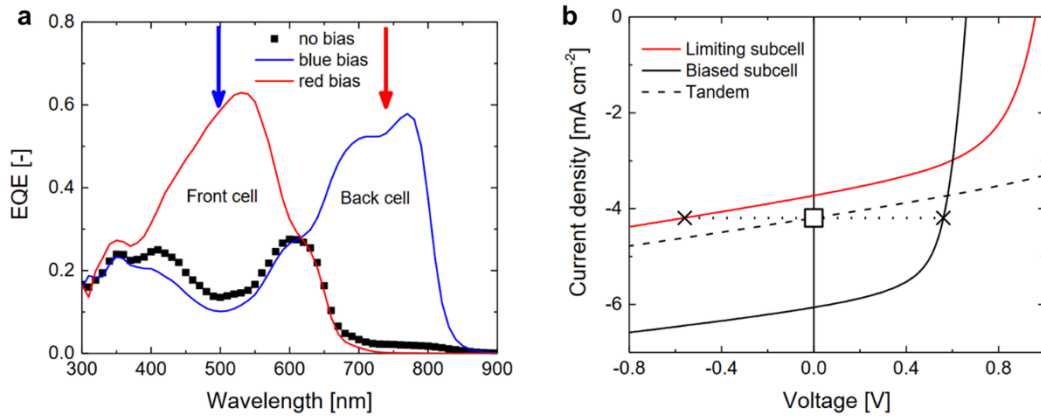
Figure 2.8: a) EQE spectrum of a tandem cell without light bias (black squares) and under blue or red bias illumination (arrows). b) Schematic J/V characteristics of the sub-cells and the tandem device under red bias illumination. Reproduced from Ref. [87].

To overcome this problem and to enable isolated controlled measurement of the EQE spectra for both sub-cells, one has to provide an excess current produced in one sub-cell facilitating the unhindered characterization of the other (now current-limiting) sub-cell. In practice this can be achieved by using (monochromatic) bias light sources, which provide a selective light bias of only one of the sub-cells. By adjusting the intensity of the bias light in a way that the absorbing sub-cell is illuminated in excess, the other sub-cell is rendered measurable with the low intensity probe light, staying current-limiting at every time during the measurement. Under illumination using frequency-controlled chopped probe light and a lock-in detection technique, the measurement now returns the spectral response (and with it the EQE spectrum) of the respective non-biased sub-cell.

However, in 2010 Gilot et al. pointed out other characteristics of organic solar cells to also have non-negligible effects on the characterization of such multi-junction devices.[58] The non-linear relation between photocurrent and illumination intensity in addition to field-assisted charge collection pose additional challenges for a correct spectral response measurement. In particular, keeping the tandem device at short circuit condition, the excess

bias illumination of one sub-cell creates an electrical field inducing a reverse bias voltage on the current-limiting sub-cell (**Figure 2.8b**). In most cases this effect leads to an overestimation of the measured current with respect to the short circuit condition. As a consequence, a correct spectral response measurement necessitates the use of an appropriate electrical forward bias to maintain the intended short circuit condition in the measured sub-cell, in addition to the illumination bias mentioned above. The intricate method to accurately determine the magnitude of the bias voltage has also been presented by Gilot et al., but in many cases it is possible to be approximated with the V_{OC} of the optically biased sub-cell.[58]

A collection of instructions combining the above mentioned methods has been summarized and reported in detail by Timmreck et al..[88] This provides a detailed protocol, which has been followed during the characterization of all multi-junction devices presented in this work.

2.2.4 Photoactive Organo-Metal Halide Perovskites for Multi-Junction Solar Cells

One of the paramount limits for multi-junction cells with organic active layers is the availability of suitable wide bandgap cells with $E_g = 1.7\text{-}1.9$ eV, which are able to provide high V_{OC} and high J_{SC} at the same time. One characteristic parameter to display losses of devices with respective active systems is the so called voltage loss ΔV_{OC}. It is defined as the difference between the voltage equivalent of the active material's bandgap (mainly attributed to the absorption onset energy) and the achieved device V_{OC}. For example, the widely used donor polymer poly[N-9′-heptadecanyl-2,7-carbazole-alt-5,5-(4′,7′-di-2-thienyl-2′,1′,3′-benzothiadiazole)] (PCDTBT) provides an energy gap of 1.88 eV, but in combination with fullerene

acceptors as [6,6]-phenyl-C_{71}-butyric acid methyl ester (PC$_{71}$BM) it only returns a V_{OC} of about 0.9 V, resulting in a loss of almost $\Delta V_{OC} = 1$ V.[89] A similar situation is found for poly[[4,8-bis[(2-ethylhexyl)oxy]benzo[1,2-b:4,5-b']dithiophene-2,6-diyl][3-fluoro-2-[(2-ethylhexyl)carbonyl]thieno[3,4-b] thiophenediyl]] (PTB7), with an energy gap of 1.63 eV but a V_{OC} of only about 0.75 V in combination with PC$_{71}$BM, meaning a loss of $\Delta V_{OC} = 0.88$ V.[90] The Janssen group (TU Eindhoven) has reported a series of wide-gap polymer donors with $E_g = 1.72$ eV and a relatively high V_{OC} of 0.85-0.99 V (minimal $\Delta V_{OC} = 0.73$ V).[91] These materials, however, came short in EQE and therefore provided only limited J_{SC}.

To overcome the lack of a suitable organic wide-gap materials, hybrid multi-junction solar cells have been identified as an interesting pathway for further improvements. This lead to the realization of devices, in which amorphous silicon (a-Si) is used as the wide-bandgap sub-cell.[92,93] Thereby a PCE in triple-junction devices of 13.2% has been demonstrated. However, to achieve the full potential of these devices, multiple additional intricate light management strategies had to be applied. It has to be noted, that the voltage loss for the a-Si sub-cell ($E_g = 1.75$ eV, $V_{OC} = 0.98$ V) was not significantly better than that of typical organic sub-cells. The main advantage of the a-Si was the high internal quantum efficiency, which is largely independent of thickness and leads to a very high EQE resulting in a substantially higher J_{SC}.
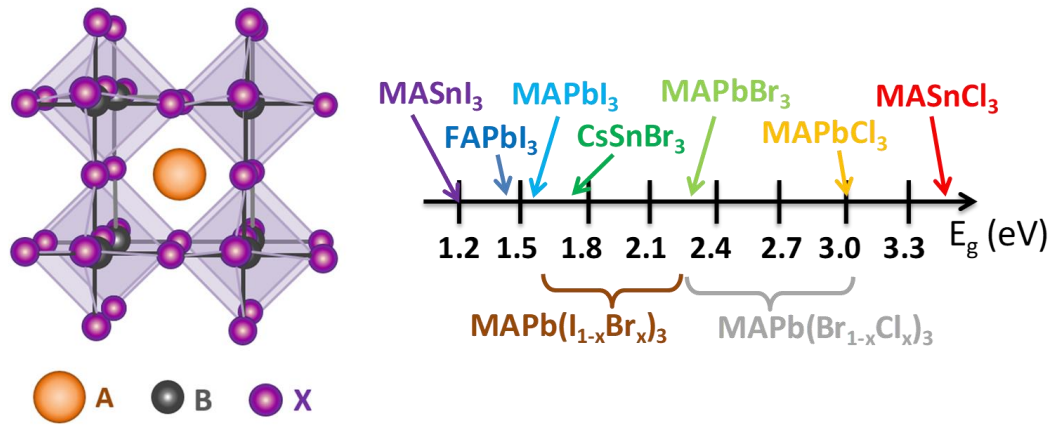
Figure 2.9: Crystal structure of ABX$_3$ perovskite (left). Bandgap tuning by variation of perovskite constituents (right).

Another emerging material class with promising properties to overcome the aforementioned difficulties are hybrid organo-metal halide perovskites. With the typical composition ABX$_3$ (left depiction in **Figure** *2.9*), this material class can be prepared by a wide range of low-temperature techniques, including solution based routes and vapor phase deposition on the basis of low cost precursors like lead iodide (PbI2) and small organic cations such as methylammonium iodide (CH$_3$NH$_3$I / MAI) or formamidinium iodide (FAI). Thus it is compatible with most of the technology facilitated in OPV manufacturing and also shares its other advantages over conventional PV techniques. Solar cells based on organo-lead halide perovskites have seen tremendous progress over the past ten years.[94] Most attractively, their bandgap energy can be tuned by their composition (shown in the left part of **Figure** *2.9*) and a very small voltage loss of only about 0.3-0.4 V has been demonstrated to be possible, using one of the most prominent representatives CH$_3$NH$_3$PbI$_3$ ("MAPbI$_3$").[95]Concomitantly, a high EQE of > 80 % has been achieved in the wavelength range of $\lambda < 800$ nm (E$_{Photon}$ > 1.55 eV). While the power conversion efficiency of perovskite based cells has soared to levels of > 25.6 %[96,97], concerns about intrinsic and extrinsic stability are still intimately linked to this photovoltaic technology.[98,99] It has been shown

that the stability of MAPbI$_3$ strongly depends on the preparation conditions and the details of the device structure.[99,100]

In general terms, there are several different degradation mechanisms, that occur in pristine perovskite layers and perovskite based devices alike. Here, just a brief overview without a detailed covering of the underlying phenomena will be given. This is presented in different work done by my colleague Kai Oliver Brinkmann.[101]

For the most part there is consensus that perovskites like MAPbI$_3$ decompose to their constituents, i.e. HI, CH$_3$NH$_2$ and PbI$_2$, in the presence of water.[102] Even the presence of a single water molecule could be sufficient to degrade an entire MAPbI$_3$ layer according to Frost et al..[103] While this issue can in principle be mitigated by a proper encapsulation, the intrinsic decomposition of CH$_3$NH$_3$PbI$_3$ to CH$_3$NH$_3$I and PbI$_2$ states a more fundamental problem, as it is thermally activated and occurs even under inert conditions.[100,104]

Alternative materials from this family, where the methylammonium ion is replaced by a formamidinium (FAPbI$_3$) or Caesium (Cs) ion (CsPbI$_3$), turned out to be more intrinsically stable against decomposition, but both materials exhibit a phase instability, which was found to negatively impact solar cell performance.[105] Here, Seok and coworkers could show that the addition of MAPbBr$_3$ to FAPbI$_3$, i.e. forming a mixed-cation/mixed-halide material, significantly improved the phase stability.[106] McMeekin et al. suspected perovskites based on MA cations to be generally unstable as they undergo phase segregation upon illumination. They proposed a mixed-cation/mixed-halide perovskite where the MA cations are replaced by Cs, i.e. FA$_{1-x}$Cs$_x$Pb(I$_{(1-y)}$Br$_y$)$_3$. For a composition of x = 0.17 and y = 0.4, a material with a bandgap of 1.74 eV resulted in solar cells with a V$_{OC}$ of 1.2 V (loss

$\Delta V_{OC} = 0.54V$) and an EQE > 90 % (for λ < 700 nm), thereby producing a J_{SC} of 19.2 mA/cm^2. This material has been shown to be compositionally stable even under continuous illumination.

In general, the addition of Cs cations, which are smaller than MA, as well as the addition of Bromine (Br) as halide component to partially replace iodine, both lead to a widening of the bandgap of the resulting perovskite (see right side of **Figure 2.9**). Thereby, a significant spectral range of the solar spectrum opens up that can be absorbed by a subsequent low-bandgap sub-cell in a multi-junction device. Due to the variability of the perovskite bandgap it is intuitive to consider preparing tandem solar cells using perovskites with different energy gaps. However, there it is a severe challenge to prepare perovskite materials with a bandgap below 1.3 eV. This range is accessible, if lead is (partially) replaced by tin (**Figure 2.9**), which results in severe stability issues.[107] More successfully, multi-junction devices consisting of a wide-gap perovskite cell and a single crystalline Si-based cell (E_g = 1.11 eV) have been considered to potentially reach efficiency levels of 30 %, with a recent publication even demonstrating a PCE of > 33 %.[96]

In contrast to that approach, the combination of a wide-gap perovskite cell with low gap organic sub-cells would enable the highly interesting opportunity to prepare multi-junction devices that provide all attractive properties of both technologies (e.g. flexible substrates, large area deposition, etc.). A semi-empirical electro-optical simulation (as already mentioned in **Paragraph 2.2.1**) assessing the potential of perovskite-organic-hybrid tandem devices will be presented within the work outlined in **Chapter 4**.

3 Organic Tandem Solar Cells

The following part will demonstrate novel approaches for metal oxide based or even all-oxide interconnects. The first approach is based on the interface of high-work-function (WF) metal oxides like molybdenum oxide (MoO_x) or vanadium oxide (VO_x) and a low-WF tin oxide (SnO_x) in inverted tandem devices. In contrast to typical p-/n-type tunnel junctions (as mentioned in **Paragraph 2.2.2**), all of those oxides are n-type semiconductors with a WF of 5.1 eV to even more than 6.5 eV (MoO_x & VO_x) and 4.0 – 4.2 eV (SnO_x), respectively[48–51,108]. First it is demonstrated that the electronic line-up at the interface of the vacuum processed MoO_x and SnO_x comprises an interface dipole, which is key to afford ideal alignment of the conduction band of MoO_x and SnO_x, without the requirement of an additional metal or organic dipole layer. The presented interconnects allow for the ideal (loss-free) addition of the open circuit voltages of the two organic sub-cells. Moreover, a route to transfer the functionality of the vacuum processed MoO_x/SnO_x architecture to a completely solution-processed equivalent will be presented, in which sol-gel VO_x and nanoparticular SnO_2 are used. In addition to the inverted device structure, these SnO_2 nanoparticles can also be used to fabricate interconnection architectures for regular stacked tandem devices. Due to the increased chemical resilience of tin oxide, in contrast to e.g. the broadly used zinc oxide (ZnO), solution-processed interconnects containing acidic PEDOT:PSS are made possible. The results will present a route for the fabrication of such an interconnect, which has been developed in cooperation with partners at the Eindhoven University of Technology (TU/e). This chapter is based on results partially published in Ref. [109] and Ref. [110].

3.1 Vacuum-processed All-Oxide Interconnects

for Inverted Tandem Devices

Here a novel all-oxide recombination interconnect is demonstrated, which is based on the interface of the high-WF metal oxide MoO_x and low-WF tin oxide (SnO_x). Remarkably, the electronic line-up at the interface between MoO_x and SnO_x forms a large intrinsic interface dipole (≈ 0.8 eV), which affords near to ideal alignment of the conduction bands of MoO_x and SnO_x, without the requirement of an additional metal or organic dipole layer (s. **Paragraph 2.2.2**). As a result, electrons extracted via the SnO_x from the upper sub-cell are efficiently handed over from the SnO_x to the MoO_x. The actual recombination of electrons with holes takes place at the interface of organic/MoO_x at the lower sub-cell. This mechanism of charge recombination is in inverse analogy to that evidenced previously in multi-junction organic light emitting diodes (OLEDs), where the individual light emitting units are connected by so-called charge generation layers which comprised high-WF transition metal oxides (TMOs).[111] Moreover, the working principle in the here presented interconnects contrasts the established picture used in the case of highly doped organic p-/n-type tunnel junctions, which have been frequently used in tandem cells.[75] There, charge recombination occurs in the center of the interconnect as electrons tunnel from the lowest unoccupied molecular orbital (LUMO) of the n-doped electron transport layer to the HOMO of the p-doped hole transport layer. The presented MoO_x/SnO_x interconnect allows for the ideal addition of the open circuit voltages (V_{OC}) of the two sub-cells. In stark contrast to the vast majority of TiO_x of ZnO based tandem interconnects, which require activation by UV light ("UV light-soaking", see **Paragraph 2.1.3**)[112,113], the presented interconnect functions even in the absence of UV spectral

components. It will be demonstrated, that this novel all-oxide interconnect will be generally applicable for the design of monolithically integrated organic multi-junction solar cells.

3.1.1 Device Structure and Characteristics

The layer sequence of the inverted tandem OSCs in this study is shown in **Figure 3.1a**. The bottom sub-cell is based on poly[N-9′-heptadecanyl-2,7-carbazole-alt-5,5-(4′,7′-di-2-thienyl-2′,1′,3′-benzothiadiazole)] (PCDTBT):[6,6]-phenyl-C_{71}-butyric acid methyl ester (PC$_{70}$BM) as photoactive material, while the upper sub-cell comprises poly[(2,5-bis(2-hexyldecyl)-2,3,5,6-tetrahydro-3,6-dioxopyrrolo[3,4-c]pyrrole-1,4-diyl)-alt-([2,2′:5′,2″-terthiophene]-5,5″-diyl)] (PDPP3T):[6,6]-phenyl-C_{61}-butyric acid methyl ester (PC$_{60}$BM).[114] The molecular structure of the donor polymers and the respective absorption spectra of the photoactive layers are shown in **Figure 3.1b,c**. The chosen approach in this case was to use well established photoactive materials[81] to test and to demonstrate the functionality of the novel interconnect. Apparently, the choice of these photoactive materials may impose limits for the achievable overall efficiency of the tandem device, but it should be noted that the presented interconnect will be applicable to future photoactive systems which may allow for elevated efficiencies. SnO$_x$ has been used as EEL, which is grown by atomic layer deposition at temperatures as low as 80 °C (see **Appendix 7.1.1** for details of the preparation). In single-junction OSCs, it has been shown that SnO$_x$ forms a universal EEL with a low-work-function, which does not rely on activation with UV light.[48] Moreover, it has been demonstrated that by the use of SnO$_x$ one can avoid the occurrence of photo-

induced degradation of the FF and V_{OC}, which is commonly encountered in ZnO based devices upon prolonged exposure to solar radiation (more on this will be described in **Chapter 5**).[115] Moreover, SnO_x has also been used as EEL for solar cells based on hybrid perovskites with improved efficiency and long-term stability.[116–119]
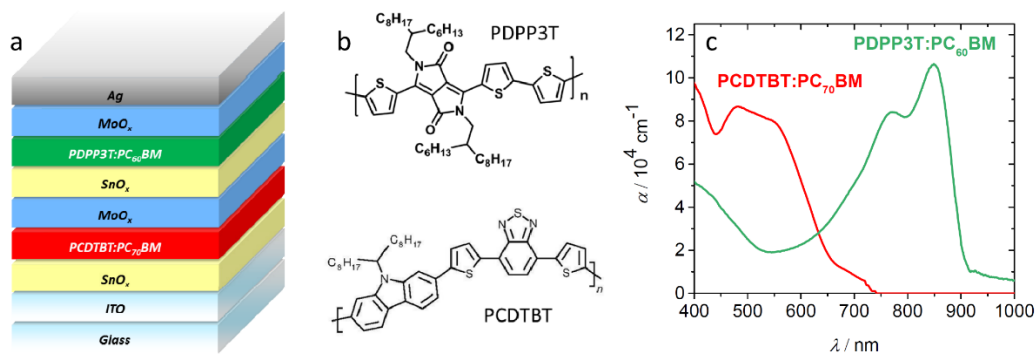

Figure 3.1: a) Layer sequence of the inverted tandem OSCs with MoO_x/SnO_x interconnect. b) Molecular structure of the absorber polymers poly[N- 9′-heptadecanyl-2,7-carbazole-alt-5,5-(4′,7′-di-2-thienyl-2′,1′,3′-benzothiadiazole)] (PCDTBT) and poly[{2,5-bis(2-hexyldecyl)-2,3,5,6-tetrahydro-3,6- dioxopyrrolo[3,4-c]pyrrole-1,4-diyl}-alt-{[2,2′:5′,2″-terthiophene]-5,5″-diyl}] (PDPP3T) used for the bottom and top sub-cells, respectively. c) Absorption spectra of both photoactive materials as used in the sub-cells of the tandem device. Reproduced from Ref.[109].

Initially, single-junction reference devices with a thickness of the photoactive layers identical to that of the sub-cells in the tandem devices have been prepared. The optimum thickness of the active layers for current matching has been determined by an optical simulation (according to the method described in **Paragraph 2.2.1**) taking into account the absorption characteristics of the photoactive layers in the tandem cell and the external quantum efficiency (EQE) of the single-junction devices (**Appendix Figure 7.1**). The optical simulation indicated an optimum thickness of the active PCDTBT:$PC_{70}BM$ layer in the bottom sub-cell of about 130 nm and a concomitant thickness of > 135 nm for the upper PDPP3T:$PC_{60}BM$ active layer. Unfortunately, the batch of PCDTBT used for these experiments, did not allow for devices with an active layer thickness substantially in excess

of 90 nm without severe losses in FF (**Appendix Figure 7.2**). Moreover, the J_{SC} did not increase significantly for a thickness higher than 90 nm. The reasons may be due to the molecular weight of the PCDTBT which did not allow for an optimum BHJ morphology. As such, a layer thickness of 90 nm have been used for the PCDTBT:PC$_{70}$BM sub-cell. For current matching, the thickness of the active PDPP3T:PC$_{60}$BM layer in the upper cell was consequently chosen to be $\approx$ 80 nm (**Appendix Figure 7.1d**). The respective characteristics of the single-junctions are shown in **Appendix Figure 7.3** and **Table 3.1**. The resulting tandem cells based on the monolithic series connection of these single-junctions by the MoO$_x$/SnO$_x$ interconnect have been characterized according to the protocol reported by Timmreck et al.[88], which has also been partially described in **Paragraph 2.2.3**.
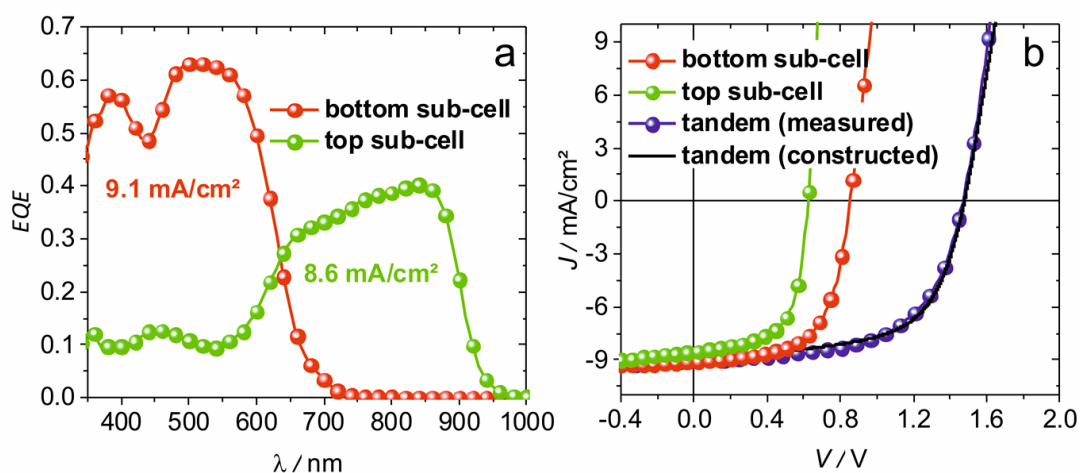
Figure 3.2: a) EQE spectra of the PCDTBT:PC$_{70}$BM (bottom) and PDPP3T:PC$_{60}$BM (top) sub-cells determined under appropriate biasing conditions.[88] b) J/V characteristics of the sub-cells as obtained from the single junction devices upon tuned illumination to achieve the Jsc, determined from the respective EQE spectra, as well as constructed and measured J/V characteristics of the tandem cell. Reproduced from Ref.[109].

Here, for the characterization of the PCDTBT:PC$_{70}$BM sub-cell, the PDPP3T:PC$_{60}$BM has been optically biased at 730 nm. Conversely, the PCDTBT:PC$_{70}$BM sub-cell has been biased at 530 nm. The resulting EQE spectra are shown in **Figure 3.2a**. The J/V characteristics of the sub-cells have been obtained from the single-junctions by tuning the illumination to

afford the J_{SC} calculated from the respective EQE spectrum (**Figure 3.2b**). From these data, the J/V characteristics of the tandem cell have been constructed. In addition the J/V characteristics of the tandem cell measured with appropriate corrections for spectral mismatch are shown. Importantly, in the tandem cells an ideal addition of the V_{OC} of the sub-cells is achieved, demonstrating the functionality of the MoO_x/SnO_x interconnect. The device efficiency is found to be up to 8.0 % (7.6 %, average over 11 devices) for the tandem cell, which is substantially higher than 5.4 % and 4.2 % for the PCDTBT:PC_{70}BM and the PDPP3T:PC_{60}BM sub-cells, respectively. Notably the J/V characteristics of the tandem cells are in excellent agreement with those constructed from J/V data of the sub-cells, which evidences the loss-free connection of both sub-cells by the MoO_x/SnO_x interconnect (**Figure 3.2b**).

Table 3.1: Characteristics of the single junction and tandem devices. The cell characteristics of the bottom and top sub-cells in the tandem stack were obtained by illuminating the single junction devices with adapted intensity to match the J_{SC} determined from the EQE analysis of the tandem cell. Characteristics of the tandem cells were measured and constructed from the J/V curves of the sub-cells. Statistical data of 11 cells are also stated. The error margins denote the standard deviation found in the set of devices. Reproduced from Ref.[109].

	V_{OC} [V]	J_{SC} [mA/cm²]	FF [%]	PCE [%]
Single junction devices				
PCDTBT:PC_{70}BM (nom. 90 nm)	0.849	10.3	62	5.4
PDPP3T:PC_{60}BM (nom. 80 nm)	0.627	10.7	63	4.6
Tandem device				
Bottom sub-cell	0.847	9.1	62	4.8
Top sub-cell	0.627	8.6	63	3.4
Tandem constructed	1.473	8.9	62	8.1
Tandem measured	1.468	9.1	60	8.0
Average of 11 devices	1.475 ± 0.012	8.4 ± 0.5	61 ± 2	7.6 ± 0.3

3.1.2 Analysis of the MoO$_x$/SnO$_x$-Interface

The loss-free connection by the MoO$_x$/SnO$_x$ interconnect and the resulting excellent functionality of the device is striking, considering the nature of this n/n-type recombination architecture. As discussed in **Paragraph 2.2.2**, the transport of electrons through this type of ICL is typically hindered by energetic barriers forming at the HEL/EEL-interface due to their significant difference in WF. To analyze the working mechanism of the MoO$_x$/SnO$_x$ interconnect in more detail, photoelectron spectroscopy (PES, performed by the group of Dr. Thomas Mayer at the Darmstadt University of Technology) as well as Kelvin probe (KP) analysis have been used to assess the energy level line-up in the interconnect. To this end, the start of this study was a 30 nm thick thermally evaporated MoO$_x$ layer. Thereafter, a step-wise deposition of SnO$_x$ layers with a thickness of 0.5–50 nm has been performed on top. The X-ray photoelectron spectroscopy (XPS) spectra for Mo3d and Sn3d are shown in **Appendix Figure 7.4.** No explicit band bending has been found in the MoO$_x$ upon deposition of SnO$_x$ on top. The resulting WF has been derived both from the secondary cut-off of the photoemission spectra (shown in **Appendix Figure 7.5a**) and the measured contact potential difference of the calibrated Kelvin probe, respectively. This experiment has been repeated for several sets of samples (**Figure 3.3a**). In both PES and KP, a strong initial lowering of the WF is observed upon deposition of SnO$_x$ on top of the MoO$_x$. The study starts at a WF of $5.1 - 5.3$ eV for MoO$_x$, which is in agreement with previous reports on thermally evaporated MoO$_x$ layers, which have seen a vacuum break.[120] Note that the MoO$_x$ in this study has also been thermally evaporated, but it had to be exposed to the glove-box atmosphere of the ALD system before deposition of the SnO$_x$.
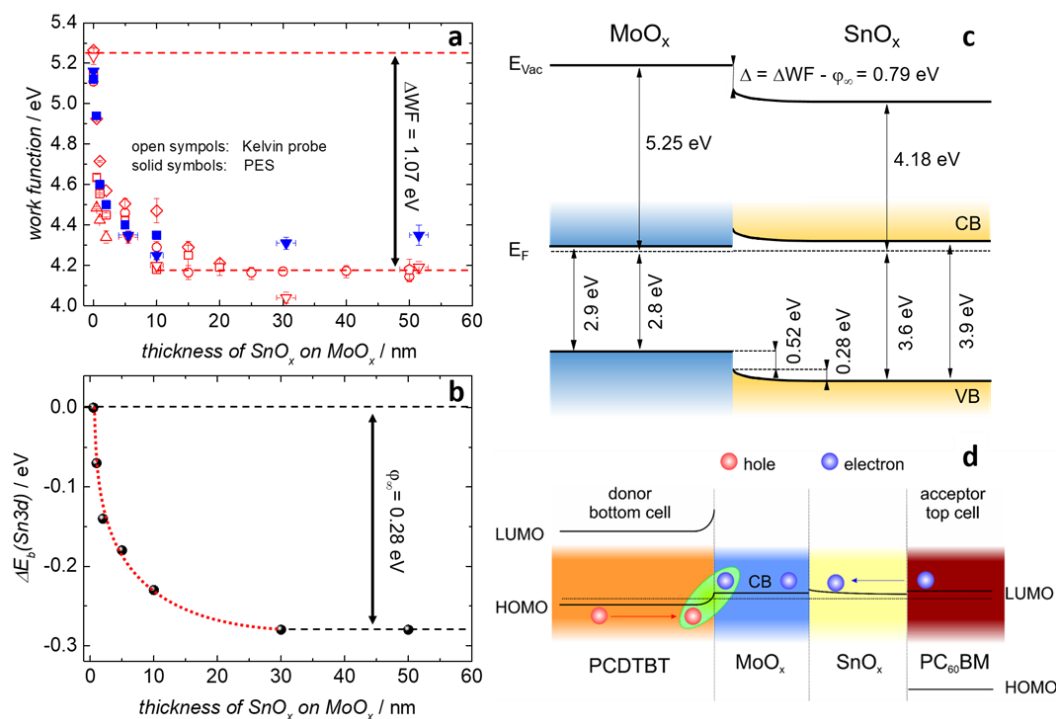
Figure 3.3: a) Variation of the work function upon deposition of SnO_x on top of MoO_x determined by photoelectron spectroscopy (PES, solid symbols) and KP (open symbols) for several sets of samples. b) Binding energy shift derived from XPS core level data of the Sn3d signal. The red dotted line is inserted as a guide to the eye. c) The energy level line-up at the MoO_x/SnO_x interface, resulting from UPS/XPS and KP analysis (the line-up including core levels is shown in **Appendix Figure 7.8**). The position of the conduction band minimum (CB) with respect to the valence band maximum has been determined from the respective optical band gap (see **Appendix Figure 7.9**). Note that the gap states in MoO_x have been omitted for simplicity. Possible band bending due to adsorbed water molecules at the surface of SnO_x is also not shown.[115] A schematic of the working mechanism of the interconnect in a tandem cell is shown in (d). For simplicity, only the energy levels of the acceptor of the top $PDPP3T:PC_{60}BM$ cell and the donor of the bottom $PCDTBT:PC_{70}BM$ cell are shown. The recombination of electrons and holes occurs at the interface of $MoO_x/PCDTBT$ (marked in green). Note that the energy levels are not to scale in this schematic. Reproduced from Ref.[109].

According to KP data, an overall WF drop of $\Delta WF = 1.07$ eV was found after deposition of 30 nm of SnO_x, lowering the WF from 5.25 eV for MoO_x to a saturated value of 4.18 eV for SnO_x (**Figure 3.3a**). Taking the XPS core level measurements into account, one can further derive a contribution of $\phi_\infty = 0.28$ eV in this WF drop (from the binding energy shift of the Sn3d peak) that can be attributed to band bending (**Figure 3.3b**). The large remaining part of the WF drop $\Delta = \Delta WF - \phi_\infty = 0.79$ eV, which occurs for < 5 nm of SnO_x, can be associated with an interface dipole.

To understand the possible origin of the large interface dipole, it is important to note that earlier work has shown a substantial lowering of the initially high-work-function of MoO_x if the Mo^{6+} species at the surface are reduced to Mo^{5+} or Mo^{4+}.[121,122] Indeed, an indication of reduced Mo^{6+} was found in the Mo3d XPS spectra, as a shoulder at lower binding energies of the main Mo^{6+} peak evolved upon deposition of SnO_x (**Appendix Figure** **7.6a**). Therefore, the interface dipole can be attributed to the partial reduction of Mo^{6+}. It should be noted that the sudden drop of the WF upon deposition of SnO_x on top of the MoO_x is not limited to the combination of MoO_x/SnO_x. In fact, it could be shown that the WF of MoO_x likewise dropped by 0.7–1.1 eV upon deposition of a few nanometers of other metal oxides by ALD, e.g., ZnO, Al_2O_3, etc. (see **Appendix Table** **7.1**). As such, the nucleation of the ALD precursors on top of the MoO_x layer gives rise to a reduction of the Mo^{6+}.

The WF of the SnO_x layers in this study is remarkably low compared to the WF of 5.7 eV reported for single crystalline SnO_2.[123] It has been shown previously that the lower WF of ALD SnO_x, as has been used here, results from Sn^{2+} surface species and adsorbed water molecules, which infer downward band-bending at the SnO_x surface.[48,124] The observed binding energy shift in the Sn3d peak corresponds to the variation of surface potential $\phi(d)$ with increasing the thickness d of the SnO_x (**Figure 3.3b**, red dotted line inserted as an eye guide). As can be seen in the discussion in **Appendix Figure 7.7**, the progression of the surface potential $\phi(d)$ cannot be described by simple textbook semiconductor physics in the framework of the Schottky model over the total thickness range in this study. If one takes defect induced gap states into account a simplified distributed states model (DSM) can be used that has been introduced by Mankel et al.,[125] which provides a significantly better approximation of the experimental

data. The carrier density in the SnO_x layer cannot directly be derived with the DSM. At least within the first 10 nm based on the Schottky model, one can roughly estimate a carrier density of $> 10^{19}$ cm^{-3}, which is orders of magnitude higher than the carrier density derived from the position of the Fermi level for thick SnO_x layers (see below). This discrepancy can possibly be explained by taking into account the ALD specific nucleation phase in the first cycles of the ALD process, which may infer a higher number of defect states, that would give rise to a higher carrier density in the first few nanometers of layer growth. Unfortunately, the overall low electrical conductivity did not allow for an unambiguous determination of the actual carrier density of the SnO_x layers by Hall techniques.

3.1.3 Working Principle of the Interconnect

The PES and KP data allow for the construction of an energy level line up at the MoO_x/SnO_x interface as shown in **Figure 3.3c**. Note that the WF and the band-bending is based on the results of the KP data. Using the WF from PES, instead, does not fundamentally change the line-up. It has to be noted that the position of the conduction band minimum (CB) has been obtained by adding the bandgap energy (E_g) of the respective material to the position of the valence band maximum that has been determined by UPS (**Appendix Figure 7.5b**). As shown in **Figure 3.3c**, both MoO_x and SnO_x are n-type semiconductors, and the large interface dipole $\Delta = 0.79$ eV between the two materials leads to a favorable alignment of the CB with only a minor energy offset on the order of 200 meV. It has to be noted that this energy offset in the CB is subject to the uncertainties in the determination of the energetic position of the CB in the respective material. An E_g of 3.9 eV and 2.9 eV for

SnO$_x$ and MoO$_x$ has been derived from the respective Tauc-plots of their optical absorption spectra (**Appendix Figure 7.9**). In the literature a bandgap for thermally evaporated MoO$_x$ has been reported in the range of 2.8–3.2 eV.[49] For SnO$_x$ grown by ALD at low temperature, ultraviolet photoelectron spectroscopy (UPS) and inverse photoemission spectroscopy (IPES) data provided a bandgap of 3.72 eV.[117] Taking the latter value as the band-gap in the shown line-up (**Figure 3.3c**) would even result in a CB offset between MoO$_x$ and SnO$_x$ close to zero. From the distance of the Fermi level and the CB edge ($E_{CB} - E_F$), a complementary estimate of the carrier density in the prepared SnO$_x$ could be derived. The effective electron mass of SnO$_2$ is $m^* = 0.4 \times m_0$.[126] With ($E_{CB} - E_F$) = 0.12–0.3 eV (depending on the technique to determine E_{CB}), the estimated carrier density varies between 4×10^{13} cm^{-3} and 5×10^{16} cm^{-3}, which indicates a relatively low doping level of the SnO$_x$ bulk layer. These values stand in contrast to the high carrier densities derived from the band bending data for the first nanometers of SnO$_x$ that can be attributed to nucleation effects in the ALD growth at the MoO$_x$/SnO$_x$ interface, as outlined above.

The WF on both sides of the interconnect appears excellently suited to interface with the donor (PCDTBT) of the lower sub-cell and the acceptor (PC$_{60}$BM) of the upper sub-cell. Consequently, a schematic can be constructed which visualizes the working mechanism of the interconnect in the tandem cells (**Figure 3.3d**). Electrons which are extracted from the upper sub-cell via the SnO$_x$/PC$_{60}$BM interface are efficiently transported in the CB of the SnO$_x$ to the CB of the MoO$_x$ where they further propagate to the PCDTBT/MoO$_x$ interface. There, they meet and recombine with the holes which are extracted from the PCDTBT. It has to be noted that even though MoO$_x$ is used for hole extraction in organic solar cells, it is an n-type material with a high-WF and an extremely deep lying CB (high electron

affinity). The electronic line up at the interface organic/MoO_x has been determined for a range of organic compounds (e.g., 4,4′-bis(N-carbazolyl)-1,1′-biphenyl (CBP), tris(4-carbazoyl-9-ylphenyl)amine, and N,N′-di(1-naphthyl)-N,N′-diphenyl-(1,1′-biphenyl)-4,4′-diamine).[49] The energetic mechanism at the MoO_x/organic interface, that leads to interfacial p-type doping of the organic layer, has already been described in **Paragraph 2.1.3**.[49] A similar finding has been reported for the interface of other high-WF TMOs adjacent to organic semiconductors, e.g., WO_3/CuPc,[127] WO_3/spiro-MeOTAD,[128] or V_2O_5/CBP.[108] Note that an interconnect based on a single layer of MoO_x (i.e., without the SnO_x) would not afford the same functionality. It has been shown that the electronic line-up at the interface of MoO_x/fullerene comprises a large energy offset between the LUMO of the fullerene and the CB of the MoO_x even in cases where the MoO_x surface had been exposed to air prior to the deposition of the fullerene.[129] As such, in the absence of SnO_x the energetic mismatch of MoO_x and fullerene would lead to substantial losses of V_{OC} for the tandem cell.

3.1.4 Influence of the Interconnect on Functionality Without UV Light

As stated initially, SnO_x has shown notable advantages compared to ZnO or TiO_x based EELs in single-junction organic solar cells. Among them the absence of light-soaking problems, in contrast to ZnO or TiO_x EELs, which need to be "activated" by UV light with photon energies larger than the band-gap of the metal oxide ($hv > E_g$).[71,85,130–135] In this regard, the use of SnO_x is favorable in cases where UV light activation is undesired or not even

possible. In multi-junction cells, the availability of UV photons to activate metal oxides in the recombination layers will be limited due to the fact, that these will partially get absorbed in the bottom sub-cell. To study this effect in tandem cells, tandem devices based on MoO_x/SnO_x or MoO_x/ZnO interconnects have been fabricated (**Figure 3.4a**). As shown in **Figure 3.4b,c**, tandem cells with either MoO_x/SnO_x or MoO_3/ZnO interconnects show similar characteristics when illuminated under full AM1.5 illumination, but both behave crucially different in absence of UV light. In this case, both SnO_x and ZnO were deposited by ALD. The remaining UV light at the interconnect is transmitted by the wide gap sub-cell due to the limited active layer thickness of $PCDTBT:PC_{70}BM$ discussed above (**Paragraph 3.1.1** & **Appendix Figure 7.2**).
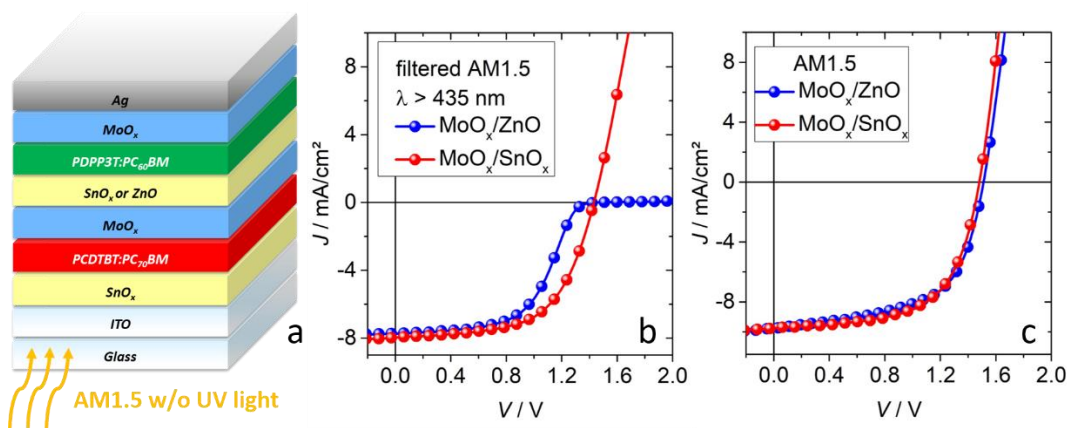

Figure 3.4: a) Layer sequence of the inverted tandem OSCs with MoO_x/ZnO or MoO_x/SnO_x recombination layers. J/V characteristics of the corresponding devices under AM1.5 illumination b) with and c) without UV blocking filter ($\lambda > 435$ nm). Reproduced from Ref.[109].

Impressively, the use of SnO_x in the interconnect allows for well-behaved solar cell characteristics with high FF and PCE even under illumination with AM1.5, where the UV components have been blocked by a filter ($\lambda > 435$ nm), whereas the device comprising ZnO shows a strongly s-shaped J/V curve under the same conditions. Note that the drop of the WF

of MoO_x inferred by the deposition of SnO_x or ZnO is comparable for both oxides as shown above (**Appendix Table 7.1**). In earlier studies, the necessity of UV activation in case of ZnO EELs has been associated with the electronic alignment at the EEL/fullerene interface.[46] Similar issues have been encountered for ZnO-based interconnects before.[112][MSI-44]

3.1.5 Interim Summary

An all-oxide MoO_x/SnO_x recombination interconnect for organic multi-junction solar cells has been demonstrated. The electronic line-up at the interface of MoO_x and SnO_x has been studied in detail by photoelectron spectroscopy and Kelvin probe analysis. A large intrinsic interface dipole (≈ 0.8 eV) has been found to infer near to ideal alignment of the conduction bands of MoO_x and SnO_x. This favorable line-up is essential for the working principle of the interconnect: The SnO_x extracts electrons from the upper sub-cell, which are then efficiently transferred to the MoO_x via the CBs, before the actual recombination with holes at the interface of organic/MoO_x of the lower sub-cell. The presented MoO_x/SnO_x interconnect allows for the ideal addition of the open circuit voltages (V_{OC}) of the two sub-cells. The resulting tandem devices significantly surpass the efficiency of the individual sub-cells. In stark contrast to similar devices based on MoO_x/ZnO which need to be activated by UV exposure, the MoO_x/SnO_x based tandem cells function without any limitation even in the absence of UV light. This concept of all-oxide MoO_x/SnO_x interconnects should be generally applicable to tandem devices with other combinations of organic BHJs or even hybrid multi-junction architectures with different photoactive material classes, as will be presented in **Chapter 4**.

3.2 Solution-Processed Interconnects for Inverted and Regular Tandem Devices

To transfer the all-oxide strategy to even more challenging fully solution-processed interconnects, various metal oxide layers (either processed via sol-gel approaches or nanoparticle dispersions) in different HEL/EEL combinations will be presented and investigated concerning the most important properties for the use in interconnection layers. As described in **Paragraph 2.2.2** these include resilience against solvents to protect the underlying sub-cell and proper alignment of energy levels to enable charge extraction from both sub-cells. Based thereon, the most promising candidates have been identified and tested in tandem devices leading to a fully solution-processed all-oxide recombination interconnect for inverted architectures. Moreover, the introduction of SnO_2 as a new solution-processed metal-oxide EEL facilitated the fabrication of novel ICLs for the regular device architecture. Due to the superior chemical resistance of SnO_2 in contrast to ZnO, the necessity of suboptimal pH-neutral PEDOT as HEL could be mitigated.

3.2.1 Basic Examination of Fully Solution-Processed Architectures

The main challenge in transferring the approach of all-oxide interconnection layers from a vacuum processed system to a completely solution-processed equivalent turned out to be the chemical protection of the underlying active layer against the solvent of subsequent processes. As discussed in **Paragraph 2.2.2** the fundamental processes (chemical and/or

physical) behind the resilience against solvents have not been completely elucidated up to this date. As a result, promising candidates for layers providing these specific properties (e.g. PEDOT:PSS) are mainly found based on empirical or phenomenological investigations. For this work the following basic qualitative examination method has been utilized. Based on the device architecture presented in **Chapter 3.1**, each combination of high- and low-WF metal oxides were subsequently processed on top of a glass substrate coated by a PCDTBT:PC$_{70}$BM BHJ and then tested by spin coating a testing solvent onto the entire stack (see **Figure 3.5** & **Figure 3.6**).
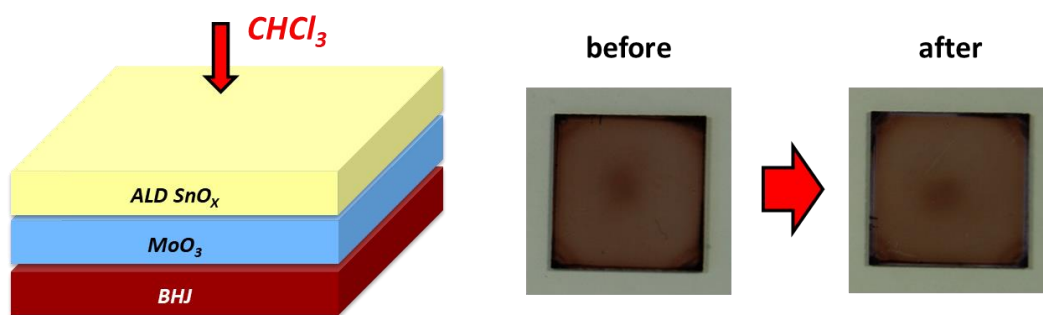

Figure 3.5: Testing the resilience upon CHCl$_3$ spin coating on top of schematic testing stack (left): For the combination of eMoO$_3$/SnO$_x$ the method is causing no visible damage of the active layer (right).

Photographs of the stack before and after spin-coating of the testing solvent indicate the amount of induced damage to the underlying BHJ. The solvent mixture used for the processing of the most promising narrow gap photoactive materials (like PDPP3T) mainly consists of chloroform (CHCl$_3$), which was therefore chosen as testing solvent. **Figure 3.5** demonstrates the exemplary layer sequence and the results for the combination of thermally evaporated MoO$_3$ and ALD-processed SnO$_x$, which has been used in the vacuum-based ICL proven functional in the previous section. As anticipated, there is no visible damage induced by the treatment with CHCl$_3$.
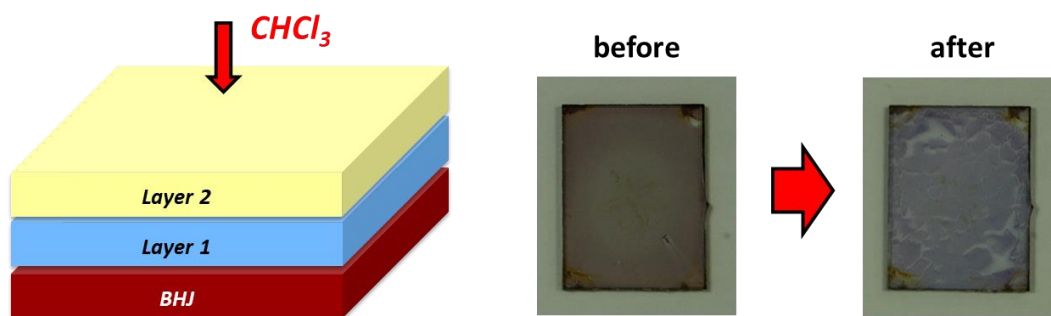
Figure 3.6: Testing the resilience upon CHCl₃ spin coating on top of different layer combinations: Schematic testing stack (left), exemplary result with layer combination sVO$_x$ (Layer 1)/sSnO$_x$ (Layer 2) (right).

The most pressing challenge was to achieve a similar chemical protection in case of interconnects comprising only solution-processed metal oxides. In order to find a suitable layer sequence with the required protection properties, several solution-processed materials have been tested. As shown in the example of **Figure 3.6**, some of the combinations of metal-oxide layers did not protect the active layer from being damaged after the CHCl₃ testing routine. The different low-WF oxides have also been tested in combination with thermally evaporated MoO$_x$ to provide a comparison to the completely solution-processed architectures, in whichused sol-gel vanadium oxide (sVO$_x$, processing details can be found in **Appendix Paragraph 7.1.1**) has been used as hole extraction layer because it showed good compatibility with various active layer systems in earlier work.[51] As described there, sVO$_x$ can be used as a replacement of eMoO$_x$ even on top of organic BHJs. Processing details for all materials can be found in **Appendix Paragraph 7.1.1**.
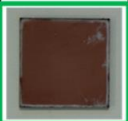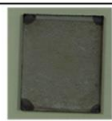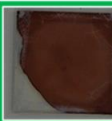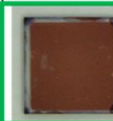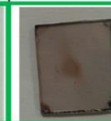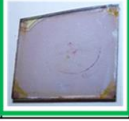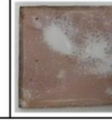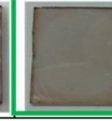
1 〼 2	"sZnO"	sSnO$_x$	sTiO$_x$	ZnO-NP	N-20X	N-21X	SnO$_2$-NP
eMoO$_3$							
sVO$_x$							

Table 3.2: Results after CHCl$_3$ treatment (as shown in **Figure 3.5** & **Figure 3.6**) for different combinations of high work-function (layer 1) and low work-function materials (layer 2) on top of a photo-active layer. The samples showing low (or even no) changes after the treatment are marked green.

For sol-gel SnO$_x$ (sSnO$_x$) different formulations have been tested[115,136] but only one exemplary result is displayed because none of them showed a sufficient resilience. The results for the tested material combinations are summarized in **Table 3.2**. The samples showing good resilience are marked in green. The different colour impression of the respective BHJs in different pictures is caused by varying absorption characteristics of the active layer due to different fullerene acceptors (either PC$_{60}$BM or PC$_{70}$BM) and layer thicknesses in different test runs. The thickness of the underlying BHJ did not have any significant influence on the outcome of the resilience tests performed on top of it. Notably, no positive effect due to thickness variations of individual metal-oxide layers (up to 300 nm) has been observed, either. In the case of sol-gel metal oxides, this can be attributed to pinholes in the layers which allow for the penetration of the solvent and (partial) dissolution of the active material underneath. It should be stressed that the independence of layer thickness was also found for eMoO$_x$. This leads to the conclusion that incorporating vacuum-processed layers of sufficient thickness does not automatically results in a resilient interconnect, as is sometimes claimed in literature.[137] The results on thermally evaporated MoO$_x$ and ALD-processed metal oxides in combination with preliminary reports discussed in **Paragraph 2.2.2** suggest, that the chemical resilience strongly depends on the specifics of the

deposition method.[76,78] The missing resilience in the case of bare $eMoO_x$ could also be attributed to pinholes originating from lower layer density in case of evaporated layers in contrast to those prepared by e.g. ALD.

The following solution-processed systems have been found to provide a resilience (tested by the method shown in **Figure 3.6**), that allowed for further testing in actual device architectures:

• sVO_x / "sZnO"

• sVO_x / AZO-NPs (N-21X, *Avantama*)

• sVO_x / ZnO-NPs (*infinityPV*)

• sVO_x / SnO_2-NPs (N-30, N-31, *Avantama*)

The sZnO is a layer prepared by a sol-gel route, which is sufficiently documented in literature.[138] It has to be noted that the exact composition of this material has not been analysed. Moreover, this sZnO has already been demonstrated in tandem interconnects in combination with $eMoO_x$.[70] In analogy to other systems, in this case a thin metal layer was needed to achieve voltage addition of the sub-cells and a moderate FF of 54 %. In addition to the known problems with this approach (see **Paragraph 2.2.2**), it already showed reproducibility problems when tested in single-junction devices during preliminary experiments. As a result, it has not been included in further investigations.

Consequently, the most promising candidates for suitable interconnection architectures in an inverted device stack have been identified as a combination of sol-gel VO_x and different formulations of metal oxide nanoparticles. The ALD-processed electron extraction layers of ZnO and

SnO$_x$ are replaced by their respective analogue based on commercially available or newly developed nanoparticle dispersions.

For regular stacked devices a different approach has been followed, by utilizing the chemical robustness of SnO$_2$, to enable an advanced recombination architecture incorporating acidic PEDOT:PSS, which has not been possible before. As alluded to in **Paragraph 2.2.2**, PEDOT:PSS is known to provide the needed resilience and is therefore not included in the chemical resilience screening study above. **Paragraph 3.2.4** will further expand on this approach.

3.2.2 Inverted Devices with ZnO-based n/n-Type Interconnects

The first encouraging tandem results in an inverted structure have been obtained by using the combination of sVO$_x$ and commercially available ZnO Nanoparticles from *InfinityPV*. As active layers PCDTBT:PC$_{70}$BM (see above) has been chosen for the bottom (wide gap) and poly((2,5-bis(2-hexyldecyl)-2,3,5,6-tetrahydro-3,6-dioxopyrrolo(3,4-c)pyrrole-1,4-diyl)-alt-((2,2'-(1,4-phenylene)bisthiophene)-5,5'-diyl)) PDPPTPT (P17) in a BHJ with PC$_{60}$BM for the top (narrow gap) sub-cell. As shown in **Figure 3.7** a first tandem with the solution-processed ICL sVO$_x$/ZnO-NP showed a behavior very similar to the reference device with the vacuum processed recombination contact eMoO$_x$/SnO$_x$. The only difference being a slight s-shape in the J/V curve of the sVO$_x$/ZnO-NP device, which will be discussed in the following.
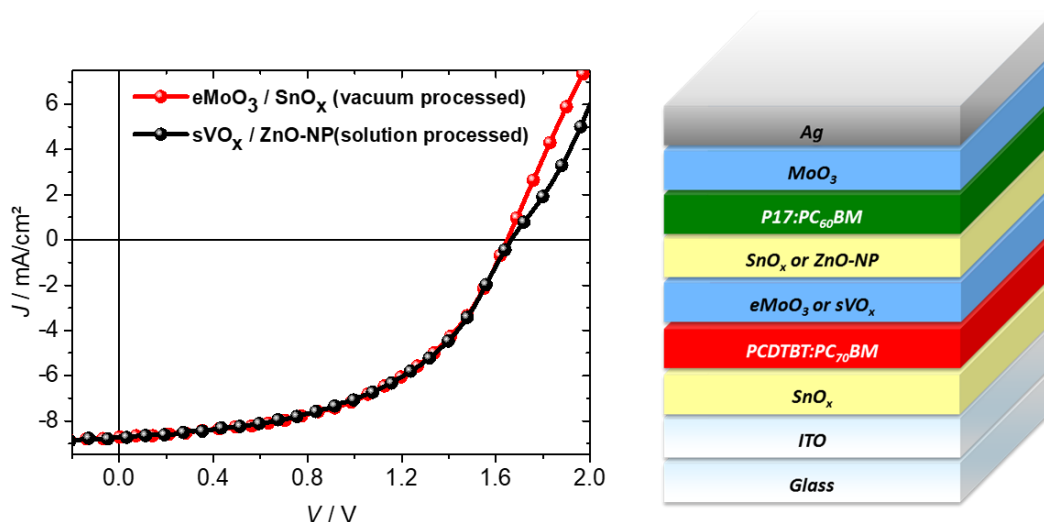
Figure 3.7: Inverted tandem devices with solution or vacuum processed all-oxide recombination layer: The tandem devices with either eMoO3/SnOx or sVOx/ZnO-NP ICL show very similar J/V curves under AM1.5 illumination. The only difference is the slighty s-shaped behaviour of the fully solution processed device.

The results of a second run of tandems in this fashion, presented in **Figure 3.8**, show that perfect addition of sub-cell open circuit voltages and distinguishable EQE characteristics for both sub-cells are achieved. From this one can conclude that the interconnection layer is intact and both sub-cells are working individually. The s-shape in the J/V curve also shown in **Figure 3.8** hints to problems at the sVOx/ZnO-interface and provokes losses in the FF of the tandem. This was already observed in an early report where a similar ICL-approach was used.[74] There, the insertion of a thin metal layer between VOx and ZnO lead to an enhanced FF of the tandem, which was attributed to a higher carrier density at the interface. To achieve the same result without an additional metal layer, tandem devices with commercially available nanoparticular aluminum doped ZnO (AZO-NPs) (*Avanatama*'s N-21X) instead of undoped ZnO (in analogy to the ALD-based approach described by Shim et al.) have been prepared.[76] Unfortunately, the FF of the devices containing AZO-NPs achieved slightly lower FFs as those with ZnO and showed lower reproducibility concerning the resilience of the ICL.

This is attributed to lower resilience of the ICL in the case of N-21X (see **Table 3.2**).

Despite the discussed problems with the sVO$_x$/ZnO-NP interconnect, also this tandem device achieves an enhanced efficiency of 7.2 % with respect to the reference single-junctions (PCE$_{PCDTBT:PC70BM}$ = 4.6 %, PCE$_{P17:PC60BM}$ = 6.1 %). It should be stressed that this and the fact that both oxides are prepared with room temperature processes is in strong contrast to all reported approaches up to this point and represents a significant improvement regarding solution-processed recombination layers without PEDOT:PSS and additional metal layers.

Device	PCE [%]	V$_{oc}$ [V]	J$_{sc}$ [mA/cm²]	FF [%]
Lower subcell in tandem	3.5	0.88	7.2	56
Upper subcell in tandem	4.3	0.82	8.1	65
Tandem	7.2	1.70	7.7	55
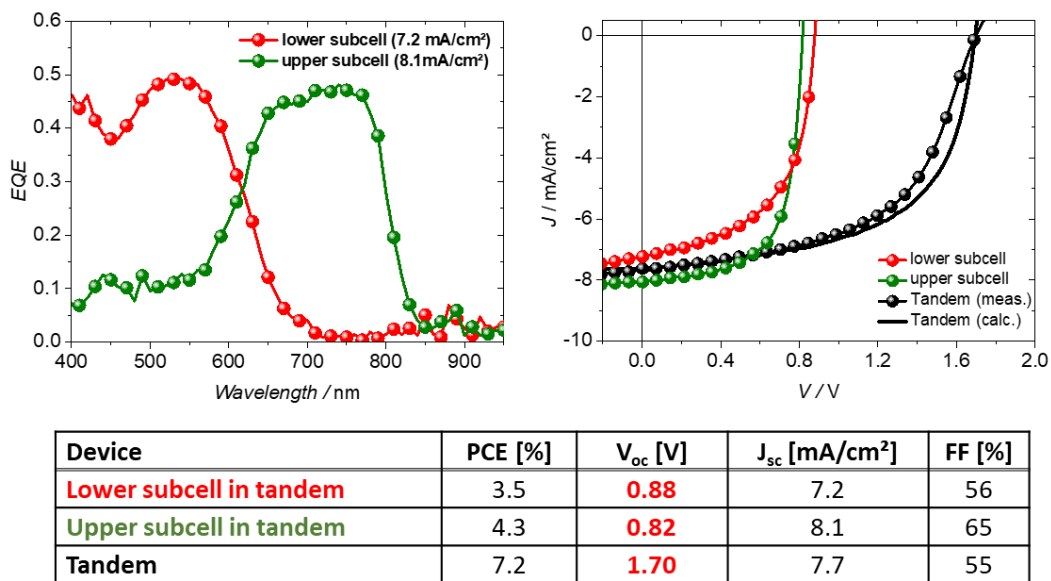
Figure 3.8: Inverted tandem device with sVO$_x$/ZnO-NP recombination layer: EQE of sub-cells (left top), J/V curves of sub-cells under tandem illumination conditions and measured and constructed tandem characteristics under illumination with AM1.5 (right top), device parameters of sub-cells and tandem device (table).

3.2.3 Solution-Processed SnO₂-based n/n-Type Interconnects

Due to the already demonstrated advantages of SnO$_x$ EELs in contrast to ZnO-based systems, the transfer to a solution process was of large interest. Within the MUJULIMA project (European Unions's 7th Framework Programme under Grant Agreement no. 604148) different newly developed SnO$_2$ nanoparticle dispersions were provided by the partner *Avantama AG* (Switzerland). Two formulations (in the following called N-30 and N-31, meanwhile commercially available) were identified as the most promising candidates in preliminary single-junction device tests. These showed, that devices based on these SnO$_2$ layers showed similar results compared to those based on ZnO. Remarkably, only N-31 showed the abovementioned advantage over ZnO with regard to UV activation (see **Figure *7.12***). After successfully testing both formulations for chemical protection properties in combination with sol-gel VO$_x$ (see **Paragraph 3.2.1**), it has been found that only N-30 showed a low enough WF on top of sVO$_x$ (4.2-4.3 eV) to allow for efficient electron extraction from the top cell, while N-31 only led to a WF of 4.5-4.6 eV. Unfortunately, it was not possible to clarify the origin of these differences between N-30 and N-31 (behaviour without UV irradiation and the decisively different WF) due to a lack of details shared by *Avantama GmbH* concerning the distinction between both SnO$_2$ nanoparticle formulations, where typically different capping agents and additives are used to stabilize the dispersion and the surface of the particles.

For the tandem devices again PCDTBT:PC$_{70}$BM has been used as wide gap active layer for the bottom sub-cell and P17:PC$_{60}$BM has been used as narrow gap material in the top sub-cell. The resulting devices comprised an ICL with sVO$_x$ as hole extractor for the lower sub-cell and both SnO$_2$ NP

formulations as electron extractor for the upper one (see **Figure 3.9**). Interestingly, both of the devices achieved only suboptimal efficiencies and showed significant differences in FF and V_{OC} (see table in **Figure 3.9**). The tandem device with N-30 achieved nearly perfect voltage addition but a relatively low FF only slightly above 50 %. In contrast to that, using N-31 instead led to a loss in V_{OC} of about 200-250 meV but a notable increase in FF to 60 %.

SnO$_2$ layer in ICL	PCE [%]	V_{oc} [V]	J_{sc} [mA/cm²]	FF [%]
N-30	5.5	1.68	6.1	53
N-31	5.7	1.46	6.3	62
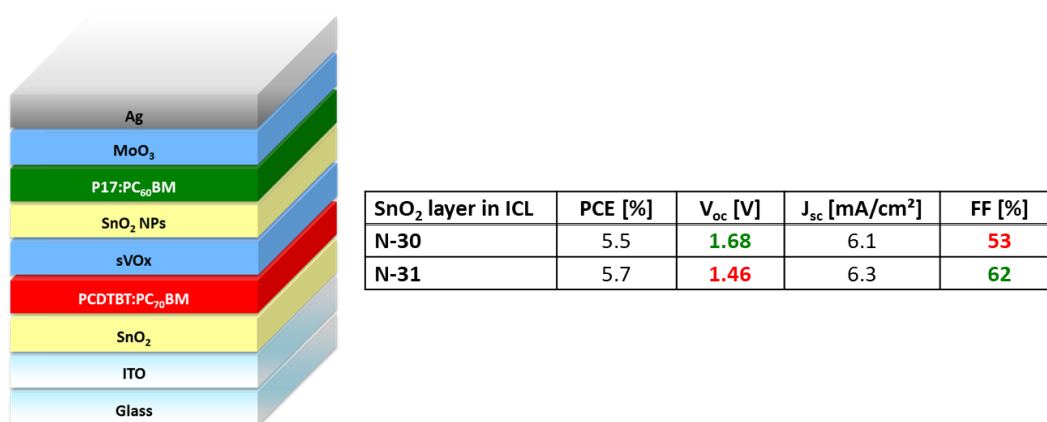
Figure 3.9: Tandem devices with solution processed ICL comprising sVO$_x$ and an SnO$_2$ layer (either N-30 or N-31). Device stack (left) and resulting parameters (right). The OSC comprising N-30 reaches good voltage addition but a low FF, while N-31 leads to a higher FF but losses in V_{OC}.

The loss in V_{OC} can be explained by the relatively high WF resulting when N-31 is processed on top of sVO$_x$ in contrast to N-30 (**Appendix Figure 7.11**). The difference in FF can be attributed to the significantly different behaviour of N-30 in single-junction devices when illuminated without UV light (**Appendix Figure 7.12**). In the tandem stack a large part of the UV light is absorbed by the lower sub-cell and is thus missing for the activation of the EEL. Depending on the EEL material, this can result in sub optimal charge extraction[46], which then infers a relatively low FF in case of N-30 and surprisingly did not seem to be an issue in the case of N-31, as also indicated by the results obtained from the respective single-junctions (see

Appendix Figure 7.12). This is another phenomenon of which the origin could not be finally clarified within this thesis due to the lack of information about N-30 and N-31, as already mentioned above.

To combine the perfect addition of V_{OC} with a high FF an approach of combining both formulations in a double SnO_2 layer has been used on top of the hole extractor (in this case sVO_x). In a first step N-30 is spincoated on top of sVO_x to lower the WF significantly. On top of this, the second SnO_2 layer is prepared by spincoating N-31 followed by the next active layer. This creates a recombination contact with sufficient contrast in WF and provides an EEL/organic interface that is supposed to not require any UV activation.

Device	PCE [%]	V_{oc} [V]	J_{sc} [mA/cm²]	FF [%]
Lower subcell in tandem	3.7	0.89	6.6	62
Upper subcell in tandem	5.2	0.82	9.5	67
Tandem (measured)	7.7	**1.70**	7.4	**61**
Tandem (calculated)	7.7	1.71	7.5	60
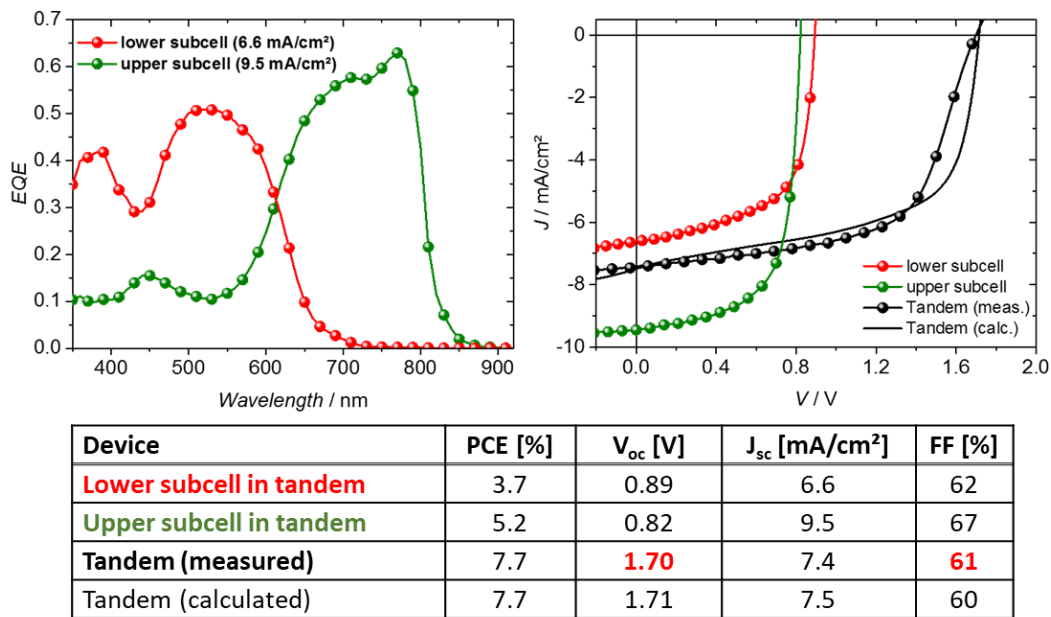
Figure 3.10: Inverted tandem device with sVO_x/SnO_2-NP recombination layer: EQE of sub-cells (left top), J/V curves of sub-cells under tandem illumination conditions and tandem under illumination with AM1.5 (right top), device parameters of sub-cells and tandem devices (table).

Figure 3.10 shows the results of the first tandem cell comprising this double-layer approach in the ICL. Remarkably, the device shows loss-free voltage addition and achieves a relatively high FF of 61 %. Moreover the device parameters of the measured tandem match the parameters of the

constructed J/V curve nearly perfectly (table in **Figure 3.10**), even though the measured curve deviates significantly (which is due to a different position of the maximum power point). While this deviation might be partially influenced by the not fully matched currents of the sub-cells in this case, it must still be concluded that the recombination architecture with the bilayered EEL is not fully functional, yet. One possible reason for the unsatisfactory functionality might be a negative influence of butanol on the properties of the underlying sVO_x, which could not be finally clarified. Despite the problems and open questions, it should be noted that this new approach led to a tandem cell with a $PCE_{Tandem} = 7.7\,\%$, that exceeded the efficiency of the reference single-junction devices ($PCE_{PCDTBT:PC70BM} = 5.2\,\%$, $PCE_{P17:PC60BM} = 7.0\,\%$). This is especially promising, considering that a completely solution-processed ICL achieved perfect voltage addition and a relatively high tandem FF in spite of a suboptimal current matching. In addition to this, the new recombination contact based on SnO_2 nanoparticles has a decisive advantage towards the already discussed interconnect comprising ZnO instead. **Figure 3.11** demonstrates, that the device with sVO_x/SnO_2 interconnect provides a functionality of the tandem device even under illumination with UV blocking filter, while the device comprising the sVO_x/ZnO-ICL is not working at all under these conditions. This is in nearly perfect analogy to the results presented for the vacuum processed ICL in **Paragraph 3.1.4** (see **Figure 3.4**).
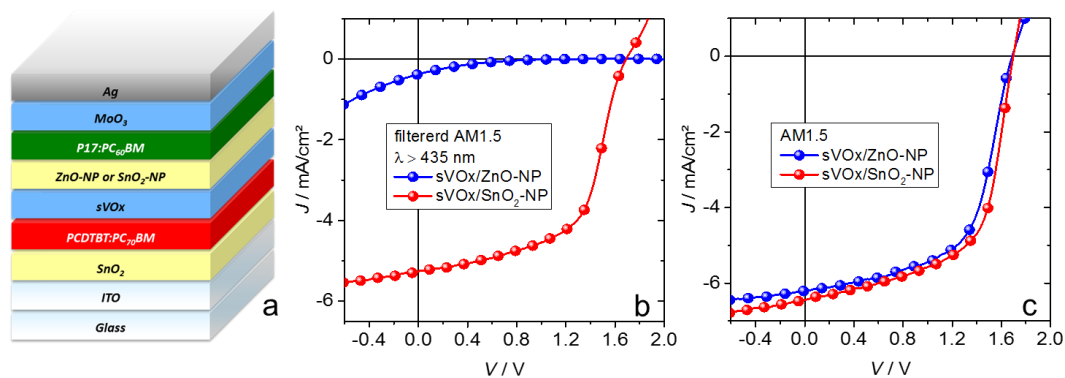
Figure 3.11: a) Layer sequence of the inverted tandem OSCs with sVO$_x$/ZnO-NP or sVO$_x$/SnO$_2$-NP recombination layers. b) J/V characteristics of the corresponding devices under AM1.5 illumination with and c) without UV blocking filter ($\lambda > 435$ nm).

3.2.4 SnO$_2$-based p/n-Type Interconnects

In addition to its displayed functionality under different illumination conditions, SnO$_x$ provides even more advantages over the broadly used ZnO. The increased chemical integrity against acidic solvents makes it suitable for the use in interconnection architectures for regular tandem device architectures, where PEDOT:PSS is used as a p-type HEL for the upper sub-cell. Within a project founded by the seventh framework programme of the EU, such an interconnect has been developed in cooperation with Dario di Carlo Rasi et al. from Rene Janssen's Group at the Eindhoven University of Technology (TU/e).[139] This paragraph has been partially published in Ref.[139].

Earlier work by the TU/e demonstrated that regular tandems comprising ZnO as the EEL on top of the lower sub-cell did not allow for the use of acidic PEDOT:PSS on top of it due to a (partial) deterioration of the underlying ZnO layer.[85] Therefore a modified, pH-neutral formulation of

the PEDOT:PSS dispersion (n-PEDOT) had to be used. Layers that have been deposited using this non acidic version, showed significantly lower work function (around 400 meV) with respect to unmodified PEDOT:PSS layers.[85,140] Therefore, the use of the pH-neutral formulation could lead to striking losses in V_{OC} when combined with specific active layers.[141,142] In tandem devices like the ones shown above, comprising PDPPTPT (P17) as the active polymer, the V_{OC} loss caused by the necessity of using n-PEDOT have been shown to be around 200 mV.[143] This can be attributed to the mismatch between the aforementioned low work function with the deep lying HOMO-level of P17 at ~ 5.48 eV.[144]

Within this work the SnO_2 based EELs already utilized above have been tested as a replacement in regular stacked tandem devices with PEDOT:PSS HELs.
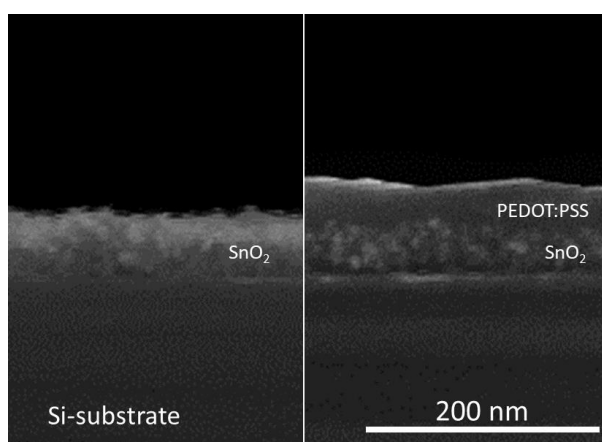
Figure 3.12: SEM cross-section of a pristine SnO_2 nanoparticle layer (left) and a EDOT:PSS layer spin coated on top of the SnO_2 layer (right) on a silicon substrate. Partially reproduced from Ref.[139].

The chemical robustness of the processed SnO_2 layer is indicated by an SEM cross section image, which shows a comparison of a pristine SnO_2 nanoparticle layer before and after the deposition of a PEDOT:PSS layer on top from an aqueous acidic dispersion (**Figure 3.12**). As can be seen, the PEDOT:PSS layer is formed on top of a still fully intact layer of SnO_2 without

any visible damage of the SnO_2. Further Kelvin Probe analysis of the layer stack on top of an ITO substrate (ITO/SnO_2/PEDOT:PSS) demonstrates a work function of 5.0 eV compared to 5.1 eV for ITO/PEDOT:PSS. This indicates the preservation of a high WF, and therefore suggests efficient hole extraction without loss of V_{OC}, which would not be possible with the use of n-PEDOT.

Configuration[a)]	V_{OC} [V]	J_{SC} [mA cm^{-2}]	FF	PCE [%]
Single junction	0.80 (0.79)	14.4 (14.4)	0.63 (0.62)	7.23 (7.03)
Single junction[b)]	0.78 (0.78)	7.34 (7.37)	0.66 (0.65)	3.77 (3.72)
Tandem	1.54 (1.54)	7.59 (7.48)	0.58 (0.58)	6.82 (6.69)

Table 3.3: Photovoltaic parameters of single and homo-tandem cells based on P17:PC$_{70}$BM in a regular structure determined with simulated AM1.5G (100 mW/cm^2) illumination. a) See the main text for a description. Values are reported for best cells with average performance in parentheses. The statistics is over four identical cells for the single junction devices and 8 cells for tandems. b) These measurements were performed under reduced light intensity to mimic the behavior of the sub-cells in the tandem. From Ref.[139].

To confirm the anticipated improvement due to incorporation of the described interconnect, tandem and single-junction devices with P17-based active layers have been fabricated (device stacks shown in **Figure 3.13a,b**). To enable a comparison with literature, P17:PC$_{70}$BM is used for the active layers of both sub-cells.[143] The device parameters of both single-junction and tandem shown in **Table 3.3** display, that the tandem device has a V_{OC} of 1.54 eV, which is around 60 meV smaller than double the V_{OC} of the single-junction device (1.60 eV), which would be theoretically expected for a monolithic double stack. Taking into account the lowering of the V_{OC} by the reduced light intensity experienced in the tandem configuration, which is found to be 20 mV per sub-cell (as can be seen in **Table 3.3**), the remaining loss in V_{OC} is only around 20 mV compared to the 200 mV demonstrated

before.[143]   Thus, the use of SnO_2 instead of ZnO and the consequent facilitation of acidic PEDOT:PSS enables the full exploitation of the photovoltaic potential of polymers with deep lying HOMO-levels.
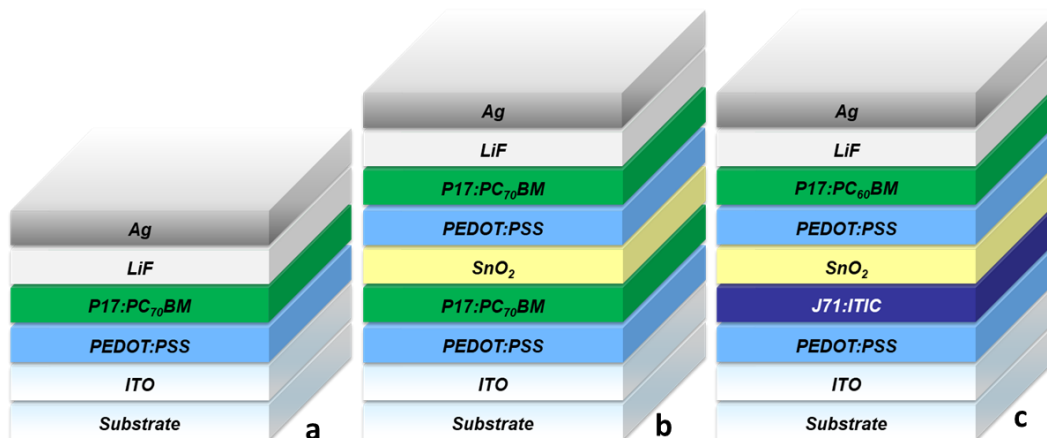
Figure 3.13: Regular device stacks of a P17-based single-junction (a), monolithic P17-based double stack tandem (b) and high efficiency tandem with J71:ITIC bottom sub-cell and P17:PCBM top sub-cell. The top EEL in all cases is a 1 nm thick thermally evaporated layer of lithium fluoride (LiF). Modified from Ref.[139].

This leads to substantially improved device parameters in regular monolithic double stacks of P17-based BHJs and, when combined with a novel, more efficient active system (J71:ITIC)[145], a tandem device with an outstanding efficiency of 10.2 % could be achieved (stack depicted in **Figure 3.13c**). It is to note, that the combination of PEDOT:PSS and SnO_2 nanoparticles could also be used to fabricate p/n-type ICLs inverted devices. This necessitated a slight modification of the PDOT:PSS deposition route and the already introduced double-layer approach for the SnO_2 layer, which resulted in an ICL providing all abovementioned benefits and enabled the fabrication of an analogous tandem cell (with a J71:ITIC bottom sub-cell and P17:PC$_{70}$BM top sub-cell), that reached similar efficiency to the regular architecture (10.4 %).

3.2.5 Summary

The combination of sol-gel VO_x and ZnO nanoparticles showed good results concerning protection against solvents and functionality in tandem devices. Perfect addition of V_{OC} is achieved but slightly s-shaped J/V characteristics result in a lowered FF of the tandem device compared to a theoretical curve constructed from the characteristics of both individual sub-cells. Nonetheless the tandem devices show a significant enhancement in power conversion efficiency with respect to the single-junctions. Tandems with such a recombination architecture comprising only solution-based room temperature processes under ambient conditions have not been reported so far.

With the use of SnO_2 nanoparticles instead of ZnO it was even possible to create an improved room temperature solution-processed all-oxide interconnect, that provides perfect addition of sub-cell V_{OC} and a higher FF than reached with ZnO. As an additional advantage towards the ZnO based interconnection layer, devices with the new sVO_x/SnO_2 architecture do no longer show impairments in FF when illuminated without the UV part of the AM1.5 spectrum. It has to be stressed, that the outstanding results involving this type of solution-processed sVO_x/SnO_2 recombination architecture have actually been achieved under suboptimal current-matching conditions for both sub-cells. This suggests the possibility for tandems with even further improved device characteristics by optimization of the individual thicknesses of the active layers. Moreover it has to be noted once more, that the demonstrated ICL, despite providing good device characteristics (loss-free voltage-addition and a high FF), does not lead to a congruence of constructed and measured J/V curves. It is up to further investigations, if this issue can be fixed by just enhancing the current-

matching conditions or if it originates from known (**Paragraph 2.2.2**) or novel ICL interface-phenomena for these new n/n-type architectures.

Additionally, the introduction of SnO_2 nanoparticles as a suitable solution-processed EEL added new possible routes for the fabrication of solution-processed p/n-type interconnects. Besides the successful application of the double-layer approach on top of a PEDOT:PSS HEL in case of inverted tandems, the chemical robustness of the SnO_2 EEL also allowed for the use of acidic PEDOT:PSS in regular architectures, which was not possible before. The entailing elimination of the voltage loss attributed to the utilization of pH-neutral PEDOT variants (e.g. in commonly used ZnO/n-PEDOT ICLs) resulted in functional tandem devices in both regular and inverted devices. This innovative recombination architecture does not only provide chemical protection for the bottom sub-cell but also nearly loss-free electric interconnection of the sub-cells, as demonstrated by two highly efficient tandem cells in both regular and inverted configuration. In conclusion, SnO_2 and PEDOT:PSS can be used as ICL for efficient conventional and inverted multi-junction devices, without the need of additional layers.

Together, these results pave the way to new possibilities to manufacture efficient multi-junction solar cells by solution- processing.

4 Perovskite/Organic Hybrid Tandem Solar Cells

Up to the start of this work, perovskite/organic tandem cells showed subpar efficiencies of around 20 %, limited by the low open circuit voltage (V_{OC}) of wide-gap perovskite cells[146] and losses introduced by the interconnect between the sub-cells.[66,147] In this chapter a two-terminal p-i-n perovskite/organic tandem cell is presented, operating near the levels predicted by simulations, based on a new semi-empirical model based on the approaches mentioned above (**Paragraph 2.2.1**). It will be shown, that the organic back-cells, based on a recently developed polymer and non-fullerene acceptor (NFA), provide a high external quantum efficiency in the near-infrared and, in surprising contrast to common concerns about limited photostability of those non-fullerene solar cells,[148] an outstanding operational stability is evidenced if excitons are predominantly generated on the NFA. This turns out to have distinctive importance in a tandem cell, where the illumination of the organic active layer is spectrally filtered by the perovskite front-cell. Most strikingly a novel interconnect based on an ultra-thin metal like indium oxide layer is presented, which offers unprecedented low optical and electrical losses compared to prominent approaches used in literature up to now.[66,149] Moreover, a simulation based on the fundamental findings of this work will provide further insight into the efficiency potential of perovskite/organic tandem architectures. This chapter has partially been published in Ref.[150].

4.1 Narrow-Bandgap Organic Sub-Cell

Due to the developments of new NFAs, OSCs started to see a second wave of outstanding advancement.[151,152] Mainly the high internal and external quantum efficiencies (IQE and EQE) in near infrared spectral regions compared to fullerene-based systems, make the NFA-based cells highly interesting for tandem devices. Being one of the most commonly used high efficient active materials in literature at the time, an organic photo-active system based on the polymer Poly[(2,6-(4,8-bis(5-(2-ethylhexyl-3-fluoro)thiophen-2-yl)-benzo[1,2-b:4,5-b']dithiophene))-alt-(5,5-(1',3'-di-2-thienyl-5',7'-bis(2-ethylhexyl)benzo[1',2'-c:4',5'-c']dithiophene-4,8-dione)] (PM6), and the NFA 2,2'-((2Z,2'Z)-((12,13-bis(2-ethylhexyl)-3,9-diundecyl12,13-dihydro-[1,2,5]thiadiazolo[3,4-e]thieno [2'',3'':4',5'] thieno [2',3':4,5]pyrrolo[3,2-g]thieno[2',3':4,5]thieno[3,2-b]indole-2,10-diyl)bis (methanylyliden)bis(5,6-difluoro-3-oxo-2,3-dihydro-1H-indene-2,1-diylidene))dimalononitrile (Y6), has been used for the narrow-gap sub-cell in the tandem architecture.[153] Their respective molecule structures can be found in **Figure 4.1a**. A p-i-n type device architecture has been employed, using thermally evaporated molybdenum-trioxide (MoO$_3$) as hole extraction layer (HEL) below the active layer and a bi-layer of evaporated fullerene C$_{60}$ and 2,9-Dimethyl-4,7-diphenyl-1,10-phenanthroline (BCP) on top for efficient electron extraction (**Figure 4.1a**). The p-i-n structure has been chosen due to requirements given by the perovskite sub-cell, which will be discussed below. The cells with binary PM6:Y6 blends (mass ratio 1:1.2) provided a power conversion efficiency (PCE) of up to 16.5 %. J/V curves and EQE spectra of the devices are displayed in **Appendix Figure 7.13a**. Notably, the EQE spectrum of these devices extends beyond 900 nm (**Figure 4.1c**). Adding a certain concentration of fullerene molecules into the

PM6:Y6 photo-active layer to form a so-called ternary system, i.e. PM6:Y6:PC$_{61}$BM (mass ratio 1:1.2:0.2), improves the blend morphology, which results in enhanced charge transport and reduced non-radiative recombination.[154,155] Thus, a notable boost in cell characteristics is achieved with a PCE up to 17.5 % (J/V curve also shown in **Appendix Figure 7.13a**). Notably the device processing turns out to be extremely robust, as can be prominently verified by the statistical results in **Appendix Figure 7.14.** What should be highlighted is a significantly enhanced EQE of > 85 % for the ternary cells in the wavelength range of λ > 650 nm, which is the spectral region of operation when combined with a wide-gap front-cell in a tandem. The absorption spectra of PM6 and Y6 (**Figure 4.1b**) show that for λ > 650 nm excitons are predominantly generated on the acceptor Y6, which will be shown to be the key that unlocks outstanding device stability.

Stability of organic solar cells with NFAs under continuous operation is still a serious concern and a subject of vigorous scientific research.[156–158] To assess the stability of the devices with binary and ternary blend active layers under the illumination conditions applicable in a prospective perovskite/organic tandem cell, a filtered white LED (labelled: LED$_{VIS}$) and a near infrared (NIR) LED (peak at 850 nm; labelled: LED$_{NIR}$) have been used as light sources, which predominantly create excitons on the donor PM6 or the acceptor Y6, respectively (**Figure 4.1b**). Under combined VIS/NIR illumination, binary and ternary devices show a notable decay of the PCE under continuous operation in the maximum power point (MPP) (**Figure 4.1d**), mainly due to a loss in fill factor (FF) (**Appendix Figure 7.15**). This degradation motif has previously been attributed to a photo-induced reorganization in the donor/acceptor blend and the formation of microscopic aggregates of NFA molecules, which leads to a reduced electron mobility and enhanced recombination.[159] Owing to their improved

blend morphology, the decay of the ternary cells is notably slower than that of the binary cells, which has also been reported earlier.[156]
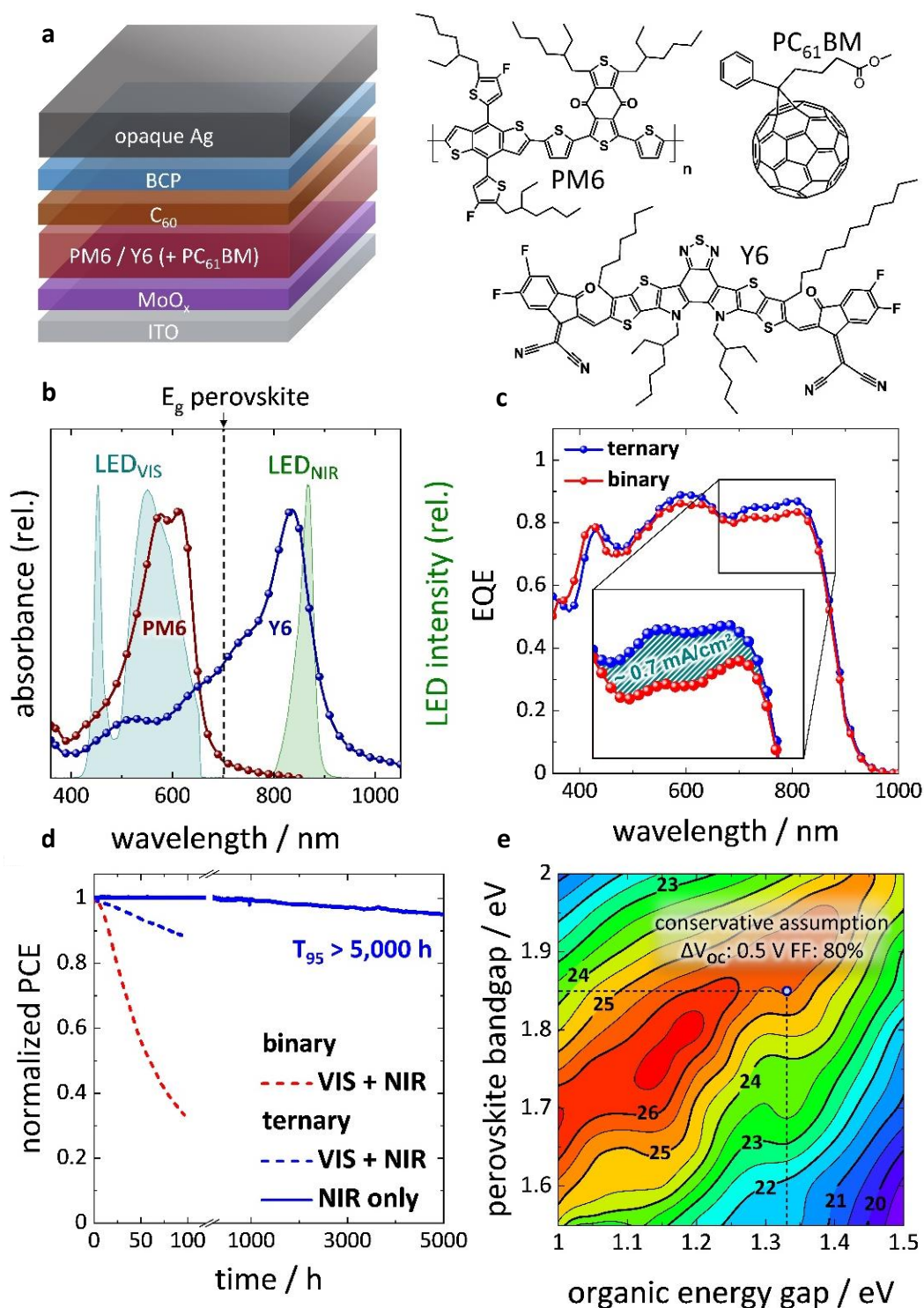

Figure 4.1: Architecture and properties of the organic sub-cell. a) Layer sequence of the single-junction OSC and chemical structure of the molecules used in the photoactive layer. b) Absorption spectra of the donor and acceptor molecules used in the photoactive layer. The vertical line marks the E_g of a possible wide-gap front-cell material. Spectra of (filtered)

LEDs used in the stability assessment to selectively excite the donor/acceptor are also shown (LEDVIS and LED NIR); rel., relative. c) EQE of binary (PM6:Y6) and ternary (PM6:Y6:PC$_{61}$BM) cells with a magnified view of the spectral region > 650 nm, which is the relevant range of operation for the OSC in a perovskite–organic tandem cell.   d) Normalized PCE showing the long-term stability of binary and ternary organic cells continuously operated using LED light sources with emission spectra shown in b (one-sun-equivalent, nitrogen atmosphere, 25 °C) in the MPP with exciton generation on both acceptor and donor (VIS + NIR) or only on the acceptor (NIR). Note the break in the x axis. T$_{95}$ denotes the time after which the initial PCE has dropped to 95 % of its initial value. e) Semi-empirical model of the tandem cell efficiency versus the energy gap of organic and perovskite sub-cells. The intersection of the dashed lines corresponds to the energy gap of the PM6:Y6:PC$_{61}$BM back-cell and the matching energy gap of the perovskite front-cell. This simulation states a conservative scenario assuming open-circuit voltage loss (ΔVoc) of 0.5 V and a FF of 80 %. A more optimistic (yet still realistic) model (ΔVoc = 0.4 V, FF = 85 %) yields a maximum efficiency higher than 31 % (see **Appendix Figure 7.20**). Reproduced from Ref.[150].

However, most strikingly, under NIR illumination, where excitons are solely generated on the Y6, the devices did not show any short-term decay (burn-in) and no degradation even under long-term continuous operation for more than 5,000 h (retaining 95 % of the original efficiency). These findings indicate that the detrimental morphological changes, discussed above, would require excitation of the donor polymer PM6 and that they can be substantially mitigated if predominantly the Y6 NFA is excited. Atomic force microscopy (AFM) and grazing incidence wide-angle X-ray scattering (GIWAXS) did not show morphological changes on continuous illumination with LED$_{VIS}$ + LED$_{NIR}$ under inert conditions, and the results of grazing incidence small-angle X-ray scattering (GISAXS) indicate only some minor morphological changes at the surface of samples after ageing (**Appendix Figure 7.16-7.18**). On the other hand, it was found that upon continuous illumination with the white LED under inert conditions the photoluminescence quantum yield of PM6 shows a notable degradation, while the Y6 is less affected (**Appendix Figure 7.19**). Therefore, photo-induced degradation of PM6 could likewise play a significant role in addition to possible morphological changes. In any event, these findings

contradict the paradigmatic association of non-fullerene solar cells with operational instability, and they present the especially encouraging prospect that the long-term operational stability of the resulting tandem cells will not be limited by the narrow-gap organic sub-cell. This is in notable contrast to all-perovskite tandems, where the (in-) stability of Sn-based narrow-gap perovskites is still a very serious issue.[160–162]

4.2   Selection of the Perovskite Active Layer

As already mentioned in **Paragraph 2.2.4**, one pathway to highly efficient tandem solar cells is the use of metal-halide perovskites as an active layer. Their general tunability in bandgap energy (E_g) can be utilized to complement another material with a certain bandgap energy, and with this construct the perfect counterpart to optimize the absorption overlap with the solar spectrum.

The PM6:Y6 organic system introduced above provides an energy-gap of 1.33 eV,[153] and a semi-empirical electro-optical simulation has been conducted to identify a suitable wide-gap PSC for a tandem. Therefore the expected PCE of the tandem device has been determined for different combinations of absorber bandgaps. The general approach of these simulations has already been introduced in **Paragraph 2.2.1**. A more specific discussion is presented here, addressing the particular details in this case.

As input data for the simulation the complex refractive indices (optical constants n & k) of all layers in the tandem stack are needed. For all layers except ITO and the perovskite and organic active layers the data was

determined either by optical absorption or spectral ellipsometry measurements. To gather data for the perovskite and organic layers with different gap energies, we proceeded as follows. At first the optical constants for known perovskite and organic absorbers were taken from literature.[163,164] The data was then offset in wavelength to obtain data for similar materials with varied energy gap. The optical constants of ITO have also been taken from literature.[165]

To determine the simulated J_{SC} of the respective tandem cells, a transfer matrix algorithm was then used to calculate the charge generation due to photon absorption inside the active layers upon illumination of the whole tandem stack with the AM1.5G spectrum. This is done for varying layer thicknesses up to 800 nm for the perovskite and up to 150 nm for the organic layer, respectively. Due to the chosen limits in layer thickness one can assume negligible transport losses inside the active layers and thus an internal quantum efficiency (IQE) of 100 % for both sub-cells, which has also been reported to be possible.[166,167] The charge generation in each active layer can be translated into a maximum possible current density $J_{SC,optimal}$ (in this optimal case every generated charge is harvested as photocurrent) of each sub-cell for each given thickness combination.

Describing the tandem device as a series connection of both sub-cells, the sub-cell providing the lower $J_{SC,optimal}$ can be considered as current limiting for the entire device. As a result the maximum J_{SC} of the tandem device is obtained by determining the highest value of all minimal $J_{SC,optimal}$ values for each thickness combination. Following this procedure, a plot of the maximum possible PCE for each combination of energy gaps can be derived (**Figure 4.1e**). According to the results for an organic energy gap of 1.33 eV, an efficiency of 25.5 % is predicted with a perovskite bandgap in the range

of 1.85-1.92 eV, assuming a tandem FF of 80 % and a loss in V_{OC} compared to E_g/q of 0.5 V, in each sub-cell. In a more optimistic scenario (FF = 85 % and loss in V_{OC} compared to E_g/q of 0.4 V), a tandem of a narrow-gap OSC (E_g = 1.15 eV) with a PSC (E_g = 1.75 eV), even provides the prospect to reach an efficiency of 31.3 % (**Appendix Figure 7.20**). Until recently[168], efficient OSCs with E_g = 1.15 eV had not been developed, so they were not available at the time of this work. Nevertheless, it will be demonstrated below, that perovskite/organic architectures, provided appropriate active materials are available, bear the potential to perform near the predicted limits of this model.

As described earlier (**Paragraph 2.2.4**) the typical ABX_3 composition of metal halide perovskites comprises methylammonium (MA^+), formamidinium (FA^+), or Cs^+ ions on the A-site, Pb^{2+} ions on the B-site, and halide ions, such as I^- or Br^-, on the X site. Some members of this family, e.g. $FA_xCs_{1-x}Pb(I_yBr_{1-y})_3$, provide the needed tunability of the bandgap energy (E_g) between 1.5-2.3 eV, mainly by variation of the I/Br ratio,[169,170] rendering them especially attractive for the design of multi-junction cells. $FA_{0.8}Cs_{0.2}Pb(I_{0.5}Br_{0.5})_3$ was selected as suitable perovskite composition with a bandgap of 1.85 eV (**Appendix Figure 7.21**). Early studies have shown, that for perovskite solar cells with E_g > 1.75 eV, the V_{OC} did not concomitantly increase with E_g, which has frequently been attributed to photo-induced halide-segregation in the perovskite into bromine- and iodine-rich domains.[171] Yet, more recently, recombination losses at the interfaces of the wide-gap perovskite and the adjacent charge extraction layers have been found to be predominately limiting the V_{OC}.[146,172] As such, a minimization of these interfacial losses has been performed in order to narrow in on the highest possible V_{OC} in the PSCs. These losses and the minimization studies will not be discussed in detail here. The specific work on the perovskite

processing, passivation strategies, and the extraction layers used in the perovskite sub-cell is detailed in a recent publication[150] and further is subject of the thesis of my colleague Kai Oliver Brinkmann.[101]
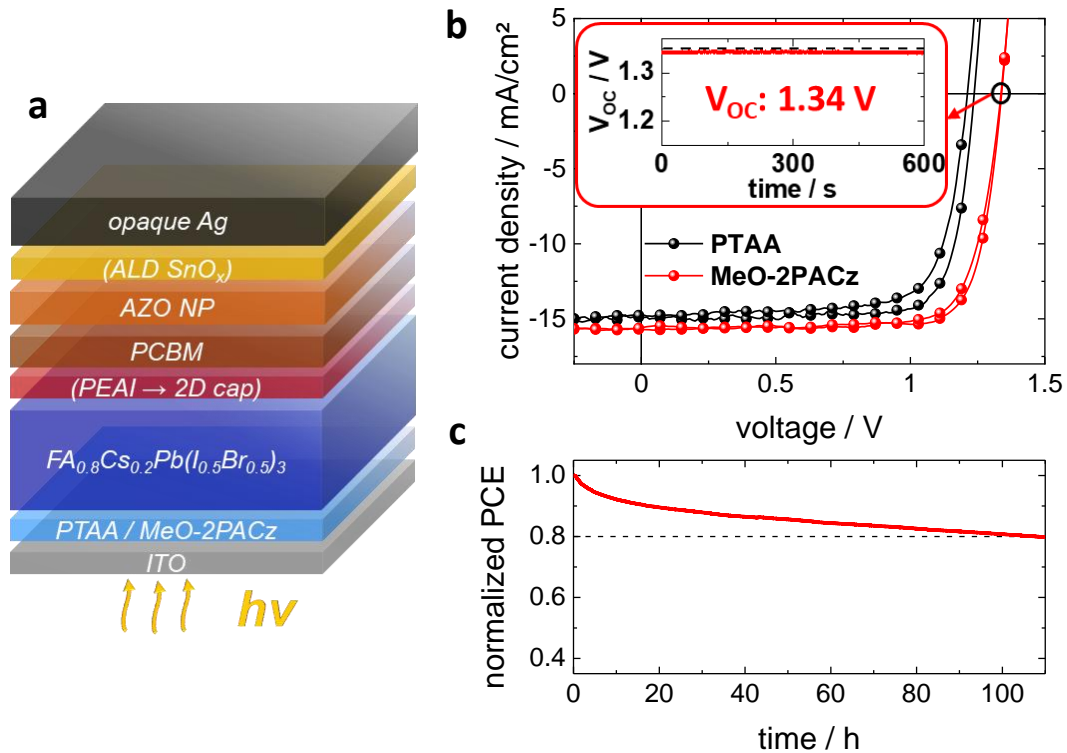
Figure 4.2: Optimized wide-gap perovskite sub-cell: a) Layer sequence of the p–i–n perovskite single junction. b) J/V characteristics for champion PSCs with a 2D capping layer (MeO-2PACz self-assembled monolayer (SAM) as the HEL) or PbI2 excess (PTAA as the HEL). The inset shows the stabilized Voc of 1.34 V for the cell with the SAM as the HEL. c) Normalized PCE versus time of the PSCs illuminated with a white LED and operated in the MPP. Reproduced from Ref.[150].

Ultimately, after the aforementioned optimization of the complete PSC architecture performed under lead of Kai Oliver Brinkmann[101], devices with hysteresis-free J/V characteristics are achieved, that provide a very high stabilized $V_{OC} = 1.34$ V (**Figure 4.2b**) with a FF that falls within a narrow range of 77-82 %. It is to be noted, that the PCE of these wide-gap PSC remains above 80 % of its initial value, when operated in the maximum power point (MPP) continuously for more than 100 hours (**Figure 4.2c**). The

bandgap of the perovskite derived from the EQE spectrum of the device (shown in **Appendix Figure 7.21b)** is 1.85 eV, which is in the range of bandgaps identified by the performed simulation and thus renders to be suitable for the intended tandem device. The final stack of the PSC (shown in **Figure 4.2a**) comprises an electron transport layer (ETL) of $PC_{61}BM$ on top of the passivated active layer and is concluded by an impermeable hybrid electron extraction layer (EEL) consisting of nanoparticulate AZO and ALD-processed SnO_x.[173] In addition to its functionality as an extraction layer this combination of nanoparticle-based and ALD-processed oxides provide outstanding encapsulation of the perovskite sub-cell, forestalling its intrinsic and extrinsic degradation mechanisms.[118] Moreover, similar to the case presented in **Chapter 3.1**, the impermeability of this ALD processed EEL is the enabling factor for the incorporation of the PSC in tandem architectures, due to its protection of the underlying device stack against following processing steps.[118,124,174] The fact, that this is only given in a p-i-n architecture (mainly because of the needed concluding ALD-SnO_x layer) defines the structure of the complementary OSC (mentioned above) and the resulting tandem device, which includes the choice and working principle of the interconnect, as will be discussed in the following part.

4.3   Low-loss All-Oxide Interconnect

In a p-i-n stacked tandem device, the interconnect facilitates the recombination of electrons from the bottom sub-cell (in this case the PSC) with the holes from the top sub-cell (in this case the OSC), ideally without any loss of V_{OC} and FF. This obviously works in direct opposite to the n-i-p stacked devices described in **Chapter 3.1**. In the simplest approach, one

could omit the top electrode of the perovskite single junction cell and position the organic cell directly on top. In this case, the interface between the low-work-function SnO_x and the high-work-function MoO_x affords only extremely poor, s-shaped J/V characteristics of the resulting tandem cell (in **Figure 4.4a**). Notably, although the materials used for the interconnect in this p-i-n structure are the same as in the n-i-p tandem device covered in **Chapter 3.1**, one does not achieve similar functionality. It should be stressed that the decisive difference between both interconnection architectures is the sequence of processing, which causes a fundamentally different energetic band alignment at the interface of both oxides. Here the MoO_x functioning as HEL in the p-i-n stacked organic sub-cell is thermally evaporated on top of a continuous layer of ALD-processed SnO_x, which concludes the EEL of the perovskite sub-cell. So, although the SnO_x is processed from the same precursor (TDMA-Sn), there are no unreacted precursor molecules at the SnO_x/MoO_x interface that would reduce the Mo^{6+} species and therefore lower the WF of the MoO_x as is the case in the n-i-p architecture. Thus there is no formation of an intrinsic interface dipole resulting in a Schottky barrier at the SnO_x/MoO_x interface ("without InO_x" in **Figure 4.4c**) and a diode-like behavior of the SnO_x/MoO_x layer sequence instead of an ohmic contact ("without InO_x" in **Figure 4.4b**).
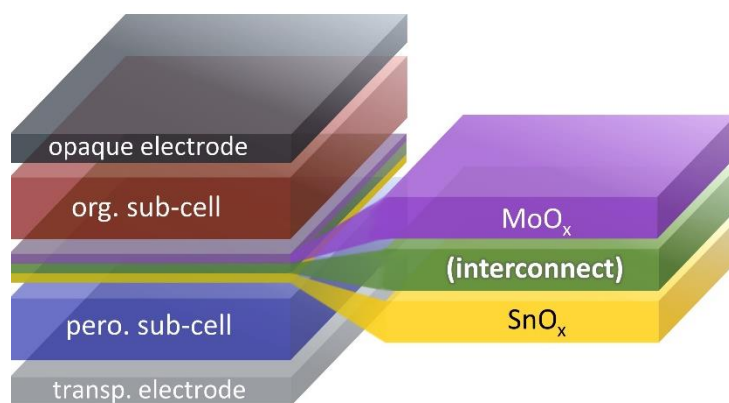

Figure 4.3: Schematic of a perovskite–organic tandem cell with InO_x or Ag as interconnect. Reproduced from Ref.[150].

To further assess the rectifying behavior inferred by the interface, test devices comprising a layer sequence of ITO/SnOₓ (20 nm)/MoOₓ (5 nm)/Au have been prepared and their J/V characteristics have been recorded. Forward bias refers to a positive bias of the MoOₓ electrode with respect to the SnOₓ electrode. To fit the J/V curves of those devices, a standard diode model was used

$$I = I_0 \left(exp \left(\frac{q(V - IR_s)}{nk_BT} \right) - 1 \right) + \frac{V - IR_s}{R_{sh}}, \tag{4.1}$$

where q is the elementary charge, n is the ideality factor, R_s and R_{sh} are the series and shunt resistance, respectively. I_0 denotes the saturation, which can be expressed by

$$I_0 = A \cdot A^* \cdot T^2 \exp \left(-\frac{q\,\phi_b}{k_BT} \right), \tag{4.2}$$

with A^* being the Richardson constant, ϕ_b denoting the Schottky-barrier height and A stating the area of the device ($A = 3.14 \times 10^{-2} cm^2$). According to Crowell[175] the Richardson constant can be described as $A^* = \frac{4\pi q m^* k_B^2}{h^3}$. With the effective mass of tin-oxide $m^* = 0.4\ m_0$ this results in $A^* = 48\ \frac{A}{cm^2 K}$.[126] I_0 is obtained from a fit of the current-voltage characteristics as shown in **Appendix Figure 7.22b** and ϕ_b can be derived. At room temperature (T = 303 K) a barrier height of $\phi_b = 0.62\ eV$ can be found (detailed temperature dependency displayed in **Appendix Figure 7.22d**). Notably, this is in excellent agreement to the results of photoelectron spectroscopy discussed further below.

As already mentioned in **Paragraph 2.2.2**, earlier approaches to render the interconnect ohmic frequently involved the insertion of thin layers of metal

between both sub-cells. However, even a Ag-layer as thin as 1 nm already introduces significant optical losses that lower the EQE of the back-cell and the overall J_{SC} of the tandem cell as discussed further below. Therefore, a novel interconnect based on an ultra-thin ALD-grown layer of indium oxide has been developed (process details can be found in the **Appendix Paragraph 7.2.1**). Here it is possible to leverage the unique property of ALD to provide utmost control over the deposited layer thickness even on the level of Ångströms, which is impossible with other deposition techniques like e.g thermal evaporation. The insertion of InO_x between SnO_x and MoO_x outstandingly improves the J/V characteristics of the tandem cells (**Figure 4.4a).** As demonstrated by XPS and ellipsometry measurements at first the growth process of InO_x on top of SnO_x shows a typical non-linear nucleation phase (with regard to the growth per cycle) prior to a linear growth behavior for higher cycle numbers (**Appendix Figure 7.28b**). Van-der-Pau- and Hall-measurements of the InO_x layer indicate the formation of a continuous layer at about 32 ALD cycles, which is strongly supported by the valence band density of states developing a metal-like behavior according to the UPS results (**Figure 4.4d,e**). Notably, even the insertion of a low number of ALD cycles of InO_x between SnO_x and MoO_x gradually improves the J/V characteristics of the tandem cells (**Figure 4.4a**). Already 32 ALD cycles, which result in a layer thickness of just ~ 1.5 nm (**Appendix Figure 7.28b**), are sufficient to render the $SnO_x/InO_x/MoO_x$ stack ohmic (**Figure 4.4b**) and therefore provide an optimal J/V characteristic of the tandem device (**Figure 4.4a**).
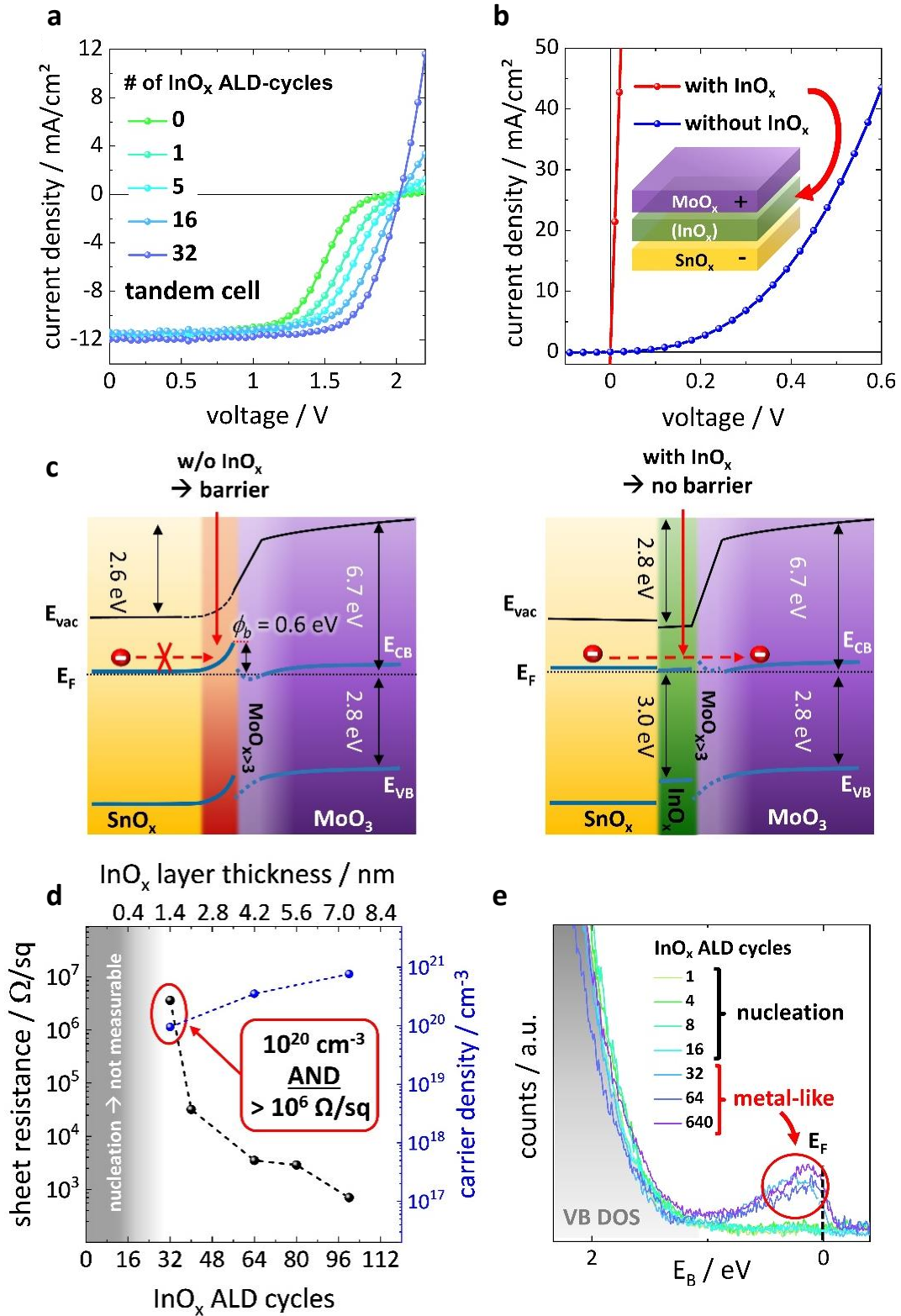
Figure 4.4: Tandem interconnect: a) J/V characteristics of tandem cells with varied thickness (number of ALD cycles) of the InOₓ interconnect. b) J/V characteristics of SnOₓ/(InOₓ)/MoOₓ diodes. c) Energetic line-up determined with and without InOₓ. Note, in the first 2 nm of the molybdenum oxide layer a mix of oxidation states for the molybdenum can be found, ranging from Mo^{2+} to Mo^{6+} (details in **Appendix Figure 7.23-7.27**). The first 2 nm of the MoOₓ is characterized by the presence of MoO_4^{2-} clusters. E_F,

Fermi level; E_{vac} , vacuum level; E_{CB} , conduction band; E_{VB} , valence band; Φ_b, energy barrier. d) Sheet resistance and carrier density versus thickness of the InO_x. (sq., square). e) UPS of the valence band (VB) density of states (DOS) of InO_x, showing the onset of a metallic behavior at 32 cycles of ALD. (a.u. arbitrary units). Reproduced from Ref.[150].

To better understand the structural and electronic properties of the interconnect, high-angle annular dark-field scanning transmission electron microscopy (HAADF-STEM), energy dispersive X-ray spectroscopy (EDS), GIWAXS and photoelectron spectroscopy have been conducted. HAADF-STEM and GIWAXS confirm that the ALD-grown InO_x and SnO_x are both amorphous and continuous (**Appendix Figure 7.30-7.36**). Elemental mapping shows that the SnO_x/InO_x interface is abrupt, and multivariate analysis[176] confirms no sign of In diffusion into the underlying SnO_x (**Appendix Figure 7.32 & 7.33**).As confirmed by highly surface-sensitive ultraviolet (UV) photoelectron spectroscopy (UPS) measurement of the Sn 4d semi-core levels, any hypothetical interdiffusion of Sn and In at the SnO_x/InO_x interface would be limited to a range of 5 Å (Supplementary Fig. 24). Another extensive study was conducted, again using photo electron spectroscopy, in cooperation with the group of Selina Olthof and Klaus Meerholz at the University of Cologne to determine the energetic line-up ("With InO_x" in **Figure 4.4c** and **Appendix Figure 7.23-7.27**). As can be derived from valence and conduction band onsets displayed in **Appendix Figure 7.25a**, a decisive difference is found upon deposition of MoO_3 on top of either SnO_x or InO_x substrate layers. While in both cases a minor band bending in the MoO_3 appears, a notably higher upward band bending in the substrate layer can only be found for the case of SnO_x/MoO_x and does not occur for InO_x/MoO_x. Conspicuously the band bending towards the SnO_x/MoO_x interface amounts to ~ 600 meV, which corresponds impeccably with the height of the Schottky-barrier determined earlier. The absence of

this barrier in the case of InO_x/MoO_x indicates, that the upward band bending found in case of SnO_x/MoO_x is completely alleviated by the insertion of the ultra-thin InO_x, enabling barrier-free transport of electrons from the bottom PSC across the $SnO_x/InO_x/MoO_x$ layer sequence. Ultimately, these electrons recombine with the holes from the OSC at the MoO_x/organic interface, which is similar to the recombination mechanism described in **Paragraph 3.1.3**.[49,109]
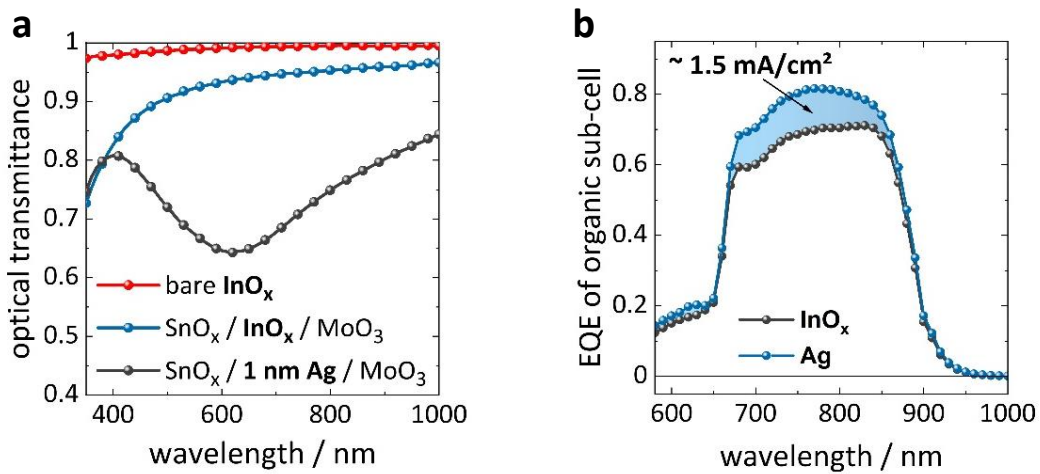
Figure 4.5: a) Optical transmittance of an interconnect based on 32 ALD cycles (approximately 1.5 nm) of InO_x, bare and sandwiched between SnO_x and MoO_x. For comparison, the InO_x has been replaced by a nominally 1 nm thick layer of Ag. b) Resulting EQE spectra of the organic back-cell with InO_x or Ag as interconnect, demonstrating the notable current losses induced by only 1 nm Ag. Reproduced from Ref.[150].

Notably, after completion of the nucleation phase (~ 32 ALD cycles), the InO_x layer shows a metallic nature with an electron density ~ 10^{20} cm^{-3} (**Figure 4.4d,e**). As the metallic InO_x layer is ultra-thin, it still provides a very high sheet resistance > 10^6 Ω/sq, which is a prerequisite for future large-area scalability as it is of critical importance to avoid shorting of the sub-cells in case of local shunt paths.[177] Moreover, high carrier densities typically infer optical absorption, which is another important reason to keep the thickness of the interconnect to a minimum.[178] Most strikingly, the

novel ultra-thin InO$_x$ interconnect with a transmittance near unity does not introduce notable optical losses (**Figure 4.5a**), which boosts the EQE of the organic back-cell and the overall J$_{SC}$ of the tandem by about 1.5 mA/cm^2 compared to the case of an interconnect based on 1 nm of Ag (**Figure 4.5b**). A direct comparison of exemplary devices with InO$_x$ and Ag interconnects is shown in **Appendix Figure 7.29,** where it can be seen, that the only significant difference between both devices appears in the J$_{SC}$. In addition to the optical advantages, ALD allows for large-area, high-throughput processing (even at atmospheric pressure),[179] and enables conformal coating of textured surfaces that frequently occur in light trapping concepts.[180] Hence, it can be foreseen that the applicability of this interconnect is not limited to perovskite/organic tandem cells but it may also be favorably used in other tandem cells.

4.4   Device Structure and Characteristics

Drawing from the significant progress outlined above, it was possible to prepare monolithic perovskite/organic tandem solar cells (device stack shown in the inset of **Figure 4.6c**) with outstanding characteristics (**Figure *4.6*b**). The EQE spectra of the PSC and OSC sub-cells of an optimized perovskite/organic tandem are shown in **Figure 4.6a**. The thicknesses of both active layers have been chosen, according to the results of the simulation mentioned above, to be around 350 nm and 120 nm for the perovskite and organic sub-cell, respectively.
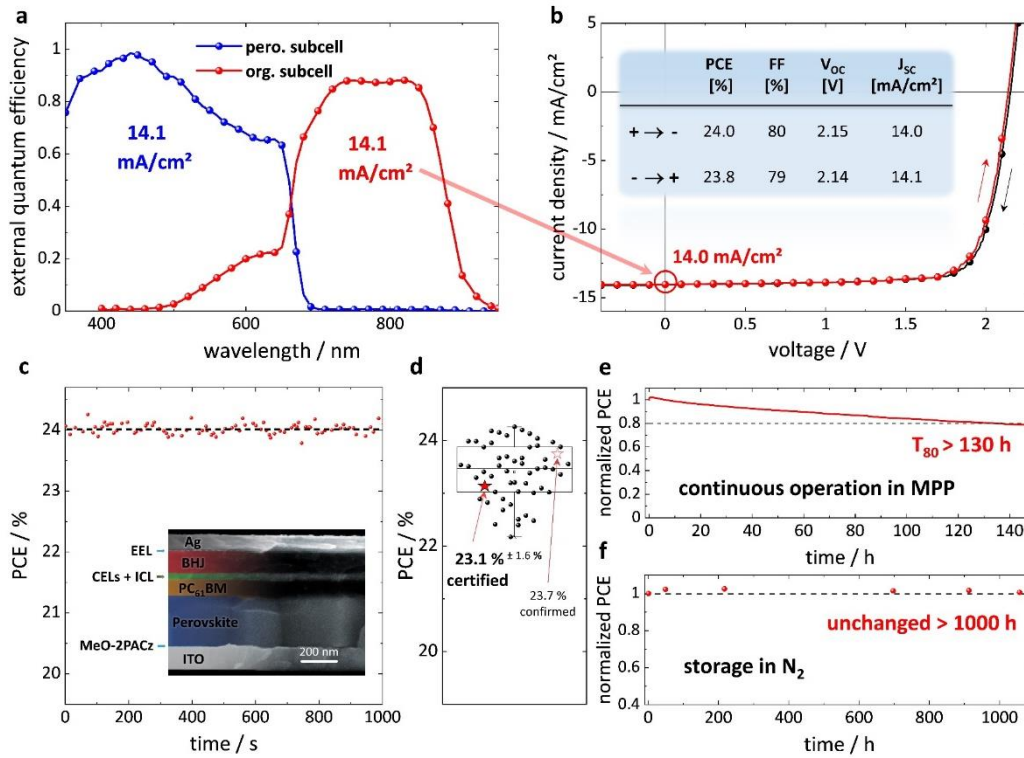
Figure 4.6: Perovskite–organic tandem cells: a) EQE spectra of both sub-cells in the tandem cell. For reduced reflection, the backside of the substrate was coated with a 100 nm thick MgF$_2$ layer. b) J/V characteristics of a tandem cell, with derived PCE, FF, open-circuit voltage (V$_{OC}$) and short-circuit current (J$_{SC}$) shown in the inset. c) Stabilized PCE of the tandem cell. Inset: SEM image of the cell cross-section. ICL, interconnecting layer; CELs, charge extraction layers. d) Statistical data of 48 tandem solar cells as derived from reverse J/V scans also containing the certified and confirmed value measured by the Fraunhofer ISE CalLab (**Appendix Figure 7.40 and Appendix Paragraphs 7.2.4 & 7.2.5**). Median line with upper and lower box ranges denoting the 25% and 75% margins. The bars denote the outermost data points that are still inside another 1.5 interquartile range. e), f) Stability of the tandem cells under continuous operation in the MPP (e) and when stored in N$_2$ (f). Reproduced from Ref.[150].

As a result excellent current matching conditions, as required in a series connection (see **Paragraph 2.2.1**), have been achieved, which is evidenced by the identical integrated current density of 14.1 mA/cm^2 for both sub-cells (**Figure 4.6a**). What immediately stands out is the extremely high EQE (> 97 %) of the perovskite sub-cell in the wavelength region around 440 nm, which seems impossible due to typical reflection and absorption losses at the air/substrate interface and inside the ITO electrode, respectively. In the course of this work, a combination of experimental data and optical simulation could be utilized to verify the high EQE to be a real (and

commonly reported) effect and - furthermore - explain its physical origins.[181] A detailed discussion of this phenomenon can be found in **Appendix Chapter 7.4**.

	scan direction	PCE [%]	FF [%]	V_{OC} [V]	J_{SC} [mA/cm²]
PSC	Reverse	16.8	81	1.34	15.6
	Forward	16.4	80	1.33	15.5
OSC	Invariant	17.5	75	0.87	26.7
Tandem	Reverse	24.0	80	2.15	14.0
	Forward	23.8	79	2.14	14.1

Table 4.1: The PCE, FF, open-circuit voltage (V_{OC}) and short-circuit current (J_{SC}) of the OSC and PSC single junctions and the tandem cell derived from their respective J/V characteristics. Note, for all cells, the Jsc agrees with the current density obtained from the EQE spectra (deviation less than 1 %). Reproduced from Ref.[150].

The high V_{OC} = 2.15 V of the tandem cell results from the serial connection of the sub-cells without any loss. This is demonstrated by comparing the measured J/V characteristics of the resulting device with the constructed tandem J/V based on characteristics of the two sub-cells (**Appendix Figure 7.37**). To emulate the J/V characteristics of the sub-cells, the measured J/V characteristics of representative single junction devices have been scaled to generate the respective short circuit current density that was derived from EQE results of the sub-cells in the tandem device (**Figure 4.6a**). The striking congruency of both, constructed and measured J/V curves, proves a lossless serial connection of both sub-cells and therefore provides evidence of perfect interconnect functionality. As a result, a champion tandem cell with a stabilized PCE of 24.0 % is achieved (**Figure 4.6b,c**). An efficiency of 23.1 % (± 1.6 %) was certified by the Fraunhofer ISE CalLab, according to the IEC

60904-3 procedure (**Figure 4.6d** and **Appendix Figure 7.40 and Appendix Paragraphs 7.2.4 & 7.2.5**). As the certification procedure inflicts some stress to the device before the actual certification (**Appendix Paragraph 7.2.3**), an additional control measurement (without certificate) was conducted by the Fraunhofer ISE CalLab without the stressing conditions, which confirmed an efficiency of 23.7 %, as had been measured in the laboratory. At the time, these devices stated the most efficient monolithic perovskite/organic tandem cells (inset **Figure 4.6c**), accompanied by devices with similar architecture and efficiency.[182]. The ALD prepared InO_x interconnect presents a unique feature of the presented devices, because it theoretically facilitates a more straightforward adaptation to roll-to-roll processes compared to the ICLs comprising ultra-thin sputtered ITO used elsewhere.[182] Incorporating further improvements in interface engineering, organic active materials or perovskite composition and passivation[183,184], other monolithic perovskite/organic tandem devices were since able to surpass the efficiency reported here, achieving champion efficiencies of over 24.4 %.[184]

Notably, the characteristics of the tandem devices presented above show a very small statistical variation (**Appendix Figure 7.38 & Figure 7.39**) resulting from an outstandingly robust processing of both the organic and especially the perovskite sub-cell.[185] An excellent stability of more than 1,000 h has been evidenced. The devices showed no sign of degradation when kept under inert atmosphere, and displayed a T_{80} of 130 h under continuous operation in the MPP (**Figure 4.6d,e**). It is to be noted, that the temporal behavior of the tandem under continuous operation is essentially governed by that of the perovskite sub-cell (see **Figure 4.2c**). As demonstrated earlier, the organic sub-cell provides outstanding operational

stability under the illumination conditions given by the tandem device structure (**Figure 4.1d**).

4.5   Summary

To conclude, a perovskite/organic tandem solar cell with an efficiency of 24.0 % has been demonstrated, setting a new milestone for perovskite/organic tandem devices, outperforming the most efficient single junction perovskite cells in p-i-n architecture at the time of the work's publication.[186] Furthermore, perovskite/organic architectures were now at par with perovskite/CIGS and all-perovskite multi-junctions.[187] This substantial achievement draws from groundbreaking progress in all parts of the tandem device. The organic sub-cells provide an enhanced efficiency in the near infrared spectral region and complement the perovskite cell. Prominently, under the filtered illumination conditions in the tandem, where excitons are solely generated on the acceptor, the devices do not show any degradation even under long-term continuous operation (> 5,000 hours). This is an unexpected finding that contradicts the paradigmatic association of non-fullerene organic solar cells with operational instability. This result is also in notable contrast to all-perovskite tandems, where the stability issues of Sn-based perovskites have to be dealt with.[160–162] Further work addressing operational stability of single junction non-fullerene solar cells will be discussed in **Chapter 5**.

As has been presented in the work of my colleague Kai Oliver Brinkmann[101], it was also possible to overcome interfacial losses that are the predominant reasons limiting the performance of wide-gap perovskite cells. This enabled access to previously unreached territory of combined

high V_{oc} and FF. At the same time, the findings evidence that the proper choice of charge extraction layers allows to mitigate the detrimental halide segregation typically encountered in mixed-halide perovskites and therefore make a big step towards long term operational stability.

Finally, a novel all-oxide interconnect for the two sub-cells was introduced, that is based on an ultra-thin metal-like indium oxide layer. The working mechanism of this interconnect has been uncovered to be similar to the approach presented for n-i-p organic/organic tandem devices (see **Chapter 3**), in the sense that a barrier-free electron transport through the ICL is enabled, leading to a recombination with holes at the HEL/organic interface. It has also been demonstrated that, due to its unprecedented low optical and electrical losses, the interconnect unlocks the exploitation of the full potential of the two sub-cells without any discount in all photovoltaic parameters. As mentioned above, the applicability of this novel type of interconnect is not limited to perovskite/organic tandem cells but is expected to likewise revolutionize other tandem architectures.

Furthermore, the experimental findings within this chapter motivated a semi-empirical simulation of an even more optimistic scenario. It can be envisioned that perovskite/organic tandem architectures bear a realistic prospect to reach efficiencies above 31 %, which will inspire further research guided by the results of this work. A comprehensive review of contemporary perovskite-organic tandem solar cells has been subject of recent work.[188]

5 Photo-Degradation of Inverted Non-Fullerene Organic Solar Cells

Over the last years, the field of organic photovoltaics made tremendous progress due to the development of new acceptor molecules instead of the commonly used fullerene acceptors. Beyond the enhancement in efficiency to over 19 %[189] an increased thermal stability of the bulk hetero junctions is achieved.[9,190] There also have been studies on operational stability, which in most recent examples also involve experiments under continuous operation in the maximum power point (MPP).[190–195] The vast majority of publications on non-fullerene active layers are utilizing an inverted device architecture with ZnO as EEL. As already mentioned in **Chapter 3**, previous reports on inverted fullerene-based OPV have indicated photo-induced degradation if ZnO-based EELs are used. Within our group, we were able to link a specific degradation effect with a loss of selectivity of the illuminated ZnO and the concomitant onset of parasitic recombination of holes at the ZnO/organic interface.[115] An introductory discussion of the underlying physical phenomena, the consequent degradation dynamics, and respective prevention strategies will be presented. In the follow-up work maximum power point (MPP) tracking is used to demonstrate that the photo-induced degradation induced by ZnO-based EELs is also substantial for fullerene-free inverted devices and that the degradation effect applies to various non-fullerene acceptors (such as ITIC[9], IT-4F[11], or IEICO[16]). It will be evidenced that the degradation is associated with the UV spectral components of the solar spectrum and it takes place even under

inert conditions, and is (partially) reversible in darkness. It will be shown that the EEL/acceptor interface is of crucial importance for the severity of the degradation effect and a route to elucidate the underlying physical effect(s) will be presented. Moreover, it will be demonstrated that the approach to eliminate photo-induced degradation, already proposed for fullerene-based cells[115], is transferable to fullerene-free inverted devices. The work presented in this chapter has partially been published in Refs.[48,115,139].

5.1 Photo-Degradation of Fullerene-based Devices with Metal-Oxide Extraction Layers

Besides the aspects detailed in **Paragraph 2.1.3**, one major motivation for the use of metal-oxide EELs is their superior stability when compared to low-WF metals like calcium (Ca), lithium (Li) etc., which establishes the prospect of improved device reliability. As already mentioned in **Chapter 3** ZnO based EELs are especially common, as they can be prepared from the liquid phase, e.g., by using nanoparticle-based dispersions, at relatively low temperatures.[60,196] While there are several reports of OSCs incorporating ZnO-based EELs in, which show a promising stability when stored without operation ("shelf-life")[197], photo-induced degradation has been found to occur in the devices upon illumination under actual operational conditions.[198–200] Analogous to the case of the light activation discussed earlier (**Paragraphs 2.1.3 & 3.1.4**), this degradation is clearly associated with the illumination by UV light (i.e., $h\nu > E_g$ of the metal oxide). As a result, a significantly lowered shunt resistance along with a substantial decay of the FF and V_{OC} is typically found to occur within minutes of illumination.

Headed by my colleague Sara Trost, an in-depth study of this phenomenon has been conducted, which provided deeper insight into the degradation mechanics and led to a suitable strategy to overcome this photo-induced degradation for fullerene-based devices.[201]

5.1.1 Device Characteristics and Degradation Pattern

Figure 5.1a shows the device structure of the inverted OSC used throughout the study with aluminum-doped zinc oxide (AZO) as EEL. As can be seen in **Figure 5.1b**, their J/V characteristics show a strong change upon illumination with AM1.5 simulated sunlight. Specifically, after 9 h of illumination, the V_{OC} has decreased by 100 mV (from 0.88 V to 0.78 V), accompanied by a simultaneous drop in FF from 62 % to 51 % (**Figure 5.1b**). Opposed to that, when a UV blocking filter (blocking $\lambda < 400$ nm) was used, the J/V characteristics remain stable (**Figure 5.1c**). This finding clearly shows that the deterioration of V_{OC} and FF is linked to the illumination with the UV spectral part of the AM1.5 spectrum.

Please note, the results shown in **Figure 5.1b,c** have been obtained in ambient air on devices without encapsulation. It is therefore important to verify that the same decay of V_{OC} and FF is likewise found under inert atmosphere (here inside a nitrogen-filled glove box) (**Figure 5.1d,e**). For this experiment, an LED light source was used to provide the UV illumination (5 mW cm^{-2}, $\lambda = 369$ nm). The intensity of the LED has been tuned to roughly correspond to the UV portion of the AM1.5 solar spectrum (i.e., about 4.6 mW cm^{-2} for $\lambda < 400$ nm). After 40 min of UV illumination the V_{OC} has dropped by 83 mV and the FF has fallen by about 10 % (absolute), which

is comparable to the results obtained under ambient conditions (**Figure 5.1b**). Immediately after UV illumination, the illumination conditions have been changed to green light (3 mW cm⁻², λ = 550 nm).
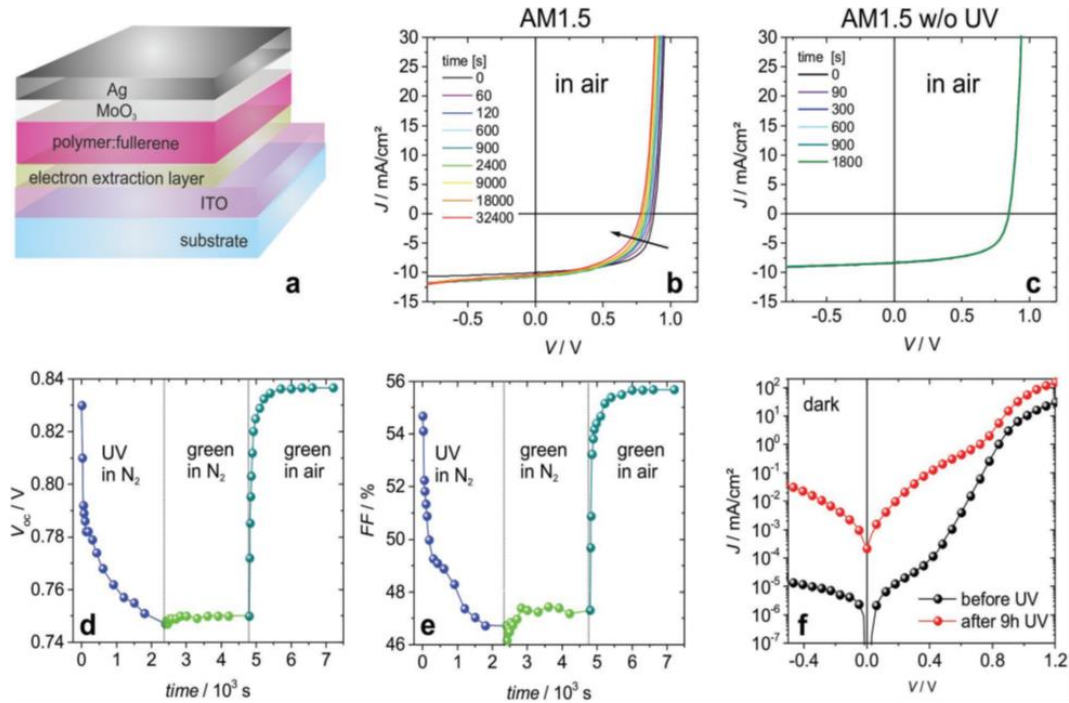

Figure 5.1: a) Layer sequence of the inverted OSCs studied here. The results shown in this panel belong to devices based on PCDTBT:PC70BM with Al:ZnO (AZO) as electron extraction layer. Variation of the J/V characteristics in "air" (b) under AM1.5 illumination and (c) under AM1.5 illumination with UV blocking filter. (d,e) Change of the Voc and FF over time upon illumination with a UV LED (5 mW cm⁻², λ = 369 nm) or a green LED (3 mW cm⁻², λ = 550 nm) in "inert atmosphere." (f) Dark J/V characteristics before and directly after illumination with a UV LED under inert atmosphere for a duration of 9 h. Reproduced from Ref. [115].

Here the Voc and FF did not deteriorate any further and remained constant. When the cells were subsequently exposed to ambient air, the J/V characteristics of the device recovered to their initial values (as before the UV-induced degradation) within 15 min (**Figure 5.1d,e**). It therefore can be concluded, that the photo-induced degradation is reversible under ambient conditions. Most remarkably, the dark characteristics of the OSCs changed significantly upon UV exposure. As shown in **Figure 5.1f**, a significant shunting component can be found in the dark J/V characteristics of the device in the degraded state. Specifically, while the shunt resistance of the

dark characteristics is about $R_{sh} = 38\ M\Omega\ cm^2$ in the pristine OSCs, it has dropped by almost three orders of magnitude to $R_{sh} = 43\ k\Omega\ cm^2$ after 9 h of UV illumination under inert conditions (measured immediately after illumination stopped). This observation is in line with previous reports and has been attributed to UV-induced oxygen desorption from the ZnO surface, which leads to a significantly increased carrier density and therefore to a higher electrical conductivity.[202] As shown in **Figure 5.2**, it was possible to demonstrate a direct correlation between the increase in carrier density from $2.4 \times 10^{18}\ cm^{-3}$ for a neat AZO layer to about $1.2 \times 10^{19}\ cm^{-3}$ after 40 min of AM1.5 illumination and the simultaneous decay of V_{OC} in the corresponding devices comprising equivalent AZO EELs.
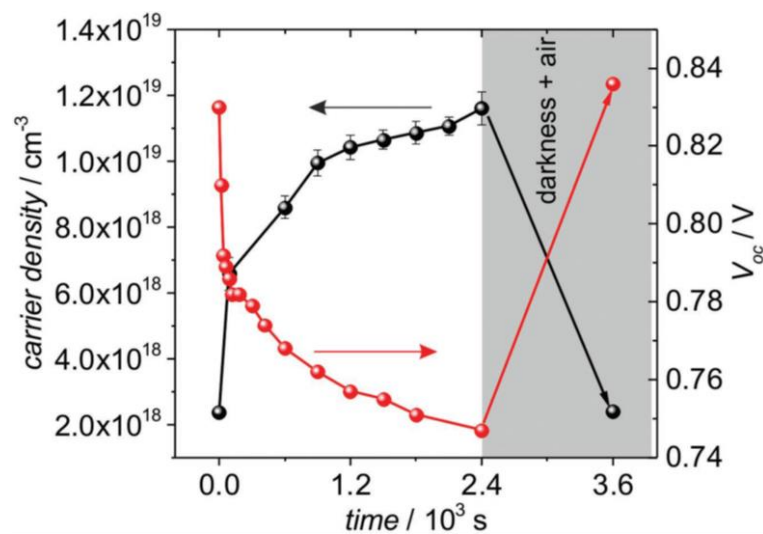
Figure 5.2: Increase of the carrier density of Al:ZnO (AZO) upon AM1.5 illumination over a duration of 40 min (black symbols). The concomitant decay of the Voc (red symbols) of an OSC using a similar AZO layer as EEL. The decay of carrier density and recovery of Voc after 20 min in darkness and air is shown as well (starting at t = 2400 s). Reproduced from Ref. [115].

This effect of an increased carrier density on the V_{OC} of inverted OSCs has been verified by fabricating devices with AZO EELs grown by ALD at different processing temperatures. The inverted cells discussed above have all been based on AZO grown at a temperature of 100°C (short AZO100) with

a carrier density of 3×10^{18} cm^{-3}. In contrast to this, the carrier density of AZO layers grown at 150°C (AZO$_{150}$) increases about nearly an order of magnitude to 2×10^{19} cm^{-3}. This results in a low R$_{sh}$ = 55 kΩ cm^2 for the device with AZO$_{150}$ EEL, which is similar to the value for the AZO$_{100}$-based device after hours of UV degradation (**Figure 5.3a**).
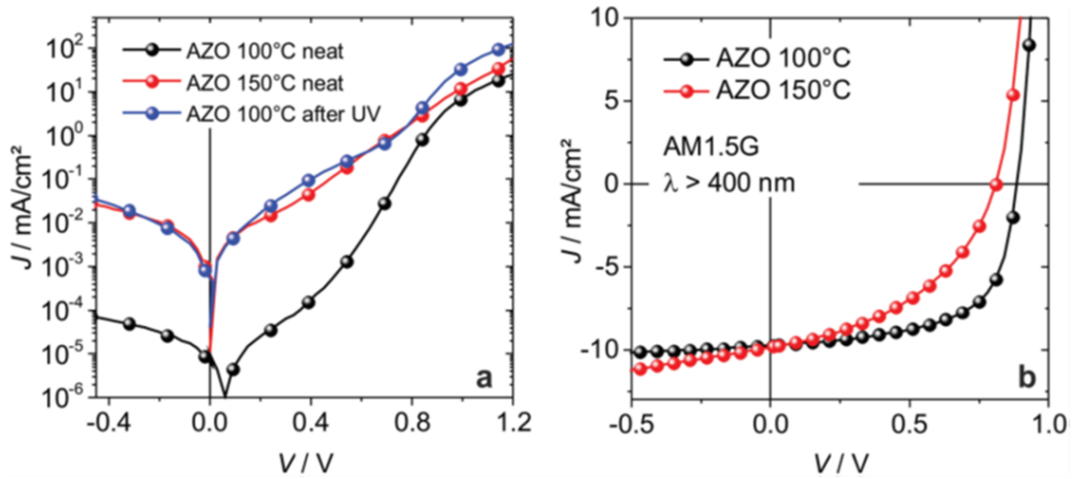
Figure 5.3: a) Dark J/V characteristics of OSCs with an EEL of AZO (100°C) and AZO (150°C) with substantially different carrier density (3×1018 cm−3 and 2×1019 cm−3, respectively). b) J/V characteristics under illumination with the filtered AM1.5G simulated solar spectrum (λ > 400 nm). Reproduced from Ref. [115].

Figure 5.3b shows the corresponding J/V curves for both devices under illumination, and demonstrates the significantly lower FF and V$_{OC}$ caused by the shunting in case of AZO$_{150}$. It is important to point out that the results shown in **Figure 5.1** are representative for several ZnO-based EELs studied in this work independent of doping or deposition technique (see **Figure 5.4**). This demonstrated generality makes ZnO-based EELs suboptimal for the utilization in stable OSCs, with the use of UV-blocking filters being also no suitable solution in the case of necessary "UV light-soaking" to reach full functionality (see **Paragraph 2.1.3**). In previous work SnO$_x$ has been introduced as EEL-material[48] without the need for UV activation (see also **Paragraph 3.1.4**), which renders it a highly interesting candidate for an alternative to alleviate UV-induced degradation. Very strikingly, the use of

SnO$_x$-EELs (prepared by ALD or via sol-gel route) led to a negligible decrease in V$_{OC}$ and FF (< 10 mV and 1 % respectively) under the same illumination conditions in devices that were otherwise identical to the ZnO-based ones above (see **Figure 5.4**).
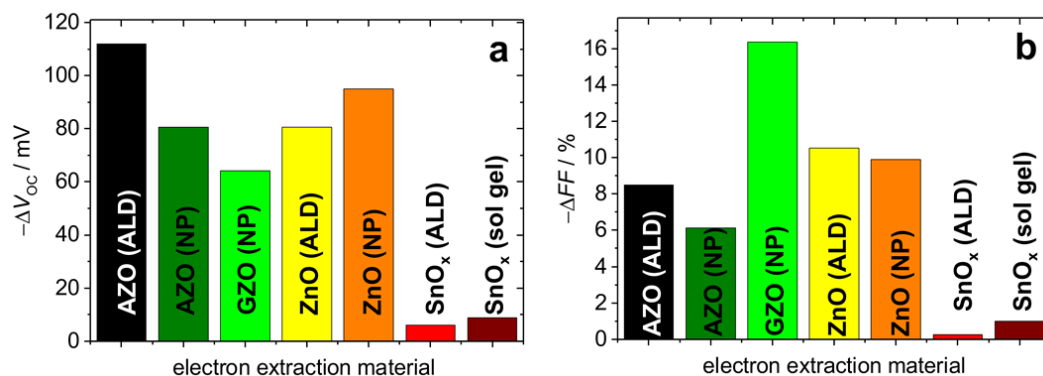
Figure 5.4: Absolute change of (a) the Voc and (b) FF of OSCs based on various electron extraction layers after illumination with UV light (5 mW cm^{-2}, $\lambda = 369$ nm) for 1 h under inert conditions. The EELs are Al:ZnO (AZO), Ga:ZnO (GZO), ZnO, and SnO$_x$. The layers have either been grown by atomic layer deposition (ALD) or were solution processed from a nanoparticle dispersion (NP) or via a sol-gel route. Reproduced from Ref. [115].

5.1.2 Analysis of the Degradation Mechanism

To generate further insight into the origin of this strikingly different behavior between the several ZnO variants and SnO$_x$, Kelvin Probe (KP) measurements and X-ray Photon Spectroscopy (XPS) have been conducted on the different EELs. The KP analysis revealed a WF change upon UV illumination for all ZnO-based EELs (**Table 5.1**). A pursuing experiment performed with an exemplary AZO$_{100}$ layer under controlled atmospheric and illumination conditions demonstrated the WF change to be reversible, when the layer is exposed to O$_2$-atmosphere. For SnO$_x$, neither the UV treatment nor the subsequent O$_2$-exposure had a significant effect on the WF (see **Figure 5.5a**).

Table 5.1: Work function of various electron extraction layers used in this study before and after illumination in air (60 min, AM1.5G including the UV spectral part). Reproduced from Ref. [115].

EEL (preparation method)	WF neat [eV]	WF after AM1.5 [eV]
AZO (ALD)	4.32	3.82
AZO (NP)	4.31	3.82
ZnO (ALD)	4.37	3.80
ZnO (NP)	4.35	3.83
Ga:ZnO (NP)	4.31	3.81
SnO$_x$ (ALD)	4.21	4.20
SnO$_x$ (sol-gel)	4.20	4.19

The WF change for ZnO-based layers, in combination with the abovementioned UV-induced increase in carrier density, suggest the underlying mechanic to be desorption of oxygen, that has already been observed to be reversible.[198] The chemisorbed O$_2^-$ species lead to a depletion region, thus an upward band bending at the surface and a higher WF.[203,204] The UV exposure then results in the electrons trapped within the O$_2^-$ to be transferred into the CB and O$_2$ to be desorbed (**Figure 5.5c**). Consequently, the carrier density of the layer increases. Within the study, this was finally identified to provoke enhanced surface recombination at the EEL/organic interface and a concomitant loss in electrode selectivity (impaired hole blocking by the EEL), that is known to reduce FF and V$_{OC}$ in associated OSCs.[205] As a remarkable addition to this, samples comprising SnO$_x$ did not show any significant changes in carrier density or electrode selectivity upon UV illumination. In contrast to the ZnO-based samples, a downward band bending at the SnO$_x$ surface could be derived from XPS-analysis of surface sensitive core-level spectra (**Figure 5.5b**). This could be attributed to water adsorbates at the surface, invoking an

accumulation layer.[206–208] These crucial differences in surface electronic structure are responsible for the decisively different behavior of SnOₓ EELs under UV exposure, in contrast to ZnO-based EEL variants. In conclusion, the utilization of SnO_x enables a mitigation of the photo-induced degradation patterns of OSCs caused by ZnO-based EELs. A more detailed discussion of this is subject of the thesis of my colleague Sara Trost.[201]
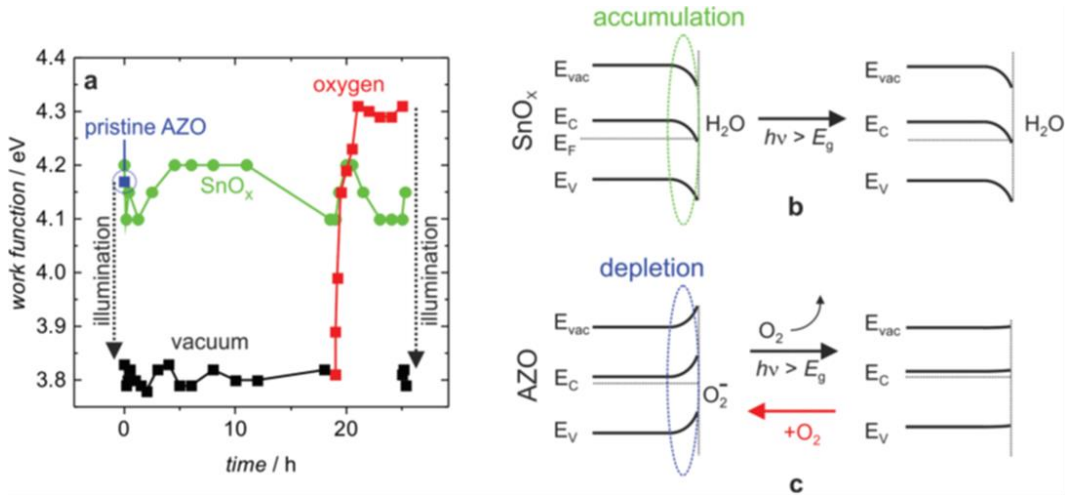
Figure 5.5: a) Work function of an AZO layer before (blue square) and after illumination with AM1.5 for 60 min upon storage in vacuum (pressure: 10^{-6} mbar) for several hours (black squares), subsequent exposure to oxygen atmosphere (red squares), and repeated illumination with AM1.5 for 60 min. For comparison, the WF of a SnO_x layer is shown (green circles), as reported in Ref. [48]. For the SnO_x, the WF before and after the illumination with AM1.5 for 60 min is identical. Schematic of the surface electronic band alignment of (b) SnO_x and (c) AZO before and after UV illumination. The H_2O shown in the case of SnO_x represents adsorbed water, which may occur as OH, H_2O, etc., at the surface.[206,207] **Table 5.2:** Work function of various electron extraction layers used in this study before and after illumination in air (60 min, AM1.5G including the UV spectral part). Reproduced from Ref. [115].

5.1.3 Interim Summary

This study demonstrates that photo-induced degradation is a general phenomenon in OSCs comprising "neat or electrically doped" ZnO-based electron extraction layers. The underlying degradation mechanism has been demonstrated to be related to desorption of chemisorbed oxygen species from the ZnO surface increasing the carrier density and leading to a selectivity loss of the electrode. This effect has been found to be triggered by the UV part of the solar spectrum and was found to be reversible upon subsequent exposure to an O_2 atmosphere. The resulting appearance of photo-induced shunts in ZnO-based OSCs occurs for devices operated in air or under inert atmosphere, and it can therefore not be avoided by using a proper encapsulation. Opposed to ZnO-based EELs, it has been demonstrated that the photo-induced degradation and the concomitant decay of the device characteristics can be overcome by the use of EELs based on SnO_x. The reason for this is the decisively different surface electronic structure of SnO_x, which is not compromised by UV-light, in contrast to ZnO-based systems. This finding is extremely important for the design of organic solar cells with a superior operational stability. Due to its availability and simple processing routine, ZnO (especially in nanoparticulate form) still is one of the most commonly applied EEL materials. This will render the above observations to be of even greater importance for future device architectures, exemplary in the case of more efficient active layers comprising other novel non-fullerene acceptor molecules.

5.2 Photo-Degradation of Fullerene-Free Devices with Metal-Oxide Extraction Layers

Non-fullerene acceptors are a promising route to further enhance the efficiency of organic solar cells. The highest efficiencies up to now of organic single junction devices reached more than 19 % utilizing absorber systems with different non-fullerene acceptor molecules.[152,189,209,210]

One of the most commonly used and well characterized fullerene-free absorber systems is Poly[(2,6-(4,8-bis(5-(2-ethylhexyl)thiophen-2-yl)-benzo[1,2-b:4,5-b']dithiophene))-alt-(5,5-(1',3'-di-2-thienyl-5',7'-bis(2-ethylhexyl)benzo[1',2'-c: 4',5'-c']dithiophene-4,8-dione)] (PBDB-T) : 3,9-bis(2-methylene-(3-(1,1-dicyanomethylene)-indanone))-5,5,11,11-tetrakis(4-hexylphenyl)-dithieno [2,3-d:2',3'-d']-s-indaceno [1,2-b:5,6-b'] dithio-phene (ITIC),[9] which reaches efficiencies of about 11 % in inverted single-junction devices and shows promising morphological stability even at elevated temperatures.[9] The current literature in this field typically addresses "shelf-life" or aspects of thermal stress to demonstrate the outstanding stability of these materials.[9,190] The vast majority of devices shown in literature use the inverted structure with ZnO as EEL, which has been shown above to infer stability issues under continuous illumination for fullerene-based OSCs (see above).[115] The degradation of non-fullerene devices under continuous illumination has been reported in manifold publications and has been attributed to a number of different mechanisms. One often observed cause for device degradation is the segregation of beneficially mixed donor and acceptor phases within the BHJ under continuous operation or even extended storage.[190,191,211–213] This has been

described using the Flory-Huggins theory, treating the acceptor as a solvent for the donor.[214] Following this approach, it is possible to explain why the typical processing methods of BHJs result in mixtures with suboptimal thermodynamic stability compared to the solar cell unfavorable segregated systems.[155] As already demonstrated above (**Chapter 4.1**), ternary blended BHJs promise a pathway to significantly higher operational stability in this regard. The added fullerene is providing different advantages and therefore reducing the segregation by mixing with both donor polymer and non-fullerene acceptor.[155,215]

Another independent mechanism behind the degradation of non-fullerene OSCs is an intrinsic molecular instability of the compounds within the BHJ. A discussion of this phenomenon for one active system (PM6:Y6) has been performed in **Chapter 4.1**. The results presented there are consistent with other reports and demonstrate that the severity of the degradation strongly depends on the spectral illumination conditions.[150,192,216]

In some reports, improved photo-stability has been reported when using the non-fullerene acceptor rhodanine-benzothiadiazole-coupled indacenodithiophene (IDTBR) blended with Poly(3-hexylthiophen-2,5-diyl) (P3HT), which however only gave a moderate efficiency of about 6%.[217] The same acceptor has been used with poly[(5,6-difluoro-2,1,3-benzothiadiazol-4,7-diyl)-alt-(3,3′′′-di(2-octyldodecyl)-2,2′;5′,2′′;5′′,2′′′-quaterthiophen-5,5′′′-diyl)] (PffBT4T-2OD) as a donor polymer, resulting in more efficient devices (PCE = 9.5%), which were claimed to show no degradation under operational conditions ("burn-in free").[218] It has to be stressed, that these claims of "burn-in free" devices have been derived from experiments, where illumination conditions without UV light were used. Another report observed UV-induced degradation patterns in OSCs

comprising a fluorinated variant of the ITIC acceptor named 3,9-bis(2-methylene-((3-(1,1-dicyanomethylene)-6,7-difluoro)-indanone))-5,5,11,11-tetrakis(4-hexylphenyl)-dithieno[2,3-d:2',3'-d']-s-indaceno[1,2-b:5,6-b']dithiophene (IT-4F).[219] Here, the degradation has been attributed to photocatalytic disintegration of the acceptor molecules at the interface between active layer and the EEL. Interestingly, the EEL in this case was ZnO-based and the effect could be mitigated by replacing ZnO with SnO_2.

In this part, it will be demonstrated that the degradation of non-fullerene OSCs similar to the ones in literature cannot be attributed to a single origin, but is the consequence of a combination of underlying mechanisms. The following section will focus on UV-induced degradation mechanisms wich are very prominent in devices comprising ITIC-like acceptor molecules. Strikingly, all of these mechanisms can be mitigated or even avoided by the utilization of SnO_x as EEL-material.

5.2.1 Characteristics and Degradation Pattern of ITIC-based Devices

Considering the results arising in literature and the ones obtained with fullerene acceptors detailed above, it can be reasoned that the photo-induced degradation in non-fullerene devices is likely to be triggered by UV illumination. Moreover one could assume that the major origin of it can be found at the interface of the EEL and the organic photoactive system, mainly in the case of ZnO-based EELs. In first experiments, inverted PBDB-T:ITIC (**Figure 5.6c**) OSCs with nanoparticle-based ZnO as EEL have been fabricated. The inverted device architecture is shown in **Figure 5.6a**. The resulting solar cell showed an efficiency of nearly 11 % (PCE = 10.9 %) with

an open circuit voltage of V_{OC} = 0.91 V and a high FF of 71 %. The results are in good agreement with similar devices reported in literature. For stability studies and the recording of potential degradation dynamics, maximum power point (MPP) tracking under continuous illumination has been performed subsequently. This method is common practice in the field of perovskite-based photovoltaics, where stability analysis has rapidly become a crucial part of standard characterization procedures. Thus, this was found to be the most reasonable approach for a contemporary degradation analysis.
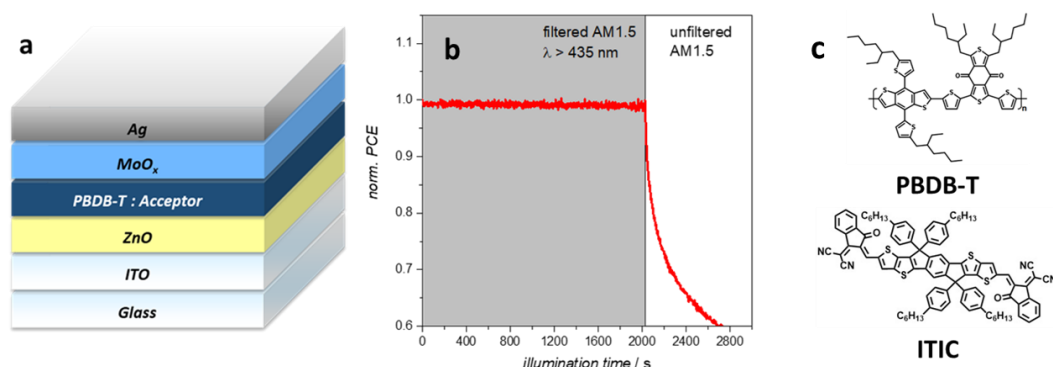
Figure 5.6: (a) Inverted device stack used in this set of experiments and (b) MPP-tracking results for the ITIC based device under varying illumination conditions. c) Molecule structure of the donor polymer (PBDB-T) and the non-fullerene acceptor (ITIC) used in the device stack (a).

For an insight into the spectral origin of the degradation (presumably in the UV part of the AM1.5 spectrum), an optional optical UV blocking filter (blocking λ < 435 nm) has been used. As can be seen in **Figure 5.6c**, there is no visible change in efficiency, when the blocking filter is used. Notably, the device stays stable for more than 30 minutes of continuous illumination and measurement. In stark contrast to this, a steep decline in device efficiency occurs abruptly as soon as the filter is removed. In analogy to fullerene-based devices above, this clearly demonstrates that the degradation of the

non-fullerene cell is linked to the UV spectral components of the AM1.5 spectrum.

Figure 5.7: Development of the J/V characteristics of ITIC based cells in N_2 atmosphere (a) under continuous UV-illumination (5 mW cm^{-2}, $\lambda = 369$ nm) and (b) after subsequent storage in darkness.

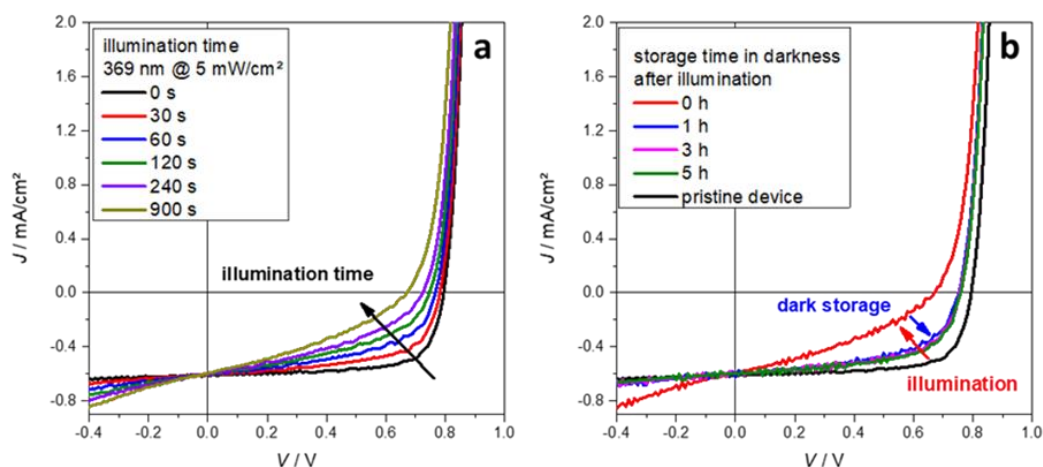To exclude photo oxidization effects of the organic compounds of the stack as the dominant degradation mechanism, measurements with identical OSCs under inert atmosphere (in this case within a N_2-filled glovebox) have been performed. To emulate the UV-portion of the solar spectrum, the devices were illuminated with an LED light source ($\lambda = 369$ nm, $P = 5$ mW cm^{-2}) in analogy to the experiments described above (see **Chapter 5.1**). The results of this study, shown in **Figure 5.7a**, demonstrate the UV induced degradation also taking place under inert conditions. Within minutes, a severe decay in V_{OC} and FF can be observed in the corresponding J/V characteristics, which is analogous with the findings for the photo-shunting of fullerene-based devices (see above). Most interestingly, this effect was also found to be partially reversible in the dark (**Figure 5.7b**), which suggests the involvement of a degradation mechanism similar to the shunting due to desorption of chemisorbed O_2^-, already known from fullerene-based OSCs (see **Chapter 5.1**). Without illumination, oxygen from the surrounding will be adsorbed at the EEL/BHJ-interface

again, leading to a recovery of the EEL's carrier selectivity. The fact that the reversibility is also observed in inert atmosphere, can be attributed to desorbed oxygen remaining "stored" within the BHJ and returning to the ZnO surface once the illumination is turned off. Moreover, **Figure 5.7b** shows, that some part of the degradation is irreversible, even after hours of dark storage, which leads to the conclusion of an additional degradation mechanism being involved.

As already mentioned above, Jiang et. al conducted a degradation analysis with ZnO EELs and a similar active system consisting of the polymer PM6 (see **Chapter 4**) and the acceptor IT-4F.[219] Their OSCs exhibited a similar degradation pattern and it was also revealed that this effect was in part reversible in the dark. They attributed the degradation to chemical disintegration if the IT-4F acceptor induced by a photocatalytic effect at the ZnO/organic interface, as shown by mass spectroscopy and optical absorption measurements. The effect was shown to be triggered by UV light and was evidenced to occur with different related acceptor molecules (e.g. ITIC). Notably, it is reasonable to assume this mechanism is irreversible, which makes it surprising, that further explanations of the effect's partial reversibility were missing. Taking into account our experience with fullerene-based devices, the findings suggest a combination of both discussed degradation mechanisms, with photo-shunting and photocatalytic decomposition being responsible for the reversible and the irreversible proportion of the overall degradation effect, respectively. Based on the results with fullerene-based devices, inverted OSCs comprising ALD-processed SnO_x as EEL were also fabricated and their behavior under AM1.5 illumination was compared to the ZnO-based equivalents (Stacks shown in **Figure 5.8a**). As shown before, SnO_x provides an interesting or even advantageous alternative as EEL, due to the suppression of photo-

shunting in fullerene based OSCs. Moreover, it has also been demonstrated by Jiang et al., that the abovementioned photocatalytic effects are inhibited when the ZnO-EEL is replaced by SnO_2.[219] As can be seen in **Figure 5.8b**, the SnO_x EEL radically improves the device's photo-stability, proving that its use enables suppression of both UV-induced degradation mechanisms in non-fullerene devices. Moreover the results demonstrate that the strategy to avoid photo-induced shunts in fullerene-based devices is also applicable for OSCs with non-fullerene acceptors.
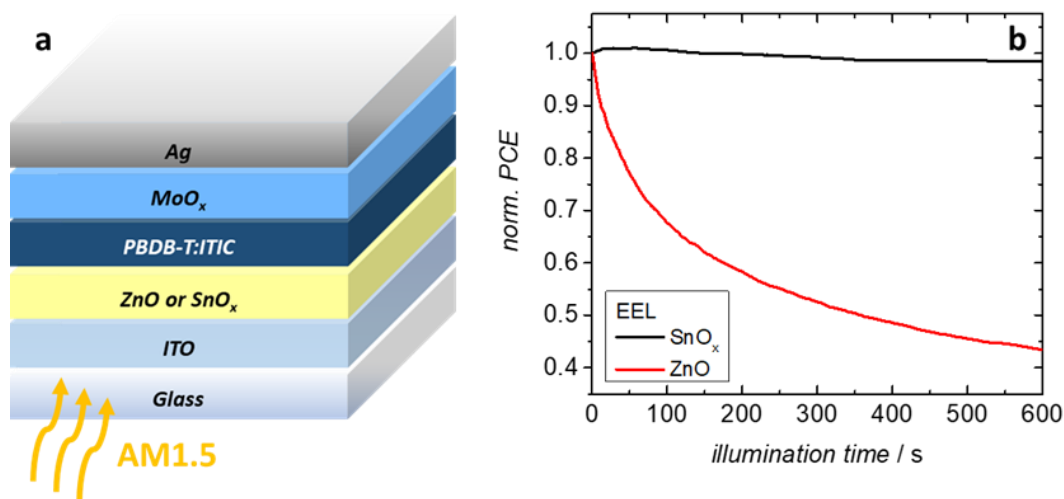
Figure 5.8: a) Device stack of the inverted fullerene free device with either ZnO or SnO_x as electron extraction layer. b) Normalized PCE of the devices under continuous AM1.5 illumination.

It is to note, that the PBDB-T:ITIC devices with SnO_x only achieved inferior device characteristics, only reaching a PCE of 7.4 % (compared to ZnO-based equivalents with PCE > 10 %), mainly due to lower V_{OC} and FF. The reason for this could not be finally clarified within the work of this thesis, but notably this has no generality for all non-fullerene acceptors, as has been demonstrated for the case of devices with BHJs comprising IT-4F[219](also see **Appendix Figure 7.42**).

5.2.2 Analysis of the Degradation Mechanism

To verify the relevance of the reported photocatalytic effects with the ZnO EEL used in this study, absorption spectra of different acceptor thin films (~ 10 nm) on top of the EEL have been analyzed before and after 20 min of UV illumination in inert atmosphere. To get a wider picture of the effect, ITIC, IT-4F, and IEICO have been included as some of the most commonly used non-fullerene acceptors and the fullerene acceptor $PC_{70}BM$ has been taken into account for comparison. The same UV illumination conditions as before (5 mW cm^{-2}, λ = 369 nm) have been provided using the LED light source. As can be seen in **Figure 5.9**, the absorption spectra of all included non-fullerene acceptor species are affected by the UV treatment, illustrated by a decrease in their respective absorption peaks.
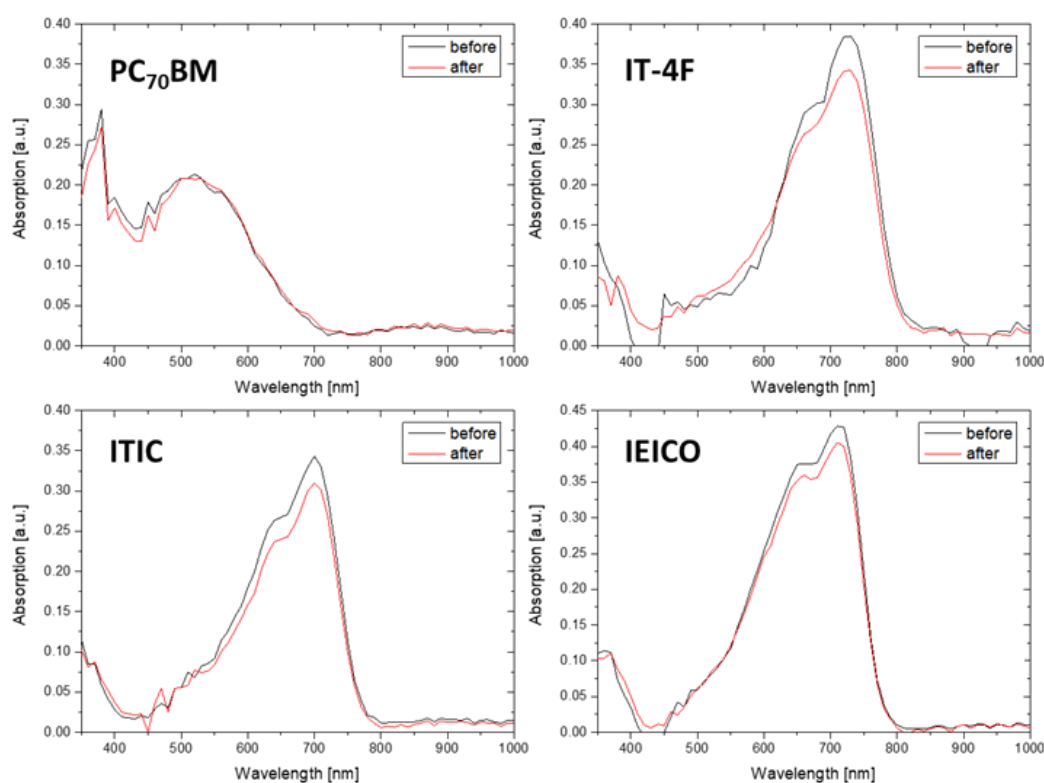

Figure 5.9: Absorption spectra of different non-fullerene acceptor films on top of a ZnO NP layer in comparison with a corresponding $PC_{70}BM$ sample before and after 20 min of simulated AM1.5 equivalent UV illumination (5 mW cm^{-2}, λ = 369 nm).

This finding is in agreement with previous results and leads to the conclusion that the used ZnO layer also induces photocatalytic decomposition of these acceptor molecules. Moreover the results confirm, that the photocatalytic disintegration is a general issue for these ladder-type non-fullerene acceptors in combination with ZnO. It should be noted, that just a decrease in the absorption peaks of all acceptor spectra has been measured, but no further changes of the spectra due to the UV treatment have been observed. Strikingly, no significant decay in the absorption spectrum of the $PC_{70}BM$ sample (**Figure 5.9**) was observed. This provides further evidence, that photo-shunting is the prevailing degradation mechanism of fullerene-based OSCs with ZnO EELs, with no relevant contribution of photocatalytic effects.
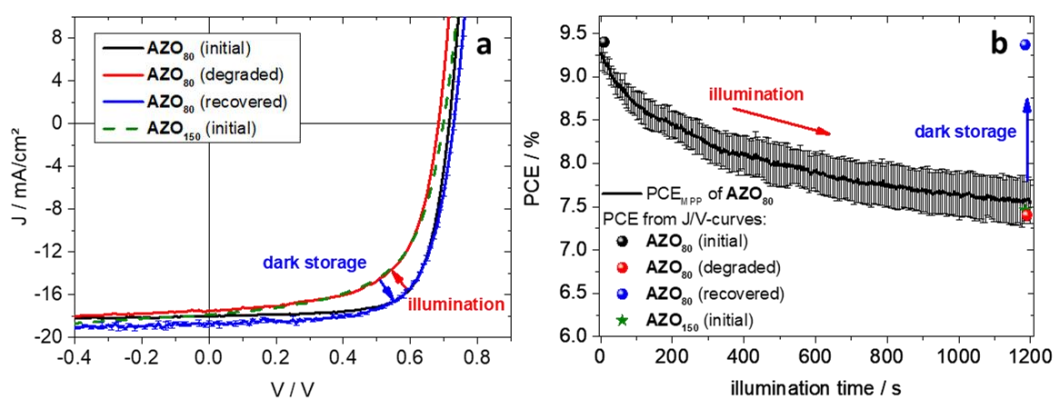
Figure 5.10: a) J/V curves of devices with different AZO EELs directly after starting the AM1.5 illumination (initial), after 20 min under AM1.5 illumination (degraded), after one week storage under dark inert conditions (recovered). b) MPP tracking results of AZO_{80} devices under full AM1.5 illumination. Extracted PCE values from J/V characteristics of an AZO_{80} device (initial, degraded, and recovered) and an initial PCE of an AZO_{150} device are also depicted.

As already mentioned above, photo-shunting was reasoned to also factor into the degradation of non-fullerene devices, due to the partial reversibility of the decay. For a further investigation of this, inverted OSCs with different ALD-processed AZO layers as EEL and a PBDB-T:IT-4F active layer have been fabricated. In analogy to the experiments conducted in the case of

fullerene-based devices, the deposition temperature of the AZO films have been varied - in this case 80°C (AZO$_{80}$) and 150°C (AZO$_{150}$) - to provide EELs with different carrier densities (see above). As can be seen in **Figure 5.10a**, the device comprising the AZO$_{80}$-EEL, does initially provide a well-shaped J/V characteristic (black line) with a high FF exceeding 70 % and a V$_{OC}$ of 0.72 V, leading to an efficiency of 9.4 %. In contrast to this, the J/V curve of the AZO$_{150}$-based device (green dashed line) shows a lower FF and V$_{OC}$, caused by the initially already higher carrier density of the EEL; this is in analogy to the results of photo-shunted fullerene-based devices (see above). **Figure 5.10b** shows the MPP-tracking results of the AZO$_{80}$-based devices, displaying the development of the PCE under full AM1.5 illumination (black line) and also the initial and final PCE values derived from the respective J/V characteristics (black and red dot, respectively). Noticeably, after 20 min of photo-induced degradation, the devices reaches a PCE similar to the initial value achieved with the AZO$_{150}$-EEL (green star, derived from J/V measurements). This is also represented by the similarities between the J/V curves of both device species, which are depicted in **Figure 5.10a** by the red line (for degraded AZO$_{80}$) and the dashed green line (initial measurement with AZO$_{150}$-EEL), respectively. This observation already indicates, that the majority of the observed degradation effect in AZO$_{80}$-based OSCs can be attributed simply to photo-shunting, without taking into account any photocatalytic effects. Even more strikingly, the observed degradation of the AZO$_{80}$-based devices is found to be entirely reversible in darkness. This is demonstrated by the J/V curve of "recovered" AZO$_{80}$-devices (one week under inert atmosphere), depicted in **Figure 5.10a** (blue line), which is remarkably similar to the initial curve with a recovered PCE of 9.4 %. As already explained above, this rules out a device degradation by

photocatalytic disintegration of acceptor molecules, because this mechanism would not be reversible.

To examine the presumed absence of photocatalytic decomposition in this case, the optical absorption spectrum of an IT-4F thin film on top of AZO$_{80}$ has been investigated, in analogy to the previous experiments done with an underlying ZnO nanoparticle layer. The resulting spectra (shown in **Figure** *5.11*) demonstrate no significant diminishing of the IT-4F absorption peak in contrast to what has been found for the samples with ZnO nanoparticles, following the same UV-treatment.
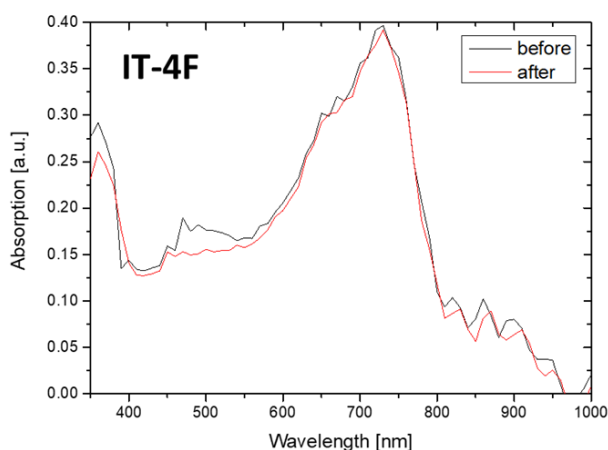
Figure 5.11: Absorption spectra of an IT-4F film on top of an ALD AZO$_{80}$ layer before and after 20 min of simulated AM1.5 equivalent UV illumination (5 mW cm^{-2}, λ = 369 nm).

This in fact supports the assumption that the IT-4F molecules are not victim to photo-induced decomposition in any way, which thus leads to the conclusion that the ALD processed AZO-layers do not provide the same photocatalytic activity as nanoparticle-based ZnO layers. This fundamental difference between ALD-processed and nanoparticle-based layers has been attributed to the different surface orientation of the respective films. In general, varying surface orientation of crystalline materials (especially metal oxides), provide different photocatalytic activity. For a layer

consisting of nanoparticles, the surface orientation can be assumed to be random, while the ALD process can afford distinct favored orientations onto the grown layer. For (doped) ZnO films there have already been several studies showing the influence of several ALD process parameters on the orientation of the film.[220–224] For AZO deposited by similar ALD-processes to ours, the films are reported to predominantly grow with c-axis orientation and less pronounced fractions of other orientations.[220,224] Therefore, a surface orientation other than the c-plane has been assumed to be responsible for the necessary photocatalytic activity in the case of the observed photo-induced decomposition of non-fullerene acceptor molecules. Unfortunately it was not possible to clarify this hypothesis with further investigations within this thesis. This is part of ongoing research and a possible route for follow-up experiments will be discussed below.

5.2.3 Summary and Outlook

As demonstrated within this chapter, photo-induced degradation of inverted non-fullerene solar cells comprising ZnO as EEL is caused by the UV part of the AM1.5 spectrum and also happens under inert atmosphere. It also is (partially) reversible in the dark and is present for different ZnO-based EELs. The results concerning the reversibility of the effect lead to the assumption that – in contrast to the case of fullerene-based OSCs – the degradation of non-fullerene devices originates from more than one underlying mechanism. In addition to the already known photo-shunting, the UV part of the spectrum also triggers a photocatalytic reaction at the ZnO/organic interface that leads to an irreversible disintegration of the non-fullerene acceptor molecule. With the help of optical absorption spectra, a generality of this effect was confirmed for several non-fullerene acceptor

species when nanoparticulate ZnO was used as EEL. In surprising contrast to this, indications for the absence of the harming photocatalytic effects was found when ALD-processed AZO was used as EEL. Here, the photo-induced degradation was still major but completely reversible, suggesting photo-shunting as the sole origin. Corroboratively, in this case it was not possible to show significant UV-induced changes in the acceptor's absorption spectrum, as was the case with ZnO nanoparticles. Thus, the disintegrating photocatalytic reaction can be postulated to only occur on ZnO surfaces with specific orientations different from the c-axis orientation, which is supposed to be the predominant surface orientation of the prepared ALD-AZO. Due to the preliminary nature of these results, there are still more investigations needed to verify this theory. In a first step, the determination of the exact orientations of the different ZnO-based EELs (for example via X-ray diffraction) would be necessary. Moreover, optical absorption measurements of acceptor layers on top of ZnO substrates with well defined orientations (e.g. commercially available ZnO single crystals) would be a route to identify the surface orientation that enables the critical photocatalytic reaction. In case this theory is evidenced, this would provide a novel understanding of photo-degradation in inverted fullerene-free OSCs. Additionally, this could lead to a decrease in severity of degradation patterns that are accompanied by the commonly used EEL materials based on ZnO. Nevertheless, the findings prove that photo-induced shunting is also a decisive degradation factor in ZnO-based non-fullerene devices and cannot be avoided through choice of a specific surface orientation of the EEL. Interestingly, it could be demonstrated that the use of SnO_x as EEL facilitates the fabrication of inverted OSCs which neither display photo-shunting nor suffer from photocatalytic decomposition of the acceptor. This adds to the already striking findings concerning SnO_x in fullerene-based

devices (**Chapter 5.1**) and makes it the most promising candidate for an EEL in future efficient and stable inverted non-fullerene solar cells. However, the results demonstrate notable differences in the initial device characteristics between SnO_x- and ZnO-based OSCs with ITIC as the acceptor (see above). Most strikingly, the SnO_x devices suffer from a substantially lowered V_{OC} and FF. This finding is very surprising, as SnO_x has been shown to be a universal EEL for fullerene-based cells which regularly provides equal or better results compared to ZnO without the need of UV activation.[48] Interestingly, in the case of IT-4F, the devices comprising SnO_x do not show inferior photovoltaic characteristics to ZnO (see **Appendix Figure 7.42**). To unravel the origin of these differences (even between non-fullerene acceptors), an in-depth study of the electronic interface structure at of SnO_x/organic- in comparison to ZnO/organic-interface for non-fullerene based systems is necessary. If an understanding of the effect could be achieved, it should be possible to mitigate the losses in case of ITIC (and possibly other acceptors) and thereby to fully harvest the beneficial properties of SnO_x regarding the absence of photo-induced degradation.

6 Conclusion

In conclusion, this work has illuminated various aspects of multi-junction solar cell technology, shedding light on the potential for improved efficiency, stability, and versatility.

The development of an all-oxide MoO_X/SnO_X recombination interconnect has showcased a remarkable alignment of conduction bands of both n-type extraction layers, enabling efficient charge transport and voltage addition, while remaining functional even without UV exposure, thus expanding its applicability. It also foreshadowed the exceptional suitability of ALD deposited layers in interconnects due to outstanding protection properties even at a low layer thickness. Moreover, the combination of sol-gel VO_X and SnO_2 nanoparticles has demonstrated promise, offering a solution-based, room-temperature process for tandem devices. The introduction of SnO_2 nanoparticles as a solution-processed EEL has not only enhanced the performance of tandem devices but has also enabled the use of acidic PEDOT:PSS in regular architectures, eliminating voltage losses. This innovative recombination architecture not only provides chemical protection but also efficient electric interconnection between sub-cells, leading to highly efficient tandem cells in both regular and inverted configurations. These results pave the way for the fabrication of efficient multi-junction solar cells through solution processing, offering a promising avenue for renewable energy technology.

Furthermore, the efforts of this work has achieved a remarkable milestone with the demonstration of a perovskite/organic tandem solar cell with an exceptional efficiency of 24.0%. At the time this was published, it was outperforming single-junction perovskite cells and was standing on par with other multi-junction technologies, which draws from progress in all

parts of the tandem device. Most strikingly, the introduction of an ultra-thin metal-like indium oxide layer as an all-oxide interconnect has demonstrated barrier-free electron transport and negligible optical and electrical losses, potentially revolutionizing future tandem architectures. The prospects for achieving efficiencies above 31% in perovskite/organic tandem architectures, as suggested by semi-empirical simulations, provide exciting directions for future research. Another noticeable feature of the novel tandem devices is their operational stability. Especially the preservation of efficiency in the organic sub-cell under tandem illumination conditions has challenged existing paradigms and opens new avenues for non-fullerene organic solar cells (in regular architecture).

Further investigations have provided crucial insights into the photo-induced degradation of inverted non-fullerene solar cells using ZnO as the electron extraction layer (EEL). It was revealed that the UV spectral component is a primary cause of this degradation, which occurs even under inert conditions. Importantly, the findings of partial reversibility in the dark suggest multiple underlying mechanisms, dependent not only on the EEL material but supposedly its surface orientation. While further investigations are needed to fully confirm these findings, the use of SnO_x as an EEL emerged as a promising solution, showing persistence to all the observed degradation mechanisms.

In summary, this work has significantly advanced our understanding of single- and multi-junction solar cells, offering innovative solutions to enhance efficiency, stability, and manufacturability. These findings hold the promise of ushering in a new era of renewable energy technology, bringing us closer to achieving sustainable and efficient solar energy conversion. Further investigations are expected to build upon these foundations, driving the field towards even greater achievements.

7 Appendix

7.1 Supplementary Information: Chapter 3

7.1.1 Experimental Details

Materials Synthesis and Device Preparation

Tin oxide was prepared by atomic layer deposition in a Beneq TFS 200 system (base pressure 1.5 mbar). As precursors, tetrakis (dimethylamino) tin(IV) (TDMASn), kept at 45 °C and water, kept at room temperature, were used. At a substrate temperature of 80 °C the growth rate was 1.056 Å per cycle. The zinc oxide layers were deposited at the same conditions (substrate temperature: 80 °C, base pressure: 1.5 mbar) using diethylzinc and water as precursors (both kept at room temperature). The inverted single junction OSCs are based on the following layer sequence: glass/indium-tin-oxide (ITO)/SnO$_x$/photoactive layer/MoO$_x$/ Ag with an active area of 0.03 cm^2. As photoactive material for the wide band gap cell, PCDTBT (supplied by 1-Material) and fullerene (PC$_{70}$BM (SES Research)) with a weight ratio of 1:4 were used. The polymer was dissolved in chlorobenzene and stirred in N$_2$ atmosphere at 80 °C for 2.5 h followed by adding the fullerene (stirring for 1.5 h). The solution was filtered (5 μm PTFE Filter) and spin coated in N$_2$ atmosphere. On the anode side, MoO$_x$ (10 nm) and Ag (100 nm) layers were thermally evaporated in high-vacuum (10^{-6} mbar). For the low-bandgap cells, either PDPP3T (P15) or PDPPPTT (P17) and fullerene (PC$_{60}$BM from American Dye Source) (weight ratio of 1:2) were dissolved in a mixture of chloroform and o-dichlorobenzene (6 vol% o-DCB) with an overall concentration of 15 mg mL^{-1}. After stirring at 90°C for 1 h the still warm solution was spin coated in N$_2$ atmosphere.

The sol-gel VO_x layers were spin-coated from isopropanol solution of vanadium(V) oxitriisopropoxide (Alfa Aesar) at 1:150 vol. ratio. The resulting layer thickness was 10 nm. The layers were subsequently stored at ambient air for 1 h for hydrolysis at room temperature.

For the sol-gel process of TiO_x layers a 1:345 vol. ratio of titanium-isopropoxide (Alfa Aesar) and isopropanol was used. The spincoating was performed under N_2 atmosphere with a speed of 2500 rpm and were subsequently stored in ambient air to hydrolyse at room temperature for 1 h. This resulted in a final layer thickness of approximately 40 nm.

One formulation of sol-gel SnO_x layers have been spin-coated from a solution of tetrakis(diethylamino)tin (TDEASn) (Sigma Aldrich) in isopropanol at 1 : 58 vol ratio. The rotational speed was varied from 700 to 9000 rpm resulting in a layer thickness varying from about 5 to 110 nm. The layers were subsequently stored in ambient air for 1 h for hydrolysis.

Following another route, sol-gel SnO_x was prepared from a precursor solution of (tetrakisdimethylamino)tin(IV) (TDMASn) (Strem Chemicals) in 2-isopropoxyethanol (vol. ratio: 1:58). Spin coating and subsequent hydrolysis and condensation in ambient air (for 1 h at room temperature) resulted in layers of 10–20 m thickness. The layers were afterward annealed at 120 °C for 1 h.

For solution-processed nanoparticulate ZnO-based layers, NP dispersions of ZnO (2.8% w/v in acetone from InfinityPV) and Al:ZnO (N-20X & N-21X, both 2.5 wt% in isopropanol, Avantama, Switzerland), were used. Before spin coating in ambient air, all dispersions were ultra-sonicated for 5 min. The typical layer thickness was 30–35 nm.

The two different nanoparticulate SnO_2 layers have been prepared from one of two NP dispersions of SnO_2 (either N-30 or N-31, both 2.5 % w/v in a

mixture of butanols, Avantama, Switzerland). The dispersions have been diluted in a 1:1 vol. ratio with isopropanol and subsequently have been ultra-sonicated for 5 min prior to spincoating in air with no further post-processing steps.

Materials Characterization

Optical parameters of the tin oxide and molybdenum oxide layers were obtained by spectral ellipsometry (M-2000V from J.A. Wollam) for thin film samples deposited on top of a Si wafer with native oxide. For determining transmission and reflection spectra a Deuterium Halogen lamp (DH-2000-BAL, OceanOptics) and a spectrometer with a range from 186 to 1041 nm (USB 2000+XR1-ES) were used. For transmission measurements, 200 nm thick SnO_x and 100 nm thick MoO_x layers were deposited on quartz substrates.

The measurements of the surface potential were done with a McAllister KP6500 Kelvin-Probe (KP) system in vacuum (10^{-6} mbar). Highly ordered pyrolytic graphite with a WF of 4.5 eV was used as reference.[225,226]

The photoelectron spectra were measured without exposing the prepared samples to ambient environment. After preparation the samples were stored in a glove-box and were transferred to the vacuum chamber in a dedicated vacuum shuttle. The XPS measurements were carried out using an ESCALAB 250 system from ThermoFisher. Monochromatic X-rays (1486.6 eV photon energy) from an Al-Kα source were used. A magnetic lens was used to have a maximum collection of photoelectrons from the sample. Data were collected with pass energy of 10 eV in normal emission. The binding energy was calibrated with the Cu^{3d}, Ag^{3d}, and Au Fermi edge.

The UPS measurements were performed using He-Iα (hυ = 21.22 eV) radiation. The experiments were carried out with a bias potential of 4 eV.

The valence band maxima and the work function were determined from the linear extrapolation of valence band edge and secondary electron edge.

Device Characterization

The solar cells were characterized in ambient air without encapsulation using a Keithley 2400-C source meter and a solar simulator (300 W Newport, AM1.5G, 100 mW cm^{-2}).

The external quantum efficiency was determined using a calibrated tunable light source consisting of a 50 W tungsten halogen lamp (Osram 64610) and a monochromator (Oriel, Cornerstone 130) in combination with a lock-in amplifier (Stanford Research Systems SR 830). For the determination of the EQE of the tandem-cells a protocol was followed as recently reported.[88] The sub-cells were therefore characterized under accurate bias light and voltage conditions. These measurements were performed using an in-house built system, where the bias light was provided by monochromatic power LEDs (Thorlabs M530L3, M730L4).

The J/V characteristics of the tandem cell were thereafter recorded upon illumination with a light source which was adjusted to compensate spectral mismatch for both active layers. Therefore, the power of the light source was changed such that the deviations between J_{SC} measured under the light source and the J_{SC} determined by EQE were equal for each reference single junction device.
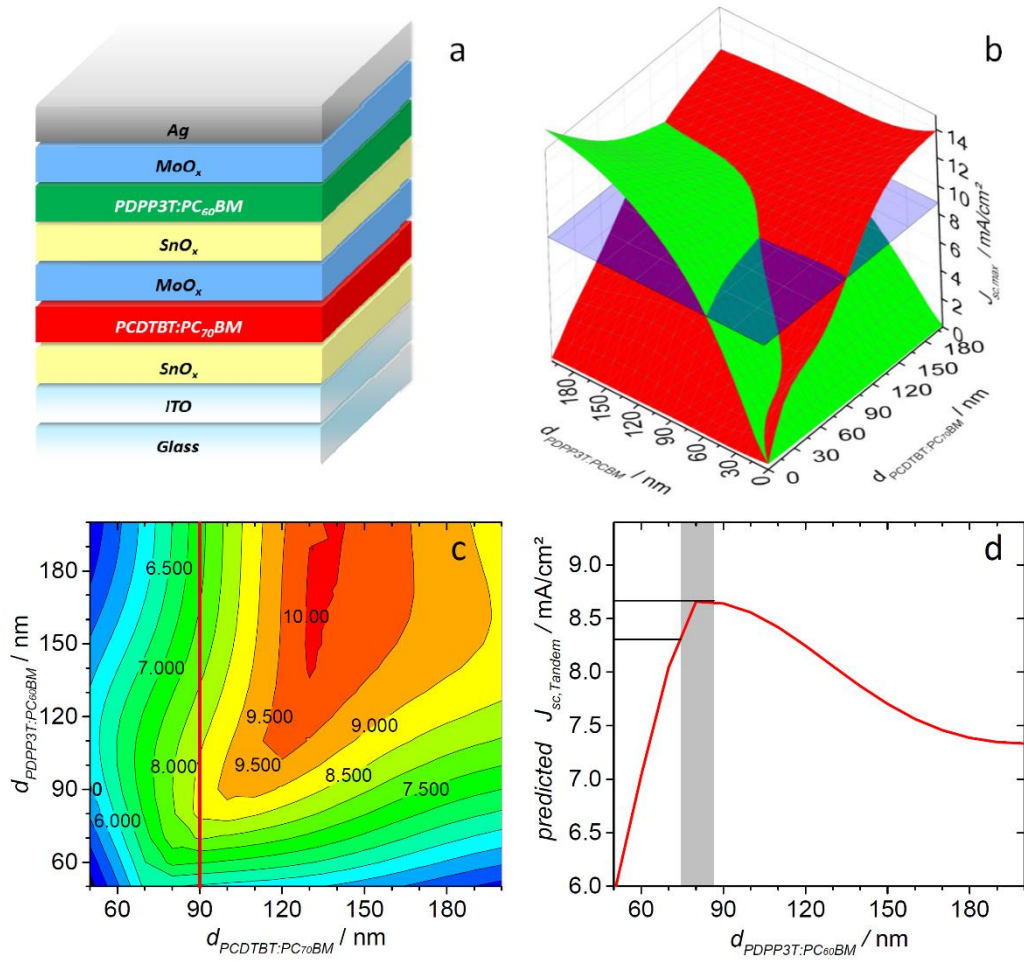
7.1.2 Additional Data and Figures

Figure 7.1: (a) Tandem device stack used in the optical transfer-matrix simulation. (b) Simulated Jsc of both sub-cells in the tandem for varied thicknesses of the active layers. The Jsc of PCDTBT:PC$_{70}$BM and PDPP3T:PCBM are described by the red and the green plane, respectively. The blue plane represents a constant J$_{SC}$ of 8.5mA/cm². The intersection of all three planes is the point chosen for the tandem device shown above. (c) Predicted Jsc of the tandem device calculated from the data shown in (b). A maximum Jsc would be expected for a thickness of the PCDTBT:PC$_{70}$BM layer of about 130 nm. Limitations of the PCDTBT batch did not allow for an active layer thickness of more than 90 nm without substantial loss of FF (see **Figure 2.1**). The red line at a PCDTBT:PC$_{70}$BM thickness of 90 nm indicates the section profile shown in (d). (d) Simulated Jsc of the tandem vs. PDPP3T:PCBM layer thickness for a given PCDTBT:PC$_{70}$BM layer of 90 nm. The best current matching (highest Jsc of about 8.5 mA/cm²) is achieved for a thickness of nominally 80 nm (grey region). Reproduced from Ref.[109].
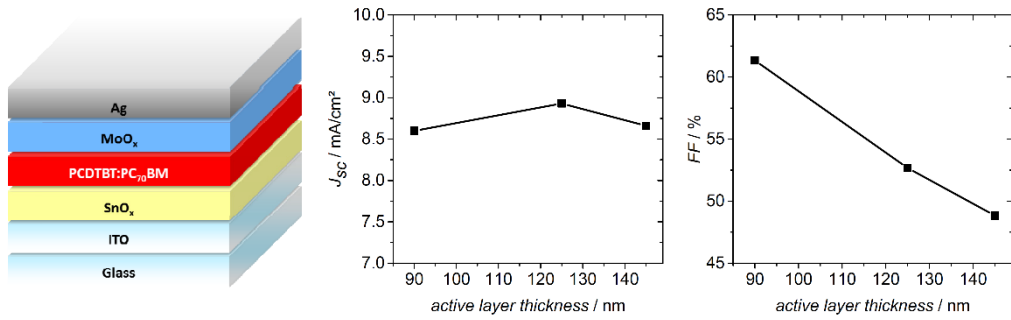
Figure 7.2: (a) Layer sequence of a PCDTBT:PC₇₀BM based single junction cell. (b) Jsc and (c) FF vs. thickness of the photo-active layer. Reproduced from Ref.[109].
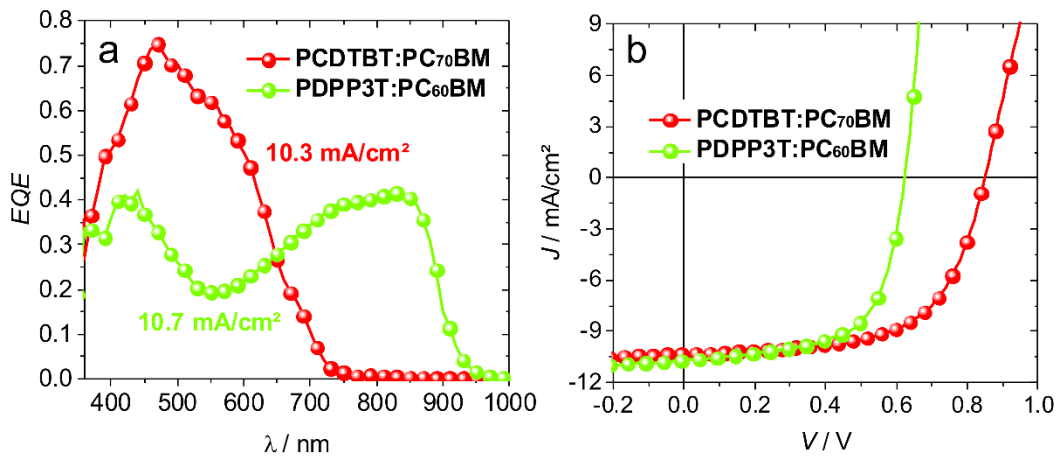
Figure 7.3: (a) EQE spectra and (b) J/V characteristics of PCDTBT:PC₇₀BM and PDPP3T:PC₆₀BM single junction devices. Reproduced from Ref.[109].
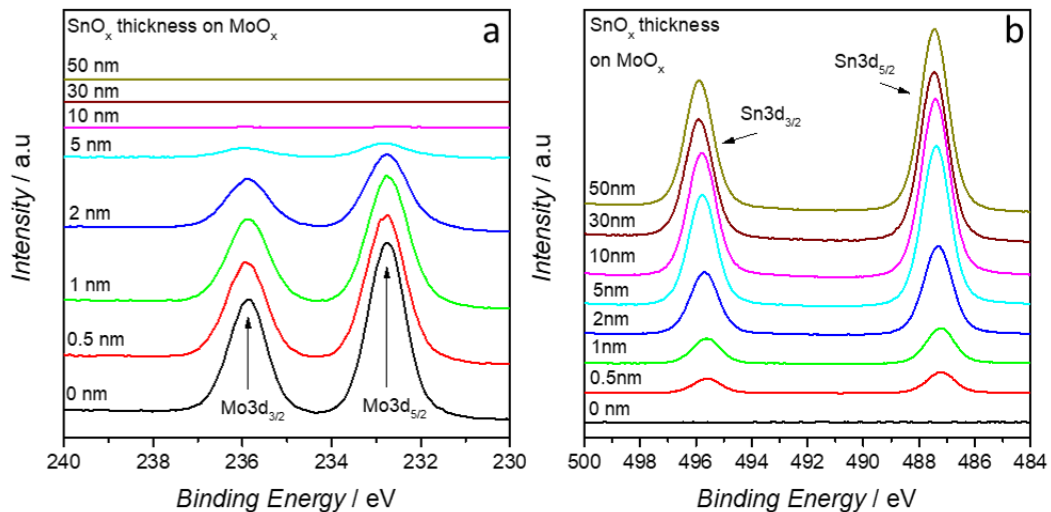
Figure 7.4: Core level spectra of (a) Mo3d and (b) Sn3d for varying SnO_x thickness on top of MoO_x. Reproduced from Ref.[109].
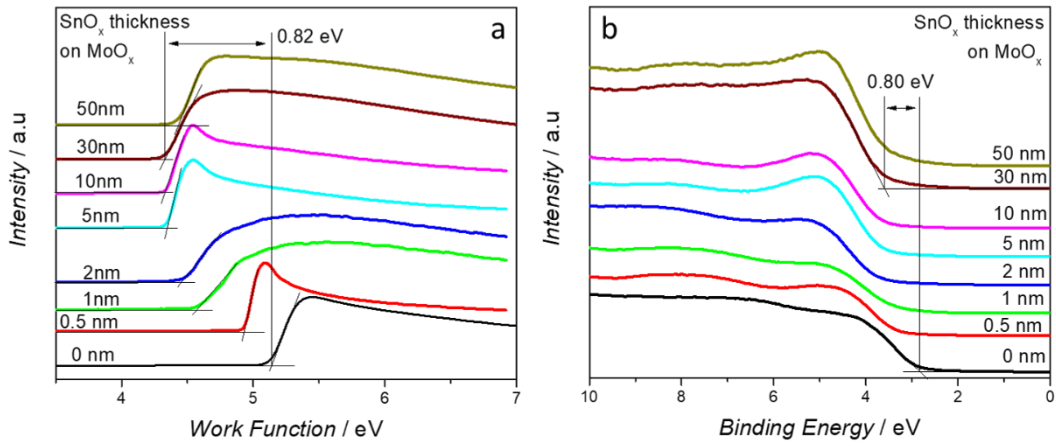
Figure 7.5: (a) Work function and (b) valance band spectra of MoOx and SnOx/MoOx for varying SnOx thickness determined from UPS measurements. The large WF offset and valence band offset can be taken from WF and VB spectra respectively. Reproduced from Ref.[109].
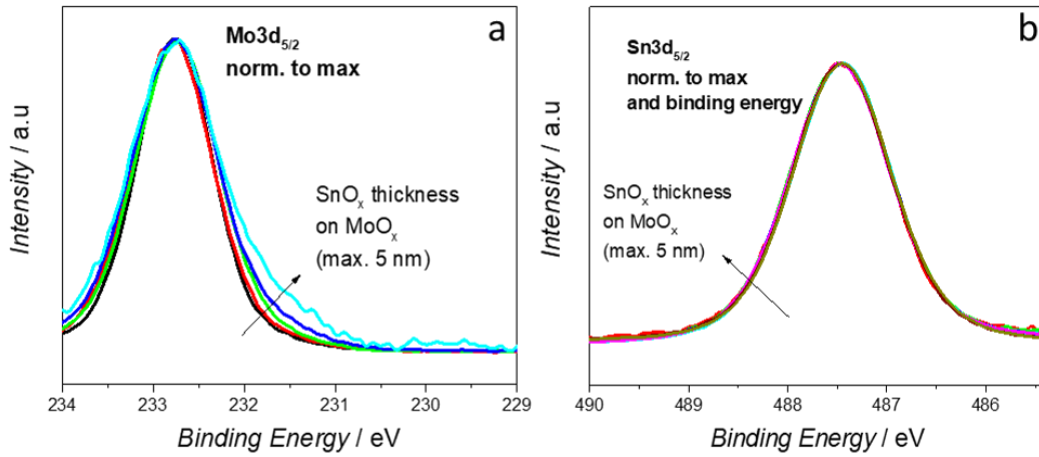
Figure 7.6: Normalized Mo3d$_{5/2}$ (a) and Sn3d$_{5/2}$ (b) peaks for increasing the SnOx thickness on top of the MoOx. Reproduced from Ref.[109].
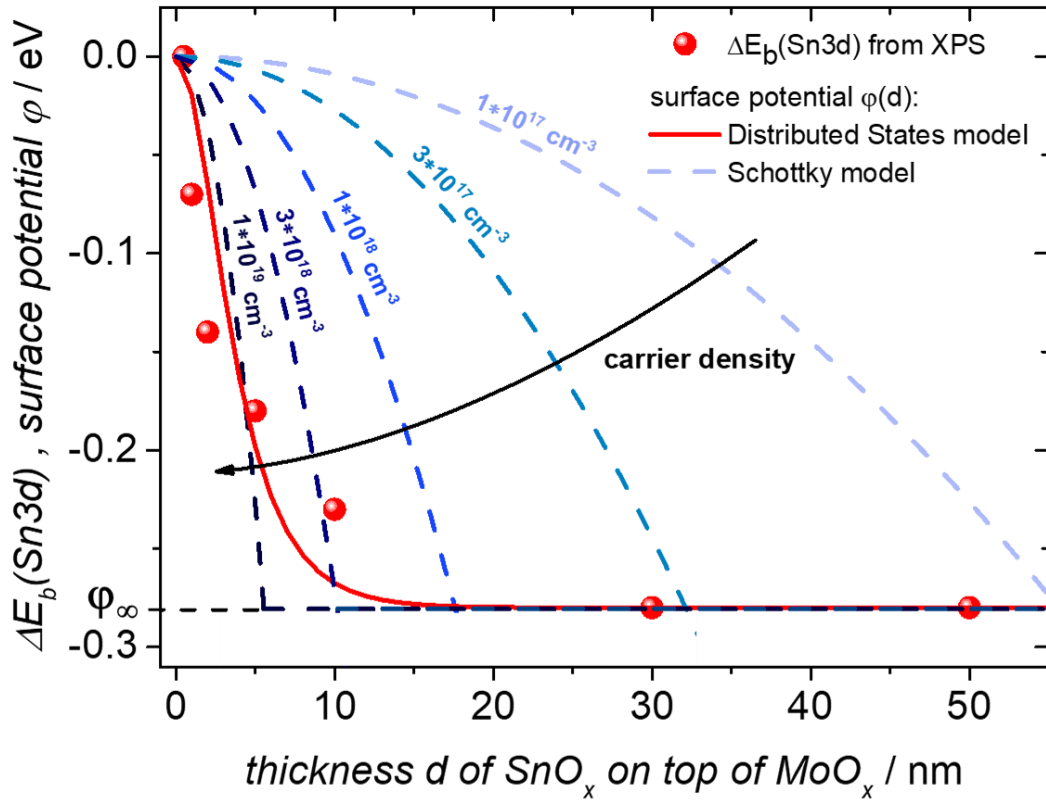
Figure 7.7: Binding energy difference of the Sn3d core level peak measured by XPS for increasing the SnOx layer thickness d on top of MoOx. The plotted curves show the theoretical progression of the surface potential for the distributed states model[125] and the textbook Schottky model. In case of the Schottky model several curves for various carrier densities are shown. Reproduced from Ref.[109].
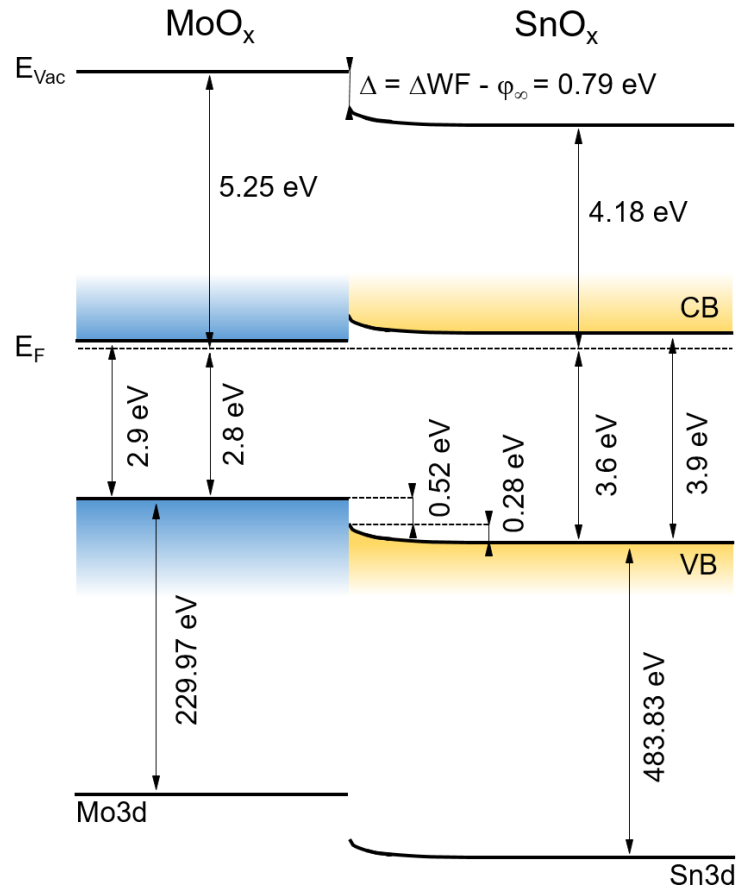
Figure 7.8: Energetic band line-up at the MoOx/SnOx interface including the core level positions of Mo3d and Sn3d determined by XPS. Reproduced from Ref.[109].
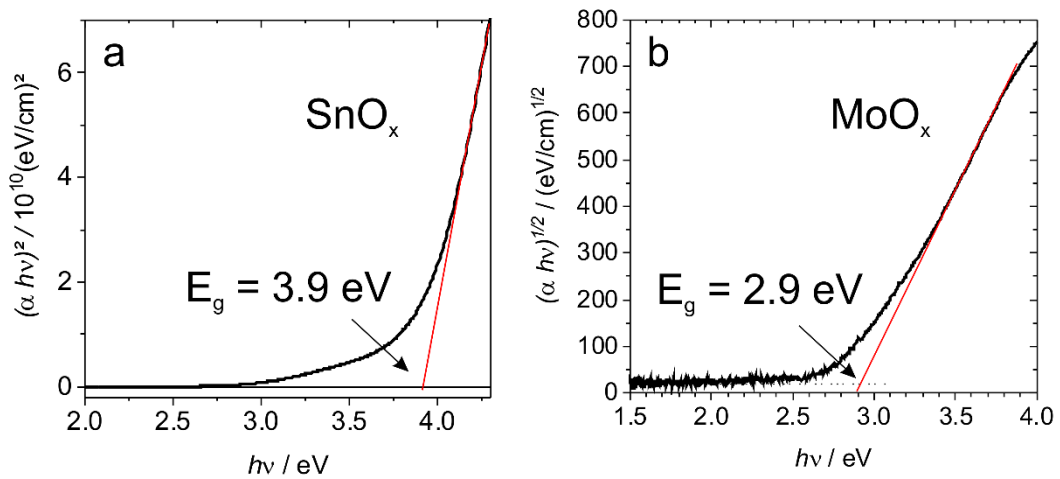
Figure 7.9: Tauc-plots of (a) SnOx prepared by ALD at 80°C under the assumption of a direct allowed transition and (b) thermally evaporated MoOx under the assumption of an indirect allowed transition. Reproduced from Ref.[109].
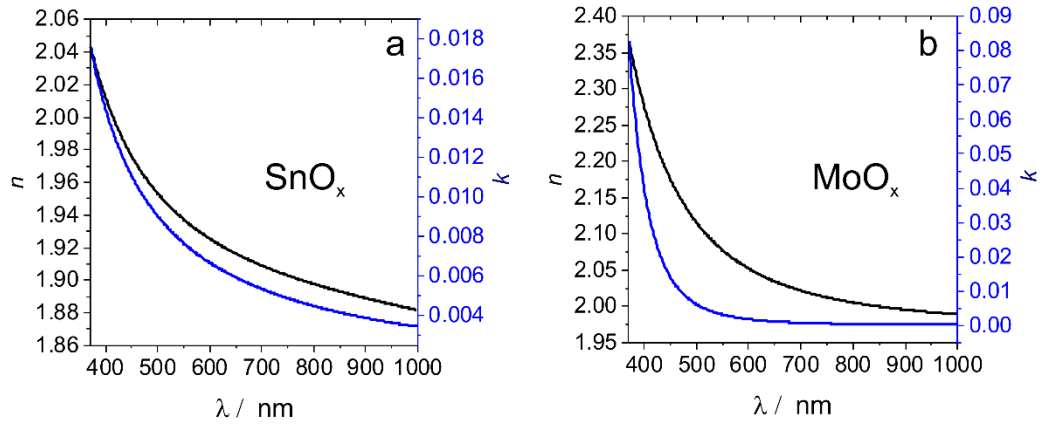
Figure 7.10: Optical constants (n, k) of SnO$_X$ prepared by ALD at 80°C (a) and thermally evaporated MoO$_X$ (b) as determined by spectral ellipsometry. Reproduced from Ref.[109].

	SnO$_X$	**ZnO**	**Al$_2$O$_3$**
Δ [eV]	0.8	0.7	1.1

Table 7.1: Work Function drop (Δ) of evaporated MoO$_X$ upon deposition of nominally 5 nm of SnO$_X$, ZnO or Al$_2$O$_3$ via atomic layer deposition. Reproduced from Ref.[109].
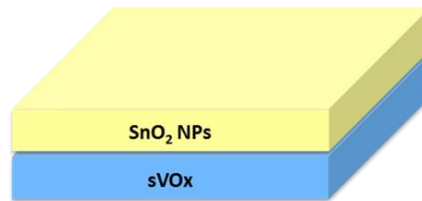
SnO$_2$ layer on top of sVO$_X$	none	N-30	N-31
Work Function [eV]	5.3	4.3	4.6

Figure 7.11: WF measurement on sVO$_X$/SnO$_2$ ICLs with different SnO$_2$ NP formulations.
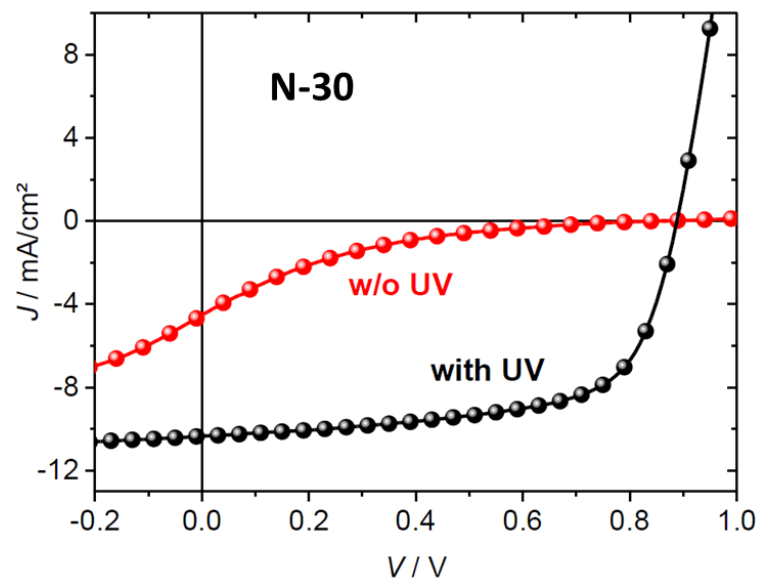
Figure 7.12: J/V characteristics for an inverted single-junction device comprising a SnO_2-based EEL comprised of nanoparticle formulation N-30. Under UV filtered illumination there is no well shaped J/V-curve resulting in a low FF.

7.2 Supplementary Information: Chapter 4

7.2.1 Experimental Details

Preparation of Perovskite Sub-Cell and Interconnect

All processing steps of each sub-cell were carried out either in an inert atmosphere or under high vacuum without inert breaks.

The layer sequence of the perovskite p–i–n sub-cell is glass/HEL/$FA_{0.8}Cs_{0.2}Pb(I_{0.5}Br_{0.5})_3$/$PC_{61}BM$/AZO-NP/ALD-$SnO_x$/ALD-$InO_x$/(Ag). ITO-coated glass (17×17 mm²) with a photoresist patterned to define the active area of 3.14 mm² was used as substrate. Tandem cells, additionally, were covered with an illumination mask reducing the active area to 1.74 mm² to match the certification procedure. After cleaning and a brief plasma treatment, PTAA (Sigma-Aldrich, 1.35 mg ml⁻¹ in toluene) or MeO-2PACz (TCI, 0.1 mM in ethanol) was spin-coated at 6,000 r.p.m. for 20 s with a ramp of 8 s and annealed at 100 °C for 30 min. For perovskite thin-film preparation, PbI_2 (0.75 M, ultra-dry from Alfa Aesar), $PbBr_2$ (0.25 M, ultra-dry from Alfa Aesar), CsBr (0.2 M, ultra-dry from Alfa Aesar) and FABr (0.8 M, from Greatcell Solar) were dissolved in a 3:7 mixture of N-methyl-pyrrolidone and dimethylformamide and stirred for at least 3 h. In some cases, an additional 20 mM PbI_2 and 10 mM $PbBr_2$ were added. Before spin-coating, 33 mM thiourea (2.5 mg ml⁻¹, Sigma-Aldrich; previously dissolved as 100 mg ml⁻¹ in dimethylformamide) was added to the precursor solution. The perovskite deposition was performed following a gas-quenching procedure, as described in earlier work.[185] Briefly, the solution was spin-coated at 3,000 r.p.m. for 120 s with a ramp of 10 s. About 15 s after the ramp was finished, a nitrogen flow (7 bar, filtered with 5.0 μm PTFE) was directed at the substrate to introduce a supersaturated intermediate phase. Subsequently, during a 20 min annealing step at 100 °C,

130

the final perovskite layer formed. PEAI (TCI, 1 mg ml^{-1} in isopropanol) was optionally spin-coated at 6,000 r.p.m. for 30 s with a ramp of 8 s followed by another annealing step of 10 min at 100 °C. The optimum PC$_{61}$BM layer thickness was found to be around 100 nm for the following process parameters: PC$_{61}$BM purchased from Ossila, 50 mg ml^{-1} in chlorobenzene, was spin-coated with 1,000 r.p.m. for 30 s and a ramp of 1 s. AZO nanoparticles were processed from an NP-dispersion (N-21X, 2.5 wt% in a mixture of alcohols, Avantama, Switzerland,) diluted with isopropanol (1:2) and spin-coated at 4,000 r.p.m. for 20 s using a ramp of 6 s. Some AZO layers were subsequently annealed at 80 °C, 90 °C or 100 °C for 90 min. For ALD deposition the solar cells were transferred into a Beneq TFS-200 reactor without inert break. SnO$_x$ layers were grown from tetrakis(dimethylamino)tin(IV) (TDMA-Sn, Strem) and water. The reactor temperature during the deposition was 80 °C, TDMA-Sn was kept in a hot source at 45 °C and water in a liquid source at room temperature. Directly thereafter, InO$_x$ was grown on top of SnO$_x$ from cyclopentadienylindium (CpIn, Strem), oxygen (purity 99.999%) and water.[227] The reactor temperature was 80 °C, CpIn was kept in a hot source at 50 °C and water was kept in a liquid source at room temperature.

Note that although the ALD processes are based on water as the oxygen source, which one might intuitively suspect to be detrimental to the active perovskite material, a single dose of H$_2$O in low-pressure ALD typically creates an environment equivalent to a maximum of 0.1% relative humidity.[228] This is substantially lower than the large variety of conditions mentioned in the literature to degrade perovskite.[229,230]

Silver was thermally evaporated in high vacuum (10^{-7} mbar).

Preparation of the Organic Sub-Cell

As hole extractor, a 15 nm layer of MoO_x was thermally evaporated in high vacuum (10^{-7} mbar). To form the binary bulk heterojunction (BHJ) PM6 and Y6 (Solarmer Materials) with a weight ratio of 1:1.2 were dissolved in chloroform (polymer concentration 7 mg ml^{-1}) and stirred for 3 h at 50 °C. For the ternary BHJ an extra amount of $PC_{61}BM$ (American Dye Source) was added, yielding a weight ratio of 1:1.2:0.2. Five minutes before BHJ processing 0.5 vol% of 1-chloronaphthalene (Sigma-Aldrich) was added to the solution. Spin-coating was carried out dynamically (solution was dropped onto the middle of the rotating substrate) at 2,500 r.p.m. for 60 s. A subsequent thermal annealing step at 100 °C was applied followed by thermal evaporation of 10 nm C_{60}, 5 nm of BCP and 100 nm Ag.

For selected tandem cells, a 100 nm thick MgF_2 layer was thermally evaporated onto the back side of the glass substrate as an antireflection layer.

J/V Characterization and Stabilized Power Output

J/V characteristics of solar cells were recorded outside the glovebox under a continuous flow of nitrogen using a Keithley 2400 source measurement unit (SMU) and a 300 W Newport solar simulator (model 91 160, AM1.5G, 100 mW cm^{-2}) calibrated with a certified IEC 60904-9-compliant Si reference cell (Rera Systems). J/V characteristics were recorded with a scanning speed of 500 mV s^{-1}. Stabilized power output recording was performed by continuously tracking the MPP under AM1.5G illumination. Stabilized Voc was recorded by continuously recording voltage without current flow. Long-term measurements were conducted by continuous MPP tracking in an N_2-purged chamber under the illumination of two high-power LED light sources (NIR: Thorlabs M850LP1, and visible: Prizmatics UHP-T-HCRI or

Thorlabs MWWHLP1 with a 630 nm low-pass filter) joined together by a dichroic mirror. The intensity of the light source(s) was set to generate a J_{sc} comparable to AM1.5G sunlight illumination, unless otherwise stated. In the case of organic single junctions, this was achieved by first tuning the intensity of the LED_{NIR} to match the Jsc to that of the tandem under AM1.5G illumination. Then the white LED_{VIS} was added to finally achieve a Jsc corresponding to that of the organic single junctions under AM1.5G illumination. For the perovskite single junctions only the white LED_{VIS} was used for illumination.

Temperature-dependent J/V scans of the recombination layers were conducted with an all-in-one solar cell characterization system (PAIOS, Fluxim) connected to a temperature-controlled cryostat (Linkham). Temperature was varied from room temperature upwards, then down and back to room temperature to ensure reproducibility.

EQE Characterization

For EQE measurements a home-built set-up containing a chopped tunable light source (LOT MSH 150) and a lock-in amplifier (NF Electronic Instruments 5610B) was used. Calibration was performed with a Thorlabs PM100D power meter with a S130VC sensor head. For determination of the EQE of the tandem cells a previously published protocol was followed55.[88] The sub-cells were therefore characterized under accurate bias conditions, to emulate operation under AM1.5G illumination. A 780 nm and a 520 nm laser diode (RLDC780-2-3 and RLCW520F, Roithner LaserTechnik) were used as bias light sources for the narrow-gap and wide-gap sub-cells, respectively.

Electrical Characterization of Thin Films

Sheet resistance was determined by measurements following the van der Pauw geometry in a home-built set-up using a Keithley 2400 SMU and Keithley 182 voltmeter. Charge carrier density was determined from Hall measurements using the same set-up and a magnetic field of 0.75 T.

Photoelectron Spectroscopy

Photoelectron spectroscopy was performed in a custom-built ultra-high vacuum system, with a base pressure $<10^{-9}$ mbar. For the detection of the photoelectrons in the UPS and X-ray photoelectron spectroscopy (XPS) measurements, a hemispherical energy analyser was used (Specs Phoibos 100). The excitation for XPS was done via a non-monochromated MgK_{α} source (from VG Scienta, $h\nu = 1{,}253.6$ eV) and for UPS by a monochromatic He source (VUV500, VG Scienta, $h\nu = 21.22$ eV). Inverse photoemission spectroscopy (IPES) was performed using a Kimball electron source (ELG-2) and a solid-state band-pass filter (Omnivac IPES2000). The samples were transferred into the measurement system without air exposure and were measured within 2 days of preparation.

The program XPSPEAK v.4.1. was used to fit the XPS spectra. For fitting of the molybdenum XPS peaks, a Shirley background was subtracted. The parameter for full width half maximum and the Lorentzian to Gaussian ratio (L:G) were kept constant for all Mo peaks, at 1.22 eV and 23, respectively. The distances between the peaks of the different Mo oxidation states were held constant, with 0.82 eV between Mo^{5+} and Mo^{6+} and 0.8 eV between Mo^{4+} and Mo^{5+}. With regard to the additional Mo feature that was observed (**Appendix Figure 2.1**): in the case of MoO_x on top of SnO_x, the position was at 0.88 eV higher binding energy compared to the Mo^{6+} signal of MoO_x, whereas on InO_x this shift was 0.74 eV.

X-ray Diffraction and Scattering

X-ray diffraction characterization was conducted with a CuK$_{\alpha 1,2}$ source (Philips C'Pert Pro MPD).

GIWAXS and GISAXS were performed on a Xenocs XEUSS 2.0 laboratory beamline using CuK$_\alpha$ radiation. Sample detector distances were 170 mm and 1,470 mm for GIWAXS and GISAXS, respectively. The incident angles were below 0.5°, and the pressure in the sample chamber during the experiment was 0.1 bar. X-ray reflectivity measurements were recorded with a GE XRD 3003 TT diffractometer in ambient environment, also using CuKα radiation. Synchrotron GIWAXS measurements were done at beamline ID10 of the ESRF under nitrogen conditions. Beam energy was 22 keV, with incidence angles varying from 0 to 0.3°.

Atomic Force Microscopy, Electron Microscopy and Spectroscopy

Scanning electron microscopy (SEM) images were obtained with a Phillips XL-30 SFEG. AFM was conducted with a Bruker Innova system.

Scanning transmission electron microscopy (STEM) was performed on a Titan Themis microscope operated at 300 kV. The aberration-corrected STEM probe had a <1 Å size and a convergence semi-angle of 24 mrad. High-angle annular dark-field (HAADF) and annular bright-field images were acquired using collection angles of 73–200 and 8–16 mrad, respectively. The cross-sectional sample for STEM was prepared by a Scios2 focused-ion beam (FIB) with a C marker layer to protect the sample surface.[231]

Energy-dipsersive spectroscopy (EDS) spectral imaging was collected by a SuperX detector. The elemental distribution within the ALD layers was examined by EDS spectrum imaging, as shown in **Appendix Figure 7.32**. It

is noteworthy that the In L and Sn L X-ray emission peaks overlap, so that the traditional quantification by integrating peak intensity over fixed windows leads to interference between the SnO_x/InO_x layers. Therefore, multivariate statistical analysis was applied to separate the X-ray emission signals from In and Sn. In this case, non-negative matrix factorization was used, an algorithm widely applied in microanalysis, including spectrum imaging of EDS and electron energy loss spectroscopy.[176,232]

Optical Characterization

Ellipsometry data for the metal oxide layers were acquired with a J.A. Woollam M-2000V ellipsometer and fitted with a Cauchy approximation. Optical simulations were carried out using SETFOS (Fluxim). Details of the simulation can be found in **Chapter 4.2**. Transmittance spectra were obtained using the same tunable light source as used for EQE (not chopped) and a power meter. The respective layers were deposited on quartz substrates. UV–visible spectra were acquired with a Jasco V-670 spectrometer. LED spectra were determined using an Ocean Optics spectrometer (USB2000+XR1-ES).

Excitation for the photoluminescence imaging measurements was performed with a 520 nm CW laser (Insaneware) through an optical fibre into an integrating sphere. The intensity of the 1 cm² laser spot was adjusted to a 1 Sun equivalent intensity by illuminating a wide-gap perovskite solar cell under short circuit and matching the current density to the Jsc under the sun simulator (for example, approximately 16 mA cm^{-2} at 100 mW cm^{-2}, or 1×10^{21} photons per m² per s for a perovskite cell with a bandgap of 1.85 eV). A second optical fibre was used from the output of the integrating sphere to an Andor SR393i-B spectrometer equipped with a silicon CCD camera (DU420A-BR-DD, iDus). The system was calibrated by using a

halogen lamp with known spectral irradiance, which was shone into the integrating sphere. A spectral correction factor was established to match the spectral output of the detector to the calibrated spectral irradiance of the lamp. The spectral photon density was obtained from the corrected detector signal (spectral irradiance) by division through the photon energy, and the photon numbers of the excitation and emission were obtained from numerical integration using Matlab. In a last step, three fluorescent test samples with high specified photoluminescence quantum yield (PLQY) (approximately 70%) supplied from Hamamatsu Photonics were measured, where the specified value could be accurately reproduced within a small relative error of less than 5%.
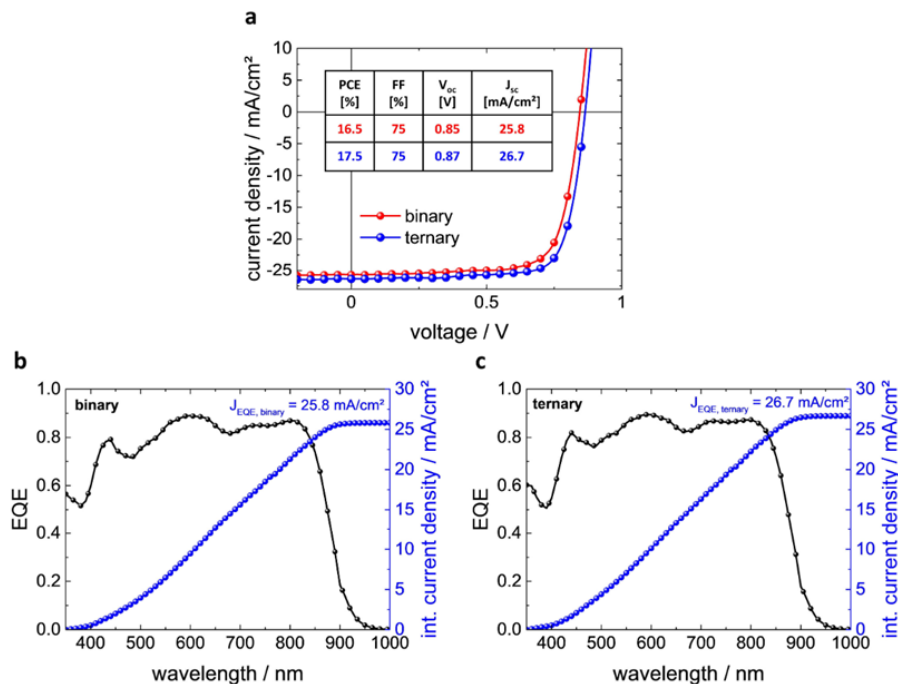
7.2.2 Additional Data and Figures

Figure 7.13: a) J/V scans and respective cell parameters of champion binary and ternary OSCs and b) EQE as well as derived short circuit current density of a binary OSC and c) a ternary OSC. Reproduced from Ref.[150].
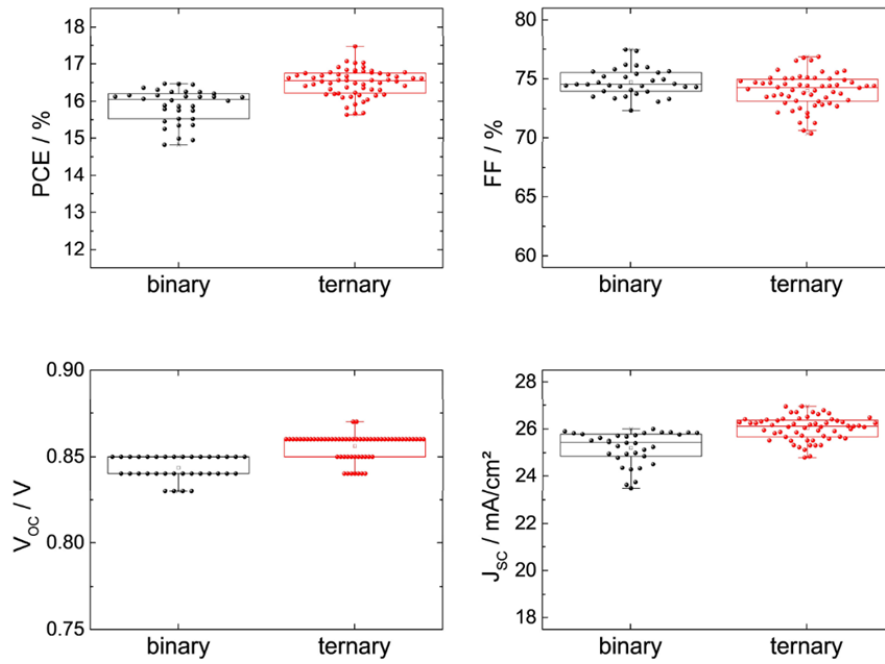
Figure 7.14: Statistics of 34 binary (PM6:Y6) and 60 ternary (PM6:Y6:PC$_{61}$BM) organic solar cells. Median line with upper and lower box ranges denoting the 25% and 75% margins. The bars denote the outermost data points that are still inside another 1.5 interquartile range. Reproduced from Ref.[150].
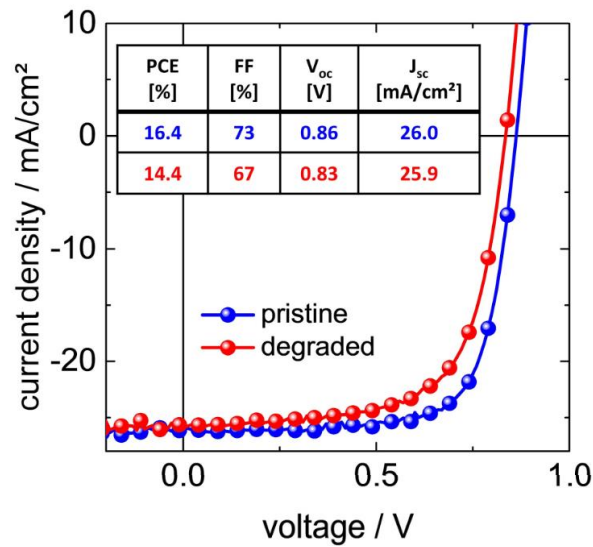

PCE [%]	FF [%]	V$_{oc}$ [V]	J$_{sc}$ [mA/cm²]
16.4	73	0.86	26.0
14.4	67	0.83	25.9

Figure 7.15: J/V curve of ternary OSCs before (pristine) and after 90h continuous illumination (degraded) with LED$_{VIS}$ + LED$_{NIR}$. Reproduced from Ref.[150].
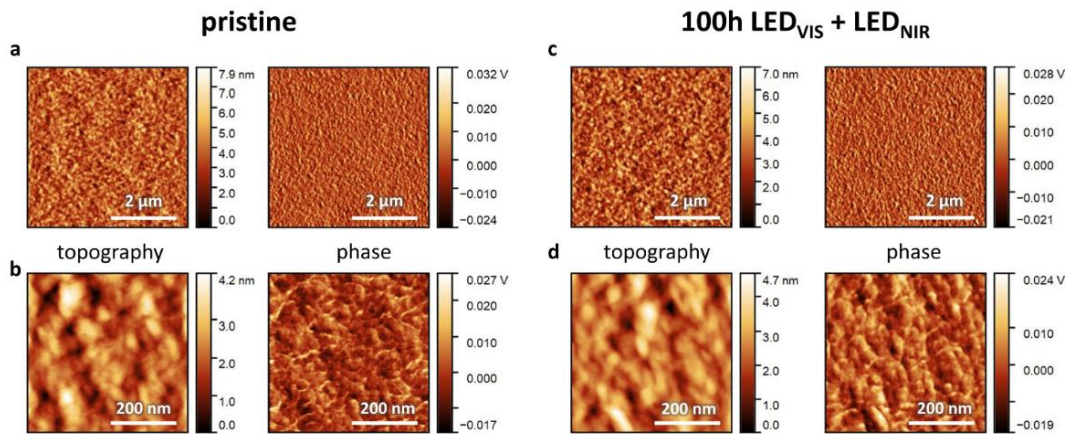
Figure 7.16: Results of atomic force microscopy (topography and phase images) of ternary (PM6:Y6:PC$_{61}$BM) bulk heterojunctions deposited on top of a silicon substrate a), b) pristine and c), d) after stressing by illumination for 100 h (LED$_{VIS}$ + LED$_{NIR}$). No obvious changes in the surface morphology can be identified after illumination stress. Reproduced from Ref.[150].
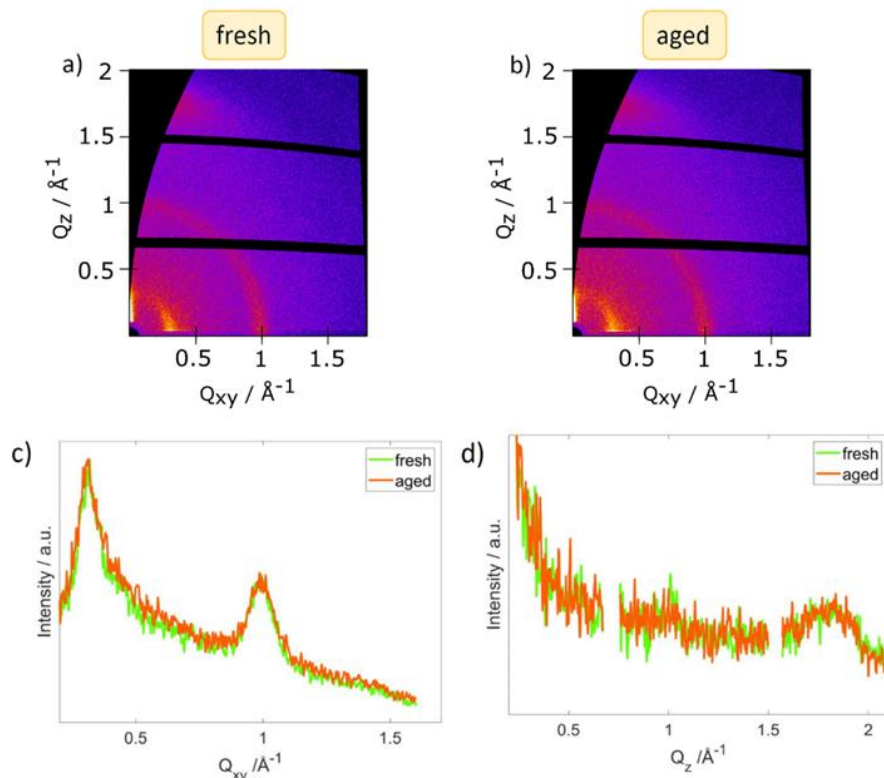

Figure 7.17: a), b), Reciprocal space maps of fresh and aged (100 h LED$_{VIS}$ + LED$_{NIR}$)ternary (PM6:Y6:PC$_{61}$BM) bulk heterojunctions obtained by grazing incidence wide angle scattering (GIWAXS) c), horizontal and d), vertical profiles of the reciprocal space maps showing no detectable sign for changes in the molecular order. Reproduced from Ref.[150].
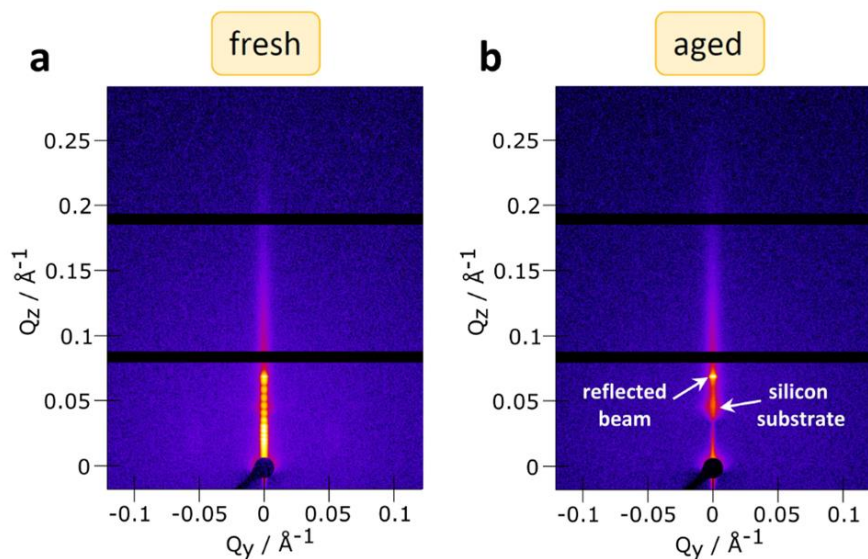
Figure 7.18: Grazing incidence small angle x-ray scattering (GISAXS) images of a), fresh and b), aged ternary bulk heterojunctions deposited on top of a silicon substrate. The strong peak at around 0.07 Å⁻¹ in Qz corresponds to the reflection from the surface of the primary beam. A further signal, positioned at 0.045 Å⁻¹ in Qz for both samples corresponds to the total reflection edge of the silicon substrate (Yoneda wing). The disappearance of the out-of-plane oscillations as well as of very weak in-plane signals (at 0.05 Å⁻¹) in GISAXS might hint to slight changes in the correlations of surface domains. Overall, no clear indication of illumination induced ordering/packing (segregation) of the bulk heterojunction could be detected. Reproduced from Ref.[150].

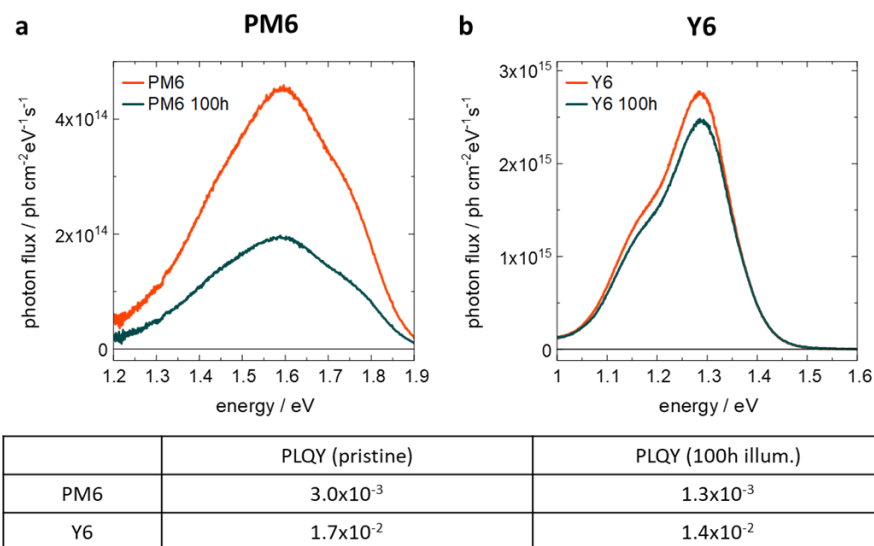|	PLQY (pristine)	PLQY (100h illum.)
PM6	3.0×10^{-3}	1.3×10^{-3}
Y6	1.7×10^{-2}	1.4×10^{-2}

Figure 7.19: Photon flux of photoluminescence for a) PM6 and b) Y6 layers pristine and after 100 h illumination with both the white (LED$_{VIS}$) and near infrared (LED$_{NIR}$) LED (**Figure 4.1c**), as well as the corresponding photoluminescence quantum yield. Reproduced from Ref.[150].
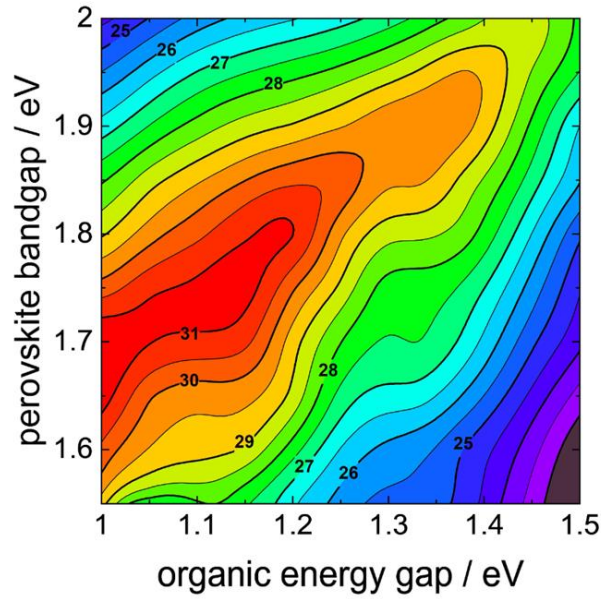
Figure 7.20: Semi-empirical model of the tandem cell efficiency vs. energy-gap of organic and perovskite sub-cells considering a more optimistic scenario with 0.4 V loss in Voc compared to E_g/q in each cell and an overall FF of 85%. Reproduced from Ref.[150].
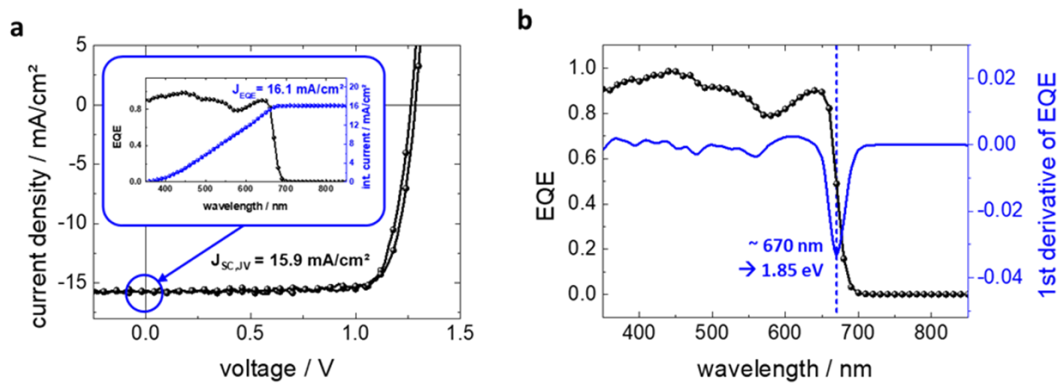

Figure 7.21: a) J/V and EQE (inset) characteristics for a representative PSC (90°C annealing) and b) estimated bandgap by 1st derivative of the EQE spectrum. Reproduced from Ref.[150].
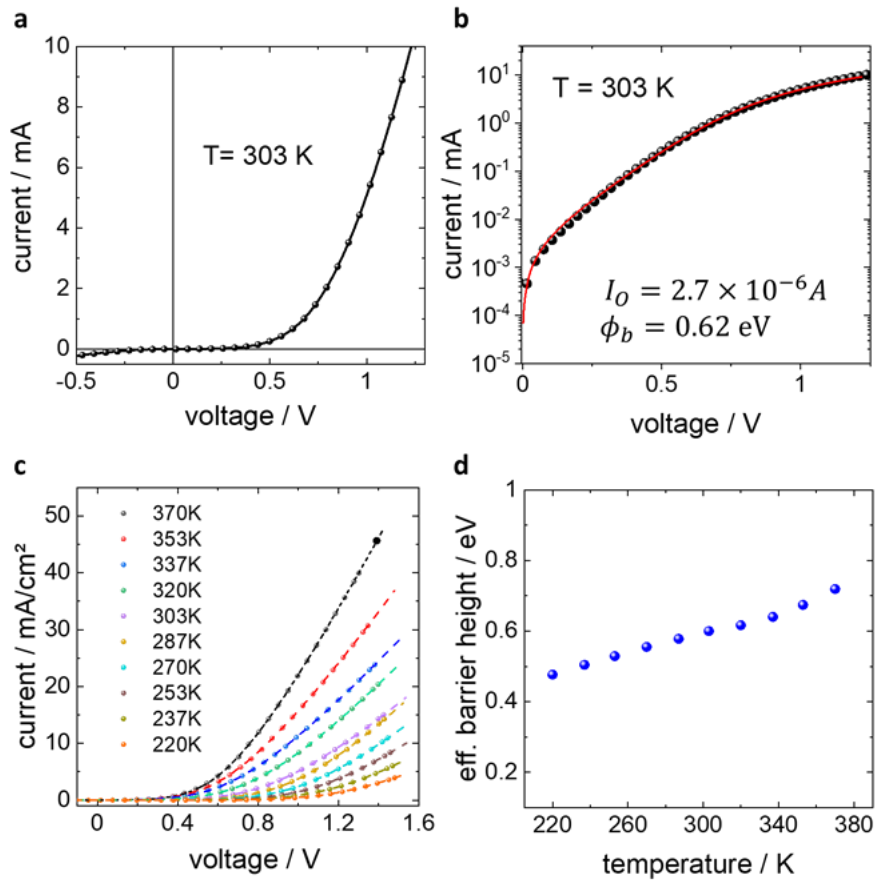
Figure 7.22: Determination of Schottky-barrier height from the J/V characteristics: a) forward J/V scans in linear and b) semi logarithmic scale. c) temperature dependent J/V scans, and d) calculated barrier heights. Reproduced from Ref.[150].
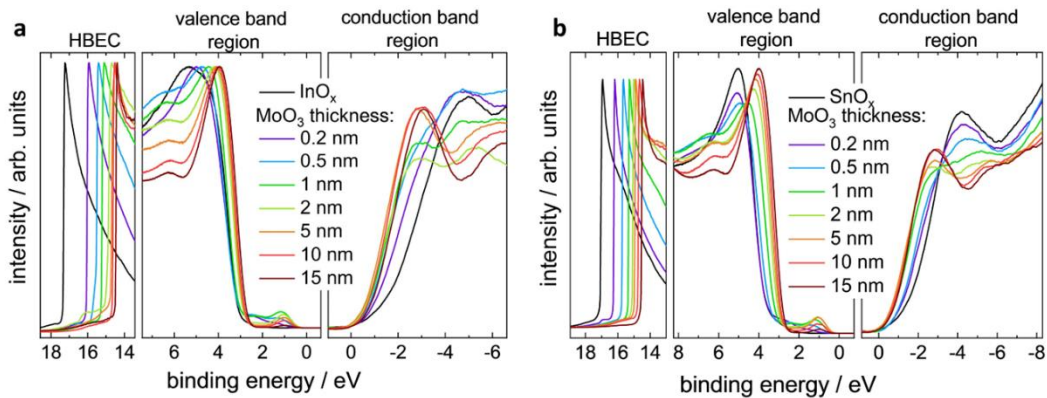
Figure 7.23: Combined UPS and IPES measurements of the interface between a, InO_x (32 cycles) and MoO_3 as well as b, SnO_x and MoO_3 . The high binding energy cutoff in the left panels shows the change in work function. For the IPES measurement only the smoothed data curves are shown. HBEC denotes the high binding energy cut-off region. Reproduced from Ref.[150].
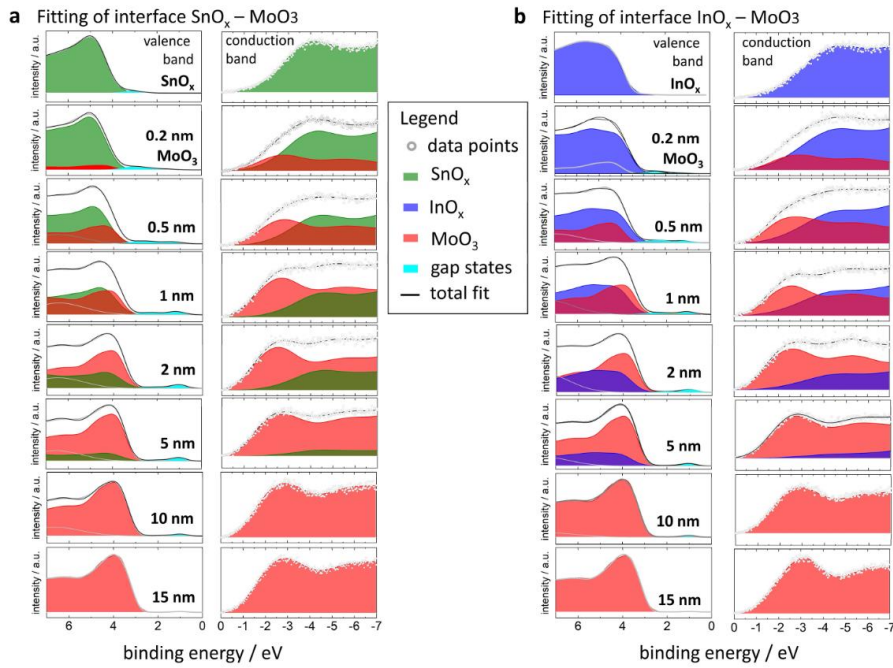
Figure 7.24: Detailed analysis of the UPS and IPES measurements (presented in **Appendix Figure 7.23**) of a, interface between SnO$_X$ and MoO$_3$ and b, InO$_X$ (32 cycles) and MoO$_3$. The individual contributions to the density of states of the three metal oxides were fitted into the UPS spectra (left panels) and IPES spectra (right panels) in order to separate the contributions to the density of states of the substrates and the MoO$_3$ overlayer. From these fits the onsets of the VB and CB are extracted which are shown in **Appendix Figure 7.25** and which are used to generate the energy level diagram (**Figure 4.4c**) in the main article. Reproduced from Ref.[150].
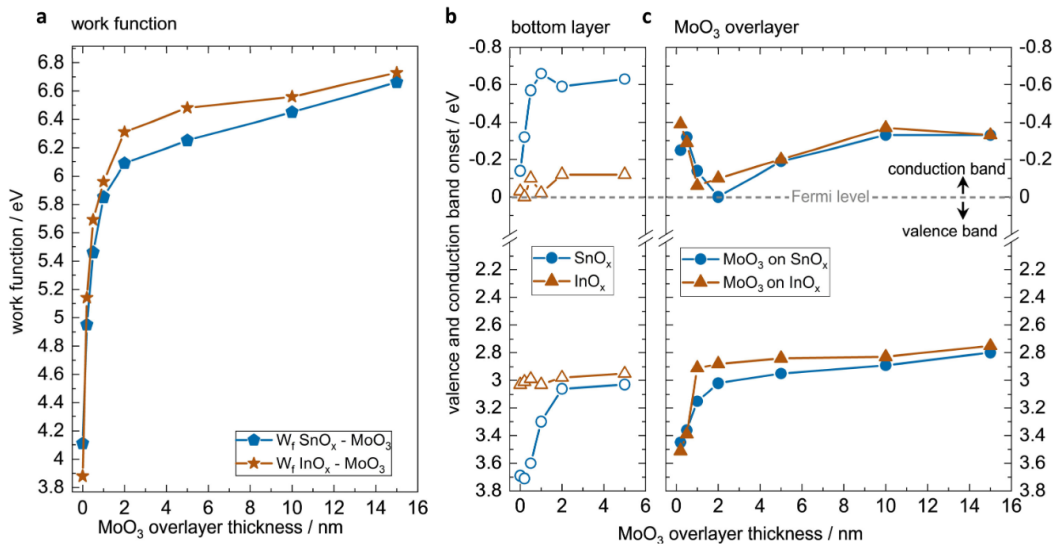
Figure 7.25: Plot summarizing the extracted energy values from **Appendix Figure 7.23 & 7.24**. The left panel shows the change in WF with increasing MoO$_3$ thickness. The right panels show changes in VB and CB onset for the underlying substrate layers (SnO$_X$ or InO$_X$) as well as the values for the MoO$_3$ overlayers on both substrates. While the upward bending of MoO$_3$ is similar in both cases, a distinct difference is found between the two

substrates, where only SnOₓ exhibits a detrimental upward bending of the VB and CB towards the interface. Reproduced from Ref.[150].
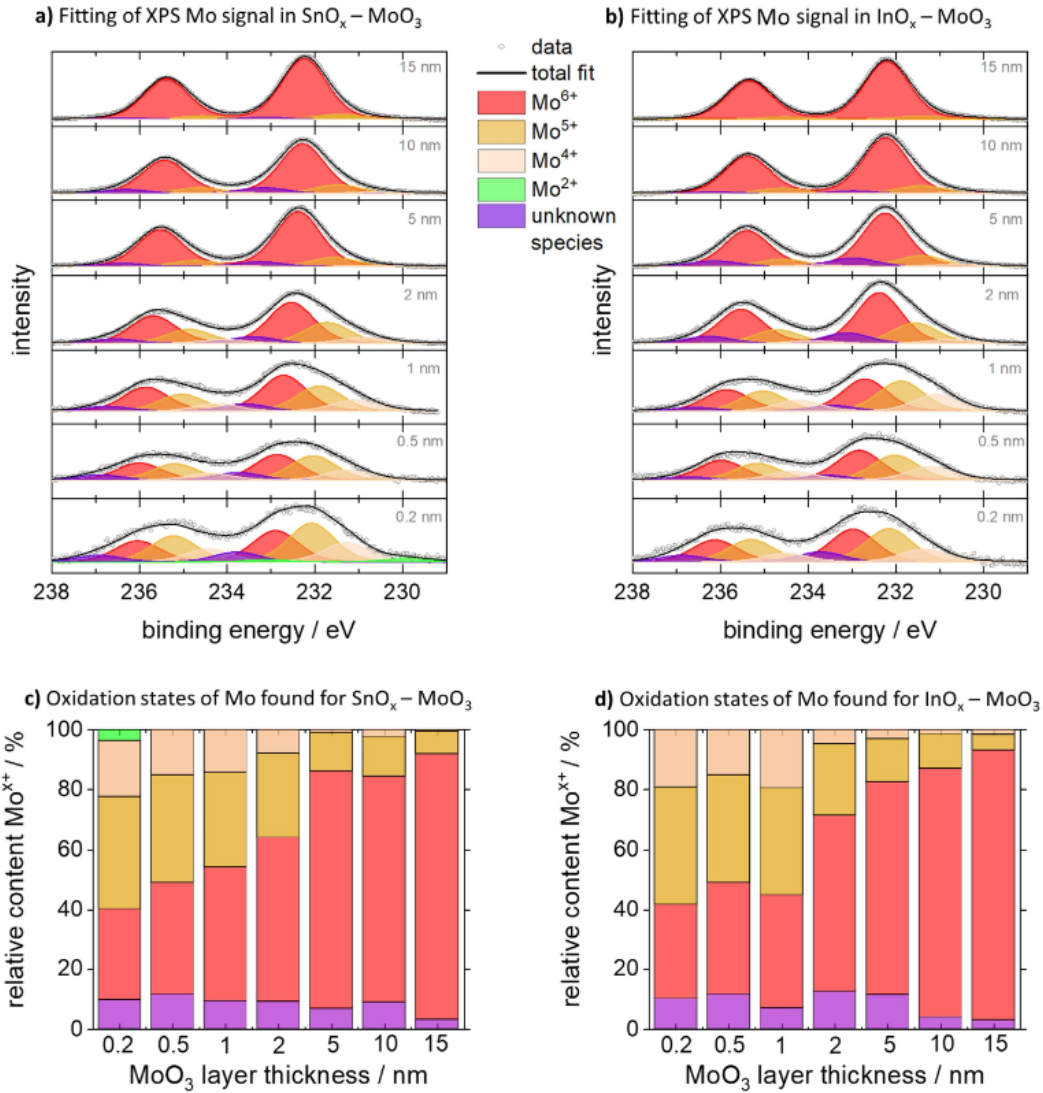
Figure 7.26: Mo core level signals of MoO₃ on a, SnOₓ and b, InOₓ fitted by Voight profiles. For thick layers of MoO₃ the predominant oxidation state is Mo⁶⁺ as expected. For thinner MoO₃ layers, i.e. closer to the interface, additional oxidation states of Mo⁵⁺, Mo⁴⁺, and Mo²⁺ occur, possibly due to an increased number of oxygen vacancies. The relative content of each species is given in subfigures c, and d, for SnOₓ and InOₓ, respectively. Surprisingly, an additional Mo feature (violet) has to be included in the fit. The presence of an Mo bond at a binding energy larger than the one of Mo⁶⁺ in MoO₃ indicates the presence of a species with stronger electron withdrawing properties (relative to Mo). Its origin is currently unclear. Since oxygen is the only element with a higher electronegativity than Mo in these samples (therefore capable of increasing the apparent core level binding energy), one can speculate on a molybdate species such as In_2MoO_4 . However, further tests are needed to identify possible reaction species; this is ongoing work and will be discussed in a separate publication. Reproduced from Ref.[150].
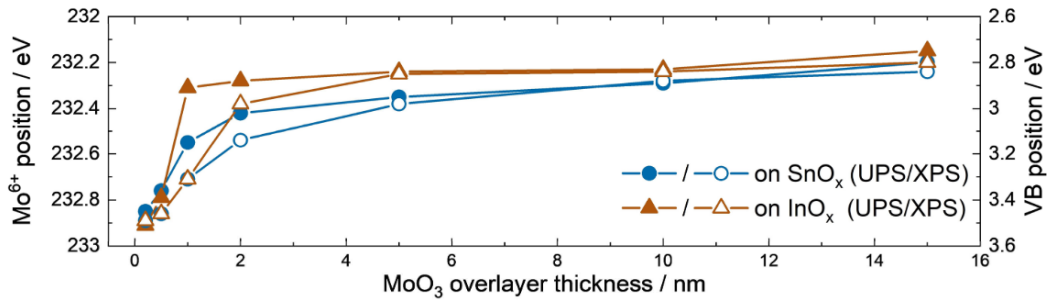
Figure 7.27: Change in energy levels of the MoO₃ layer as function of film thickness on either SnOₓ (blue) or InOₓ (brown). The filled symbols represent the change in VB onset, already presented in **Appendix Figure 7.23**. The open symbols represent the change in the Mo⁶⁺ core level signal, extracted from the fits in **Appendix Figure 7.24**. Slight differences at low coverage are likely due to differences in probing depth (~2 nm for UPS and ~10 nm for XPS), but overall the two measurements agree well and show the band bending present at this interface of the interconnecting layer. Reproduced from Ref.[150].
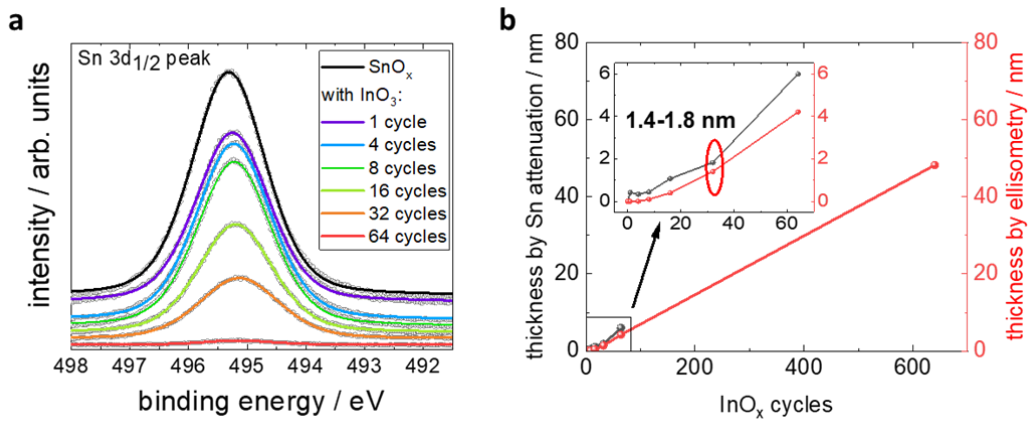
Figure 7.28: a) Sn 3d₁/₂ XPS core level signal for pure SnOₓ as well as for SnOₓ covered by an increasing number of ALD cycles of InOₓ. b) calculated layer thickness of the InOₓ overlayer, extracted from the attenuation of the Sn core level peaks (left axis) or derived by ellipsometry (right axis). The inset shows the region of interest confirming a layer thickness of 1.4-1.8 nm for 32 growth cycles. Reproduced from Ref.[150].
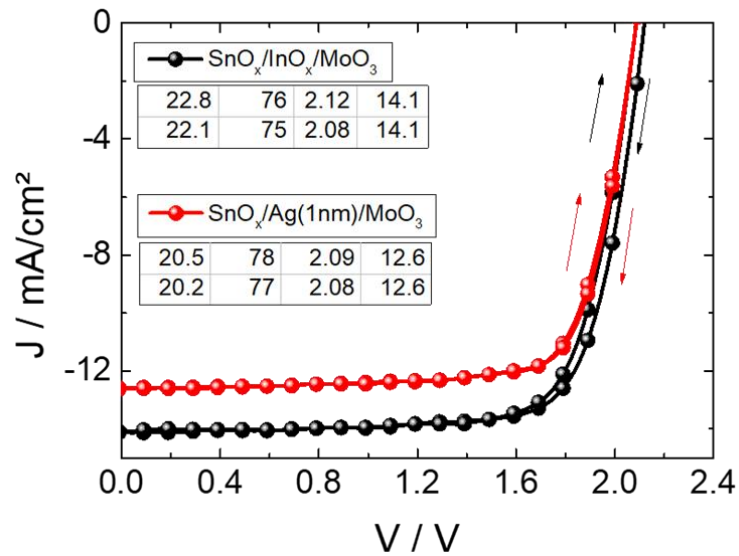
Figure 7.29: Comparison of representative J/V characteristics of perovskite/organic tandem cells employing either 1 nm of evaporated silver or ~1.5 nm InOx deposited by atomic layer deposition as interconnecting layer. No MgF2 AR coating was applied on the backside of the glass substrate, here. Reproduced from Ref.[150].
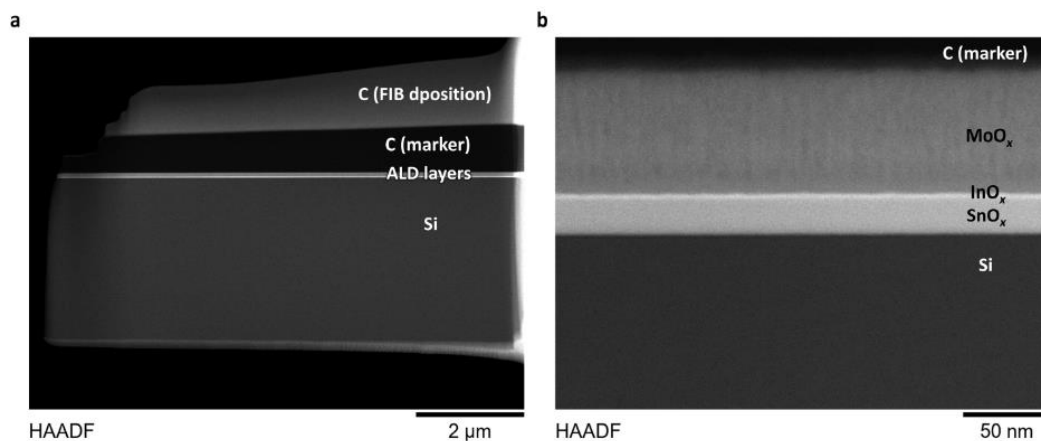
Figure 7.30: High angle annular dark field (HAADF)-STEM images of deposited SnOx / InOx / MoOx layers on a silicon substrate at a, 2 μm and b, 50 nm scales showing continuous ALD growth of both SnOx and InOx layers. Reproduced from Ref.[150].
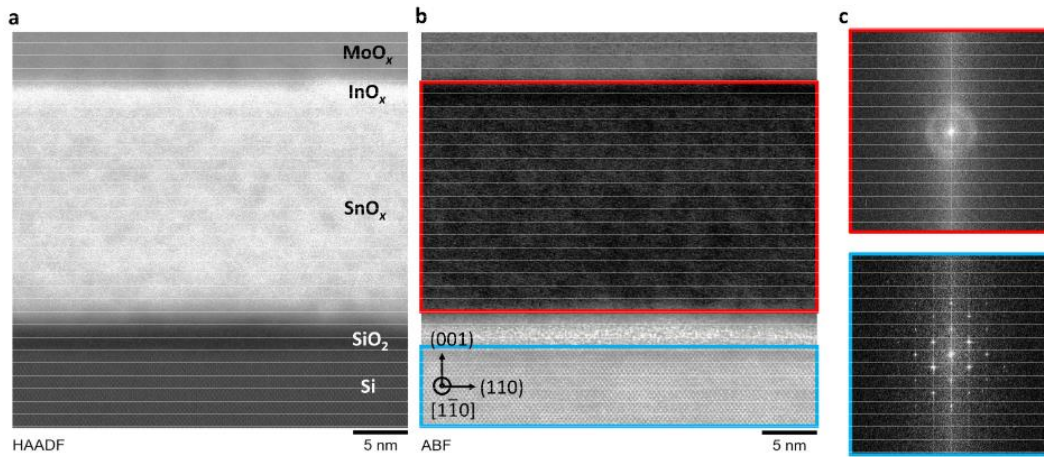
Figure 7.31: a, High angle annular dark field (HAADF) and b, annular bright field of a silicon / native oxide / SnOx / InOx / MoOx stack and c, respective fast Fourier transformed images of SnOx / InOx (top, red frame) and Si (bottom, blue frame) showing the contrast between the crystalline silicon wafer and the amorphous ALD layers covering it. Reproduced from Ref.[150].
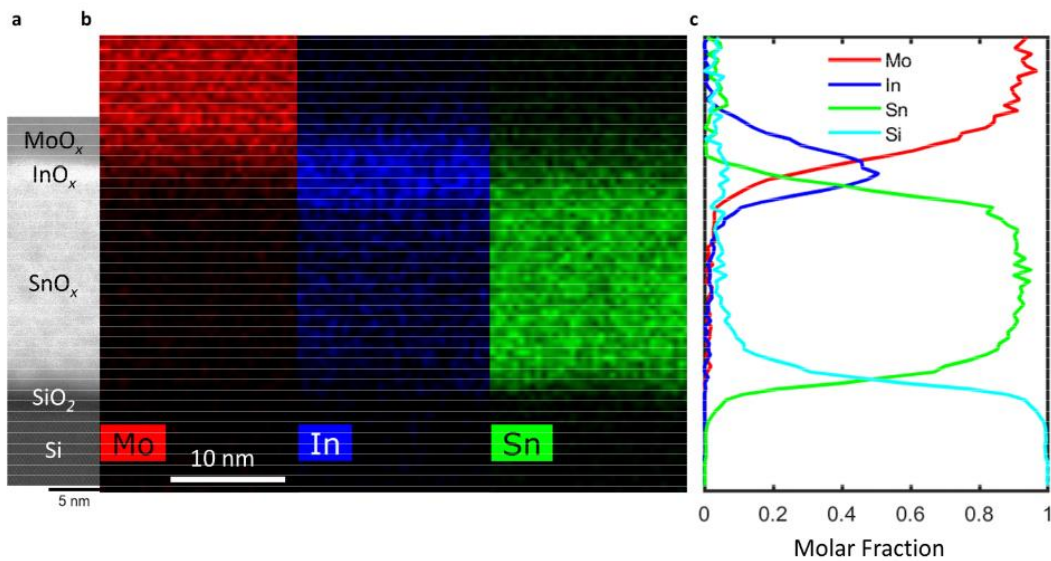
Figure 7.32: a, High angle annular dark field (HAADF) measurement of silicon / native oxide / SnOx / InOx / MoOx and b, respective EDS elemental maps. The EDS count maps of In-La and Sn-La are plotted together with Mo-La. However, as In-La (3.29 eV) are very close to Sn-La (3.44) and overlap with Sn-Ln (3.27 eV), there are spurious counts inside the SnOx layer that contribute to the In-Lα integration window. To separate the overlapping signals, multivariate statistical analysis was applied to separate EDS signals from the InOx and SnOx layers. 14, 15 The resulting line profiles of Mo, In, and Sn are plotted in c, According to these line profiles, each layer is clearly separated. The soft edges of the elemental profiles (width about 2 nm) result from roughness of the layers (~2 nm, see Appendix **Figure 7.33**) and the collection of the EDS signals from the entire 100 nm thick TEM lamella. Therefore, it is noted that the EDS data does not indicate interdiffusion of elements between the layers. Reproduced from Ref.[150].
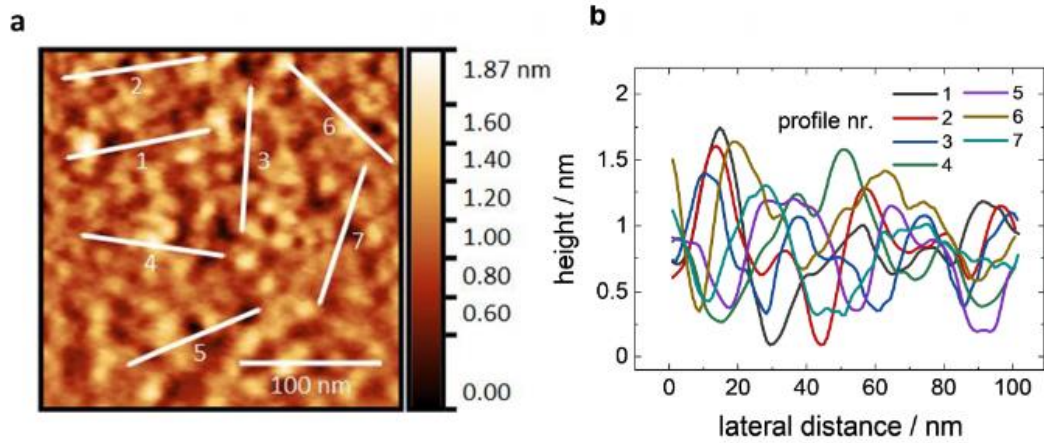
Figure 7.33: a, Topography of a 20 nm thick tin oxide layer grown by ALD on a silicon substrate. Seven 100 nm traces are marked, indicating the extracted height profiles, shown in b. Reproduced from Ref.[150].
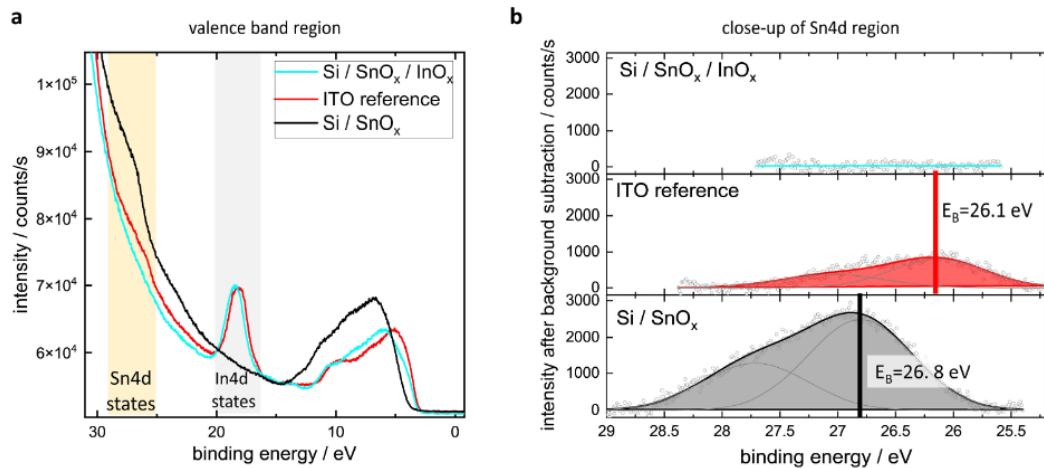
Figure 7.34: UV photoelectron spectroscopy measurements on SnO_x, SnO_x/InO_x, as well as an ITO reference layer using He II excitation at 40.81 eV. a, Valence band region of the three samples, showing semi-core signals of Sn4d and In4d. b, Close-up of the Sn4d region, after a linear background subtraction has been performed. The data is fitted by two peaks corresponding to the Sn4d$_{5/2}$ and Sn4d$_{3/2}$ doublet. In contrast to the ITO and the SnOx layers, for the InO_x (32 cycles; thickness of 1.5 nm) on top of SnO_x no signal of the Sn4d semi-core levels could be detected. With an estimated sampling depth of about 1 nm, this result indicates that, if mixing between the InO_x and the SnO_x layers were to occur, it would be limited to the first 5 Angstroms of the InO_x layer adjacent to the SnO_x. Reproduced from Ref.[150].
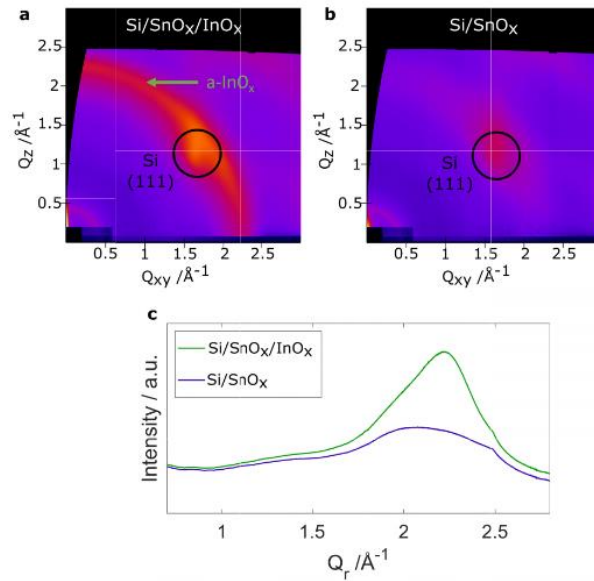
Figure 7.35: Bulk GIWAXS measuremnets of a), 20 nm InO$_x$ on top of 20 nm SnO$_x$ and b), only 20 nm SnO$_x$ on top of a silicon substrate (incidence angle 0.3°, probing depth > 500 nm). With the probing depth exceeding the deposited layer thickness, some reflection due to the [111] planes of the Si substrate can also be seen (marked by a circle). c), Radial profiles of the data shown in a) and b). Reproduced from Ref.[150].
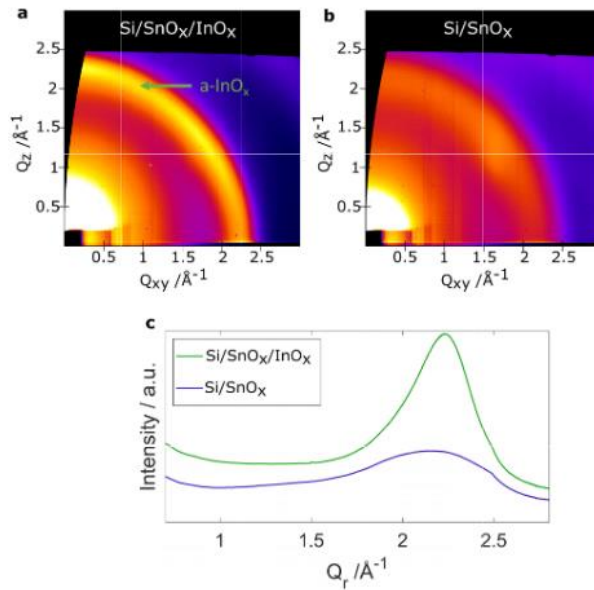
Figure 7.36: Surface GIWAXS measurements of a), 20 nm InO$_x$ on top of 20 nm SnO$_x$ and b), only 20nm SnO$_x$ on top of a silicon substrate (incidence angle 0.12° probing depth about 2 nm) as well as c), respective radial profiles. Reproduced from Ref.[150].
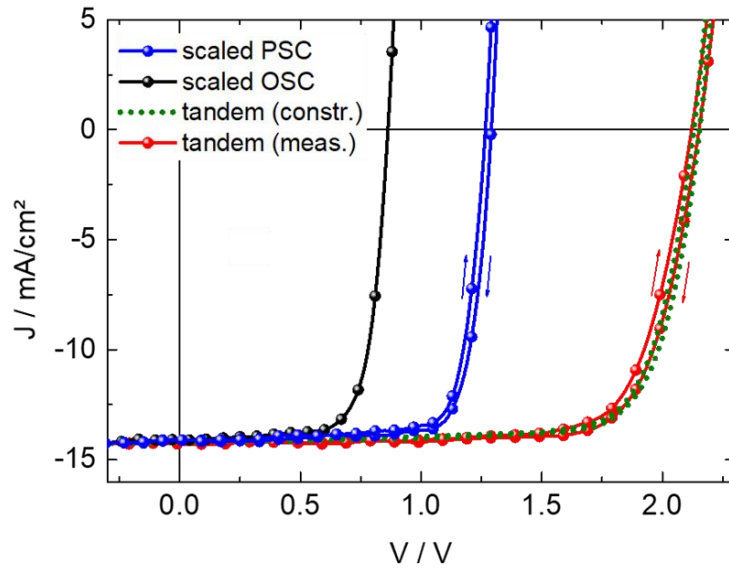
Figure 7.37: Construction of the theoretical J/V curves of the tandem device from the serial connection of both sub-cells. To emulate the J/V characteristics of the sub-cells, the measured J/V characteristics of representative single junction devices have been scaled to generate the respective short circuit current density that was derived from EQE results of the sub-cells in the tandem device. Reproduced from Ref.[150].
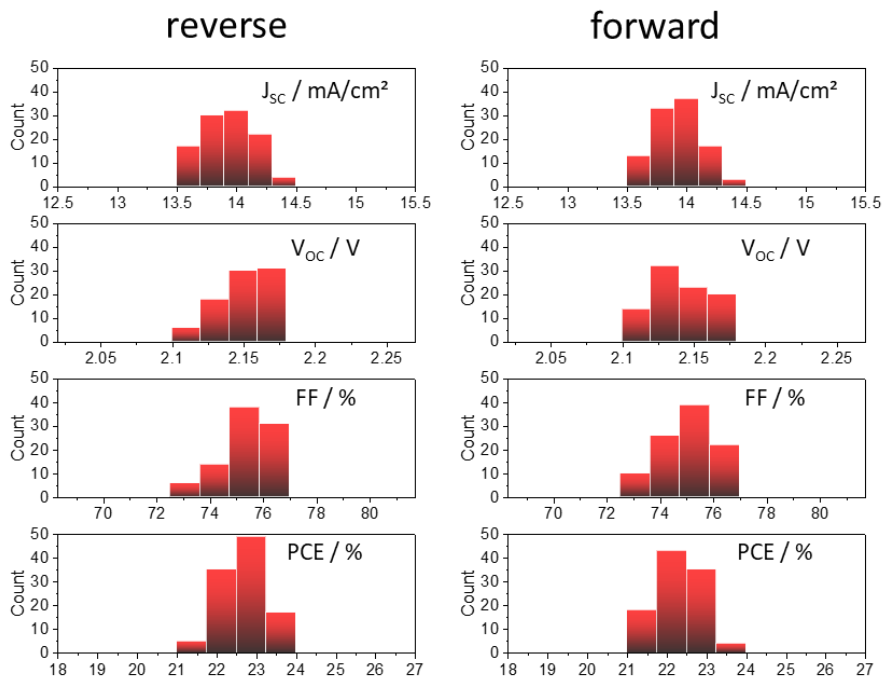
Figure 7.38: Statistics (binned) of 106 perovskite/organic tandem solar cells with InOx interconnect. Reproduced from Ref.[150].
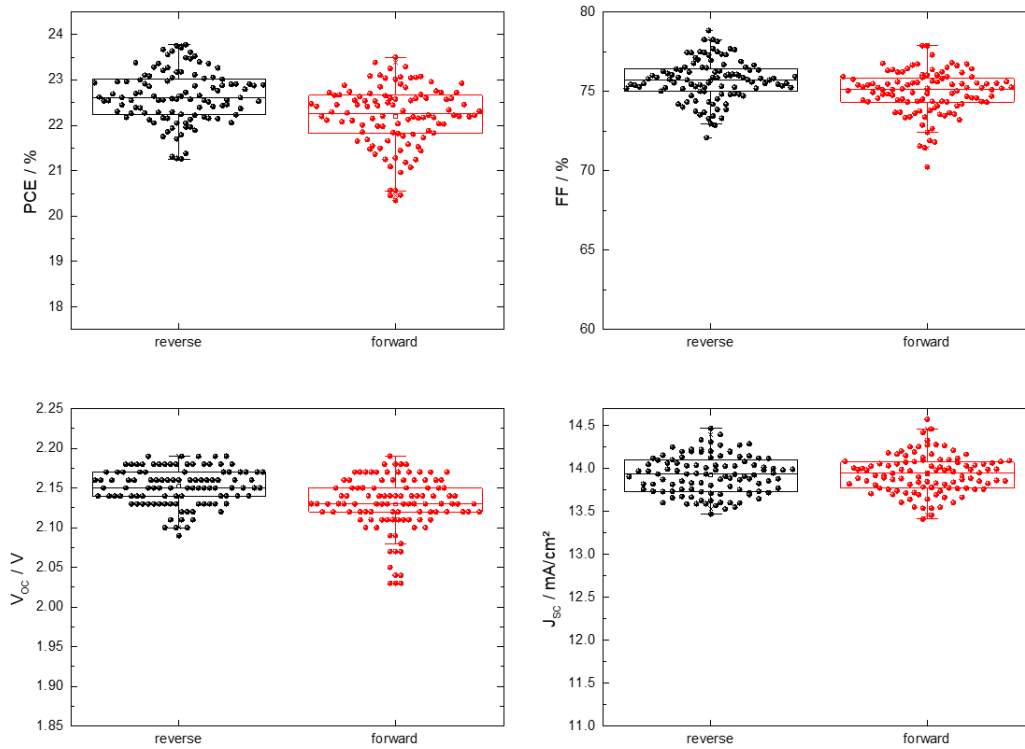
Figure 7.39: Statistics (box plot, 25% - 75% with mean line and data overlay) of 106 perovskite/organic tandem solar cells with InO$_x$ interconnect. Reproduced from Ref.[150].

7.2.3 Certification Details

Stress Due to the Certification Process of the Tandem Solar Cell

The certification procedure involves the measurement of the external quantum efficiency prior to J-V certification. This EQE measurement procedure, which is done in ambient air, takes about 1 hour and inflicts some severe asymmetric stressing of each sub-cell due to the necessary monochromatic light biasing.[233] These EQE measurement conditions infer some degradation of the cell, that would not occur under "normal" operation of the cell under AM 1.5 solar illumination. This is clearly visible if one compares the integrated current values derived from the certified EQE measurement (≥ 14 mA/cm² for both sub-cells, **Appendix Figure 7.40a**

& Appendix Paragraph 7.2.4) with the value of 13.2 mA/cm² resulting from a J/V measurement thereafter (**Appendix Figure 7.40b**). Nevertheless, the Fraunhofer ISE CalLab certified an efficiency of 23.1 % for this stressed cell (**Appendix Paragraph 7.2.5**) and confirmed 23.7 % for a sister cell, that had not undergone the stressing in a prior EQE measurement. In this case the spectral illumination characteristics calibrated for the certified sister cell were used. The latter efficiency is identical to what has been measured for the same cell prior to shipping the cell to the Fraunhofer ISE CalLab (**Appendix Figure 7.41**). As such, the validity of our measurement can be confirmed. The respective value is labeled as "confirmed" in the main text of **Chapter 4**.
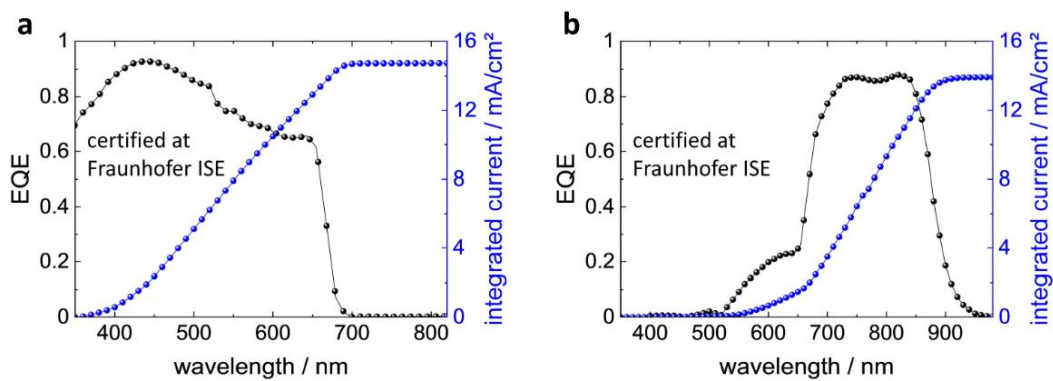
Figure 7.40: Certified EQE spectra measured at the ISE Fraunhofer CalLab (also see **Appendix Paragraph 7.2.4**) as well as derived integrated current values of a, the perovskite and b, the organic sub-cell. Reproduced from Ref.[150].
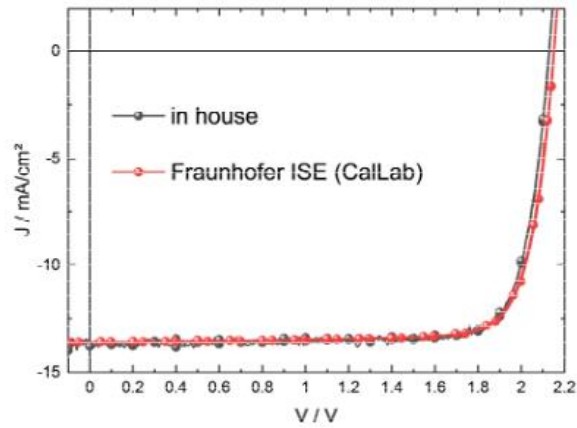
		PCE [%]	FF [%]	V_{oc} [V]	J_{sc} [mA/cm²]
in house	reverse	23.8	81	2.13	13.7
	forward	23.7	81	2.13	13.8
Fraunhofer ISE CalLab	reverse	23.8	81	2.15	13.6
	forward	23.6	81	2.15	13.6

Figure 7.41: Direct comparison of the same tandem cell measured first in our own lab (in house) and then at Fraunhofer ISE CalLab without stress due to a prior EQE measurement (see above) using the light source calibration obtained from the certified cell shown in **Appendix Paragraphs 7.2.4 & 7.2.5**. Reproduced from Ref.[150].

7.2.4 Official Certification Documents I

Fraunhofer ISE CalLab PV Cells

Heidenhofstr.2

79110 Freiburg

Werkskalibrierschein
Proprietary calibration report

10004087UWW0620

Gegenstand *Object*	**multi-junction solar cell**
Hersteller *Manufacturer*	**Uni Wuppertal**
Typ *Type*	**PSC/OSC**
Fabrikat/Serien-Nr. *Serial number*	**UWW004 / 4b**
Auftraggeber *Customer*	**Bergische Universität Wuppertal** **Rainer-Gruenter-Str. 21** **42119 Wuppertal** **Deutschland**
Auftragsnummer *Order No.*	**087UWW0620**
Anzahl der Seiten *Number of pages*	**6**
Datum der Kalibrierung *Date of calibration*	**09.07.2021**

Kalibrierscheine ohne Unterschrift haben keine Gültigkeit. *Calibration certificates without signature are not valid.*

Datum *Date*	Leiter des Kalibrierlaboratoriums *Head of the calibration laboratory*	Bearbeiter *Person in charge*
13.07.2021	*Jochen Hohl-Ebinger*	*Astrid Semeraro*

Fraunhofer
ISE

CalLab
PV Cells

1. Beschreibung des Kalibriergegenstandes

Description of the calibrated object
Das Messobjekt ist eine multi-junction solar cell. Typ: OSC/PSC
The device under test is a OSC/PSC multi-junction solar cell .

2. Messverfahren

Measurement procedure

Die Kalibrierung des Kalibrierobjektes wird gemäß /1/ mit einem Zweilampen-DC-Sonnensimulator durchgeführt. Die Einstrahlung wird mit Hilfe einer Monitorzelle während der gesamten Messdauer aufgenommen und deren Schwankungen bezüglich der Messung korrigiert. Die Divergenz der Randstrahlen ist < 5°. Die Solarzelle wird auf einem Vakuumprobentisch thermisch stabilisiert.
The calibration of the test sample was performed at Standard Testing Conditions (STC) with a dual light steady-state solar simulator according to /1/. The irradiance is controlled with a monitor cell during the measurement in order to correct fluctuations. The divergence of the peripheral beams is < 5°. The solar cell is kept at a constant temperature

Rückführung der Referenzsolarzellen/*Traceability of the reference solar cells* :

Identitäts-Nr. / Identity-Nr. :	Kalibrierschein-Nr./ Certificate-Nr. :	Rückführung/ Traceability :
020010	47057-PTB-20	PTB
011-2012	47045-PTB-20	PTB

Die Korrektur der spektralen Fehlanpassung (Mismatch), die durch die Abweichung der spektralen Verteilung des Sonnen Simulators vom Standard-Spektrum AM1.5G /3/ in Kombination mit den verschiedenen spektralen Empfindlichkeiten von Referenzzelle und Messobjekt entsteht /4/, wurde durch eine erweiterte Mismatchberechnung /4/ - wie in /2/ beschrieben - korrigiert.
Dazu wurde die spektrale Verteilung der Bestrahlung (Sonnensimulator) mit einem Spektralradiometer und die spektrale Empfindlichkeit des Messobjektes mit einem laserbasierten Messplatz /5/ gemessen (s. Kalibrierschein Nr: 9004087UWW0620).
The spectral mismatch - caused by the deviation of the simulator spectrum from the standard spectrum AM1.5G /3/ in combination with the difference between the spectral response of the reference cell and that of the device under test (DUT) – is calculated by a generalized mismatch correction /3/ as described in /2/.
For the spectral mismatch correction the spectral distribution of the solar simulator is measured with a spectroradiometer, the spectral response of the DUT is measured with a laser-based setup according to /5/ (cf. Calibration Mark: 9004087UWW0620).

Der P_{MPP} wurde durch MPP-Tracking über 300s bestimmt. Der angegebene P_{MPP} ist der Mittelwert von 57-356s dieser stabilisierten Messung. Anschließend wurde die IV-Kennlinie in zwei Richtungen (V_{OC} -> I_{SC} und I_{SC} -> V_{OC}) aufgenommen.
The P_{MPP} was determined by MPP-Tracking for 300s. The reported P_{MPP} represents the average value of the range 57-356s of this stabilized measurement. Afterwards, the IV-curve was determined with a scan in both directions (V_{OC} -> I_{SC} and I_{SC} -> V_{OC}).

Fraunhofer
ISE

CalLab
PV Cells

10004087UWW0620

Die Rückführung der Spektralmessung auf SI-Einheiten erfolgte über den Vergleich mit einer Standardlampe.
The traceability of the measurement of the spectral distribution to SI-Units is achieved using a standard lamp for the calibration of the spectroradiometer.

Identitäts-Nr. / *Identity-Nr. :*	Kalibrierschein-Nr./ *Certificate-Nr. :*	Rückführung/ *Traceability :*
BN-9101-451	40006-20-PTB	PTB

3. Messbedingungen
Measurement conditions

Standardtestbedingungen (STC) / *Standard Testing Conditions (STC)* :

Absolute Bestrahlungsstärke /
Total irradiance : 1000 W/m^2

Temperatur des Messobjektes /
Temperature of the DUT : 25 °C

Spektrale Bestrahlungsstärke /
Spectral irradiance distribution : AM1.5G Ed.4 (2019)

Die Messung der IV-Kennlinie (Strom-Spannungs-Kennlinie) des Messobjektes erfolgt mit Hilfe eines Vierquadranten-Netzteiles und eines Kalibrierwiderstandes.
The measurement of the IV-curve is performed with a 4-quadrant power amplifier and a calibration resistor.

4. Messergebnis
Measurement results

Fläche / *Area* (da)[1]: = (0.0174 ± 0.0011) cm^2
[1] *: (t) = total area, (ap) = aperture area, (da) = designated illumination area /7/*

Kennlinienparameter des Messobjektes unter Standardtestbedingungen (STC) / *IV-curve parameter under Standard Testing Conditions (STC)* :

		Vorwärtsrichtung / *forwards scan direction*			Rückwärtsrichtung / *reverse scan direction*			steady state MPP		
V_{oc}	=	(2160 ±	22) mV	(2163 ±	22) mV					
I_{SC} (Ed.2 - 2008)	=	(0.2301 ±	0.0048) mA	(0.2304 ±	0.0048) mA					
I_{MPP}	=	0.21	mA	0.22	mA		(0.2157 ±	0.0063) mA		
V_{MPP}	=	1867.2	mV	1877.8	mV		(1871 ±	37) mV		
P_{MPP}	=	0.401	mW	0.405	mW		(0.403 ±	0.012) mW		
FF	=	80.64	%	81.25	%					
η	=						(23.1 ±	1.6) %		

Fraunhofer
ISE

CalLab
PV Cells

10004087UWW0620

Angegeben ist jeweils die erweiterte Messunsicherheit, die sich aus der Standardmessunsicherheit durch Multiplikation mit dem Faktor *k*=2 ergibt. Sie wurde gemäß dem "Guide to the expression of Uncertainty in Measurement" ermittelt. Sie entspricht bei einer Normalverteilung der Abweichungen vom Messwert einer Überdeckungswahrscheinlichkeit von 95%.

The expanded measurement uncertainty resulting from the standard measurement uncertainty multiplied with a factor k=2 is specified. The calculation was carried out according to the "Guide to the expression of Uncertainty in Measurement". The value corresponds to a Gaussian distribution denoting the deviations of the measurement value within a probability of 95%.

5. Zusatzinformationen

Additional information

Fraunhofer
ISE

CalLab
PV Cells

10004087UWW0620

Steady State Pmpp

Fraunhofer
ISE

CalLab
PV Cells
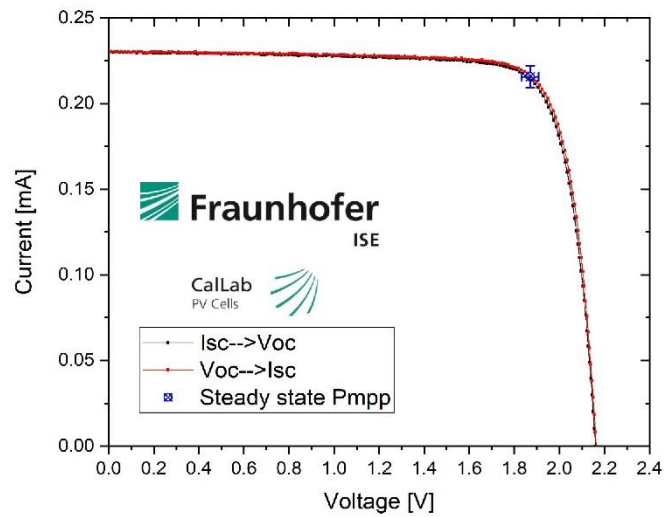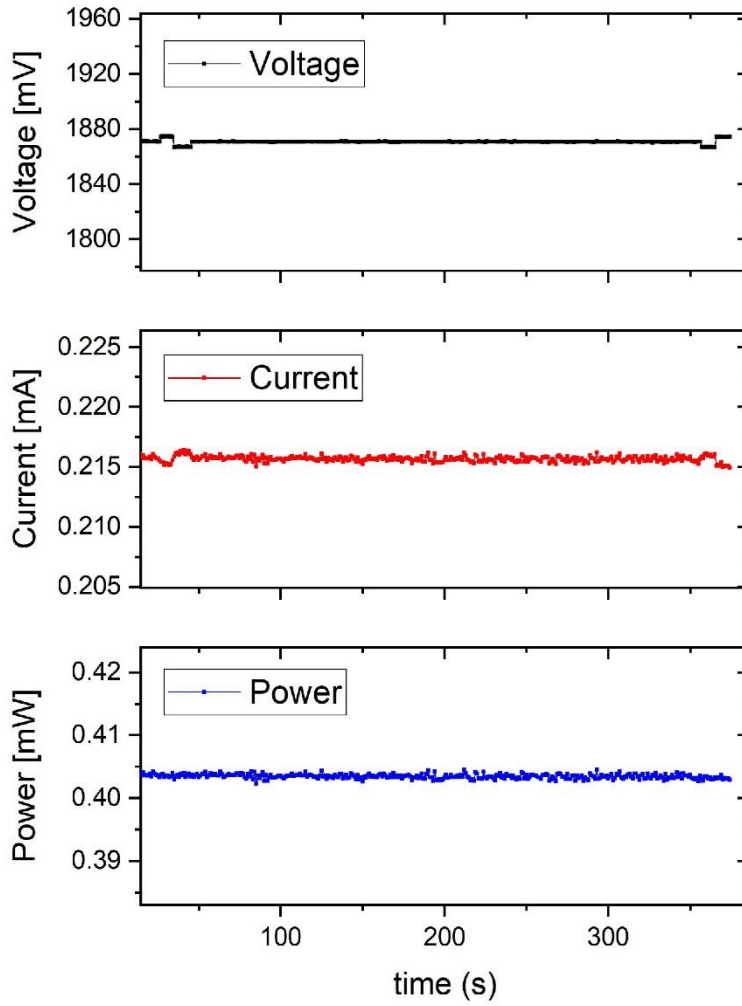
6.Literatur
Literature

/1/ IEC 60904-1-Ed.3:2020, *Photovoltaic devices - Part 1: Measurement of photovoltaic current-voltage characteristics*

/2/ M. Meusel, R. Adelhelm, F. Dimroth, A.W. Bett, W. Warta Spectral Mismatch Correction and Spectrometric Characterization of Monolithic III–V Multi-junction Solar Cells Prog. Photovolt: Res. Appl. 10 (2002) p. 243–255

/3/ IEC 60904-3-Ed.4:2019, *Photovoltaic devices - Part 3: Measurement principles for terrestrial photovoltaic (PV) solar devices with reference spectral irradiance data*

/4/ IEC 60904-7-Ed.4:2019, *Photovoltaic devices - Part 7: Computation of the spectral mismatch error introduced in the testing of a photovoltaic device*

/5/ IEC 60904-8-Ed.3:2014, *Photovoltaic devices - Part 8: Measurement of the spectral responsivity of a photovoltaic (PV) device*

/6/ IEC 60904-9-Ed.3:2020, *Photovoltaic devices - Part 9: Solar simulator performance requirements*

/7/ M.A. Green, K. Emery, Y. Hishikawa, W. Warta, and E. D. Dunlop, *Solar cell efficiency tables (version 39)*. Progress in Photovoltaics: Research and Applications, 2012. 20: p. 12-20.

Ende des Kalibrierscheins / End of certificate

7.2.5 Official Certification Documents II

Fraunhofer ISE CalLab PV Cells

Heidenhofstr.2

79110 Freiburg

Messbericht
Measurement report

9004087UWW0620

Gegenstand *Object*	**multi-junction solar cell**
Hersteller *Manufacturer*	**Uni Wuppertal**
Typ *Type*	**PSC/OSC**
Fabrikat/Serien-Nr. *Serial number*	**UWW004 / 4b**
Auftraggeber *Customer*	**Bergische Universität Wuppertal** **Rainer-Gruenter-Str. 21** **42119 Wuppertal** **Deutschland**
Auftragsnummer *Order No.*	**087UWW0620**
Anzahl der Seiten *Number of pages*	**8**
Datum der Messung *Date of measurement*	**08.07.2021**

Kalibrierscheine ohne Unterschrift haben keine Gültigkeit. *Calibration certificates without signature are not valid.*

Datum *Date*	Leiter des Kalibrierlaboratoriums *Head of the calibration laboratory*	Bearbeiter *Person in charge*
13.07.2021	*Jochen Hohl-Ebinger*	*Astrid Semeraro*

Fraunhofer
ISE

CalLab
PV Cells

9004087UWW0620

1. Beschreibung des Messgegenstandes
Description of the measurement object

Das Messobjekt ist eine Solarzelle, Typ: PSC/OSC. Die Stabilität der Solarzelle wurde nicht untersucht.
The device under test is a PSC/OSC solar cell. The temporal stability of the solar cell performance was not controlled.

2. Messverfahren
Measurement procedure

Bestimmt wird der Wert der absoluten differentiellen spektralen Bestrahlungsstärkeempfindlichkeit im Wellenlängenbereich ca. 300-1200 nm bei dem angegebenen Kurzschlussstrom. Die Kalibrierung der Solarzelle wurde mit einem Lasermonochromator mit dem DSR-Messverfahren /1/ und entsprechend /2/ durchgeführt. Die Messung wird im Zweistrahlverfahren durchgeführt und verwendet gleichzeitig:
a) eine stationäre Biasbestrahlung mit Bestrahlungsstärken E_B, welche jedoch nicht explizit gemessen werden. Ihre Variation erlaubt unterschiedliche Kurzschlussströme I_{SC} (E_B), sowie
b) eine zeitlich modulierte, quasi-monochromatische Messstrahlung. Ihre Bestrahlungsstärke wird bestimmt mit einer primarkalibrierten Referenzsolarzelle (rückgeführt: PTB).
The absolute differential spectral responsivity is determined in a wavelength range from 300 nm to 1200 nm at a short circuit current bias.eee The measurement is done with laser-monoochromator setup with the DSR method according to /1/ and /2/ in a two-beam geometry, using the two irradiation beams simultaneously:
a) A stationary bias irradiation with irradiances E_B (not measured explicitly).
The variation of E_B allows different short circuit currents I_{SC} (E_B).
b) A time-modulated quasi-monochromatic measurement irradiation. The irradiance is determined by a primary calibrated reference solar cell (PTB).

Rückführung der Referenzsolarzelle/*Traceability of the reference solar cell* :

Identitäts-Nr. / *Identity-Nr.* :	Kalibrierschein-Nr./ *Certificate-Nr.* :	Rückführung/ *Traceability* :
020059	47033-PTB-21	PTB

161

Fraunhofer
ISE

CalLab
PV Cells

9004087UWW0620

3. Messbedingungen

Measurement conditions

Der Arbeitspunkt der Solarzelle wird durch den Bias-Strom im I_{SC} definiert.

The operating point of the solar cell is defined by a bias current under short circuit conditions.

	top cell	bot cell
Bias Strom/*Bias current* :	0 mA	0 mA
Bias Spannung/Bias voltage:	611.54 mV	702.36 mV
Nominalwert der Temperatur des Messobjekts/		
Nominal Value of the temperature of the object:	25 °C	25 °C

Die Klemmenspannung der Solarzelle wird durch einen Strom-Spannungswandler auf unter 0,03 V_{OC} geregelt. Die Frequenz des getakteten quasimonochromatischen Messlichtes lag bei 133 Hz. Die spektrale Bandbreite (Halbwertsbreite) liegt unter 5 nm. Die Temperatur der Solarzelle wird mit einem Tastsensor ermittelt und auf (25±0,5)°C eingestellt.

The voltage at the solar cell is set to below 0.03 V_{OC} by a current-voltage-converter. The frequency of the chopped quasi-monochromtatic measurement light is at 133 Hz. The spectral bandwith (full width at half maximum) is below 5 nm. The temperature of the solar cell is determined by a sensor and adjusted to (25±0.5)°C.

Fraunhofer
ISE

CalLab
PV Cells

9004087UWW0620

4. Messergebnis
Measurement results

top cell

Wellenlänge Wavelength / nm	$*\eta_{ext}$ /	s / mA*W^{-1}*m^2
310.0	0.0392	0.00002
320.0	0.478	0.00022
350.0	0.699	0.000344
360.0	0.743	0.0003759
370.0	0.771	0.0004009
380.0	0.805	0.0004299
390.0	0.849	0.00046565
400.0	0.877	0.0004934
410.0	0.899	0.00051804
420.0	0.917	0.0005414
430.0	0.926	0.0005598
440.0	0.927	0.0005731
450.0	0.927	0.0005865
460.0	0.917	0.0005933
470.0	0.904	0.0005973
480.0	0.893	0.0006024
490.0	0.875	0.0006025
500.0	0.857	0.0006026
510.0	0.845	0.0006062
520.0	0.837	0.0006120
529.4	0.775	0.000577
540.7	0.746	0.000567
551.2	0.747	0.0005788
561.0	0.722	0.0005695
572.2	0.699	0.0005627
580.4	0.694	0.0005661
592.1	0.687	0.0005721
602.4	0.667	0.0005653
612.2	0.654	0.0005630
621.5	0.649	0.0005674
633.4	0.651	0.0005794
642.8	0.656	0.0005931
654.6	0.616	0.0005669
668.0	0.325	0.0003052
679.5	0.0693	0.0000662
690.0	0.0166	0.0000161
696.3	0.00626	0.0000061
700.0	0.000403	0.0000004
710.0	0.00252	0.0000025
740.0	0.00175	0.0000018
780.0	0.00218	0.0000024
820.0	0.00340	0.00000392
860.0	0.00280	0.0000034

Fraunhofer
ISE

CalLab
PV Cells

bottom cell

Wellenlänge *Wavelength* / nm	$*\eta_{ext}$ /	s / mA*W^{-1}*m²
400.0	0.00477	0.0000027
420.0	0.00653	0.00000385
440.0	0.00521	0.00000321
460.0	0.000559	0.00000036
480.0	0.00910	0.0000061
500.0	0.0204	0.0000143
520.0	0.00794	0.0000058
561.0	0.123	0.0000969
580.4	0.163	0.0001324
602.4	0.202	0.0001707
612.2	0.211	0.0001816
621.5	0.224	0.0001951
633.4	0.229	0.0002034
643.9	0.231	0.0002091
654.6	0.259	0.0002380
667.8	0.485	0.0004541
679.5	0.659	0.0006289
690.0	0.729	0.0007055
694.6	0.741	0.0007228
700.0	0.774	0.0007607
710.0	0.811	0.0008085
720.0	0.840	0.0008493
730.0	0.865	0.0008857
740.0	0.869	0.0009030
750.0	0.871	0.0009170
760.0	0.867	0.0009246
770.0	0.861	0.0009304
780.0	0.857	0.0009386
790.0	0.859	0.0009520
800.0	0.864	0.0009702
810.0	0.873	0.0009926
820.0	0.880	0.0010124
830.0	0.875	0.0010189
840.0	0.863	0.0010171
850.0	0.810	0.0009665
860.0	0.716	0.0008641
870.0	0.589	0.0007195
880.0	0.444	0.0005482
890.0	0.306	0.0003825
900.0	0.200	0.0002523
910.0	0.123	0.0001574
920.0	0.0735	0.0000949
930.0	0.0442	0.0000577
940.0	0.0281	0.0000371
950.0	0.0112	0.0000150
960.0	0.00750	0.0000101
970.0	0.00303	0.0000041
980.0	0.00320	0.0000044

Fraunhofer
ISE

CalLab
PV Cells

9004087UWW0620

bottom cell

Wellenlänge Wavelength / nm	*η_{ext} /	s / mA*W^{-1}*m^2
980.0	0.00320	0.0000044

*Spektrale Bestrahlungsstärkeempfindlichkeit und externe Quanteneffizienz stehen in folgendem Zusammenhang /
Spectral responsivity and External Quantum Efficiency are related as follows:

$$\eta_{ext}(\lambda) = \frac{J(\lambda)/q}{E(\lambda)/h\nu} = \frac{h\nu}{q}\frac{J(\lambda)}{E(\lambda)} = \frac{hc}{nq\lambda}\frac{s(\lambda)}{a} = 1239{,}8\frac{nm\cdot W}{A}\frac{s(\lambda)}{n\lambda a}$$

c: Vakuumlichtgeschwindigkeit/ *speed of light in a vacuum*
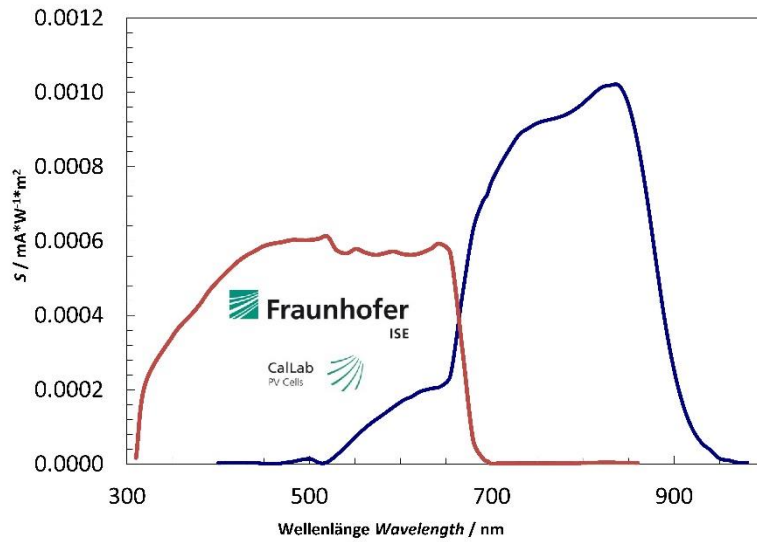h: Planck'sches Wirkungsquantum/ *Planck constant*
q: Elementarladung/ *elementary charge*
n: Brechungsindex Luft/ *refraction index*
$\eta_{ext}(\lambda)$: externe Quanteneffizienz/ *external quantum efficiency*
s(λ): spektrale Bestrahlungsstärkeempfindlichkeit/ *spectral responsivity*
a: Fläche/ *area*

Fraunhofer
ISE

CalLab
PV Cells

9004087UWW0620

6. Literatur

Literature

/1/ J. Metzdorf, Calibration of Solar Cells. 1: *The Differential Spectral Responsivity Method*, Applied Optics 26 (1987) p.1701-1708

/2/ IEC 60904-8-Ed.3:2014, *Photovoltaic devices - Part 8: Measurement of the spectral responsivity of a photovoltaic (PV) device*

7.3 Supplementary Information: Chapter 5

7.3.1 Experimental Details

Materials Synthesis and Device Preparation

SnO_x, ZnO, and Al:ZnO interlayers were deposited by ALD in a Beneq TFS 200 ALD reactor (substrate temperature 80, 100 or 150 °C as noted in the text). As precursors for SnO_x, tetrakis(dimethylamino)tin(IV) (TDMASn), kept at 45 °C, and water, kept at room temperature, were used as reported earlier.[48] ZnO was deposited from diethyl zinc and water. The Al:ZnO layers were prepared as a nano-laminate consisting of a repeated deposition of 50 cycles ZnO and 2 cycles Al_2O_3, as reported previously.[234]

For solution-processed ZnO-based layers, NP dispersions of ZnO (2.8% w/v in acetone from InfinityPV), Al:ZnO, and Ga:ZnO (both 2.5 wt% in isopropanol, Prod. No. 8045 and 8072, respectively, Nanograde AG, Switzerland) were used. Before spin coating in ambient air, all dispersions were ultra-sonicated for 5 min. The typical layer thickness was 30–35 nm.

Sol-gel SnO_x was prepared from a precursor solution of TDMASn in 2-isopropoxyethanol (vol. ratio: 1:58). Spin coating and subsequent hydrolysis and condensation in ambient air (for 1 h at room temperature) resulted in layers of 10–20 m thickness. The layers were afterward annealed at 120 °C for 1 h.

The inverted polymer-fullerene OSCs studied in **Chapter 5.1** were based on the following layer sequence: glass/ITO/EEL/photoactive layer/MoO_3/Ag (see **Figure 5.1a**) with an active area of 0.03 cm^2. As polymer:fullerene blend, poly[N-9′-heptadecanyl-2,7-carbazole-alt-5,5- (4′,7′-di-2-thienyl-2′,1′,3′-benzothiadiazole)] (PCDTBT) (supplied by 1-material) and fullerene $PC_{70}BM$ (SES Research) with a weight ratio of 1:4 were used. The polymer

was dissolved in chlorobenzene and stirred in N_2 atmosphere at 80 °C for 2.5 h followed by adding the fullerene (stirring for 1.5 h). The still warm solution (70 °C) was filtered (5 µm PTFE Filter) and spin coated at 2100 rpm for 40 s (layers thickness ≈ 60 nm) in N_2 atmosphere. On the anode side, MoO_3 (25 nm) and Ag (100 nm) layers were thermally evaporated in high vacuum (10^{-7} mbar).

For inverted OSCs comprising fullerene-free active layers analyzed in **Chapter 5.2**, the same layer sequence was used with slightly thinner evaporated top contact of MoO_3 (10 nm) and Ag (80 nm). The active layer was prepared by mixing PBDB-T and the acceptor (ITIC, IT-4F, or IEICO, respectively) in a 1:1 weight ratio. The mix was dissolved in chlorobenzene (30 mg/ml) and stirred in N_2 atmosphere at 50 °C for at least 6 hours. 30 min before spincoating 0.5 vol % of 1,8-diiodooctane was added. After cooling down for 1 min the solution was filtered (0.2 µm PTFE) and spincoated in N_2.

For the samples used in the absorption experiments described in **Paragraph 5.2.2** a quartz substrate was first coated with ZnO-nanoparticles (InfinityPV, see above) via spincoating or AZO80 via ALD process (see above). The acceptor layers have been prepared by dissolving each of the respective acceptor molecules ($PC_{70}BM$, ITIC, IT-4F, IEICO) in chlorobenzene (5 mg/ml). The solutions were stirred for at least 6 hours before being spincoated in N_2 with varying rotation speeds to obtain a final layer thickness < 10 nm for every material.

Materials and Device Characterization

The sheet resistance was measured with the Van-der-Pauw method. Hall measurements were performed in air using a home-built setup including an electromagnet with a magnetic flux density of 0.75 T. For the hall

measurement the layers were deposited on glass. For determining transmission and reflection spectra a Deuterium Halogen lamp (DH-2000-BAL, OceanOptics) and a spectrometer with a range 186–1041 nm (USB 2000+XR1-ES) were used. For transmission measurements, 200 nm thick SnO_x layers were deposited on quartz substrates. The measurements of the surface potential were done with a McAllister KP6500 Kelvin-Probe (KP) system under controlled atmosphere (vacuum (10^{-6} mbar), pure oxygen, air). Highly ordered pyrolytic graphite with a WF of 4.5 eV was used as reference.[225] XPS measurements were performed using a Physical Electronics PHI 5700 multi-technique surface analysis system, connected to an integrated UHV system equipped with deposition chambers for sample synthesis. This setup allowed measuring uncontaminated surfaces by transferring the sample to the characterization chamber without breaking UHV conditions.

7.3.2 Additional Data and Figures
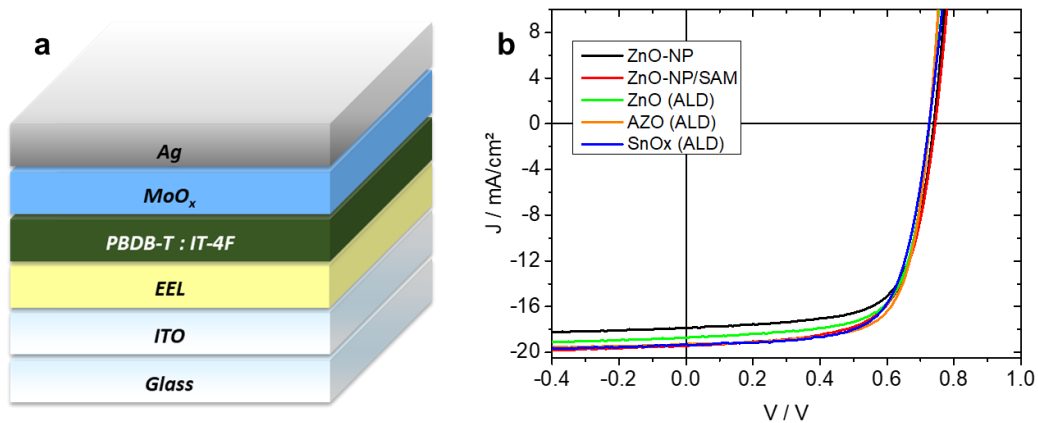
EEL	PCE [%]	FF [%]	Voc [V]	Jsc [mA/cm²]
ZnO-NP	9.09 ± 0.19	68.9 ± 0.9	0.74 ± 0.01	17.8 ± 0.2
ZnO-NP/SAM	9.55 ± 0.22	66.1 ± 0.9	0.74 ± 0.01	19.4 ± 0.4
ZnO (ALD)	9.48 ± 0.37	69.5 ± 1.3	0.73 ± 0.01	18.7 ± 0.8
AZO (ALD)	9.83 ± 0.28	70.7 ± 1.4	0.73 ± 0.01	19.2 ± 0.3
SnO$_x$ (ALD)	9.61 ± 0.07	68.3 ± 0.6	0.73 ± 0.01	19.4 ± 0.1

Figure 7.42: Inverted devices with PBDB-T:IT-4F active layer: a) Inverted device stack, b) J/V curves of representative devices with different EEL materials. The Table contains the resulting characteristic parameters of multiple devices each.

7.4 Excursus: On the Origin of Near-Unity EQE in Perovskite Solar Cells

Within a short time perovskite solar cells had a large impact on the entire field of photovoltaics,[235,236] inter alia through their high J_{SC}. As elaborated in **Paragraph 2.1.4**, the EQE provides a more detailed information about the respective solar cells and enables insight into possible spectral mismatch in the determination of the J_{SC} when using simulated sunlight. Therefore, the EQE belongs to the standard characteristics typically reported for solar cells.[237] The following section addresses a commonly reported phenomenon, that an extremely high EQE up to 98 % is encountered in a large number of publications (including the data presented in **Chapter 4.4**) Even though very high internal quantum efficiencies (IQE) up to unity have been reported for perovskite solar cells quite early,[167,238] the high EQE is puzzling as the transmittance of commonly used glass/ITO substrates is below 90 % (even with antireflective coating) in the spectral range where these high EQE values are typically reported (see **Figure 7.46**). Therefore, reports of such high values appear somewhat unrealistic and cast doubts not only on the measurements in this work but on EQE characterization of perovskite solar cells in general. As already mentioned in **Chapter 4.4**, a combination of experimental data and optical simulations are used to explain the root cause of the high EQE. This section has been partially published in Ref.[181].

7.4.1 Results and Discussion

As an example, an EQE spectrum of a single-junction PSC based on $FA_{0.8}Cs_{0.2}(PbI_{0.5}Br_{0.5})_3$ in analogy to the wide bandgap cell ($E_g = 1.85$ eV) in **Chapter 4.2** is presented (**Figure 7.43**). For these devices a maximum EQE(λ) (i.e. EQE_{max} of 97%) is observed for $\lambda_{max\ EQE} = 440$ nm. The literature

provides a plethora of articles that likewise report an $EQE_{max} \geq 95\%$ almost exclusively located inside a very narrow spectral region between 400 and 500 nm.[160,235,239–248]
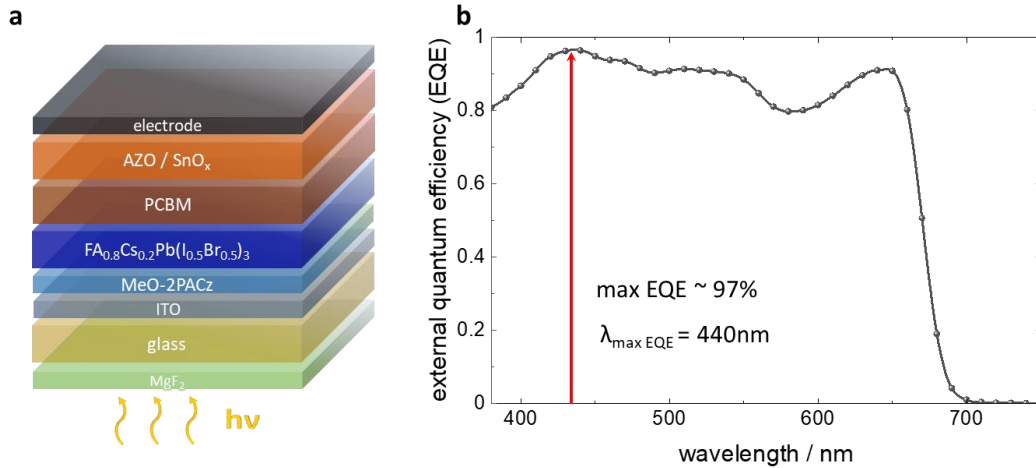

Figure 7.43: Layer sequence of a bottom-illuminated perovskite solar cell, that we have used as an example in this study (a). External quantum efficiency (EQE) spectrum of the respective cell with the maximum EQE marked with a red arrow.

To understand the origin of the high EQE values and to support their validity, an optical simulation has been conducted, using a layer sequence as shown in **Figure 7.44a**, considering the ITO layer to have a thickness of 140 nm and a sheet resistance of 12 Ωsq^{-1}. In analogy to **Chapter 4** a 100 nm thick antireflective coating of MgF_2 was added to the backside of the glass/ITO substrates. With the thickness of the glass substrate (0.7 mm) exceeding the coherence limit of the incoming light, the MgF_2 basically only serves as an antireflection layer to lower the reflectance at the air/glass transition without impacting the optical properties on the opposite side ("ITO-side") of the substrate. Considering the very high absorption coefficient of many photoactive perovskites reported in the spectral region between 400 and 500 nm, it was assumed that all the light that is finally transmitted into the perovskite layer, will be absorbed. Therefore, the stack shown in **Figure 7.44a** is considered sufficient and additional layers (charge

transport layers and electrode) on top of the perovskite are not expected to substantially influence the result.

The transmittance and reflectance of the incident light has been calculated in case of (photoactive) material with a varied refractive index at 440 nm in the range between 1 (air) and 4 (**Figure 7.44b**) on top of the ITO. While a simulated reflectance of about 25 % and a transmittance of 75 % at 440 nm can be found in the case of n = 1 (air), a substantial increase in transmittance (and decrease in reflectance) can be observed for materials with larger n. Specifically, $FA_{0.8}Cs_{0.2}(PbI_{0.5}Br_{0.5})_3$ has a refractive index of n ≈ 2.65 at 440 nm,[164] which results in a calculated transmittance into the perovskite of 97 % (reflectance 3 %). Exemplary transmittance spectra for n = 1 (air) and n = 2.65 (perovskite) are shown in **Figure 7.44c**.
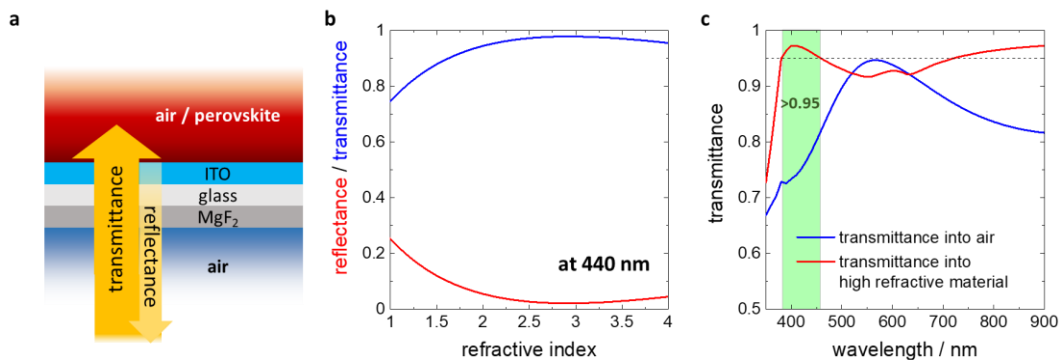

Figure 7.44: a) Layer sequence of the simulated cell stack, b) transmittance and reflectance at 440 nm in dependency of the refractive index of the material on top of the ITO electrode, c) simulated transmittance spectra in case of perovskite or air adjacent to the ITO electrode. The green area marks the spectral region where the transmittance exceeds 95%.

Remarkably, in case of the perovskite this depicts a maximum transmittance of > 97 % at around 410 nm with overall less variations in the spectral region between 400 and 900 nm. On the contrary, for n = 1 (air) the transmittance shows a minimum between 400 and 500 nm and overall a strong spectral variation. Notably, the simulated spectrum of the transmittance in case of air is in good agreement with the measured transmittance of the ITO/glass substrate (see **Figure 7.46**). Consequently, even though a pristine ITO/glass

substrate provides a significantly lower spectral transmittance, the high refractive index of the perovskite absorber on top of ITO gives rise to a very high fraction of the incident light to be coupled into the active medium. This is supported by a measurement of reflectance comparing glass/ITO to glass/ITO/ $FA_{0.8}Cs_{0.2}(PbI_{0.5}Br_{0.5})_3$ for the targeted wavelength region, as shown in **Figure 7.50**. To transfer the findings to solar cells, demonstrators have been fabricated to directly compare the measured EQE spectra with the spectral transmittance resulting from the simulation data. In the spectral region of the maximum EQE, there is a favorable agreement of measurement and simulation, as pictured in **Figure 7.45a,b**. For simplicity, an IQE of 100 % has been assumed for the perovskite as earlier reports have shown.[167,238] Note, a similar agreement between measurement and simulation is found for samples without MgF_2 antireflective layer (**Figure 7.51**). The spectral variations of the measured EQE spectrum for $\lambda > 500$ nm can be explained by the limited thickness and absorption coefficient of the perovskite layer in these devices for higher wavelength regions, while in the simulation the absorber medium was assumed to be infinitely thick. In these solar cells with a perovskite layer thickness in the range of 300-450 nm, light with $\lambda > 500$ nm is partially transmitted by the perovskite. As a consequence, the subsequent layers of the device stack (**Figure 7.43a**), such as PCBM, AZO/SnO_X and the metal electrode are important for the optics and affect the EQE spectrum. For completeness, **Figure 7.45c** displays the well-behaved almost hysteresis-free J/V characteristics of the fabricated cells along with the relevant photovoltaic parameters extracted.
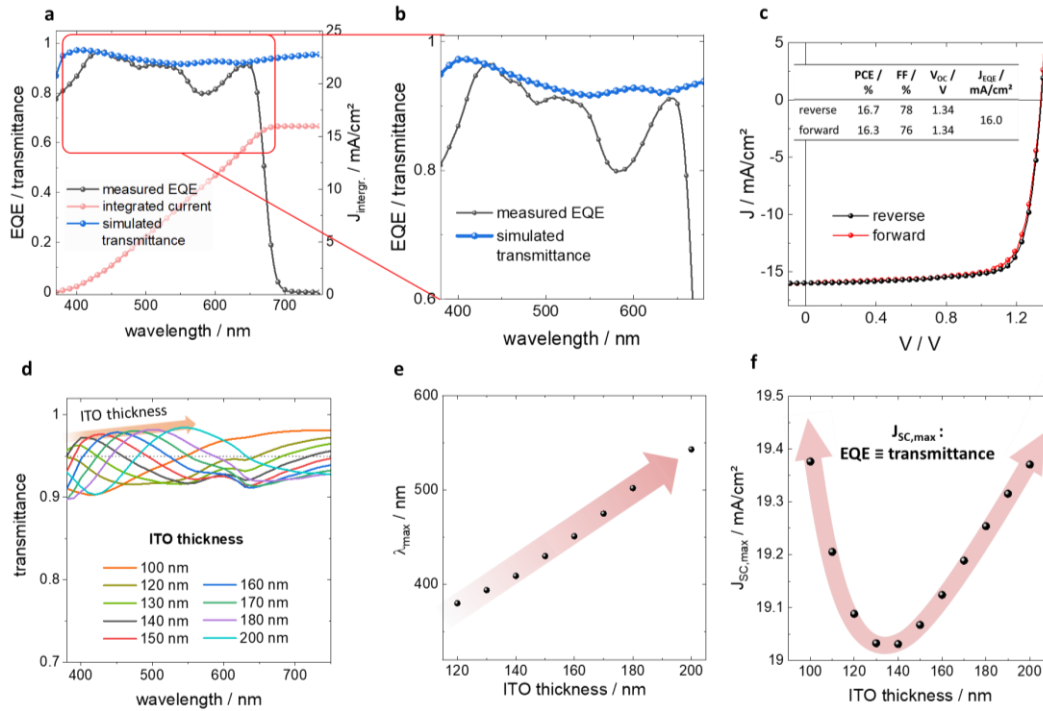
Figure 7.45: Measured EQE spectrum of our exemplary solar cells, in direct comparison with simulated data for transmittance into the perovskite and calculated integrated current density ($J_{integr.}$) (a,b), respective J/V characteristics of the solar cell (c). Statistical data of fabricated solar cells can be found in **Figure 7.53**. Simulated transmittance into the perovskite for a varied thickness of the ITO electrode (d). Position of the transmittance maximum in dependency of the ITO thickness (e). Maximum integrated current ($J_{SC,max}$), assuming EQE equal to the respective transmittance displayed in (d) and an IQE of unity for various ITO thicknesses (f).

To also clarify the origin of variations in the spectral position λ_{max} of the maximum in the EQE (EQE$_{max}$), a variation of ITO electrode thickness d in the simulations (between 100-200 nm) was performed and the spectral transmittance into the perovskite was determined. Very strikingly λ_{max} shows a notable red-shift with increasing ITO layer thickness (**Figure 7.45d**). As a result, the thickness of the transparent bottom electrode may be an important means to tune the spectral absorption characteristics and another important aspect for further optimization of the optics of the device stack. To identify a possible optimum in transmittance that would afford a maximum in J_{SC}, a calculation of the hypothetical integrated $J_{SC,max}$ in dependency of the ITO layer thickness was performed as follows. For

simplicity an internal quantum efficiency of unity was assumed and EQE was set equal to the respective transmittance (displayed in **Figure** *7.45***d**) for the perovskite over the spectral range from 400-700 nm. As visible in **Figure** *7.45***f** this estimation gives surprising insight, highlighting that not only thinner, but also thicker ITO layers may prove beneficial for overall cell performance.

7.4.2 Conclusion

Within this work it was possible to clarify the origin of very high maximum EQE values > 95% that were reported for perovskite solar cells in the literature and that were observed in devices presented above (also **Chapter 4**). By using a combined approach based on experimental data and optical simulation it was possible to show that the high refractive index of halide perovskites enables a high transmittance of incident light into the photoactive medium, which notably exceeds the values obtained for the neat glass/ITO substrates measured in air. In the presented example, the EQE spectrum of the devices showed a high $EQE_{max} = 97\%$ located at around $\lambda_{max} = 440$ nm, that was in favorable agreement with the simulated transmittance spectrum. Variations of λ_{max} are related to thickness variations of the transparent ITO electrode.

7.4.3 Methodical Details

Optical simulations have been performed with the simulation software SETFOS (Fluxim Ag, Switzerland), that is based on a transfer matrix algorithm to calculate optical absorption, reflection and transmission of a given assembly of layers. As input data for the simulation the (complex) refractive indices (optical constants n & k) of the implemented materials are considered. The optical constants of ITO have been taken from literature.[165]

The spectral dispersion of the implemented perovskite has been derived from literature values by applying an additional wavelength offset to take into account the bandgap of 1.85 eV of the perovskite used.[164] Note, for simplicity a constant refractive index (n = 1) of air has been assumed (neglecting dispersion).

Solar cell fabrication was done in analogy to the methods presented in **Paragraph 7.2.1**.
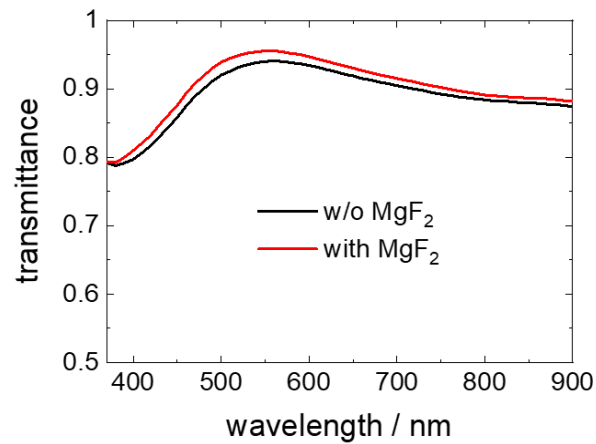
7.4.4 Additional Data and Figures

Figure 7.46: Transmittance of typical glass / ITO substrates used for solar cell fabrication.

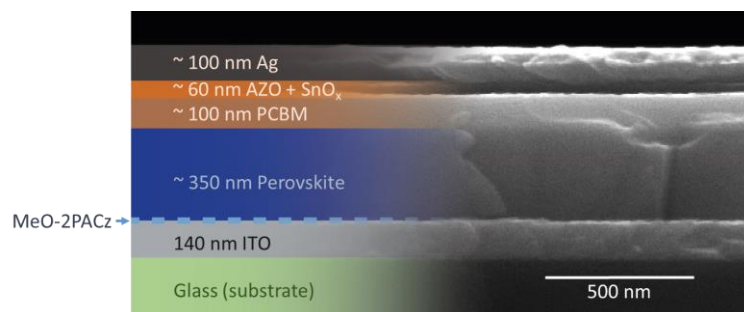**Figure 7.47:** Cross sectional SEM image of a perovskite solar cell shown in **Figure 4.2**a.
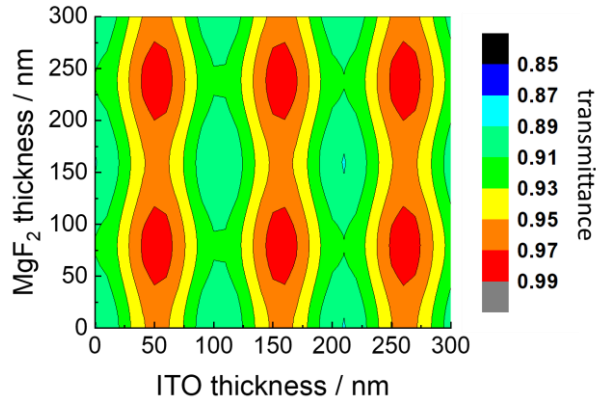
Figure 7.48: Simulated maximal transmittance at 440 nm into high refractive material in dependence of ITO thickness as well as MgF$_2$ antireflective coating.
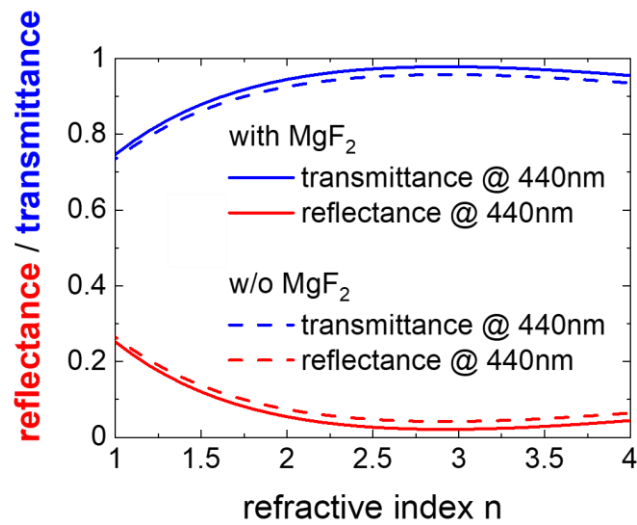
Figure 7.49: transmittance and reflection at 440 nm with respective stack in dependency of its refractive index with and without 100 nm MgF$_2$ antireflective coating.
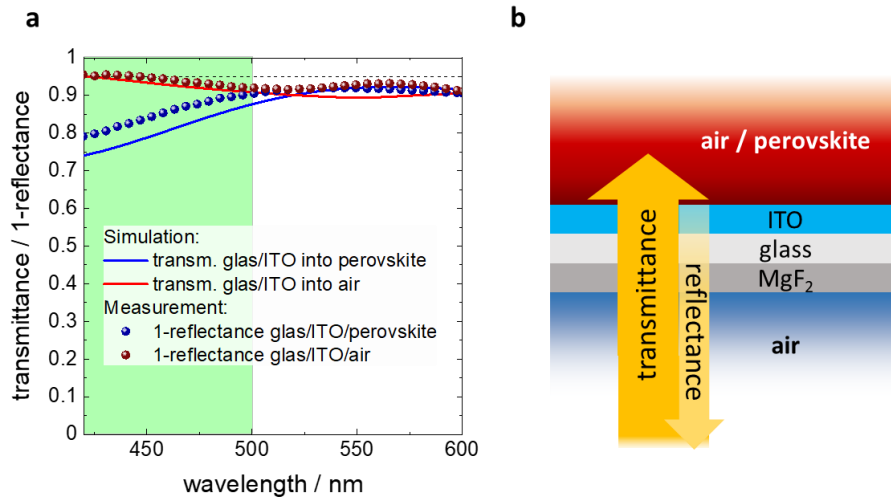
Figure 7.50: Simulated transmission into either perovskite material or air compared with measured 1-reflectance data (note, samples were w/o antireflective coating in this experiment) (a) and respective schematic layer setup for simulation & measurement (b).

	PCE / %	FF / %	V_{OC} / V	J_{EQE} / mA/cm²
reverse	15.7	80	1.29	15.2
forward	15.4	79	1.28	
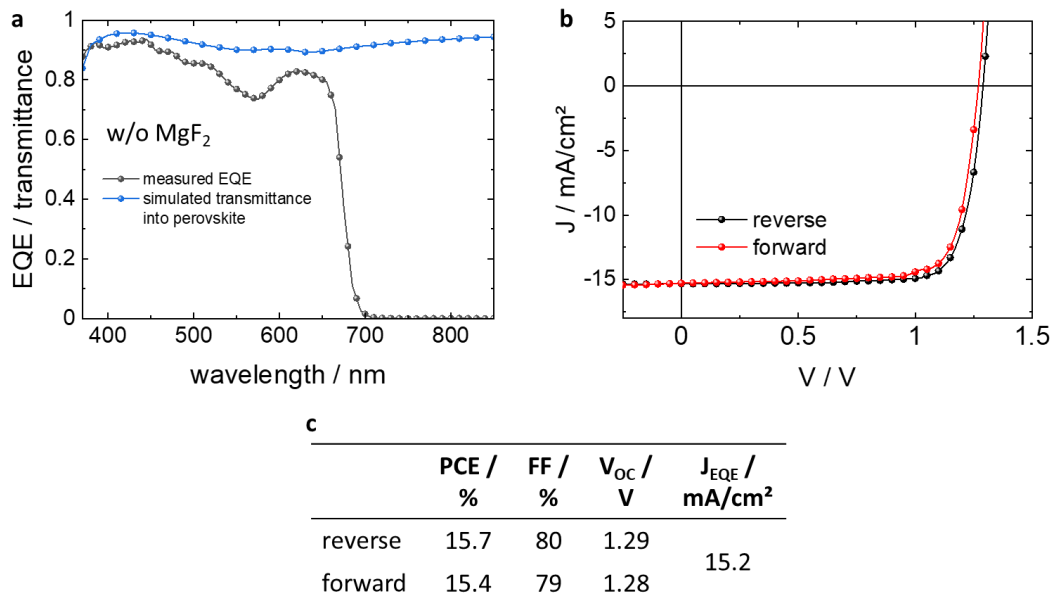
Figure 7.51: Representative EQE super-positioned with simulated transmittance into high refractive material w/o anti-reflective coating (a), and respective J/V (b) and solar cell characteristics (c).
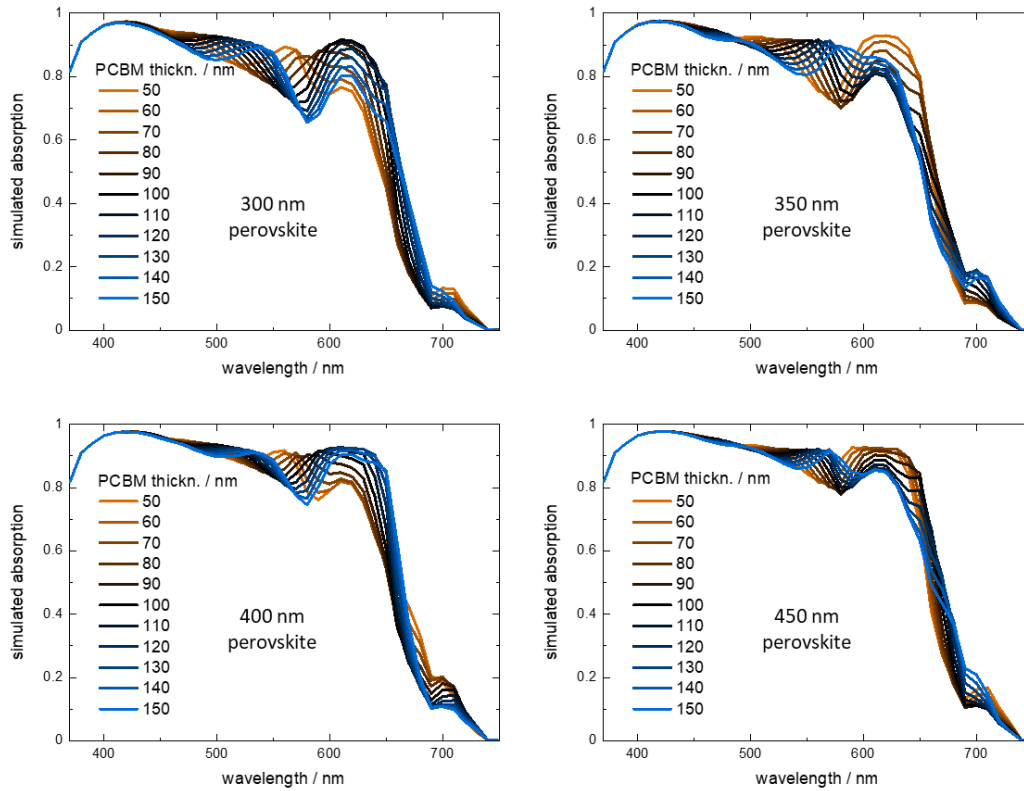
Figure 7.52: Simulated absorption in the active material of a full device stack with varied PCBM thickness for 300 nm, 350 nm, 400 nm and 450 nm assumed thickness of the active material.
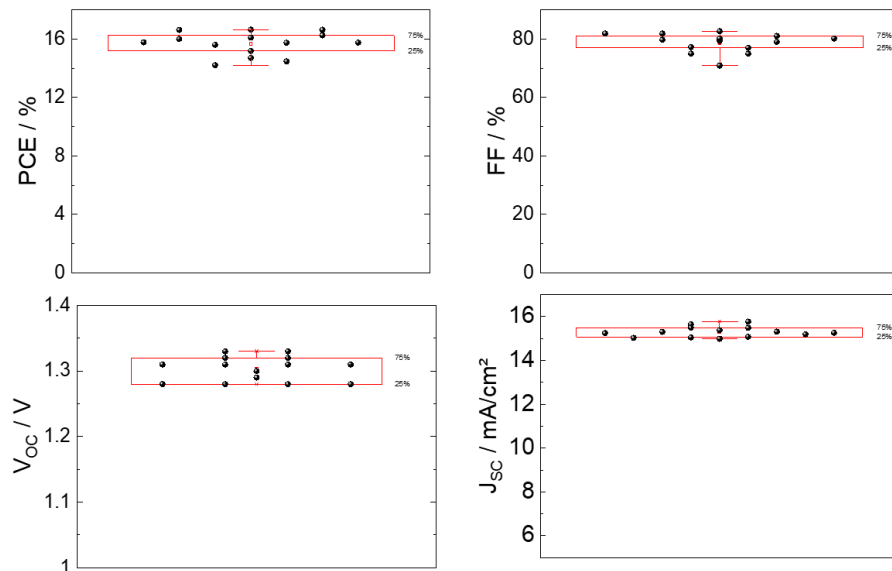
Figure 7.53: Statistics of J/V characteristics for a set of 14 perovskite solar cells. The boxes mark the range of 25% and 75% of the recorded data points.

Bibliography

[1]   International Energy Agency, *World Eenrgy Outlook 2022*, IEA Publications, Paris, **2022**.

[2]   E. Bellini, *PV Mag.* **2023**.

[3]   M. Victoria, N. Haegel, I. M. Peters, R. Sinton, A. Jäger-Waldau, C. del Canizo, C. Breyer, M. Stocks, A. Blakers, I. Kaizuka, K. Komoto, A. H. M. Smets, *Joule* **2021**, *5*, 1041.

[4]   C. K. Chiang, C. R. Fincher, Y. W. Park, A. J. Heeger, G. MacDiarmid, *Pysical Rev. Lett.* **1978**, *40*, 1978.

[5]   H. Shirakawa, E. J. Louis, A. G. Macdiarmid, C. K. Chiang, A. J. Heeger, *J. Chem. Soc., Chem. Commun.* **1977**, 578.

[6]   R. N. Marks, J. J. M. Halls, D. D. C. Bradley, R. H. Friend, A. B. Holmes, *J. Phys. Condens. Mat.* **1994**, *6*, 1379.

[7]   S. Barth, H. Bässler, *Phys. Rev. Lett.* **1997**, *79*, 4445.

[8]   B. A. Gregg, *J. Phys. Chem. B* **2003**, *107*, 4688.

[9]   W. Zhao, D. Qian, S. Zhang, S. Li, O. Inganäs, F. Gao, J. Hou, *Adv. Mater.* **2016**, *28*, 4734.

[10]   W. Zhao, S. Zhang, J. Hou, *Sci. China* **2016**, *59*, 1.

[11]   W. Zhao, S. Li, H. Yao, S. Zhang, Y. Zhang, B. Yang, J. Hou, *J. Am. Chem. Soc.* **2017**, *139*, 7148.

[12]   Y. Liang, Z. Xu, J. Xia, S. T. Tsai, Y. Wu, G. Li, C. Ray, L. Yu, *Adv. Mater.* **2010**, 22, 1.

[13]   G. Xu, L. Chen, Y. Chen, H. Lei, Z. Liao, N. Yi, J. Liu, *J. Mater. Chem. A* **2019**, *7*, 4145.

[14]   H. Yao, Y. Cui, R. Yu, B. Gao, H. Zhang, J. Hou, *Angew. Chemie* **2017**, *129*, 1.

[15]   H. Yao, Y. Chen, Y. Qin, R. Yu, Y. Cui, B. Yang, S. Li, K. Zhang, J. Hou, *Adv. Mater.* **2016**, *28*, 8283.

[16]   Y. Cui, C. Yang, H. Yao, J. Zhu, Y. Wang, G. Jia, F. Gao, *Adv. Mater.* **2017**, *29*, 1703080.

[17]   N. S. Sariciftci, L. Smilowitz, A. J. Heeger, F. Wudi, *Science (80-.).* **1992**, *258*, 27.

[18]   L. Smilowitz, N. S. Sariciftci, R. Wu, C. Gettinger, A. J. Heeger, F. Wudl, *Phys. Rev. B* **1993**, *47*, 13835.

[19]   J. Hustings, R. Bonné, R. Cornelissen, F. Morini, R. Valcke, K. Vandewal, J. V Manca, *Front. Photonics* **2022**, *3*, 1.

[20]   N. S. Sariciftci, L. Smilowitz, *Synth. Met.* **1993**, *59*, 333.

[21]   V. Dyakonov, G. Zoriniants, M. Scharber, C. J. Brabec, R. A. J. Janssen, J. C. Hummelen, N. S. Sariciftci, *Phys. Rev. B* **1999**, *59*, 8019.

[22]   J. De Ceuster, E. Goovaerts, A. Bouwen, J. C. Hummelen, V. Dyakonov, *Phys. Rev. B* **2001**, *64*, 195206.

[23]   W. Shockley, H. J. Queisser, *J. Appl. Phys.* **1961**, *32*, 510.

[24]   J. Benduhn, K. Tvingstedt, F. Piersimoni, S. Ullbrich, Y. Fan, M. Tropiano, K. A. Mcgarry, O. Zeika, M. K. Riede, C. J. Douglas, S. Barlow, S. R. Marder, D. Neher, D. Spoltore, K. Vandewal, *Nat. Energy* **2017**, *2*, 17053.

[25]   W. Shockley, *Electrons and Holes in Semiconductors (with Applications to Transistor Electronics)*, D. Van Nostrand Company, Inc., Princeton, NJ, **1950**.

[26]   H. Hoppe, D. Meissner, *Mol. Cryst. Liq. Cryst.* **2002**, *385*, 233.

[27]   J.-L. Brédas, J. E. Norton, J. Cornil, V. Coropceanu, *Acc. Chem. Res.* **2009**, *42*, 1691.

[28]   H. Sirringhaus, *Adv. Mater.* **2005**, *17*, 2411.

[29]   C. D. Dimitrakopoulos, D. J. Mascaro, *IBM J. Res. Dev.* **2001**, *45*, 11.

[30]   N. Tessler, Y. Preezant, N. Rappaport, Y. Roichman, *Adv. Mater.* **2009**, *21*, 2741.

[31]   G. Yu, J. Gao, J. C. Hummelen, F. Wudl, A. J. Heeger, *Science (80-.).* **1995**, *270*, 1789.

[32]   B. Kippelen, J.-L. Brédas, *Energy Environ. Sci.* **2009**, *2*, 251.

[33]   T. J. Savenije, J. M. Warman, A. Goossens, *Chem. Phys. Lett.* **1998**, *287*, 148.

[34]   L. A. A. Petterson, L. S. Roman, O. Inganäs, *J. Appl. Phys.* **1999**, *86*, 487.

[35]   B. Chen, X. Qiao, C.-M. Liu, C. Zhao, H.-C. Chen, K.-H. Wei, B. Hu, *Appl. Phys. Lett.* **2013**, *102*, 193302.

[36]   G. F. A. Dibb, F. C. Jamieson, A. Maurano, J. Nelson, J. R. Durrant, *J. Phys. Chem. Lett.* **2013**, *4*, 803.

[37]   B. Qi, J. Wang, *Phys. Chem. Chem. Phys.* **2013**, *15*, 8972.

[38]   W. Tress, S. Corvers, K. Leo, M. Riede, *Adv. Energy Mater.* **2013**, *3*, 873.

[39]   V. D. Mihailetchi, L. J. A. Koster, P. W. M. Blom, *Appl. Phys. Lett.* **2004**, *85*, 970.

[40]   Y. Park, V. Choong, Y. Gao, B. R. Hsieh, C. W. Tang, *Appl. Phys. Lett.* **1996**, *68*, 2699.

[41]   K. Sugiyama, H. Ishii, Y. Ouchi, K. Seki, *J. Appl. Phys.* **2000**, *87*, 295.

[42]   J. Blochwitz, T. Fritz, M. Pfei, K. Leo, D. M. Alloway, P. A. Lee, N. R. Armstrong, *Org. Electron.* **2001**, *2*, 97.

[43]   R. Steim, F. R. Kogler, C. J. Brabec, *J. Mater. Chem.* **2010**, *20*, 2499.

[44]   K. X. Steirer, P. F. Ndione, N. E. Widjonarko, M. T. Lloyd, J. Meyer, E. L. Ratcliff, A. Kahn, N. R. Armstrong, C. J. Curtis, D. S. Ginley, J. J. Berry, D. C. Olson, *Adv. Energy Mater.* **2011**, *1*, 813.

[45]   M. Y. Lin, C. Y. Lee, S. C. Shiu, I. J. Wang, J. Y. Sun, W. H. Wu, Y. H. Lin, J. S. Huang, C. F. Lin, *Org. Electron. physics, Mater. Appl.* **2010**, *11*, 1828.

[46]   S. Trost, K. Zilberberg, A. Behrendt, A. Polywka, P. Görrn, P. Reckers, J. Maibach, T. Mayer, T. Riedl, *Adv. Energy Mater.* **2013**, *3*, 1437.

[47]   S. Trost, T. Becker, K. Zilberberg, A. Behrendt, A. Polywka, R. Heiderhoff, P. Görrn, T. Riedl, *Sci. Rep.* **2015**, *5*, 7665.

[48]   S. Trost, A. Behrendt, T. Becker, A. Polywka, P. Görrn, T. Riedl, *Adv. Energy Mater.* **2015**, *5*, 1500277.

[49]   J. Meyer, S. Hamwi, M. Kröger, W. Kowalsky, T. Riedl, A. Kahn, *Adv. Mater.* **2012**, *24*, 5408.

[50]   K. Zilberberg, H. Gharbi, A. Behrendt, S. Trost, T. Riedl, *ACS Appl. Mater. Interfaces* **2012**, *4*, 1164.

[51]   K. Zilberberg, S. Trost, J. Meyer, A. Kahn, A. Behrendt, D. Lützenkirchen-hecht, R. Frahm, T. Riedl, *Adv. Funct. Mater.* **2011**, *21*, 4776.

[52]   M. Campoy-Quiles, T. Ferenczi, T. Agostinelli, P. G. Etchegoin, Y. Kim, T. D. Anthopoulos, P. N. Stavrinou, D. D. C. Bradley, J. Nelson, *Nat. Mater.* **2008**, *7*, 158.

[53]   B. Y. Yao, J. Hou, Z. Xu, G. Li, Y. Yang, *Adv. Funct. Mater.* **2008**, *18*, 1783.

[54]   B. L. Chen, Z. Hong, G. Li, Y. Yang, *Adv. Mater.* **2009**, *21*, 1434.

[55]   B. Z. Xu, L. Chen, G. Yang, C. Huang, J. Hou, *Adv. Funct. Mater.* **2009**, *19*, 1227.

[56]   G. Dennler, K. Forberich, T. Ameri, C. Waldauf, P. Denk, C. J. Brabec, K. Hingerl, A. J. Heeger, K. Hingerl, *J. Appl. Phys.* **2007**, *102*, 123109.

[57]   A. Hadipour, B. de Boer, P. W. M. Blom, *Org. Electron. physics, Mater. Appl.* **2008**, *9*, 617.

[58]   J. Gilot, M. M. Wienk, R. A. J. Janssen, *Adv. Funct. Mater.* **2010**, *20*, 3904.

[59]   D. J. D. Moet, P. de Bruyn, J. D. Kotlarski, P. W. M. Blom, *Org. Electron.* **2010**, *11*, 1821.

[60]   J. Gilot, I. Barbu, M. M. Wienk, R. A. J. Janssen, *Appl. Phys. Lett.* **2007**, *91*, 113520.

[61]   M. Y. Chan, S. L. Lai, K. M. Lau, *Appl. Phys. Lett.* **2006**, *89*, 163515.

[62]   A. K. K. Kyaw, D. H. Wang, D. Wynands, J. Zhang, T. Nguyen, G. C. Bazan, A. J. Heeger, *Nano Lett.* **2013**, *13*, 3796.

[63]   E. New, T. Howells, P. Sullivan, T. S. Jones, *Org. Electron.* **2013**, *14*, 2353.

[64]   Y. Zhang, A. K. Pandey, C. Tao, Y. Fang, H. Jin, P. L. Burn, P. Meredith, *Appl. Phys. Lett.* **2013**, *102*, 013302.

[65]   G. D. Sharma, M. L. Keshtov, A. R. Khokhlov, D. Tasis, C. Galiotis, *Org. Electron.* **2014**, *15*, 348.

[66]   X. Chen, Z. Jia, Z. Chen, T. Jiang, L. Bai, F. Tao, J. Chen, X. Chen, T. Liu, X. Xu, C. Yang, W. Shen, W. E. I. Sha, H. Zhu, Y. (Michael) Yang, *Joule* **2020**, *4*, 1.

[67]   W. E. I. Sha, H. Zhang, Z. S. Wang, H. L. Zhu, X. Ren, F. Lin, A. K. Jen, W. C. H. Choy, *Adv. Energy Mater.* **2018**, *8*, 1701586.

[68]   R. Cariou, J. Benick, F. Feldmann, O. Höhn, H. Hauser, P. Beutel, N. Razek, M. Wimplinger, B. Bläsi, D. Lackner, M. Hermle, G. Siefer, S. W. Glunz, A. W. Bett, F. Dimroth, *Nat. Energy* **2018**, *3*, 326.

[69]   C.-H. Chou, W. L. Kwan, Z. Hong, L. Chen, Y. Yang, *Adv. Mater.* **2011**, *23*, 1282.

[70]   A. Puetz, F. Steiner, J. Mescher, M. Reinhard, N. Christ, D. Kutsarov, H. Kalt, U. Lemmer, A. Colsmann, *Org. Electron. physics, Mater. Appl.* **2012**, *13*, 2696.

[71]   B. S. Sista, M. Park, Z. Hong, Y. Wu, J. Hou, W. L. Kwan, G. Li, Y. Yang, *Adv. Mater.* **2010**, *22*, 380.

[72]   L. Zuo, C. Chang, C. Chueh, S. Zhang, H. Li, *Energy Environ. Sci.* **2015**, *8*, 1712.

[73]   J. W. Shim, Y. Zhou, C. Fuentes-Hernandez, A. Dindar, Z. Guan, H. Cheun, A. Kahn, B. Kippelen, *Sol. Energy Mater. Sol. Cells* **2012**, *107*, 51.

[74]   T. T. Larsen-Olsen, E. Bundgaard, K. O. Sylvester-Hvid, F. C. Krebs, *Org. Electron.* **2011**, *12*, 364.

[75]   R. Timmreck, S. Olthof, K. Leo, M. K. Riede, **2010**, 1.

[76]   J. W. Shim, C. Fuentes-hernandez, Y. Zhou, A. Dindar, T. M. Khan, A. J. Giordano, H. Cheun, M. Yun, S. R. Marder, *Adv. Energy Mater.* **2014**, *4*, 1400048.

[77]   S. Lu, X. Guan, X. Li, W. E. I. Sha, F. Xie, H. Liu, J. Wang, F. Huang, W. C. H. Choy, *Adv. Energy Mater.* **2015**, *5*, 1500631.

[78]   K. Kawano, N. Ito, T. Nishimori, J. Sakai, K. Kawano, N. Ito, T. Nishimori, J. Sakai, *Appl. Phys. Lett.* **2006**, *88*, 073514.

[79]   M. P. de Jong, L. J. van Ijzendoorn, M. J. A. de Voigt, *Appl. Phys. Lett.* **2000**, *77*, 2255.

[80]   B. F. So, D. Kondakov, *Adv. Mater.* **2010**, *22*, 3762.

[81]   W. Li, A. Furlan, K. H. Hendriks, M. M. Wienk, R. a J. Janssen, *J. Am. Chem. Soc.* **2013**, *135*, 5529.

[82]   D. Di Carlo Rasi, K. H. Hendriks, M. M. Wienk, R. A. J. Janssen, *Adv. Mater.* **2018**, *1803836*, 1.

[83]   A. R. bin M. Yusoff, D. Kim, H. P. Kim, F. K. Shneider, W. J. da Silva, J. Jang, *Energy Environ. Sci.* **2015**, *8*, 303.

[84]   C. C. Chen, W. H. Chang, K. Yoshimura, K. Ohya, J. You, J. Gao, Z. Hong, Y. Yang, *Adv. Mater.* **2014**, 5670.

[85]   J. Gilot, M. M. Wienk, R. a. J. Janssen, *Appl. Phys. Lett.* **2007**, *90*, 143512.

[86]   X. Du, O. Lytken, M. S. Killian, J. Cao, T. Stubhan, M. Turbiez, P. Schmuki, H. Steinrück, L. Ding, R. H. Fink, N. Li, C. J. Brabec, *Adv. Energy Mater.* **2016**, *7*, 1601959.

[87]   D. Di Carlo Rasi, Tandem , Triple , and Quadruple Junction Polymer Solar Cells, TU Eindhoven, **2018**.

[88]   R. Timmreck, T. Meyer, J. Gilot, H. Seifert, T. Mueller, A. Furlan, M. M. Wienk, D. Wynands, J. Hohl-Ebinger, W. Warta, R. a. J. Janssen, M. Riede, K. Leo, *Nat. Photonics* **2015**, *9*, 478.

[89]   S. H. Park, A. Roy, S. Beaupré, S. Cho, N. Coates, J. S. Moon, D. Moses, M. Leclerc, K. Lee, A. J. Heeger, *Nat. Photonics* **2009**, *3*, DOI 10.1038/NPHOTON.2009.69.

[90]   L. Lu, L. Yu, *Adv. Mater.* **2014**, *26*, 4413.

[91]   C. Duan, R. E. M. Willems, J. J. van Franeker, B. J. Bruijnaers, M. M. Wienk, R. A. J. Janssen, *J. Mater. Chem. A* **2016**, *4*, 1855.

[92]   S. Roland, S. Neubert, S. Albrecht, B. Stannowski, M. Seger, A. Facchetti, R. Schlatmann, B. Rech, D. Neher, *Adv. Mater.* **2015**, *27*, 1262.

[93] H. Tan, A. Furlan, W. Li, K. Arapov, R. Santbergen, M. M. Wienk, M. Zeman, A. H. M. Smets, R. A. J. Janssen, *Adv. Mater.* **2016**, *28*, 2170.

[94] M. Grätzel, *Nat. Mater.* **2014**, *13*, 838.

[95] A. Ishii, A. K. Jena, T. Miyasaka, *APL Mater.* **2014**, *2*, 091102.

[96] M. A. Green, E. D. Dunlop, M. Yoshita, N. Kopidakis, K. Bothe, G. Siefer, X. Hao, *Prog. Photovoltaics Res. Appl.* **2023**, *31*, 651.

[97] Y. Zhao, F. Ma, Z. Qu, S. Yu, T. Shen, H.-X. Deng, X. Chu, X. Peng, Y. Yuan, X. Zhang, J. You, *Science (80-.).* **2022**, *377*, 531.

[98] N. H. Tiep, Z. Ku, H. J. Fan, *Adv. Energy Mater.* **2016**, *6*, 1501420.

[99] T. Leijtens, G. E. Eperon, N. K. Noel, S. N. Habisreutinger, A. Petrozza, H. J. Snaith, *Adv. Energy Mater.* **2015**, *5*, 1500963.

[100] G. Divitini, S. Cacovich, F. Matteocci, A. Di Carlo, C. Ducati, *Nat. Energy* **2016**, *1*, 15012.

[101] K. O. Brinkmann, Functional Layers and Interfaces for Perovskite Single- and Multi-Junction Solar Cells, University of Wuppertal, **2022**.

[102] G. Niu, W. Li, F. Meng, L. Wang, H. Dong, Y. Qiu, *J. Mater. Chem. A* **2014**, *2*, 705.

[103] J. M. Frost, K. T. Butler, F. Brivio, C. H. Hendon, M. Van Schilfgaarde, A. Walsh, *Nano Lett.* **2014**, *14*, 2584.

[104] B. Conings, J. Drijkoningen, N. Gauquelin, A. Babayigit, J. D. Haen, L. D. Olieslaeger, A. Ethirajan, J. Verbeeck, J. Manca, E. Mosconi, F. De Angelis, H. Boyen, *Adv. Energy Mater.* **2015**, *5*, 1500477.

[105] N. Pellet, P. Gao, G. Gregori, T. Yang, M. K. Nazeeruddin, J. Maier, M. Grätzel, *Angew. Chemie* **2014**, *53*, 3151.

[106] N. J. Jeon, J. H. Noh, W. S. Yang, Y. C. Kim, S. Ryu, J. Seo, S. Il Seok, *Nature* **2015**, *517*, 476.

[107] F. Hao, C. C. Stoumpos, R. P. H. Chang, M. G. Kanatzidis, **2014**, *136*, 8094.

[108] J. Meyer, K. Zilberberg, T. Riedl, A. Kahn, *J. Appl. Phys.* **2011**, *110*, 033710.

[109] T. Becker, S. Trost, A. Behrendt, I. Shutsko, A. Polywka, P. Görrn, P. Reckers, C. Das, T. Mayer, D. Di Carlo Rasi, K. H. Hendriks, M. M. Wienk, R. A. J. Janssen, T. Riedl, *Adv. Energy Mater.* **2017**, 17020533.

[110] D. Di Carlo Rasi, P. M. J. G. van Thiel, H. Bin, K. H. Hendriks, G. H. L. Heintges, M. M. Wienk, T. Becker, Y. Li, T. Riedl, R. A. J. Janssen, *Sol. RRL* **2019**, *3*, 1800366.

[111] S. Hamwi, J. Meyer, M. Kröger, T. Winkler, M. Witte, T. Riedl, A. Kahn, W. Kowalsky, *Adv. Funct. Mater.* **2010**, *20*, 1762.

[112] J. Adams, G. D. Spyropoulos, M. Salvador, N. Li, S. Strohm, L. Lucera, S. Langner, F. Machui, H. Zhang, T. Ameri, M. M. Voigt, F. C. Krebs, C. J. Brabec, *Energy Environ. Sci.* **2015**, *8*, 169.

[113] S. Kouijzer, S. Esiner, C. H. Frijters, M. Turbiez, M. M. Wienk, R. a. J. Janssen, *Adv. Energy Mater.* **2012**, *2*, 945.

[114]   J. C. Bijleveld, A. P. Zoombeld, A. G. J. Mathijssen, M. M. Wienk, M. Turbiez, D. M. de Leeuw, R. A. J. Janssen, *J. Am. Chem. Soc.* **2009**, *131*, 16616.

[115]   S. Trost, T. Becker, A. Polywka, P. Görrn, M. F. Oszajca, N. A. Luechinger, D. Rogalla, M. Weidner, P. Reckers, T. Mayer, T. Riedl, *Adv. Energy Mater.* **2016**, *6*, 1600347.

[116]   J. P. Correa Baena, L. Steier, W. Tress, M. Saliba, S. Neutzner, T. Matsui, F. Giordano, J. Jacobsson, A. R. Srimath Kandada, S. M. Zakeeruddin, A. Petrozza, A. Abate, M. K. Nazeeruddin, M. Grätzel, A. Hagfeldt, *Energy Environ. Sci.* **2015**, *8*, 2928.

[117]   T. Hu, T. Becker, N. Pourdavoud, J. Zhao, K. O. Brinkmann, R. Heiderhoff, T. Gahlmann, Z. Huang, S. Olthof, K. Meerholz, D. Többens, B. Cheng, Y. Chen, T. Riedl, *Adv. Mater.* **2017**, *29*, 1606656.

[118]   K. O. Brinkmann, J. Zhao, N. Pourdavoud, T. Becker, T. Hu, S. Olthof, K. Meerholz, L. Hoffmann, T. Gahlmann, R. Heiderhoff, M. F. Oszajca, N. A. Luechinger, D. Rogalla, Y. Chen, B. Cheng, T. Riedl, *Nat. Commun.* **2017**, *8:13938*, 1.

[119]   J. Zhao, K. O. Brinkmann, T. Hu, N. Pourdavoud, T. Becker, T. Gahlmann, R. Heiderhoff, A. Polywka, P. Görrn, Y. Chen, B. Cheng, T. Riedl, *Adv. Energy Mater.* **2017**, *7*, 1602599.

[120]   S. R. Hammond, J. Meyer, N. E. Widjonarko, P. F. Ndione, A. K. Sigdel, A. Garcia, A. Miedaner, M. T. Lloyd, A. Kahn, D. S. Ginley, J. J. Berry, D. C. Olson, *J. Mater. Chem.* **2012**, *22*, 3249.

[121]   M. T. Greiner, L. Chai, M. G. Helander, W. M. Tang, Z. H. Lu, *Adv. Funct. Mater.* **2013**, *23*, 215.

[122]   M. Vasilopoulou, A. M. Douvas, D. G. Georgiadou, L. C. Palilis, S. Kennou, L. Sygellou, A. Soultati, I. Kostis, G. Papadimitropoulos, D. Davazoglou, P. Argitis, *J. Am. Chem. Soc.* **2012**, *134*, 16178.

[123]   M. Batzill, K. Katsiev, U. Diebold, *Appl. Phys. Lett.* **2004**, *85*, 5766.

[124]   A. Behrendt, C. Friedenberger, T. Gahlmann, S. Trost, T. Becker, K. Zilberberg, A. Polywka, P. Görrn, T. Riedl, *Adv. Mater.* **2015**, *27*, 5961.

[125]   E. Mankel, C. Hein, M. Kühn, T. Mayer, *Phys. Status Solidi A* **2014**, *211*, 2040.

[126]   M. Nagasawa, S. Shionoya, S. Makishima, *J. Phys. Soc. Japan* **1965**, *20*, 1093.

[127]   T. Mayer, C. Hein, E. Mankel, W. Jaegermann, M. M. Müller, H.-J. Kleebe, *Org. Electron.* **2012**, *13*, 1356.

[128]   R. Hock, T. Mayer, W. Jaegermann, *J. Mater. Chem. C* **2012**, *116*, 18146.

[129]   I. Irfan, M. Zhang, H. Ding, C. W. Tang, Y. Gao, *Org. Electron.* **2011**, *12*, 1588.

[130]   H. Schmidt, K. Zilberberg, S. Schmale, H. Flügge, T. Riedl, W. Kowalsky, *Appl. Phys. Lett.* **2010**, *96*, 243305.

[131]   M. R. Lilliedal, A. J. Medford, M. V Madsen, K. Norrman, F. C. Krebs, *Sol. Energy Mater. Sol. Cells* **2018**, *94*, 2018.

[132]   J. Kim, G. Kim, Y. Choi, J. Lee, S. H. Park, K. Lee, *J. Appl. Phys.* **2012**, *111*, 114511.

[133]   S. H. Kim, S. H. Park, K. Lee, *Curr. Appl. Phys.* **2010**, *10*, 3.

[134]   R. Steim, S. A. Choulis, P. Schilinsky, C. J. Brabec, *Appl. Phys. Lett.* **2008**, *92*, 093303.

[135] C. S. Kim, S. S. Lee, E. D. Gomez, J. B. Kim, Y. L. Loo, *Appl. Phys. Lett.* **2009**, *94*, 113302.

[136] S. Trost, K. Zilberberg, A. Behrendt, T. Riedl, *J. Mater. Chem.* **2012**, *22*, 16224.

[137] T. Ameri, G. Dennler, C. Lungenschmied, C. J. Brabec, *Energy Environ. Sci.* **2009**, *2*, 347.

[138] P. de Bruyn, D. J. D. Moet, P. W. M. Blom, *Org. Electron.* **2010**, *11*, 1419.

[139] D. Di Carlo Rasi, P. M. J. G. Van Thiel, H. Bin, K. H. Hendriks, H. L. Gaël, M. M. Wienk, T. Becker, Y. Li, T. Riedl, R. A. J. Janssen, **2019**, 1.

[140] J. Gilot, Polymer Tandem Solar Cells, **2010**.

[141] S. Esiner, H. Van Eersel, M. M. Wienk, R. A. J. Janssen, *Adv. Mater.* **2013**, *25*, 2932.

[142] S. Esiner, G. W. P. Van Pruissen, M. M. Wienk, R. A. J. Janssen, *J. Mater. Chem. A* **2016**, *4*, 5107.

[143] K. Zhang, B. Fan, R. Xia, X. Liu, Z. Hu, H. Gu, S. Liu, H. Yip, L. Ying, F. Huang, Y. Cao, *Adv. Energy Mater.* **2018**, *8*, 1703180.

[144] K. H. Hendriks, G. H. L. Heintges, V. S. Gevaerts, M. M. Wienk, R. A. J. Janssen, *Angew. Chemie* **2013**, *125*, 8499.

[145] H. Bin, L. Gao, Z. Zhang, Y. Yang, Y. Zhang, C. Zhang, S. Chen, L. Xue, C. Yang, M. Xiao, Y. Li, *Nat. Commun.* **2016**, *7*, 13651.

[146] S. Mahesh, J. M. Ball, R. D. J. Oliver, D. P. Mcmeekin, B. Johnston, H. J. Snaith, *Energy Environ. Sci.* **2020**, *13*, 258.

[147] C. Li, Y. Wang, W. C. H. Choy, *Small Methods* **2020**, *4*, 2000093.

[148] L. Zhan, S. Li, T. Lau, Y. Cui, X. Lu, M. Shi, C. Li, H. Li, J. Hou, H. Chen, *Energy Environ. Sci.* **2020**, *13*, 635.

[149] S. Gu, R. Lin, Q. Han, Y. Gao, H. Tan, J. Zhu, *Adv. Mater.* **2020**, *32*, 1907392.

[150] K. O. Brinkmann, T. Becker, F. Zimmermann, C. Kreusel, T. Gahlmann, M. Theisen, T. Haeger, S. Olthof, C. Tückmantel, M. Günster, T. Maschwitz, F. Göbelsmann, C. Koch, D. Hertel, P. Caprioglio, L. Merten, A. Hinderhofer, L. Gomell, S. Zhang, F. Schreiber, S. Albrecht, K. Meerholz, D. Neher, M. Stolterfoht, T. Riedl, *Nature* **2022**, *604*, 280.

[151] C. Yan, S. Barlow, Z. Wang, H. Yan, A. K. Jen, S. R. Marder, X. Zhan, *Nat. Rev. Mater.* **2018**, *3*, 18003.

[152] Q. Liu, Y. Jiang, K. Jin, J. Qin, J. Xu, W. Li, J. Xiong, J. Liu, *Sci. Bull.* **2020**, *65*, 272.

[153] J. Yuan, Y. Zhang, L. Zhou, G. Zhang, H. Yip, T. Lau, X. Lu, *Joule* **2019**, *3*, 1140.

[154] R. Yu, H. Yao, Y. Cui, L. Hong, C. He, J. Hou, *Adv. Mater.* **2019**, *31*, 1902302.

[155] Y. Zhu, A. Gadisa, Z. Peng, M. Ghasemi, L. Ye, Z. Xu, S. Zhao, H. Ade, *Adv. Energy Mater.* **2019**, *9*, 1900376.

[156] N. Gasparini, S. H. K. Paleti, J. Bertrandie, G. Cai, G. Zhang, A. Wadsworth, X. Lu, H. Yip, I. McCulloch, D. Baran, *ACS Energy Lett.* **2020**, *5*, 1371.

[157] A. Armin, W. Li, O. J. Sandberg, Z. Xiao, L. Ding, J. Nelson, D. Neher, K. Vandewal, S. Shoaee, T. Wang, H. Ade, T. Heumüller, C. J. Brabec, P. Meredith, *Adv. Energy Mater.* **2021**, 20003570.

[158] N. Liang, W. Jiang, J. Hou, Z. Wang, *Mater. Chem. Front.* **2017**, *1*, 1291.

[159] X. Du, T. Heumüller, W. Gruber, O. Almora, A. Classen, J. Qu, F. He, T. Unruh, N. Li, C. J. Brabec, *Adv. Mater.* **2020**, *32*, 1908305.

[160] R. Lin, K. Xiao, Z. Qin, Q. Han, C. Zhang, M. Wei, M. I. Saidaminov, Y. Gao, J. Xu, M. Xiao, A. Li, J. Zhu, E. H. Sargent, H. Tan, *Nat. Energy* **2019**, *4*, 864.

[161] F. Hao, C. C. Stoumpos, R. P. H. Chang, M. G. Kanatzidis, *J. Am. Chem. Soc.* **2014**, *136*, 8094.

[162] D. Zhao, C. Chen, C. Wang, M. M. Junda, Z. Song, C. R. Grice, Y. Yu, C. Li, B. Subedi, N. J. Podraza, X. Zhao, G. Fang, R. Xiong, K. Zhu, Y. Yan, *Nat. Energy* **2018**, *3*, 1093.

[163] H. Sun, T. Liu, J. Yu, T. Lau, G. Zhang, Y. Zhang, M. Su, Y. Tang, R. Ma, B. Liu, J. Liang, K. Feng, X. Lu, X. Guo, F. Gao, H. Yan, *Energy Environ. Sci.* **2019**, *12*, 3328.

[164] C.-W. Chen, Y.-S. Hsiao, C.-Y. Chen, H.-W. Kang, Z.-Y. Huang, H. Lin, *J. Mater. Chem. A* **2015**, *3*, 9152.

[165] E. Centurioni, *Appl. Opt.* **2005**, *44*, 7532.

[166] L. Perdigón-Toro, H. Zhang, A. Markina, J. Yuan, S. M. Hosseini, C. M. Wolff, G. Zuo, M. Stolterfoht, Y. Zou, F. Gao, D. Andrienko, S. Shoaee, D. Neher, *Adv. Mater.* **2020**, *32*, 1906763.

[167] Q. Lin, A. Armin, R. C. R. Nagiri, P. L. Burn, P. Meredith, *Nat. Photonics* **2015**, *9*, 106.

[168] Z. Jia, Q. Ma, Z. Chen, L. Meng, N. Jain, I. Angunawela, S. Qin, X. Kong, X. Li, Y. M. Yang, H. Zhu, H. Ade, F. Gao, Y. Li, *Nat. Commun.* **2023**, *14*, 1236.

[169] D. P. McMeekin, G. Sadoughi, W. Rehman, G. E. Eperon, M. Saliba, M. T. Hörantner, A. Haghighirad, N. Sakai, L. Korte, B. Rech, M. B. Johnston, L. M. Herz, H. J. Snaith, *Science (80-.).* **2016**, *351*, 151.

[170] S. Tao, I. Schmidt, G. Brocks, J. Jiang, I. Tranca, K. Meerholz, S. Olthof, *Nat. Commun.* **2019**, *10*, 2560.

[171] D. J. Slotcavage, H. I. Karunadasa, M. D. McGehee, *ACS Energy Lett.* **2016**, *1*, 1199.

[172] F. Peña-Camargo, P. Caprioglio, F. Zu, E. Gutierrez-partida, C. M. Wol, K. O. Brinkmann, S. Albrecht, T. Riedl, N. Koch, D. Neher, M. Stolterfoht, *ACS Energy Lett.* **2020**, *5*, 2728.

[173] T. Duong, H. Pham, T. C. Kho, P. Phang, K. C. Fong, D. Yan, Y. Yin, J. Peng, A. Mahmud, S. Gharibzadeh, B. A. Nejand, I. M. Hossain, M. R. Khan, N. Mozaffari, Y. Wu, H. Shen, J. Zheng, H. Mai, W. Liang, C. Samundsett, M. Stocks, K. Mcintosh, G. G. Andersson, U. Lemmer, B. S. Richards, U. W. Paetzold, A. Ho-ballie, Y. Liu, D. Macdonald, A. Blakers, J. Wong-leung, T. White, K. Weber, K. Catchpole, *Adv. Energy Mater.* **2020**, *10*, 1903553.

[174] T. Gahlmann, K. O. Brinkmann, T. Becker, C. Tückmantel, C. Kreusel, F. Van Hassend, S. Weber, T. Riedl, *Adv. Energy Mater.* **2020**, *10*, 1903897.

[175] C. R. Crowell, *Solid State Electron.* **1965**, *8*, 395.

[176] S. Zhang, C. Scheu, *Microscopy* **2018**, *67*, i133.

[177] A. F. Palmstrom, G. E. Eperon, T. Leijtens, R. Prasanna, S. N. Habisreutinger, W. Nemeth, E. A. Gaulding, S. P. Dunfield, M. Reese, S. Nanayakkara, T. Moot, J. Werner, J. Liu, B. To, S. T. Christensen, M. D. McGehee, M. F. A. M. van Hest, J. M. Luther, J. J. Berry, D. T. Moore, *Joule* **2019**, *3*, 2193.

[178] J. R. Bellingham, W. A. Phillips, C. J. Adkins, *J. Mater. Sci. Lett.* **1992**, *11*, 263.

[179] L. Hoffmann, K. O. Brinkmann, J. Malerczyk, D. Rogalla, T. Becker, D. Theirich, I. Shutsko, P. Görrn, T. Riedl, *ACS Appl. Mater. Interfaces* **2018**, *10*, 6006.

[180] Y. Hou, E. Aydin, M. De Bastiani, C. Xiao, F. H. Isikgor, D. Xue, B. Chen, H. Chen, B. Bahrami, A. H. Chowdhury, A. Johnston, S. Baek, Z. Huang, M. Wei, Y. Dong, J. Troughton, R. Jalmood, A. J. Mirabelli, T. G. Allen, E. van Kerschaver, M. I. Saidaminov, D. Baran, Q. Qiao, K. Zhu, S. De Wolf, E. H. Sargent, *Science (80-.).* **2020**, *367*, 1135.

[181] K. O. Brinkmann, T. Becker, F. Zimmermann, C. Kreusel, T. Gahlmann, T. Haeger, T. Riedl, *Sol. RRL* **2021**, *5*, 2100371.

[182] W. Chen, Y. Zhu, J. Xiu, G. Chen, H. Liang, S. Liu, H. Xue, E. Birgersson, J. W. Ho, X. Qin, J. Lin, R. Ma, T. Liu, Y. He, A. M.-C. Ng, X. Guo, Z. He, H. Yan, A. B. Djurišić, Y. Hou, *Nat. Energy* **2022**, *7*, 229.

[183] S.-Q. Sun, X. Xu, Q. Sun, Q. Yao, Y. Cai, X.-Y. Li, Y.-L. Xu, W. He, M. Zhu, X. Lv, F. R. Lin, A. K.-Y. Jen, T. Shi, H.-L. Yip, M.-K. Fung, Y.-M. Xie, *Adv. Energy Mater.* **2023**, *13*, 2204347.

[184] X. Wang, D. Zhang, B. Liu, X. Wu, X. Jiang, S. Zhang, Y. Wang, D. Gao, L. Wang, H. Wang, Z. Huang, X. Xie, T. Chen, Z. Xiao, Q. He, S. Xiao, Z. Zhu, S. Yang, *Adv. Mater.* **2023**, *35*, 2305946.

[185] K. O. Brinkmann, J. He, F. Schubert, J. Malerczyk, C. Kreusel, F. Van Hassend, S. Weber, J. Song, J. Qu, T. Riedl, *ACS Appl. Mater. Interfaces* **2019**, *11*, 40172.

[186] X. Zheng, Y. Hou, C. Bao, J. Yin, F. Yuan, Z. Huang, K. Song, J. Liu, J. Troughton, N. Gasparini, C. Zhou, Y. Lin, D. Xue, B. Chen, A. K. Johnston, N. Wei, M. N. Hedhili, M. Wei, A. Y. Alsalloum, P. Maity, B. Turedi, C. Yang, D. Baran, T. D. Anthopoulos, Y. Han, Z. Lu, O. F. Mohammed, F. Gao, E. H. Sargent, O. M. Bakr, *Nat. Energy* **2020**, *5*, 131.

[187] A. Al-Ashouri, A. Magomedov, M. Roß, M. Jost, M. Talaikis, G. Chistiakova, T. Bertram, J. A. Marquez, E. Köhnen, E. Kasparavicius, S. Levcenco, L. Gil-Escrig, C. J. Hages, R. Schlatmann, B. Rech, T. Malinauskas, T. Unold, C. A. Kaufmann, L. Korte, G. Niaura, V. Getautis, S. Albrecht, *Energy Environ. Sci.* **2019**, *12*, 3356.

[188] K. O. Brinkmann, P. Wang, F. Lang, W. Li, X. Guo, F. Zimmermann, S. Olthof, D. Neher, Y. Hou, M. Stolterfoht, T. Wang, A. B. Djurišić, T. Riedl, *Nat. Rev. Mater.* **2024**, *9*, 202.

[189] L. Zhu, M. Zhang, J. Xu, C. Li, J. Yan, G. Zhou, W. Zhong, T. Hao, J. Song, X. Xue, Z. Zhou, R. Zeng, H. Zhu, C. Chen, R. C. I. Mackenzie, Y. Zou, J. Nelson, Y. Zhang, Y. Sun, F. Liu, *Nat. Mater.* **2022**, *21*, 656.

[190] G. E. Park, S. Choi, S. Y. Park, D. H. Lee, M. J. Cho, *Adv. Energy Mater.* **2017**, *7*, 1700566.

[191] M. B. Upama, M. Wright, M. A. Mahmud, N. K. Elumalai, A. Mahboubi Soufiani, D. Wang, C. Xu, A. Uddin, *Nanoscale* **2017**, *9*, 18788.

[192] T. Liu, Q. C. Burlingame, M. R. Ivancevic, X. Liu, J. Hu, B. P. Rand, Y. Loo, *Adv. Energy Mater.* **2023**, *13*, 2300046.

[193]   Y. Li, X. Huang, K. Ding, K. M. Sheriff, H. Ade, S. R. Forrest, L. Ye, H. Liu, C. Li, *Nat. Commun.* **2021**, *12*, 1.

[194]   A. Labiod, O. A. Ibraikulov, S. D.- Seignon, S. Ferry, B. Heinrich, S. Méry, S. Fall, H. J. Tchognia Nkuissi, T. Heiser, C. Cabanetos, P. Leclerc, Nicolas, Lévêque, *Org. Electron.* **2022**, *107*, 106549.

[195]   A. J. Clarke, J. Luke, R. Meitzner, J. Wu, Y. Wang, H. K. H. Lee, E. M. Speller, H. Bristow, H. Cha, M. J. Newman, K. Hooper, A. Evans, F. Gao, H. Hoppe, I. McCulloch, U. S. Schubert, T. M. Watson, J. R. Durrant, W. C. Tsoi, J. Kim, Z. Li, *Cell Reports Phys. Sci.* **2021**, *2*, 100498.

[196]   S. Ben Dkhil, D. Duché, M. Gaceur, A. K. Thakur, F. B. Aboura, L. Escoubas, J. Simon, A. Guerrero, J. Bisquert, G. Garcia-belmonte, Q. Bao, M. Fahlman, C. Videlot-ackermann, O. Margeat, J. Ackermann, *Adv. Energy Mater.* **2014**, 1400805.

[197]   J. You, C. Chen, L. Dou, S. Murase, H. Duan, S. A. Hawks, T. Xu, H. J. Son, L. Yu, G. Li, Y. Yang, *Adv. Mater.* **2012**, *24*, 5267.

[198]   A. Manor, E. a. Katz, T. Tromholt, F. C. Krebs, *Adv. Energy Mater.* **2011**, *1*, 836.

[199]   Z. Kam, X. Wang, J. Zhang, J. Wu, *ACS Appl. Mater. Interfaces* **2015**, *7*, 1608.

[200]   M. Prosa, M. Tessarolo, M. Bolognesi, O. Margeat, D. Gedefaw, M. Gaceur, C. Videlot-ackermann, M. R. Andersson, M. Muccini, M. Seri, J. Ackermann, *ACS Appl. Mater. Interfaces* **2016**, *8*, 1635.

[201]   S. Trost, Elektronenextraktionsschichten Für Invertierte Organische Solarzellen, Univesity of Wuppertal, **2016**.

[202]   F. Verbakel, S. C. J. Meskers, R. A. J. Janssen, *Appl. Phys. Lett.* **2006**, *89*, 102103.

[203]   D. A. Melnick, *J. Chem. Phys.* **1957**, *26*, 1136.

[204]   W. H. Hirschwald, *Acc. Chem. Res.* **1985**, *18*, 228.

[205]   J. Reinhardt, M. Grein, C. Bühler, M. Schubert, U. Würfel, *Adv. Energy Mater.* **2014**, *4*, 1400081.

[206]   S. Semancik, D. F. Cox, *Sensors and Actuators* **1987**, *12*, 101.

[207]   H. J. Michel, H. Leiste, K. D. Schierbaum, J. Halbritter, *Appl. Surf. Sci.* **1998**, *126*, 57.

[208]   M. Batzill, U. Diebold, *Prog. Surf. Sci.* **2005**, *79*, 47.

[209]   Y. Lin, Y. Firdaus, F. H. Isikgor, M. I. Nugraha, E. Yengel, G. T. Harrison, R. Hallani, A. El-labban, H. Faber, C. Ma, X. Zheng, A. Subbiah, C. T. Howells, O. M. Bakr, I. Mcculloch, S. De Wolf, L. Tsetseris, T. D. Anthopoulos, *ACS Energy Lett.* **2020**, *5*, 2935.

[210]   F. Liu, L. Zhou, W. Liu, Z. Zhou, Q. Yue, W. Zheng, R. Sun, W. Liu, S. Xu, H. Fan, L. Feng, Y. Yi, W. Zhang, *Adv. Mater.* **2021**, *33*, 2100830.

[211]   K.-N. Zhang, Z.-N. Jiang, T. Wang, M.-S. Niu, L. Feng, C.-C. Qin, S.-K. So, X.-T. Hao, *Sol. RRL* **2020**, *4*, 2000165.

[212]   K. Zhou, J. Xin, W. Ma, *ACS Energy Lett.* **2019**, *4*, 447.

[213]   H. Hu, M. Ghasemi, Z. Peng, J. Zhang, J. J. Rech, W. You, H. Yan, H. Ade, *Adv. Mater.* **2020**, *32*, 2005348.

[214] Z. Peng, N. Stingelin, H. Ade, J. J. Michels, *Nat. Rev. Mater.* **2023**, *8*, 439.

[215] F. Liu, C. Li, J. Li, C. Wang, C. Xiao, Y. Wu, W. Li, *Chinese Chem. Lett.* **2019**, *31*, 865.

[216] P. Weitz, V. Marc, L. Corre, X. Du, K. Forberich, C. Deibel, C. J. Brabec, T. Heumüller, *Adv. Energy Mater.* **2023**, *13*, 2202564.

[217] N. Gasparini, M. Salvador, S. Strohm, T. Heumueller, I. Levchuk, A. Wadsworth, J. H. Bannock, J. C. de Mello, H. J. Egelhaaf, D. Baran, I. McCulloch, C. J. Brabec, *Adv. Energy Mater.* **2017**, *7*, 1.

[218] H. Cha, J. Wu, A. Wadsworth, J. Nagitta, S. Limbu, S. Pont, Z. Li, J. Searle, M. F. Wyatt, D. Baran, J. S. Kim, I. McCulloch, J. R. Durrant, *Adv. Mater.* **2017**, *29*, 1.

[219] Y. Jiang, L. Hu, X. Dong, F. Qin, T. Liu, L. Hu, X. Jiang, Y. Zhou, *Mater. Horizons* **2019**, *6*, 1438.

[220] N. P. Dasgupta, S. Neubert, W. Lee, O. Trejo, J.-R. Lee, F. B. Prinz, *Chem. Mater.* **2010**, *22*, 4769.

[221] S. A. Kukushkin, A. V Osipov, A. I. Romanychev, *Surf. Phys. Thin Film.* **2016**, *58*, 1448.

[222] V. Lujala, J. Skarp, M. Tammenmaa, T. Suntola, *Appl. Surf. Sci.* **1994**, *82/83*, 34.

[223] Ł. Wachnicki, T. Krajewski, G. Ł, B. Witkowski, B. Kowalski, K. Kopalko, J. Z. Domagala, M. Guziewicz, M. Godlewski, E. Guziewicz, *Thin Solid Films* **2010**, *518*, 4556.

[224] Y. Geng, L. Guo, S. Xu, Q. Sun, S. Ding, H. Lu, D. W. Zhang, *J. Phys. Chem. C* **2011**, *115*, 12317.

[225] J. W. G. Wildöer, L. C. Venema, A. G. Rinzler, R. E. Smalley, C. Dekker, *Nature* **1998**, *391*, 59.

[226] O. Pellegrino, M. Rei Vilar, G. Horowitz, A. M. Botelho do Rego, *Mater. Sci. Eng. C* **2002**, *22*, 367.

[227] J. A. Libera, J. N. Hryn, W. Elam, *Chem. Mater.* **2011**, *23*, 2150.

[228] V. Zardetto, B. L. Williams, A. Perrotta, F. Di Giacomo, M. A. Verheijen, R. Andriessen, W. M. M. Kessels, M. Creatore, *Sustain. Energy Fuels* **2017**, *1*, 30.

[229] W. Wei, Y. H. Hu, *Int. J. Energy Res.* **2017**, *41*, 1063.

[230] J. Yang, B. D. Siempelkamp, D. Liu, T. L. Kelly, *ACS Nano* **2015**, *9*, 1955.

[231] S. Zhang, I. Ahmet, S. Kim, O. Kasian, A. M. Mingers, P. Schnell, M. Ko, J. Lim, A. Fischer, K. J. J. Mayrhofer, S. Cherevko, B. Gault, R. Van De Krol, C. Scheu, *ACS Appl. Energy Mater.* **2020**, *3*, 9523.

[232] M. Shiga, K. Tatsumi, S. Muto, K. Tsuda, Y. Yamamoto, T. Mori, T. Tanji, *Ultramicroscopy* **2016**, *170*, 43.

[233] P. Caprioglio, S. Caicedo-Dávila, T. C. Yang, C. M. Wolff, F. Pena-Camargo, P. Fiala, B. Rech, C. Ballif, D. Abou-ras, M. Stolterfoht, S. Albrecht, Q. Jeangros, D. Neher, *ACS Energy Lett.* **2021**, *6*, 419.

[234] J. Meyer, P. Görrn, S. Hamwi, H.-H. Johannes, T. Riedl, W. Kowalsky, *Appl. Phys. Lett.* **2008**, *93*, 073308.

[235]   J. Jeong, M. Kim, J. Seo, H. Lu, P. Ahlawat, A. Mishra, Y. Yang, M. A. Hope, F. T. Eickemeyer, M. Kim, Y. J. Yoon, I. W. Choi, B. P. Darwich, S. J. Choi, Y. Jo, J. H. Lee, B. Walker, S. M. Zakeeruddin, L. Emsley, U. Rothlisberger, A. Hagfeldt, D. S. Kim, M. Grätzel, J. Y. Kim, *Nature* **2021**, *592*, 381.

[236]   https://www.nrel.gov/pv/cell-efficiency.html, "National Renewable Enery Laboratory, Best Research-Cell Efficiency Chart," **2023**.

[237]   J. A. Christians, J. S. Manser, P. V Kamat, *J. Phys. Chem. Lett.* **2015**, *6*, 852.

[238]   B. Yang, O. Dyck, J. Poplawsky, J. Keum, A. Puretzky, S. Das, I. Ivanov, C. Rouleau, G. Duscher, D. Geohegan, K. Xiao, *J. Am. Chem. Soc.* **2015**, *137*, 9210.

[239]   S. Moghadamzadeh, I. M. Hossain, T. Duong, S. Gharibzadeh, T. Abzieher, H. Pham, H. Hu, P. Fassl, U. Lemmer, B. A. Nejand, U. W. Paetzold, *J. Mater. Chem. A* **2020**, *8*, 24608.

[240]   G. Kakavelakis, T. Maksudov, D. Konios, I. Paradisanos, G. Kioseoglou, E. Stratakis, E. Kymakis, *Adv. Energy Mater.* **2017**, *7*, 1602120.

[241]   S. S. Mali, J. V Patil, H. Arandiyan, C. K. Hong, *J. Mater. Chem. A* **2019**, *7*, 17516.

[242]   M. Jeong, I. W. Choi, E. M. Go, Y. Cho, M. Kim, B. Lee, S. Jeong, Y. Jo, H. W. Choi, J. Lee, J. Bae, S. K. Kwak, D. S. Kim, C. Yang, *Science (80-.).* **2020**, *369*, 1615.

[243]   J. Li, H. Cao, X. Wang, H. Zhu, Z. Dong, L. Yang, S. Yin, *ACS Appl. Energy Mater.* **2019**, *2*, 2506.

[244]   S. Gharibzadeh, I. M. Hossain, P. Fassl, B. A. Nejand, T. Abzieher, M. Schultes, E. Ahlswede, P. Jackson, M. Powalla, S. Schäfer, M. Rienäcker, T. Wietler, R. Peibst, U. Lemmer, B. S. Richards, U. W. Paetzold, *Adv. Funct. Mater.* **2020**, *30*, 1909919.

[245]   G. Kim, H. Min, K. S. Lee, D. Y. Lee, S. M. Yoon, S. Il Seok, *Science (80-.).* **2020**, *370*, 108.

[246]   T. Duong, Y. Wu, H. Shen, J. Peng, X. Fu, D. Jacobs, E. Wang, T. C. Kho, K. C. Fong, M. Stocks, E. Franklin, A. Blakers, N. Zin, K. Mcintosh, W. Li, Y. Cheng, T. P. White, K. Weber, K. Catchpole, *Adv. Energy Mater.* **2017**, *7*, 1700228.

[247]   B. Chen, S. Baek, Y. Hou, E. Aydin, M. De Bastiani, B. Scheffel, A. Proppe, Z. Huang, M. Wei, Y. Wang, E. Jung, T. G. Allen, E. Van Kerschaver, F. P. G. De Arquer, M. I. Saidaminov, S. Hoogland, S. De Wolf, E. H. Sargent, *Nat. Commun.* **2020**, *11*, 1257.

[248]   R. Wang, J. Xue, K.-L. Wang, Z.-K. Wang, Y. Luo, D. Fenning, G. Xu, S. Nuryyeva, T. Huang, Y. Zhao, J. L. Yang, J. Zhu, M. Wang, S. Tan, I. Yavuz, K. N. Houk, Y. Yang, *Science (80-.).* **2019**, *366*, 1509.